Matthias Ruf

Experimental Multi-Scale Characterization Using Micro X-Ray Computed Tomography

14

Experimental Multi-Scale Characterization Using Micro X-Ray Computed Tomography

Von der Fakultät Bau- und Umweltingenieurwissenschaften
der Universität Stuttgart zur Erlangung der Würde
eines Doktor-Ingenieurs (Dr.-Ing.)
genehmigte Abhandlung

vorgelegt von

Matthias Ruf

aus

Singen (Hohentwiel)

Hauptberichter:	Prof. Dr.-Ing. Holger Steeb
Mitberichter:	Prof. Dr. Gioacchino Viggiani
	Dr. Beatriz Quintal

Tag der mündlichen Prüfung: 3. Juli 2023

Institut für Mechanik (Bauwesen) der Universität Stuttgart

Lehrstuhl für Kontinuumsmechanik

Prof. Dr.-Ing. H. Steeb

2023

Editors:

Prof. Dr.-Ing. Dr. h. c. W. Ehlers
Prof. Dr.-Ing. Dipl.-Math. techn. F. Fritzen
Prof. Dr.-Ing. M.-A. Keip
Prof. Dr.-Ing. H. Steeb

Acknowledgements

Abstract

The effective mechanical and hydro-mechanical behavior of porous media, granular solids, and related materials with complex morphologies is intimately linked to their internal microstructure on the pore/grain scale. For microstructural characterization, transmission micro X-Ray Computed Tomography (µXRCT) has emerged as a crucial three-dimensional (3D) imaging technique that can provide structural information from the micrometer to centimeter scale. Due to its non-destructive nature, it can be excellently combined with time-dependent investigations, either ex situ or in situ. In particular, the possibility of coupling mechanical or hydro-mechanical characterization with µXRCT-based 3D imaging in situ allows many physical phenomena to be studied in more detail and consequently understood more comprehensively. For example, the microstructure evolution can be observed under various controlled boundary conditions and linked to measured effective quantities. New insights and improved understanding can ultimately positively influence modeling approaches.

In order to be able to perform such multi-scale studies, a modular, open, and versatile lab-based µXRCT system was developed within the scope of this work. It provides a spatial resolution of down to less than $10\,\mu m$. The developed system has an integrated universal testing machine that enables in situ compressive, tensile, and torsional studies as well as their combinations, parallel or sequential. Furthermore, hydro-mechanical coupled phenomena can be investigated using appropriate equipment, such as triaxial flow cells. Thanks to the open and modular concept, the developed system can be used in the future for a wide variety of multiphysics research questions and can be considered as an open experimental platform.

Employing the established system, various multi-scale phenomena from different material classes are motivated and partly investigated in more detail within this work. For this purpose, classical experimental characterization methods are combined with µXRCT-based 3D imaging ex situ as well as in situ. Among others, 3D imaging is combined with ultrasound wave propagation measurements to investigate the influence of artificially generated crack networks in Carrara marble by different thermal treatment protocols. Load-sequence effects are demonstrated on an open-cell foam sample. An in situ workflow is shown to investigate the not-well-understood effective stiffness behavior of biphasic monodisperse granular packings of stiff and soft particles of different volume fractions at different stress states. The fracturing of a rock sample in a triaxial flow cell shows possibilities of application in the context of fracture mechanics. All resulting data sets, including metadata, are available via the Data Repository of the University of Stuttgart (DaRUS).

Kurzzusammenfassung

Das effektive mechanische und hydromechanische Verhalten auf der Kontinuumsskala von porösen Medien, granularen Festkörpern sowie verwandten Materialien mit komplexer Morphologie ist eng mit ihrer Mikrostruktur auf der Poren-/Kornskala verknüpft. Für die Charakterisierung der Mikrostruktur hat sich die absorptionsbasierte mikro-Röntgen-Computertomographie (µXRCT) als wichtiges dreidimensionales (3D) bildgebendes Verfahren etabliert, das Informationen von der Mikrometer- bis zur Zentimeter-Skala liefern kann. Da es sich um ein zerstörungsfreies Verfahren handelt, kann dieses hervorragend mit zeitabhängigen Untersuchungen ex-situ als auch in-situ verbunden werden. Insbesondere durch die Möglichkeit der Kopplung von mechanischer beziehungsweise hydromechanischer Charakterisierung mit der µXRCT-basierten 3D-Bildgebung in-situ lassen sich viele physikalische Phänomene genauer untersuchen und folglich umfänglicher verstehen. Zum Beispiel lässt sich die Evolution der Mikrostruktur unter verschiedensten kontrollierten Randbedingungen beobachten und letztlich eine Verbindung mit Messgrößen auf der effektiven Skala herstellen. Neue Erkenntnisse beziehungsweise ein verbessertes Verständnis kann sich letztendlich positiv auf Modellierungsansätze auswirken.

Um solche Multiskalenuntersuchungen durchführen zu können, wurde im Rahmen dieser Arbeit ein modulares, offenes und vielseitig einsetzbares Labor-basiertes µXRCT-System entwickelt, das eine räumliche Auflösung von bis zu weniger als $10\,\mu m$ bietet. Dieses System verfügt über eine integrierte Universalprüfmaschine und ermöglicht in-situ Druck-, Zug- und Torsionsuntersuchungen sowie deren Kombinationen, parallel oder sequenziell. Durch den Einsatz entsprechender Apparaturen wie beispielsweise triaxialer Durchflusszellen, lassen sich darüber hinaus hydromechanisch gekoppelte Phänomene untersuchen. Dank des offenen und modularen Konzepts kann dieses System in Zukunft für unterschiedlichste multiphysikalische Fragestellungen eingesetzt und als offene experimentelle Plattform verstanden werden.

Mittels des etablierten Systems werden verschiedene Multiskalenphänomene aus unterschiedlichen Materialklassen motiviert und teils vertieft untersucht. Dazu werden klassische experimentelle Charakterisierungsmethoden mit der µXRCT-basierten 3D-Bildgebung ex-situ als auch in-situ kombiniert. Unter anderem wird die 3D-Bildgebung in Kombination mit Ultraschallwellenausbreitungsmessungen genutzt, um den Einfluss verschiedener thermischer Behandlungsprotokolle zur künstlichen Rissnetzwerkerzeugung in Carrara Marmor zu untersuchen. Belastungs-Reihenfolgeeffekte werden an einer offenzelligen Schaumprobe demonstriert. Es wird ein Arbeitsablauf gezeigt, um das effektive Steifigkeitsverhalten zweiphasiger monodisperser granularer Packungen bestehend aus steifen und weichen Partikeln unterschiedlicher Volumenanteile bei unterschiedlichen Spannungszuständen bildgebend zu untersuchen. Die Rissbildung in einer Gesteinsprobe in einer triaxialen Durchflusszelle zeigt Möglichkeiten der Anwendung im Rahmen der Bruchmechanik. Sämtliche entstandenen Datensätze inklusive Metadaten stehen über das Daten Repositorium der Universität Stuttgart (DaRUS) zur freien Verfügung.

Contents

Deutschsprachige Zusammenfassung

Motivation

Das effektive mechanische und hydromechanische Verhalten auf der Kontinuumsskala von porösen Medien, granularen Festkörpern sowie verwandten Materialien mit komplexer Morphologie ist eng mit ihrer Mikrostruktur auf der Poren-/Kornskala verbunden. Für ein besseres allgemeines Verständnis, aber auch für zahlreiche Anwendungen, ist es von entscheidender Bedeutung, die makroskopische Skala in Kombination mit der Mikroskala zu betrachten. Für die Charakterisierung der Mikroskala spielen bildgebende Verfahren eine große Rolle. Poröse Medien, u.a., sind wie Festkörper von Natur aus nicht transparent. Es gibt jedoch verschiedene zerstörungsfreie hochauflösende dreidimensionale (3D) Bildgebungsverfahren, mit denen sich die innere Struktur auflösen lässt. Auf der Grundlage solcher 3D-Bilder kann die Mikrostruktur auf verschiedene Weise analysiert und charakterisiert werden. Die verfügbaren bildgebenden Verfahren lassen sich nach dem zugrundeliegenden physikalischen Prinzip, den untersuchbaren Materialien, der erreichbaren Auflösung, der Größe des Sichtfelds und damit der Probengröße und anderen Kriterien unterscheiden. Die absorptionsbasierte mikro-Röntgen-Computertomographie (µXRCT), die Informationen vom Mikrometer- bis zum Zentimetermaßstab liefern kann, hat sich über die vergangenen Jahre in vielen wissenschaftlichen Bereichen zu einer Standard-3D-Bildgebungsmethode entwickelt.

Da es sich bei der µXRCT um ein zerstörungsfreies Bildgebungsverfahren handelt, kann dieses sehr gut mit zeitaufgelösten Untersuchungen verbunden werden. Abhängig vom genauen Untersuchungsvorhaben kann das eigentliche Experiment dabei ex-situ, in-situ oder, wie bei zerstörenden Methoden üblich, post mortem durchgeführt werden. Die ex-situ Untersuchung ist an viele Randbedingungen geknüpft. Am wichtigsten ist, dass das zu untersuchende Objekt durch den Ein- und Ausbau nicht beeinträchtigt wird, d.h. die entsprechenden Randbedingungen erhalten werden, was oft schwierig oder sogar unmöglich ist. Für sehr langsam ablaufende Untersuchungen (z.B. Kriech-, Korrosions-, Auflösungs-, und Ausfällungsvorgänge) ist die ex-situ Untersuchung trotzdem meist der bevorzugte Ansatz, da das verwendete Bildgebungssystem nicht für längere Zeit (Tage bis mehrere Monate) "blockiert" wird. Darüber hinaus gibt es Experimente, die nicht ohne erheblichen Aufwand innerhalb eines µXRCT-Systems durchgeführt werden können. Für viele Untersuchungen kann die in-situ Durchführung jedoch aus unterschiedlichsten Gründen als Goldstandard erachtet werden. Im Zusammenhang mit der mechanischen und hydromechanischen Charakterisierung von Deformationsexperimenten (z.B. Zug-/Druckversuch) und hydromechanisch gekoppelten Prozessen in porösen Medien ist diese besonders relevant.

Abbildung 0.1 zeigt ein Beispiel für einen in-situ durchgeführten einachsigen Druckversuch an einer offenzelligen Polyurethanschaumprobe. Die effektive Spannungs-Dehnungskurve kann in die drei Bereiche eingeteilt werden: (i) linear-elastischer Bereich, (ii) Kollapsbereich und (iii) Verdichtungsbereich. Durch die µXRCT-Bildgebung bei verschiedenen
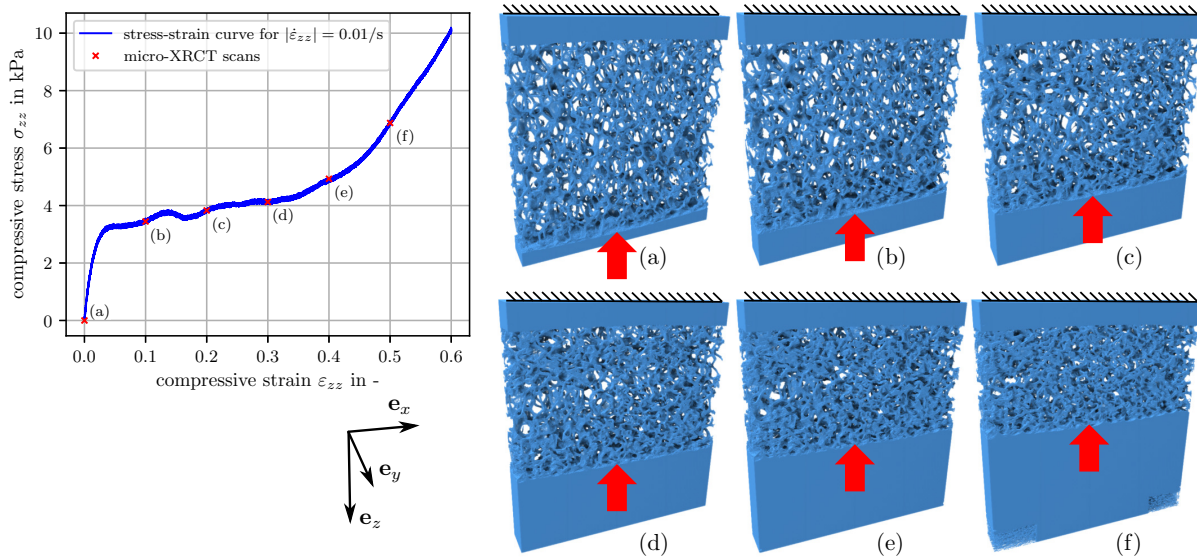
Abbildung 0.1: Einachsiger Druckversuch einer offenzelligen, retikulierten Polyurethan (PUR) Schaumprobe (10 Poren pro Zoll) mit Veränderung der Mikrostruktur bei verschiedenen Deformationszuständen. Die Bilder zeigen ein segmentiertes Teilvolumen des mittleren Bereichs der zylindrischen Schaumstoffprobe (Durchmesser 52 mm, Länge 50 mm) und demonstrieren den elastischen Kollaps des porösen Mediums [104].

Verformungszuständen kann die makroskopisch beobachtbare Materialantwort verstanden werden. Zum Beispiel wird das Plateau der Spannungs-Dehnungs-Kurve durch ein ausgeprägtes elastisches Ausknicken der Zellstege verursacht, die hauptsächlich parallel zur Belastungsrichtung ausgerichtet sind, wodurch der sogenannte Kollapsbereich entsteht. Die aus den 3D-Bildern gewonnene Geometrie kann für verschiedenste numerische Untersuchungen und Modellierungsansätze genutzt werden. Weitere Beispiele sind Strömungsprozesse durch poröse Medien unter Reservoir-Bedingungen (hoher Druck und Temperatur) oder das Verhalten von Rissen unter solchen Bedingungen.

Um derartige in-situ Experimente überhaupt durchführen zu können, müssen jedoch zunächst geeignete Apparaturen entwickelt und implementiert werden. Nur damit lassen sich die entsprechenden Randbedingungen für das Experiment aufbringen und kontrollieren und eventuell weitere Größen messen. Je nach Art des Experiments handelt es sich bei den dafür verwendeten Apparaturen oft um sehr spezifische Einzellösungen.

Im Rahmen dieser Arbeit wurde ein modular aufgebautes, offenes, und vielseitig einsetzbares µXRCT-System entwickelt, das neben hochauflösenden Scans von Objekten unter Umgebungsbedingungen eine offene experimentelle Plattform für mechanische und hydromechanische in-situ Untersuchungen verschiedenster Materialien und Prozesse bietet. Durch die Integration einer Universalprüfmaschine ist es verhältnismäßig einfach, in-situ Druck-/Zug- und Torsionsprüfungen sowie deren Kombination (mehrachsige Belastung) gleichzeitig oder nacheinander durchzuführen. Bei nichtlinearem Materialverhalten, kann die multiaxiale Belastung zu Reihenfolgeneffekten führen (keine lineare Superposition), die aus Sicht der mechanischen Modellierung sehr interessant und anspruchsvoll sind. Durch die Möglichkeit der axialen Lastaufbringung durch die integrierte Prüfmaschine

ist die Implementierung von triaxialen Durchflusszellen für hydromechanisch gekoppelte Fragestellungen einfach umsetzbar. Ebenso einfach ist die Durchführung von Ermüdungsversuchen mittels Piezo-Aktuatoren bei unterschiedlichen Druckschwellbelastungen. Auch die Untersuchung anderer multiphysikalischer Probleme (Kopplung mechanischer, hydraulischer, thermischer, chemischer, usw. Prozesse) ist in Zukunft denkbar und mit entsprechenden Erweiterungen zu realisieren.

Mittels des etablierten Systems wurden im Rahmen dieser Arbeit verschiedene Multiskalenphänomene aus unterschiedlichen Materialklassen (poröse Medien, Schäume, granulare Festkörper) betrachtet. Dazu wurde die traditionelle experimentelle Charakterisierung mit der µXRCT basierten Bildgebung in unterschiedlichster Weise ex-situ und in-situ kombiniert. Im Einzelnen wurde die Bildgebung kombiniert mit (i) mechanischer Belastung, (ii) mechanischer Belastung gekoppelt mit Ultraschallwellenausbreitungsmessungen sowie, (iii) hydromechanischen Untersuchungen.

Stand der Forschung

Bildgebende Verfahren bieten die Möglichkeit, die Mikrostruktur von Materialien aufzulösen und darauf basierend zu charakterisieren. Zu den klassischen bildgebenden Techniken zählen beispielsweise die Lichtmikroskopie und die Rasterelektronenmikroskopie [30]. Ein wesentlicher Nachteil dieser klassischen bildgebenden Verfahren ist jedoch, dass man auf die Untersuchung einer zweidimensionalen (2D) Darstellung eines 3D-Objekts beschränkt ist. Es wird kritisch, wenn die zu untersuchende Probe nicht ohne weiteres geschnitten werden kann oder wenn die Gefahr besteht, dass dadurch die Mikrostruktur beeinträchtigt wird. Da es sich zudem meist um zerstörende Verfahren handelt, sind zeitaufgelöste Untersuchungen schwierig oder überhaupt nicht möglich. Aus diesem Grund wurden 3D-Bildgebungsverfahren entwickelt. Eine Übersicht und Vergleich gängiger Methoden im materialwissenschaftlichen Kontext findet sich beispielsweise in Referenz [137].

Eine sehr wichtige Methode ist die absorptionsbasierte Röntgen-Computertomographie (XRCT), die auf der materialabhängigen Abschwächung von Röntgenstrahlung beruht [13, 146]. Durch einen Rotationsscan werden zahlreiche Projektionsbilder des zu untersuchenden Objekts aufgenommen, auf deren Grundlage die innere Struktur des Objekts digital rekonstruiert werden kann. Ursprünglich wurde die XRCT-Bildgebung von und für die Medizin entwickelt. Während die herkömmliche medizinische XRCT-Bildgebung im Allgemeinen Auflösungen im Submillimeterbereich oder weniger nutzt (Voxelgrößen $\geq 100\,\mu\text{m}$), bezieht sich die µXRCT-Bildgebung auf Auflösungen im Mikrometerbereich (Voxelgrößen $\geq 0.1\,\mu\text{m}$). Darüber hinaus sind bei der nano-XRCT-Bildgebung Auflösungen im Nanometerbereich möglich (Voxelgrößen bis zu $\approx 10\,\text{nm}$ klein) [146]. Die zeitliche Entwicklung entspricht dabei der Reihenfolge der genannten Verfahren. Es muss jedoch beachtet werden, dass mit zunehmender Auflösung die Probengröße immer kleiner und die Scandauer aufgrund des geringeren möglichen Röntgenstrahlflusses in Laborsystmen deutlich zunimmt. Je nach geforderter Scanqualität und Auflösung sind Scanzeiten von bis zu 20 Stunden und mehr für eine 3D-Bildgebung keine Seltenheit. Für die im Rahmen dieser Arbeit relevanten Fragestellungen und Untersuchungen zu mechanischen

und hydromechanischen Mehrskalenproblemen, die versuchen, die mikrostrukturelle Ebene (Poren-/Kornskala) mit der Kontinuumsskala zu verbinden, können die Proben aus repräsentativen Gründen nicht beliebig klein werden. In diesem Zusammenhang bietet die µXRCT-Bildgebung einen hervorragenden Kompromiss zwischen der erreichbaren Auflösung, der Größe des Sichtfelds und der Probengröße. Die µXRCT hat ihren Weg in eine Vielzahl von Forschungsgebieten gefunden, wie verschiedene Übersichtsarbeiten im Kontext der Materialwissenschaften [66, 115, 116, 126–128, 137], Geowissenschaften und Geologie [15, 144], Biologie und Biomimikry (Bionik) [73, 79], Lebensmittelwissenschaften [118] bis hin zur Qualitätsbewertung von landwirtschaftlichen Produkten [55] zeigen.

Da es sich um eine zerstörungsfreie Methode handelt, ist die µXRCT-Bildgebung oft der erste Schritt in einem mehrstufigen Charakterisierungsprozess, in dem auch andere zerstörende Bildgebungsverfahren involviert sind. Zudem ermöglicht erst die Zerstörungsfreiheit der Methode zeitaufgelöste Untersuchungen. In diesem Zusammenhang wird häufig der Begriff "4D µXRCT" verwendet. Damit soll die räumliche und zeitliche Auflösung zum Ausdruck kommen. Jeder Zeitschritt wird durch einen vollständigen µXRCT-Scan repräsentiert. Je nach technischer Ausführung der Bildgebung kann dabei zwischen (i) Zeitraffer-Bildgebung und (ii) dynamischer bzw. kontinuierlicher Bildgebung unterschieden werden. Die Zeitraffer-Bildgebung kann dabei noch weiter in ex-situ sowie un/unterbrochenes in-situ Scannen unterteilt werden [23, 25]. Bis auf wenige Ausnahmen bezieht sich die dynamische bzw. kontinuierliche Bildgebung derzeit noch hauptsächlich auf die sogenannte Synchrotron-basierte µXRCT [23].

Die Synchrotron-basierte µXRCT [82, 124] ist von der Labor-basierten µXRCT abzugrenzen. Diese kann jedoch nur an speziellen Teilchenbeschleunigern praktiziert werden. Synchrotron-Röntgenstrahlung ist in ihrer sogenannten Brillanz (Photonen/Zeit/Fläche/Raumwinkel/Energiebandbreite) und Monochromatizität nicht direkt mit der Strahlung einer laborgestützten Röntgenquelle vergleichbar. Die hohe Brillanz von Synchrotronstrahlung führt zu weniger systematischen Bildartefakten und ermöglicht zeitlich deutlich höher aufgelöste Scans. Letzteres ist vor allem für die Untersuchung von transienten Phänomenen von großer Bedeutung. So berichtete beispielsweise Referenz [65] über einen in-situ Zugversuch der mit 20 Hz (vollständige Scans) zeitlich aufgelöst wurde, durchgeführt an der TOMCAT-Beamline der Swiss Light Source (SLS) [123].

In den letzten zwei Jahrzehnten haben immer mehr Forscher:innen aus verschiedenen Bereichen von den Möglichkeiten der in-situ µXRCT-Bildgebung profitiert, wie die wachsende Anzahl an Veröffentlichungen zeigt [128, 152]. Zur Durchführung der eigentlichen Untersuchung werden in erster Linie hochspezifische, speziell angefertigte Zellen verwendet, welche die Randbedingungen des zu untersuchenden Prozesses nachbilden können. Eine Übersicht über die typischerweise eingesetzten Zellen für verschiedene Zwecke wie monotone Zug-/Druckbelastung, zyklische Belastung und thermische Beanspruchung (Wärme sowie Kühlung) ist in Referenzen [10, 24] zu finden. Designs von Zellen (Triaxialzellen und triaxiale Durchflusszellen) zur Untersuchung von Geomaterialien und Gesteinen unter hohem Druck und hoher Temperatur werden beispielsweise in Referenzen [22, 84] beschrieben. Die Spezifikationen der Zellen basieren in der Regel auf den genauen atmosphärischen Bedingungen, die nachgeahmt werden sollen, auf der vorgesehenen Probengröße sowie teils auch auf der genutzten Bildgebungshardware.

Auch wenn die Synchrotron-basierte µXRCT sehr viele Vorteile bietet, so ist die Labor-basierte µXRCT, vor allem aus Gründen der einfachen Zugänglichkeit, für viele Forscher:innen sehr interessant. Folglich entwickeln sich die Labor-basierten Möglichkeiten parallel. Hervorzuheben ist vorallem, dass bei vielen Untersuchungen die Bildgebungsgeschwindigkeit nur sekundär relevant ist, da viele Prozesse langsam ablaufen, periodisch sind oder näherungsweise in einem Gleichgewichtszustand angehalten werden können. Es erscheinen zunehmend mehr Arbeiten, die reine in-situ Laboruntersuchungen hervorheben. Eine Übersichtsarbeit über Labor-basierte in-situ Untersuchungen mit Schwerpunkt auf technischen Materialien findet sich in Referenz [150]. Darüber hinaus werden vermehrt Apparaturen für in-situ Untersuchungen vorgestellt, die intrinsisch für den Einsatz in Laborsystemen konzipiert sind [21, 151]. Beispielsweise wurde jüngst eine Apparatur vorgestellt, die Untersuchungen bis zu $1000\,°C$ ermöglichen soll [151]. Darüber hinaus gibt es vielversprechende Ansätze, um beispielsweise das Verschiebungsfeld im Rahmen eines Deformationsversuchs aus einer sehr geringen Anzahl an betrachteten Projektionswinkeln zu ermitteln, wenn ein vollständig hochaufgelöster Scan des initialen Probenzustands vorliegt [48, 60, 131]. Außerdem gibt es den ersten kommerziellen Laborscanner "Dyna-Tom" [16, 43], der für dynamische Untersuchungen optimiert ist. Dieser soll unter optimalen Bedingungen vollständige Scans in weniger als $10\,s$ ermöglichen [16]. Mikrofokus-Röntgenquellen, die auf einer Flüssigmetall-Jet-Anode anstelle einer Festkörper-Anode basieren und daher deutlich höhere Röntgenflüsse liefern können, sind ebenfalls eine äußerst vielversprechende Technologie, die eine weitere signifikante Steigerung der Bildgebungsgeschwindigkeit und -möglichkeiten in Labor-basierten Systemen bietet [19, 33, 58].

Bislang wurde nur die absorptionsbasierte µXRCT-Bildgebung betrachtet. Anstatt den physikalischen Effekt der materialabhängigen Röntgenstrahlungsabschwächung zu nutzen, können auch andere Wechselwirkungsmechanismen von Röntgenstrahlung mit Materie wie Phasenverschiebung [9, 68, 78], Streuung [27], Beugung [81, 127], und Fluoreszenzanalyse [67] ausgenutzt werden. Diese Verfahren können sehr hilfreich sein, wenn die Kontrastinformationen aus der absorptionsbasierten µXRCT nicht ausreichend sind oder komplementäre Informationen erforderlich sind [44, 127]. Jedoch sind nicht alle Verfahren Labor-basiert physikalisch möglich. Neben Verfahren, die Röntgenstrahlung einsetzen, gibt es weitere Möglichkeiten, die für die 3D-Bildgebung in Frage kommen. Zu nennen sind hier die Magnetresonanztomographie [8], die Neutronentomographie [124], die Ultraschalltomographie [53], die Elektronentomographie [59] und die photoakustische Tomographie [49], ohne Anspruch auf Vollständigkeit.

Zusammenfassend lässt sich sagen, dass es eine breite Palette von 3D-Bildgebungsverfahren gibt, die auf unterschiedlichen physikalischen Effekten basieren. Die Unterschiede liegen in der Auflösung und damit verbunden im untersuchbaren Probenvolumen, in der Aufnahmegeschwindigkeit und in der Empfindlichkeit gegenüber der chemischen Probenzusammensetzung. Ein wesentlicher Vorteil der Labor-gestützten absorptionsbasierten µXRCT-Bildgebung ist ihr einfaches physikalisches Prinzip und damit einhergehend deren Implementieurng. All dies macht sie zu einer ausgezeichneten Methode, um die innere Morphologie vom Mikrometer- bis zum Zentimetermaßstab eines breiten Spektrums von Materialien zu visualisieren und zahlreiche mechanische und hydromechanische Multiskalenphänomene zu untersuchen.

Gliederung der Arbeit

Die vorliegende Dissertation ist kumulativ und in zwei Teile gegliedert. Im Rahmen der Präambel, **Kapitel 1–3**, erfolgt die Einordnung sowie die Vermittlung der erforderlichen Grundlagen. Die angehängten **Kapitel I–IV** im zweiten Teil der Arbeit sind Kopien von Zeitschriftenartikeln, die für diese Dissertation verwendet werden. Die Ko-Autorenschaft wurde genutzt, um an zahlreichen Forschungsprojekten mitzuwirken. Eine Auswahl der daraus entstandenen Arbeiten ist in **Appendix A–C** enthalten. Sie dienen als erweiterte Anwendungsbeispiele untersuchter Mehrskalenphänomene im Rahmen dieser Arbeit. Eine Liste sämtlicher Veröffentlichungen findet sich im nächsten Abschnitt bzw. in Abschnitt 1.4.

Präambel

Nach dem einleitenden **Kapitel 1** gliedert sich die Arbeit wie folgt.

Kapitel 2 befasst sich mit den zum Verständnis der folgenden Kapitel erforderlichen Grundlagen und ist in zwei Abschnitte unterteilt. In Abschnitt 2.1 werden die wichtigsten Elemente der absorptionsbasierten µXRCT-Bildgebung zusammengefasst. Die Physik der Röntgenstrahlen, ihre Wechselwirkung mit der Materie und die Röntgenbildgebung, auf der die µXRCT direkt basiert, werden behandelt. Ein Schlüsselelement der µXRCT ist die Volumenrekonstruktion des untersuchten Objekts auf der Grundlage vieler aufgenommener Projektionsbilder aus verschiedenen Richtungen. Da dies ein grundlegender und konsequent durchgeführter Schritt innerhalb der Arbeit ist, wird der angewandte FDK-Algorithmus motiviert. Darüber hinaus werden die Themen Bildqualität und Artefakte angeschnitten. Diese zu kennen und zu verstehen ist für die korrekte Dateninterpretation und die richtige Auswahl der Bildgebungsparameter unerlässlich.

Ein Ziel der vorliegenden Arbeit ist die Etablierung eines vielseitig einsetzbaren Instruments zur Visualisierung der Mikrostruktur von Materialien unter mechanischen und hydromechanischen Belastungsbedingungen, um damit verschiedene Multiskalenphänomene untersuchen zu können. Das heißt, ausgehend von einer Referenzkonfiguration wird eine neue Konfiguration erreicht (Gleichgewichtszustand vorausgesetzt), von der eine neue Momentaufnahme der veränderten Mikrostruktur erstellt wird. Die Verbindung zur klassischen Kontinuumsmechanik ergibt sich aus den Veränderungen, z.B. der Verformung der inneren Struktur, die im Idealfall aus einer Zeitreihe von 3D-Bildern extrahiert werden kann, z.B. durch Bildkorrelationsverfahren. Im Falle einer Deformation kann eine Verbindung zu der in der Kontinuumsmechanik verwendeten kinematischen Beschreibung hergestellt werden. Daher sind in Abschnitt 2.2 einige Grundlagen der Kontinuumsmechanik zusammengefasst, gefolgt von einer kurzen Beschreibung der eingesetzten mechanischen und hydromechanischen Untersuchungsmethoden.

Die darauf aufbauenden Kapitel (Publikationen) finden sich in den **Kapiteln I–IV**. Deren Inhalt und Einordnung in den Gesamtkontext der vorliegenden Arbeit wird im nächsten Unterabschnitt ausführlicher dargelegt. Abschließend wird die vorliegende Arbeit in **Kapitel 3** zusammengefasst, gefolgt von einem kurzen Ausblick.

Publikationen

In **Kapitel I** wird die Implementierung, die Leistungsevaluation und die Demonstration eines selbst entwickelten und aufgebauten offenen, modularen und flexibel einsetzbaren µXRCT-Systems vorgestellt. Ein Beispiel, dass die Vorteile des modularen Systemkonzepts verdeutlichen soll, ist die hardwarebasierte Verbesserung von Ringartefakten auf der Grundlage einer Pixelkarte des Detektors, die zwischen schlechten und guten Detektor-Pixeln unterscheidet. Durch das offene Konzept des Systems, stellt dieses eine optimale Ausgangsplattform zur Durchführung von in-situ Multiphysik-Experimenten durch entsprechende Erweiterungen dar, wie mittels einem Beispiel demonstriert wird. Das System wurde in vielen verschiedenen Forschungskooperationen eingesetzt. Es wurden zahlreiche verschiedene Arten von Materialien untersucht und erste post mortem- und Zeitraffer ex-/in-situ-Experimente durchgeführt. Ausgewählte Datensätze, einschließlich Metadaten, wurden als Teil der zugehörigen Veröffentlichungen oder als unabhängige Datensätze unter CC BY-Lizenz über das Daten-Repositorium der Universität Stuttgart (DaRUS) veröffentlicht, was die breite Palette möglicher Anwendungen sowie die erreichte Bildqualität demonstriert. Als anspruchsvolles hochauflösendes Beispiel wird in dieser Arbeit der Scan einer Carrara-Marmorkernprobe gezeigt, in die durch thermische Behandlung ein Rissnetzwerk künstlich eingebracht wurde. Aufgrund der begrenzten räumlichen Auflösung ist die zuverlässige Segmentierung und Quantifizierung von Größen wie die Rissöffnung schwierig. In einem solchen Fall sind die Möglichkeiten der bildbasierten Charakterisierung begrenzt und insbesondere die Quantifizierung bedarf Vorsicht, wie in der separaten gemeinsamen Arbeit Lee *et al.* [61] ausführlicher dargestellt wird.

Basierend auf dem im vorangegangenen Kapitel vorgestellten Beispiel wurde in **Kapitel II** das entwickelte µXRCT-System verwendet, um die Auswirkungen verschiedener Wärmebehandlungsprotokolle auf Carrara-Marmor Kernproben genauer zu untersuchen. Insbesondere wurde der Einfluss einer schnellen gegenüber einer langsamen Abkühlung und die damit verbundenen Auswirkungen auf die Probengröße untersucht. Die µXRCT-Bildgebung hilft, die Mechanismen auf der Mikroskala besser zu verstehen. Die weitere Quantifizierung der resultierenden Rissnetzwerke zur Unterscheidung zwischen den Protokollen ist jedoch schwierig und teilweise sogar unmöglich, je nach angewandter Wärmebehandlungsmethode. In Folge dessen, wurde ergänzend auf traditionelle, nicht-invasive Charakterisierungtechniken zurückgegriffen. Es wurden P-Wellen- und S-Wellen-Geschwindigkeitsmessungen sowie Messungen der effektiven Volumenänderung durchgeführt. In Kombination mit den qualitativen Ergebnissen aus der 3D-Bildgebung konnte das erzeugte relative Rissvolumen als treibende Größe auf der Mikroskala für die Entwicklung der effektiven Ultraschallwellengeschwindigkeiten identifiziert werden. Dieses Kapitel zeigt einerseits den Nutzen von 3D-Bilddaten, andererseits aber auch die Notwendigkeit, diese mit anderen physikalischen Charakterisierungsmethoden zu kombinieren bzw. evaluieren, was hier in einem ex-situ/post mortem Multiskalenansatz durchgeführt wurde.

Kapitel III befasst sich mit der Erweiterung des in **Kapitel I** vorgestellten µXRCT-Systems durch die Integration eines Lastrahmen unter Verwendung einer Universalprüfmaschine. Dieser Ansatz bietet die Möglichkeit, flexibel verschiedene mechanische (Druck, Zug und Torsion) und in Kombination mit speziellen Zellen auch hydromechanische Experimente in-situ durchzuführen. Es werden drei in-situ durchgeführte Beispiele ver-

schiedener Materialklassen motiviert und ausgewählte Ergebnisse gezeigt. Das erste Beispiel befasst sich mit der lastfolgeabhängigen Verformung einer Polyurethanschaumprobe. Das zweite Beispiel zeigt den Einsatz einer Ödometerzelle mit integriertem Ultraschall-Durchschalltechnik-Setup zur Untersuchung des Steifigkeitsverhaltens granularer Medien bei kleinen Deformationen, das in **Kapitel IV** und **Appendix B** näher beschrieben wird. Das letzte Beispiel zeigt die in-situ hydromechanische Untersuchung und Erzeugung eines Risses in einer Kalksteinprobe in einer triaxialen Durchflusszelle.

Kapitel IV widmet sich der im zweiten Anwendungsbeispiel des vorangegangenen Kapitels nur kurz motivierten Forschungsfrage aus Sicht der Implementierung. Details über den Hintergrund werden erläutert und es wird exemplarisch der gesamten Arbeitsablauf für die mehrskalige Charakterisierung von granularen Festkörpern mittels in-situ µXRCT gezeigt. Dazu werden granulare Packungen betrachtet, die aus zweiphasigen Mischungen monodisperser Glas- und Gummipartikel mit unterschiedlichen Zusammensetzungen hergestellt wurden. Die 3D-Visualisierung der Packungen bei unterschiedlichen Vorspannungen wird mit Ultraschallmessungen in-situ kombiniert, um die effektive Steifigkeit bei kleinen Deformationen zu bestimmen. Die grundlegende Forschungsfrage befasst sich mit einem besseren Verständnis des nicht-klassischen Steifigkeitsverhaltens der zweiphasigen granularen Packungen aus steifen und weichen Partikeln, das nicht mit klassischen Theorien beschrieben werden kann. Es werden einige beispielhafte Ergebnisse gezeigt. Die ausführliche physikalische Interpretation und Diskussion erfolgt in einem separaten Beitrag, der in **Appendix B** zu finden ist.

Appendix – Ausgewählte Beiträge als Koautor

In **Appendix A** wurde aus einem der in **Kapitel II** vorgestellten Datensätze ein numerisches Modell abgeleitet, um die Dispersion und Abschwächung seismischer Wellen durch "Squirt-Flow" in Rissnetzen zu berechnen und zu untersuchen. Dieses Anwendungsbeispiel soll zudem zeigen, wie 3D-Datensätze die Verbindung zwischen Experiment und numerischer Simulation darstellen. Auf der Grundlage dieses Ansatzes können physikalische Effekte genauer untersucht und potentiell besser verstanden werden.

In **Appendix B** wird die physikalische Interpretation und Diskussion zwischen der effektiven Materialreaktion granularer Packungen, bestehend aus zweiphasigen Mischungen monodisperser Glas- und Gummipartikel unterschiedlicher Zusammensetzungen, und dem aus µXRCT-Bildern extrahierten Kontaktnetzwerk gegeben. Es kann als Fortsetzung von **Kapitel IV** verstanden werden, in dem die eigentliche Forschungsfrage zu beantworten versucht wird.

In **Appendix C** werden die Ergebnisse einer Zusammenarbeit zur Untersuchung des Transports von gelösten Stoffen in einer vollständig gesättigten Sandpackung mittels Synchrotron-basierter µXRCT-Bildgebung gezeigt. Im Detail wurden Verunreinigungs- und Reinigungsprozesse unter ähnlichen hydrodynamischen Bedingungen untersucht, um die erhebliche Diskrepanz zwischen den Zeitskalen von Reinigung und Verunreinigung zu verstehen. Dies ist ein exemplarisches Beispiel dafür, wie Forschungsfragen, die eine höhere zeitliche Auflösung erfordern, durch den Übergang von der Labor- zur Synchrotron-basierter µXRCT untersucht werden können.

Dokumentation eigener Publikationen

Nachfolgend sind die im Rahmen dieser Arbeit veröffentlichten Zeitschriftenpublikationen und Datensätze aufgeführt. Der Status bezieht sich auf das aktuelle Datum (August 2023).

Veröffentlichungen als Erstautor genutzt für die vorliegende Dissertation (international peer-reviewed journals):

1. Ruf, M. & Steeb, H.: An open, modular, and flexible micro X-ray computed tomography system for research. *Review of Scientific Instruments* **91** (2020), 113102. https://doi.org/10.1063/5.0019541. (Kapitel I)

2. Ruf, M. & Steeb, H.: Effects of thermal treatment on acoustic waves in Carrara marble. *International Journal of Rock Mechanics and Mining Sciences* **159** (2022), 105205. https://doi.org/10.1016/j.ijrmms.2022.105205. (Kapitel II)

3. Ruf, M.; Lee, D. & Steeb, H.: A multifunctional mechanical testing stage for micro X-ray computed tomography. *Review of Scientific Instruments* **94** (2023), 085115. https://doi.org/10.1063/5.0153042. (Kapitel III)

4. Ruf, M.; Taghizadeh, K. & Steeb, H.: Multi-scale characterization of granular media by in situ laboratory X-ray computed tomography. *GAMM-Mitteilungen* **45** (2022), e20220001. https://doi.org/10.1002/gamm.202200011. (Kapitel IV)

Weitere Veröffentlichungen und Buchbeiträge (peer-reviewed):

1. Hermann, S.; Schneider, M.; Flemisch, B.; Frey, S.; Iglezakis, D.; Ruf, M.; Schembera, B.; Seeland, A. & Steeb, H.: Datenmanagement im SFB 1313. *Bausteine Forschungsdatenmanagement* **1** (2020), 28–38. https://doi.org/10.17192/BFDM.2020.1.8085.

2. Lissa, S.; Ruf, M.; Steeb, H. & Quintal, B.: Effects of crack roughness on attenuation caused by squirt flow in Carrara marble. In *SEG Technical Program Expanded Abstracts 2020*, Society of Exploration Geophysicists 2020, pp. 2439–2443. https://doi.org/10.1190/segam2020-3427789.1.

3. Schuck, B.; Teutsch, T.; Alber, S.; Ressel, W.; Steeb, H. & Ruf, M.: Study of air void topology of asphalt with focus on air void constrictions – a review and research approach. *Road Materials and Pavement Design* **22** (2021), 1–19. https://doi.org/10.1080/14680629.2021.1907215.

4. Balcewicz, M.; Siegert, M.; Gurris, M.; Ruf, M.; Krach, D.; Steeb, H. & Saenger, E. H.: Digital rock physics: A geological driven workflow for the segmentation of anisotropic Ruhr sandstone. *Frontiers in Earth Science* **9** (2021), 673753. https://doi.org/10.3389/feart.2021.673753.

5. Lissa, S.; Ruf, M.; Steeb, H. & Quintal, B.: Digital rock physics applied to squirt flow. *Geophysics* **86** (2021), MR235–MR245. https://doi.org/10.1190/geo2020-0731.1. (Appendix A)

6. Chen, Y.; Steeb, H.; Erfani, H.; Karadimitriou, N. K.; Walczak, M. S.; Ruf, M.; Lee, D.; An, S.; Hasan, S.; Connolley, T.; Vo, N. T. & Niasar, V.: Nonuniqueness of hydrodynamic dispersion revealed using fast 4D synchrotron X-ray imaging. *Science Advances* **7** (2021), eabj0960. https://doi.org/10.1126/sciadv.abj0960. (Appendix C)

7. Hommel, J.; Gehring, L.; Weinhardt, F.; Ruf, M. & Steeb, H.: Effects of enzymatically induced carbonate precipitation on capillary pressure-saturation relations. *Minerals* **12** (2022), 1186. https://doi.org/10.3390/min12101186.

8. Lee, D.; Karadimitriou, N.; Ruf, M. & Steeb, H.: Detecting micro fractures: a comprehensive comparison of conventional and machine-learning-based segmentation methods. *Solid Earth* **13** (2022), 1475–1494. https://doi.org/10.5194/se-13-1475-2022.

9. Teutsch, T.; Gönninger, L.; Ruf, M.; Steeb, H. & Ressel, W.: Microstructural characterisation and analysis of coarse aggregates in asphalt drill cores. *Road Materials and Pavement Design* **24** (2023), 2714–2736. https://doi.org/10.1080/14680629.2022.2164333.

10. Ruf, M.; Steeb, H. & Karadimitriou, N.: Visualization of the uniaxial compression of open-cell foams. In Médici, E. F. & Otero, A. D. (eds.): *Album of Porous Media*. Springer International Publishing, Cham, Switzerland 2023, pp. 117–117. https://doi.org/10.1007/978-3-031-23800-0_97.

11. Taghizadeh, K.; Ruf, M.; Luding, S. & Steeb, H.: X-ray 3D imaging–based microunderstanding of granular mixtures: Stiffness enhancement by adding small fractions of soft particles. *Proceedings of the National Academy of Sciences* **120** (2023), e2219999120. https://doi.org/10.1073/pnas.2219999120. (Appendix B)

Datensatzveröffentlichungen über das Data Repository der Universität Stuttgart (DaRUS):

1. Ruf, M. & Steeb, H.: micro-XRCT data set of open-pored asphalt concrete (2020), https://doi.org/10.18419/darus-639.

2. Ruf, M. & Steeb, H.: micro-XRCT data set of Carrara marble with artificially created crack network: fast cooling down from 600°C (2020), https://doi.org/10.18419/darus-682.

3. Ruf, M. & Steeb, H.: micro-XRCT data set of an in-situ flow experiment with an X-ray transparent flow cell (2020), https://doi.org/10.18419/darus-691.

4. Ruf, M. & Steeb, H.: micro-XRCT data set of Carrara marble with artificially created crack network: slow cooling down from 600°C (2020), https://doi.org/10.18419/darus-754.

5. Vahid Dastjerdi, S.; Steeb, H.; Ruf, M.; Lee, D.; Weinhardt, F.; Karadimitriou, N. & Class, H.: micro-XRCT dataset of enzymatically induced calcite precipitation (EICP) in a microfluidic cell (2021), https://doi.org/10.18419/DARUS-866.

6. Ruf, M.; Steeb, H.; Gebert, J.; Schneider, R. & Helwig, P.: Sample 1 of human femoral heads: micro-XRCT data sets (2021), https://doi.org/10.18419/DARUS-1177.

7. Ruf, M.; Balcewicz, M.; Saenger, E. H. & Steeb, H.: Digital rock physics: A geological driven workflow for the segmentation of anisotropic Ruhr sandstone: micro-XRCT data set (2021), https://doi.org/10.18419/darus-1152.

8. Ruf, M.; Teutsch, T.; Alber, S.; Steeb, H. & Ressel, W.: micro-XRCT data sets of a stone mastic asphalt drill core before and after a uniaxial compression test (sample 2): sample 2-1 (2021), https://doi.org/10.18419/darus-1641.

9. Ruf, M.; Teutsch, T.; Alber, S.; Steeb, H. & Ressel, W.: micro-XRCT data sets of a stone mastic asphalt drill core before and after a uniaxial compression test (sample 2): sample 2-2 (2021), https://doi.org/10.18419/darus-1833.

10. Ruf, M.; Teutsch, T.; Alber, S.; Steeb, H. & Ressel, W.: micro-XRCT data sets of a stone mastic asphalt drill core before and after a uniaxial compression test (sample 2): sample 2-3 (2021), https://doi.org/10.18419/darus-1834.

11. Ruf, M. & Steeb, H.: Effects of thermal treatment on acoustic waves in Carrara marble: measurement data (2021), https://doi.org/10.18419/DARUS-1862.

12. Ruf, M.; Lee, D.; Piotrowski, J.; Huisman, J. A. & Steeb, H.: micro-XRCT data sets of subflorescent salt crusts from evaporation of MgSO4 solution with 0.32 mol/L initial concentration (2021), https://doi.org/10.18419/darus-2002.

13. Ruf, M.; Lee, D.; Piotrowski, J.; Huisman, J. A. & Steeb, H.: micro-XRCT data sets of subflorescent salt crusts from evaporation of MgSO4 solution with 0.64 mol/L initial concentration (2021), https://doi.org/10.18419/darus-1848.

14. Ruf, M.; Lee, D.; Piotrowski, J.; Huisman, J. A. & Steeb, H.: micro-XRCT data sets of subflorescent salt crusts from evaporation of MgSO4 solution with 0.96 mol/L initial concentration (2021), https://doi.org/10.18419/darus-2003.

15. Ruf, M.; Taghizadeh, K. & Steeb, H.: micro-XRCT data sets and in situ measured ultrasonic wave propagation of a pre-stressed monodisperse rubber and glass particle mixture with 50% volume rubber content (2021), https://doi.org/10.18419/darus-2208.

16. Ruf, M.; Taghizadeh, K. & Steeb, H.: micro-XRCT data sets and in situ measured ultrasonic wave propagation of a pre-stressed monodisperse rubber and glass particle mixture with 30% volume rubber content (2022), https://doi.org/10.18419/DARUS-2833.

17. Ruf, M.; Hommel, J. & Steeb, H.: Enzymatically induced carbonate precipitation and its effect on capillary pressure-saturation relations of porous media - micro-XRCT dataset of medium column (sample 3) (2022), https://doi.org/10.18419/darus-2906.

18. Ruf, M.; Hommel, J. & Steeb, H.: Enzymatically induced carbonate precipitation and its effect on capillary pressure-saturation relations of porous media - micro-XRCT dataset of high column (sample 4) (2022), https://doi.org/10.18419/darus-2907.

19. Ruf, M.; Hommel, J. & Steeb, H.: Enzymatically induced carbonate precipitation and its effect on capillary pressure-saturation relations of porous media - micro-XRCT dataset of low column (sample 10) (2022), https://doi.org/10.18419/darus-2908.

20. Ruf, M. & Steeb, H.: In situ micro-XRCT data sets of an open-cell polyurethane foam sample under combined loading conditions (compression + torsion, tension) (2023), https://doi.org/10.18419/DARUS-2834.

21. Ruf, M.; Lee, D. & Steeb, H.: In situ performed fracturing experiment of a limestone sample using an X-ray transparent triaxial cell: micro-XRCT data sets and measurement data (2023), https://doi.org/10.18419/darus-3106.

22. Ruf, M.; Taghizadeh, K. & Steeb, H.: micro-XRCT data sets and in situ measured ultrasonic wave propagation of pre-stressed monodisperse rubber and glass particle mixtures with 10%, 20%, 40%, and 60% volume rubber content: sample 1 (2023), https://doi.org/10.18419/DARUS-3436.

23. Ruf, M.; Taghizadeh, K. & Steeb, H.: micro-XRCT data sets and in situ measured ultrasonic wave propagation of pre-stressed monodisperse rubber and glass particle mixtures with 10%, 20%, and 30% volume rubber content: samples 2 and 3 (2023), https://doi.org/10.18419/DARUS-3437.

List of Acronyms (Preamble)

ART	Algebraic Reconstruction Technique
a-Se	amorphous-Selenium
a-Si	amorphous-Silicon
CCD	Charge-Coupled Device
CGLS	Conjugate Gradient Least Squares
CdTe	Cadmium-Tellurid
COR	Center Of Rotation
CMOS	Complementary Metal-Oxide-Semiconductor
CsI	Cesium Iodide
DaRUS	Data Repository of the University of Stuttgart
DIC	Digital Image Correlation
DQE	Detective Quantum Efficiency
DVC	Digital Volume Correlation
FAIR	Finding, Accessibility, Interoperability, and Reusability
FDK	cone beam reconstruction algorithm named by developers initials: Feldkamp, Davis, Kress [20]
Gadox	Gadolinium oxysulfide (Gd_2O_2S)
GDE	Geometric Detection Efficiency
MTF	Modulation Transfer Function
NOE	Number Of Elements
ODD	Object-Detector-Distance
PEEK	Polyether ether ketone
PUR	Polyurethane
SART	Simultaneous Algebraic Reconstruction Technique
SDD	Source-Detector-Distance
SIRT	Simultaneous Iterative Reconstruction Technique
SNR	Signal-to-Noise Ratio
SOD	Source-Object-Distance
XRCT	X-Ray Computed Tomography
µXRCT	micro X-Ray Computed Tomography
2D	two-Dimensional
3D	three-Dimensional
3M KI	3 molar potassium iodide

Preamble

Chapter 1:
Introduction and Overview

1.1   Motivation

The effective mechanical and hydro-mechanical behavior on the continuum scale (macro scale) of porous media, granular solids, and related materials with complex morphologies is intimately linked to their internal microstructure on the pore/grain scale (micro scale). To improve the general understanding, but also for numerous applications, it is crucial to consider the macroscopic scale combined with the micro scale. For the characterization of the micro scale, imaging techniques play a major role. Porous media, among others, like most solids, are inherently opaque. However, there are several non-destructive high-resolution three-dimensional (3D) imaging techniques that can be used to resolve the internal structure. Based on such 3D images, the microstructure can be characterized and analyzed in various ways. The available imaging techniques can be distinguished according to the underlying physical principle, the materials that can be examined, the achievable resolution, the size of the field of view, and, thus, the specimen size and other criteria. Transmission micro X-ray Computed Tomography (µXRCT), which can provide information from the micrometer to the centimeter scale, has become a standard 3D visualization technique in many scientific fields over the past years.

Thanks to the non-destructive nature of µXRCT, it can be combined with time-resolved investigations. Depending on the exact investigation project, the actual experiment can be carried out ex situ, in situ or, as is usual with destructive methods, post mortem. The ex situ examination is linked to many boundary conditions. The most relevant condition is that the examined object is not influenced by the installation and removal, i.e., the corresponding boundary conditions have to be maintained exactly, which is often difficult or even impossible. However, for very slowly proceeding investigations (e.g., creep, corrosion, dissolution, precipitation processes), the ex situ investigation is usually the favored approach since the imaging system used is not blocked for a long time (days to several months). In addition, there are experiments that cannot be implemented within the imaging system without considerable effort. For many investigations, however, experiments carried out in situ can be considered the gold standard for a wide variety of reasons. In the context of mechanical and hydromechanical characterization of deformation experiments (e.g., tension/compression test) and hydro-mechanically coupled processes in porous media, this is particularly relevant.

Figure 1.1 shows an example of an in situ performed uniaxial compression test of an open-cell, reticulated polyurethane foam sample. The effective stress-strain curve consists of three regimes: (i) linear-elastic regime, (ii) collapse regime, and (iii) densification regime. By µXRCT imaging at different deformation states, the macroscopically observable material response can be understood. For instance, the plateau of the stress-strain curve is caused by distinct elastic buckling of the cell columns mainly oriented parallel to the load-
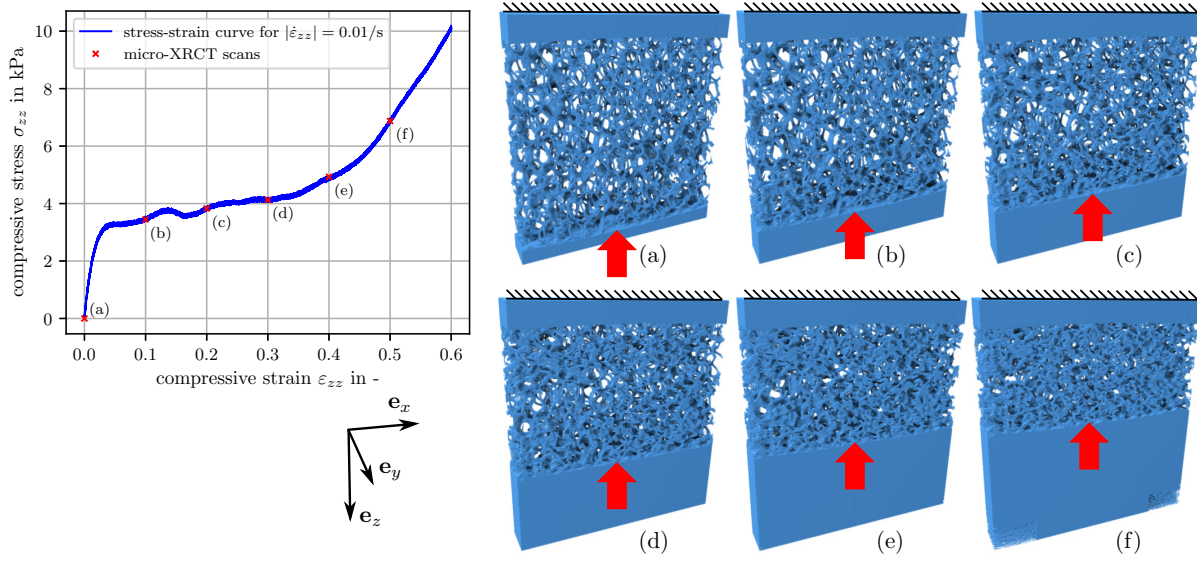
Figure 1.1: Uniaxial compression test of an open-cell reticulated polyurethane (PUR) foam sample (10 pores per inch) with microstructure evolution for different deformation states. The images show a segmented subvolume of the center region of the cylindrical foam sample (diameter $52\,\text{mm}$, length $50\,\text{mm}$) and demonstrate the elastic collapse of the porous medium [104].

ing direction, giving rise to the name collapse region. The geometry from the acquired 3D images can be used for various further numerical investigations. Other examples include flow through porous media under reservoir conditions or the behavior of cracks under such conditions.

However, to perform such in situ experiments at all, appropriate apparatuses must first be developed and implemented in order to be able to impose and control the corresponding boundary conditions for the experiment and potentially measure other quantities. Depending on the type of experiment, the apparatuses used for this purpose are often very specific individual solutions.

In the context of this work, an open, versatile, modularly designed laboratory µXRCT system was built up, which provides an open experimental platform for mechanical and hydro-mechanical in situ investigations of a wide variety of materials and processes. By integrating a universal testing machine, it is possible to perform in situ compression/tension and torsion experiments as well as their combination (multi-axial loading), simultaneously or sequentially. In the case of a nonlinear material response, multi-axial loading can lead to sequence effects (no linear superposition), which are very interesting and challenging from a mechanical modeling point of view. Due to the axial external load application by the integrated testing machine, the implementation of triaxial cells for hydro-mechanical investigations is relatively simple. Likewise, the implementation of fatigue tests using piezo-actuators at different compression swell loading. The investigation of other multi-physics problems (coupling of mechanical, hydraulic, thermal, chemical, etc. processes) is also conceivable and to implement with appropriate extensions.

Using the established system, various multi-scale phenomena from different material classes (porous media, foams, granular solids) are considered in this work. For this pur-

pose, traditional experimental characterization was combined with µXRCT based imaging in various ways ex situ and in situ. Specifically, imaging was combined with (i) mechanical loading, (ii) mechanical loading coupled with ultrasonic wave propagation measurements, and (iii) hydro-mechanical investigations.

1.2 State of the art

Imaging techniques offer the possibility of resolving the microstructure of materials and characterizing them based on this. Conventional imaging techniques include, for instance, optical light microscopy and scanning electron microscopy of planar sections [30]. However, a major drawback of classical imaging techniques is that one is limited to studying a two-dimensional (2D) representation of a 3D object. It becomes critical if the sample to be examined cannot simply be sliced or if there is a risk of it being altered as a result. In addition, since most of the procedures are destructive, time-resolved examinations are difficult or not possible at all. For these reasons, 3D imaging methods have been developed. An overview and comparison of common methods in a materials science context can be found, for example, in Ref. [137].

A very important method is transmission X-Ray Computed Tomography (XRCT), which is based on the specific X-ray attenuation of materials [13, 146]. By a rotational scan, numerous images of the object of interest are taken, on which basis the object can be digitally reconstructed. Originally XRCT was developed by and for the medical community. While conventional medical XRCT generally refers to submillimeter resolutions or poorer (voxel sizes $\geq 100\,\mu m$), µXRCT refers to micrometer resolutions (voxel sizes $\geq 0.1\,\mu m$). In addition, in nano-XRCT, nanometer resolution is possible (down to voxel sizes $\approx 10\,nm$) [146]. The development over time in terms of maximum resolution is as listed above. It must be noted, however, that as the resolution increases, the specimen size becomes progressively smaller and the scanning time significantly longer due to the lower possible X-ray beam flux in laboratory systems. Depending on the required scan quality and resolution, scanning times of up to $20\,h$ and more are not unusual. For questions and investigations of mechanical and hydro-mechanical multi-scale problems relevant in the course of this work, which try to connect the micro-structural level (pore/grain scale) with the continuum scale, the specimens cannot become arbitrarily small due to representative reasons. In this context µXRCT offers an excellent compromise between the achievable resolution, field of view, and specimen size. µXRCT found its way into a wide variety of research fields as different review works in the context of materials science [66, 115, 116, 126–128, 137], geoscience and geology [15, 144], biology and biomimicry (bionics) [73, 79], food science [118] up to the quality evaluation of agricultural produce [55] show.

Because it is a non-destructive method, µXRCT imaging is often the first step in a multi-scale workflow involving other destructive imaging modalities. Its non-destructive nature also allows the possibility of temporal investigations. In this context, the term "4D µXRCT" is often used to express the spatial and temporal resolution. Each time step is represented by a complete µXRCT scan. Depending on the implementation, it has to

be differentiated between (i) time-lapse imaging and (ii) dynamic or continuous imaging. Time-lapse imaging can be further subdivided into ex situ as well as un/interrupted in situ scanning [23, 25]. With few exceptions, dynamic or continuous imaging currently still mainly refers to so-called synchrotron-based µXRCT [23].

Synchrotron-based µXRCT [82, 124] is to be distinguished from laboratory-based µXRCT. Synchrotron-based µXRCT is only possible at dedicated particle accelerators. Synchrotron X-ray radiation cannot be compared directly in its so-called brilliance (photons/time/area/ solid angle/energy bandwidth) and monochromaticity with X-ray radiation generated by laboratory-based X-ray sources. The high brilliance of synchrotron radiation leads to less systematic imaging artifacts and enables much higher temporal resolution. The latter is essential for the study of transient phenomena. For instance, Ref. [65] reported an in situ tensile test at $20\,\mathrm{Hz}$ time resolution (full scans) performed at the TOMCAT beamline of the Swiss Light Source (SLS) [123].

In the last two decades, more and more researchers from different fields have benefited from the available possibilities of in situ µXRCT imaging, as the growth of publications shows [128, 152]. To perform the actual experiment, primarily highly specific custom-built stages are used to mimic the process under investigation. An overview of typically used stages for different purposes, such as monotonic tension/compression loading, cyclic loading, and thermal loading (heating and cooling), is given in Refs. [10, 24]. Cell designs (triaxial and triaxial flow cells) to study geomaterials and rocks under high pressure and temperature are described, for instance, in Refs. [22, 84]. The design specifications are usually based on the environmental conditions they want to mimic, the specimen size, and, the imaging hardware used.

Although synchrotron-based µXRCT offers many advantages, laboratory-based µXRCT is of great interest to many researchers, mainly for ease of access. Consequently, laboratory-based capabilities are developing in parallel. In many experiments, imaging speed is only secondarily relevant since many processes are slow, periodic, or can be paused at an approximately equilibrium state. An increasing number of papers appears that emphasize pure in situ laboratory investigations. A review of laboratory-based in situ investigations focusing on engineering materials can be found in Ref. [150]. In addition, apparatuses for in situ investigations intrinsically designed for use in laboratory systems are presented [21, 151]. For example, an apparatus has recently been published to enable investigations up to $1000\,°\mathrm{C}$ [151]. In addition, there are promising approaches to determine, for example, the displacement field in the context of deformation experiments from a few considered projection angles when a full high-resolution scan of the initial sample state is available [48, 60, 131]. There is also the first commercial laboratory scanner, "DynaTom" [16, 43], which is optimized for dynamic investigations. It promises complete scans in less than $10\,\mathrm{s}$ under optimal conditions [16]. Micro-focus X-ray sources, based on a liquid-metal-jet anode instead of a solid-anode and, thus, can deliver significantly higher X-ray fluxes, are also an extremely promising technology that offers a further significant increase in imaging speed and possibilities in lab-based systems [19, 33, 58].

So far, only transmission µXRCT was considered. Instead of using the physical effect of different material attenuation, also other interaction mechanisms of X-rays with matter like phase-shift [9, 68, 78], scattering [27], diffraction [81, 127], and fluorescence analyses

[67] can be exploited. Such methods can be beneficial when the contrast information from transmission µXRCT is insufficient or complementary information is required [44, 127]. However, not all of these physical effects can be addressed in the laboratory.

Apart from methods that use X-rays, other techniques are used for 3D imaging at different scales. Mention is nuclear magnetic resonance imaging [8], neutron tomography [124], ultrasonic tomography [53], electron tomography [59], and photoacoustic tomography [49] without any claim to completeness.

In summary, there is a wide range of 3D imaging techniques that take advantage of different physical effects. The differences are in the resolution and, thus, the possible sample volume, the acquisition speed, and the sensitivity to the sample's chemical composition. A key point of laboratory-based transmission µXRCT is its simple physical principle and related relatively simple implementation. All this together makes it an excellent method for visualizing the internal morphology from micrometer to centimeter scale of a wide variety of materials and, consequently, for studying numerous mechanical and hydro-mechanical multi-scale phenomena.

1.3   Outline of the thesis

The present dissertation is cumulative and divided into two parts. Within the preamble, **Chapters 1–3**, the classification as well as the communication of the necessary basics is done. The appended **Chapters I–IV** in the second part of the thesis are copies of journal articles used for this dissertation. Co-authorship was used to collaborate on numerous projects. A selection of resulting papers is included in **Appendix A–C**. They serve as extended examples of investigated physical phenomena in the scope of this work. A list of all own publications can be found in Subsection 1.4.

Preamble

After this introducing **Chapter 1**, the thesis is structured as follows.

Chapter 2 deals with the required fundamentals to understand the following chapters and is divided into two sections. In Section 2.1, the most crucial parts of transmission µXRCT imaging are summarized. It covers X-rays physics, their interaction with matter, and X-ray imaging, where µXRCT is directly based. A key element in µXRCT is the volume reconstruction of the unknown 3D object based on many acquired projection images from different directions. Since this is a fundamental and consistently performed step within the work, the applied FDK algorithm is motivated. Moreover, image quality and artifacts are discussed. Knowing and understanding those is essential for the correct data interpretation and the proper scan parameter selection.

The thesis aims for a versatile tool to image the microstructure of materials under mechanical and hydro-mechanical loading conditions to investigate different multi-scale phenomena. That means, starting from a reference configuration, a new configuration is reached (equilibrium state assumed), from which a new snapshot of the changed microstructure is taken. The connection to classical continuum mechanics results from the

changes, e.g., the deformation of the internal structure, which can be extracted from a time series of 3D images in the ideal case, e.g., by image correlation methods. A link to the kinematical description used in continuum mechanics can be established in case of deformation. Therefore, in Section 2.2, some basics from continuum mechanics are summarized, together with a brief description of the applied mechanical and hydro-mechanical characterization methods.

The following **Chapters I–IV** (publications) build on these fundamentals. Their content and classification in the present work's overall framework are described in the next subsection.

Finally, the present work is summarized in **Chapter 3** followed by a short outlook.

Publications

In **Chapter I**, the implementation, the performance evaluation, and demonstration of an in-house developed and built-up open, modular, and flexible µXRCT setup is presented. The shown example of hardware-based improvement of ring artifacts using a detector pixel map, distinguishing between bad (e.g., "dead") and good pixels, highlights the modular concept's advantages. By its open design, this system is ready for the extension to perform in situ multiphysics experiments, as demonstrated in an example. The system has been used in many different research collaborations. Numerous different kinds of materials were imaged and investigated, and first post mortem and time-lapsed ex/in situ experiments were carried out. Selected scan data sets, including metadata, were published as part of the related articles or as independent data sets under a CC BY license using the Data Repository of the University of Stuttgart (DaRUS), demonstrating the wide range of possible applications as well as the achieved image quality. For more details, see the list of own publications below, Subsection 1.4, for a current overview. As a challenging high-resolution example within this chapter, a scan of an artificially fractured Carrara marble core sample by thermal treatment is shown. Due to spatial resolution limitations, the reliable segmentation and quantification of measures like fracture aperture is challenging. In such a case, image-based characterization is limited and must be used with care, as shown in detail in the collaborative work Lee *et al.* [61].

Based on the application example introduced in the previous chapter, in **Chapter II**, the developed µXRCT system was used to investigate the effect of different thermal treatment protocols on Carrara marble. In particular, the influence of fast cooling versus slow cooling and associated specimen size effects were investigated. µXRCT imaging helps to understand the mechanisms on the micro scale better. However, further quantifying the resulting crack networks to distinguish between the protocols is challenging and partly even impossible, depending on the applied thermal treatment method. Therefore, traditional non-destructive characterization of the core samples on the core scale is performed. For this, P-wave and S-wave velocity measurements as well as effective volume change measurements, are carried out. Combined with the qualitative results from the 3D imaging, the generated relative crack volume could be identified as a structural influencing parameter for the evolution of the effective wave velocities. This chapter shows, on the one hand, the usefulness of 3D image data and, on the other, also the necessity of combin-

ing it with other physical characterization methods, as performed here in an ex situ/post mortem multi-scale approach.

Chapter III deals with the extension of the µXRCT system presented in **Chapter I** by a load frame using a universal testing machine with two integrated rotational tables. This approach offers the possibility to perform flexibly different mechanical (compression, tension, and torsion) and, in combination with special cells, hydro-mechanically coupled experiments in situ. Three examples of in situ investigations of different material classes are motivated, and selected results are shown. The first example focuses on the loading sequence-dependent deformation of a polyurethane foam sample. The second example shows the usage of an oedometer cell with an integrated wave propagation measurement setup to determine the small-strain stiffness response of a generic granular media sample, described in more detail in **Chapter IV** and **Appendix B**. The last example shows the in situ hydro-mechanical testing and fracturing of a limestone rock sample in a triaxial flow cell.

Chapter IV is dedicated to the research question only briefly motivated in the second application example of the previous chapter from a technical implementation perspective. It gives more details about the background and covers in an exemplary manner the entire workflow for the multi-scale characterization of granular media by in situ laboratory µXRCT. Granular packings consisting of biphasic mixtures of monodisperse glass and rubber particles at different volume fractions are considered for this. 3D imaging of the granular packings under different pre-stresses is combined in situ with ultrasound measurements to determine the small-strain stiffness. The fundamental research question deals with a better understanding of the non-classical stiffness behavior of the mixtures not covered by classical theories. Some exemplary results are shown. The extensive physical interpretation and discussion are given in a separate work in **Appendix B**.

Appendix – Selected examples as co-author

In **Appendix A**, from one of the presented data sets in **Chapter II** a numerical model was derived to compute and study the seismic-wave moduli dispersion and attenuation due to squirt flow. This application example also intends to show how 3D data sets represent the bridge between experiment and numerical simulation. Based on this approach, physical effects can be studied and potentially understood in more detail.

In **Appendix B**, the physical interpretation and discussion between the effective material response of granular packings prepared with biphasic mixtures of monodisperse glass and rubber particles at different fractions and the contact network extracted from µXRCT images is given. It can be considered as a continuation of **Chapter IV** in which the actual research question is attempted to be answered.

In **Appendix C**, the outcome of a collaboration investigating the solute transport in a fully saturated sand packing using synchrotron µXRCT is shown. In detail, contamination and cleanup processes at similar hydrodynamic conditions were studied to understand the significant discrepancy between the cleanup and contamination time scales. It is an example of how research questions requiring higher temporal resolution can be studied by moving from laboratory to synchrotron µXRCT.

1.4   List of own publications

Below, the journal publications and data sets published in the course of this work are listed. The status is with regard to the present date (August 2023).

Full papers used for the cumulative dissertation (international peer-reviewed journals):

1. Ruf, M. & Steeb, H.: An open, modular, and flexible micro X-ray computed tomography system for research. *Review of Scientific Instruments* **91** (2020), 113102. https://doi.org/10.1063/5.0019541. (Chapter I)

2. Ruf, M. & Steeb, H.: Effects of thermal treatment on acoustic waves in Carrara marble. *International Journal of Rock Mechanics and Mining Sciences* **159** (2022), 105205. https://doi.org/10.1016/j.ijrmms.2022.105205. (Chapter II)

3. Ruf, M.; Lee, D. & Steeb, H.: A multifunctional mechanical testing stage for micro X-ray computed tomography. *Review of Scientific Instruments* **94** (2023), 085115. https://doi.org/10.1063/5.0153042. (Chapter III)

4. Ruf, M.; Taghizadeh, K. & Steeb, H.: Multi-scale characterization of granular media by in situ laboratory X-ray computed tomography. *GAMM-Mitteilungen* **45** (2022), e20220001. https://doi.org/10.1002/gamm.202200011. (Chapter IV)

Other full papers and book chapters (peer-reviewed):

1. Hermann, S.; Schneider, M.; Flemisch, B.; Frey, S.; Iglezakis, D.; Ruf, M.; Schembera, B.; Seeland, A. & Steeb, H.: Datenmanagement im SFB 1313. *Bausteine Forschungsdatenmanagement* **1** (2020), 28–38. https://doi.org/10.17192/BFDM. 2020.1.8085.

2. Lissa, S.; Ruf, M.; Steeb, H. & Quintal, B.: Effects of crack roughness on attenuation caused by squirt flow in Carrara marble. In *SEG Technical Program Expanded Abstracts 2020*, Society of Exploration Geophysicists 2020, pp. 2439–2443. https://doi.org/10.1190/segam2020-3427789.1.

3. Schuck, B.; Teutsch, T.; Alber, S.; Ressel, W.; Steeb, H. & Ruf, M.: Study of air void topology of asphalt with focus on air void constrictions – a review and research approach. *Road Materials and Pavement Design* **22** (2021), 1–19. https://doi.org/10.1080/14680629.2021.1907215.

4. Balcewicz, M.; Siegert, M.; Gurris, M.; Ruf, M.; Krach, D.; Steeb, H. & Saenger, E. H.: Digital rock physics: A geological driven workflow for the segmentation of anisotropic Ruhr sandstone. *Frontiers in Earth Science* **9** (2021), 673753. https://doi.org/10.3389/feart.2021.673753.

5. Lissa, S.; Ruf, M.; Steeb, H. & Quintal, B.: Digital rock physics applied to squirt flow. *Geophysics* **86** (2021), MR235–MR245. https://doi.org/10.1190/geo2020-0731.1. (Appendix A)

6. Chen, Y.; Steeb, H.; Erfani, H.; Karadimitriou, N. K.; Walczak, M. S.; Ruf, M.; Lee, D.; An, S.; Hasan, S.; Connolley, T.; Vo, N. T. & Niasar, V.: Nonuniqueness of hydrodynamic dispersion revealed using fast 4D synchrotron X-ray imaging. *Science Advances* **7** (2021), eabj0960. https://doi.org/10.1126/sciadv.abj0960. (Appendix C)

7. Hommel, J.; Gehring, L.; Weinhardt, F.; Ruf, M. & Steeb, H.: Effects of enzymatically induced carbonate precipitation on capillary pressure-saturation relations. *Minerals* **12** (2022), 1186. https://doi.org/10.3390/min12101186.

8. Lee, D.; Karadimitriou, N.; Ruf, M. & Steeb, H.: Detecting micro fractures: a comprehensive comparison of conventional and machine-learning-based segmentation methods. *Solid Earth* **13** (2022), 1475–1494. https://doi.org/10.5194/se-13-1475-2022.

9. Teutsch, T.; Gönninger, L.; Ruf, M.; Steeb, H. & Ressel, W.: Microstructural characterisation and analysis of coarse aggregates in asphalt drill cores. *Road Materials and Pavement Design* **24** (2023), 2714–2736. https://doi.org/10.1080/14680629.2022.2164333.

10. Ruf, M.; Steeb, H. & Karadimitriou, N.: Visualization of the uniaxial compression of open-cell foams. In Médici, E. F. & Otero, A. D. (eds.): *Album of Porous Media*. Springer International Publishing, Cham, Switzerland 2023, pp. 117–117. https://doi.org/10.1007/978-3-031-23800-0_97.

11. Taghizadeh, K.; Ruf, M.; Luding, S. & Steeb, H.: X-ray 3D imaging–based microunderstanding of granular mixtures: Stiffness enhancement by adding small fractions of soft particles. *Proceedings of the National Academy of Sciences* **120** (2023), e2219999120. https://doi.org/10.1073/pnas.2219999120. (Appendix B)

Dataset publications using the Data Repository of the University of Stuttgart (DaRUS):

1. Ruf, M. & Steeb, H.: micro-XRCT data set of open-pored asphalt concrete (2020), https://doi.org/10.18419/darus-639.

2. Ruf, M. & Steeb, H.: micro-XRCT data set of Carrara marble with artificially created crack network: fast cooling down from 600°C (2020), https://doi.org/10.18419/darus-682.

3. Ruf, M. & Steeb, H.: micro-XRCT data set of an in-situ flow experiment with an X-ray transparent flow cell (2020), https://doi.org/10.18419/darus-691.

4. Ruf, M. & Steeb, H.: micro-XRCT data set of Carrara marble with artificially created crack network: slow cooling down from 600°C (2020), https://doi.org/10.18419/darus-754.

5. Vahid Dastjerdi, S.; Steeb, H.; Ruf, M.; Lee, D.; Weinhardt, F.; Karadimitriou, N. & Class, H.: micro-XRCT dataset of enzymatically induced calcite precipitation (EICP) in a microfluidic cell (2021), https://doi.org/10.18419/DARUS-866.

6. Ruf, M.; Steeb, H.; Gebert, J.; Schneider, R. & Helwig, P.: Sample 1 of human femoral heads: micro-XRCT data sets (2021), https://doi.org/10.18419/DARUS-1177.

7. Ruf, M.; Balcewicz, M.; Saenger, E. H. & Steeb, H.: Digital rock physics: A geological driven workflow for the segmentation of anisotropic Ruhr sandstone: micro-XRCT data set (2021), https://doi.org/10.18419/darus-1152.

8. Ruf, M.; Teutsch, T.; Alber, S.; Steeb, H. & Ressel, W.: micro-XRCT data sets of a stone mastic asphalt drill core before and after a uniaxial compression test (sample 2): sample 2-1 (2021), https://doi.org/10.18419/darus-1641.

9. Ruf, M.; Teutsch, T.; Alber, S.; Steeb, H. & Ressel, W.: micro-XRCT data sets of a stone mastic asphalt drill core before and after a uniaxial compression test (sample 2): sample 2-2 (2021), https://doi.org/10.18419/darus-1833.

10. Ruf, M.; Teutsch, T.; Alber, S.; Steeb, H. & Ressel, W.: micro-XRCT data sets of a stone mastic asphalt drill core before and after a uniaxial compression test (sample 2): sample 2-3 (2021), https://doi.org/10.18419/darus-1834.

11. Ruf, M. & Steeb, H.: Effects of thermal treatment on acoustic waves in Carrara marble: measurement data (2021), https://doi.org/10.18419/DARUS-1862.

12. Ruf, M.; Lee, D.; Piotrowski, J.; Huisman, J. A. & Steeb, H.: micro-XRCT data sets of subflorescent salt crusts from evaporation of MgSO4 solution with 0.32 mol/L initial concentration (2021), https://doi.org/10.18419/darus-2002.

13. Ruf, M.; Lee, D.; Piotrowski, J.; Huisman, J. A. & Steeb, H.: micro-XRCT data sets of subflorescent salt crusts from evaporation of MgSO4 solution with 0.64 mol/L initial concentration (2021), https://doi.org/10.18419/darus-1848.

14. Ruf, M.; Lee, D.; Piotrowski, J.; Huisman, J. A. & Steeb, H.: micro-XRCT data sets of subflorescent salt crusts from evaporation of MgSO4 solution with 0.96 mol/L initial concentration (2021), https://doi.org/10.18419/darus-2003.

15. Ruf, M.; Taghizadeh, K. & Steeb, H.: micro-XRCT data sets and in situ measured ultrasonic wave propagation of a pre-stressed monodisperse rubber and glass particle mixture with 50% volume rubber content (2021), https://doi.org/10.18419/darus-2208.

16. Ruf, M.; Taghizadeh, K. & Steeb, H.: micro-XRCT data sets and in situ measured ultrasonic wave propagation of a pre-stressed monodisperse rubber and glass particle mixture with 30% volume rubber content (2022), https://doi.org/10.18419/DARUS-2833.

17. Ruf, M.; Hommel, J. & Steeb, H.: Enzymatically induced carbonate precipitation and its effect on capillary pressure-saturation relations of porous media - micro-XRCT dataset of medium column (sample 3) (2022), https://doi.org/10.18419/darus-2906.

18. Ruf, M.; Hommel, J. & Steeb, H.: Enzymatically induced carbonate precipitation and its effect on capillary pressure-saturation relations of porous media - micro-XRCT dataset of high column (sample 4) (2022), https://doi.org/10.18419/darus-2907.

19. Ruf, M.; Hommel, J. & Steeb, H.: Enzymatically induced carbonate precipitation and its effect on capillary pressure-saturation relations of porous media - micro-XRCT dataset of low column (sample 10) (2022), https://doi.org/10.18419/darus-2908.

20. Ruf, M. & Steeb, H.: In situ micro-XRCT data sets of an open-cell polyurethane foam sample under combined loading conditions (compression + torsion, tension) (2023), https://doi.org/10.18419/DARUS-2834.

21. Ruf, M.; Lee, D. & Steeb, H.: In situ performed fracturing experiment of a limestone sample using an X-ray transparent triaxial cell: micro-XRCT data sets and measurement data (2023), https://doi.org/10.18419/darus-3106.

22. Ruf, M.; Taghizadeh, K. & Steeb, H.: micro-XRCT data sets and in situ measured ultrasonic wave propagation of pre-stressed monodisperse rubber and glass particle mixtures with 10%, 20%, 40%, and 60% volume rubber content: sample 1 (2023), https://doi.org/10.18419/DARUS-3436.

23. Ruf, M.; Taghizadeh, K. & Steeb, H.: micro-XRCT data sets and in situ measured ultrasonic wave propagation of pre-stressed monodisperse rubber and glass particle mixtures with 10%, 20%, and 30% volume rubber content: samples 2 and 3 (2023), https://doi.org/10.18419/DARUS-3437.

Chapter 2:
Fundamentals

This chapter introduces the necessary basics to understand the following chapters. It starts with fundamentals of laboratory transmission micro X-ray computed tomographic imaging. Subsequently, the connection between 3D imaging and continuum mechanics is motivated, and the employed mechanical and hydro-mechanical testing methods are briefly recapitulated as far as required.

2.1 Basics of micro X-ray computed tomography

X-ray Computed Tomography (XRCT) is a non-destructive 3D imaging technique that allows the visualization of internal features of objects by using X-rays. With XRCT, an object can be virtually reconstructed (computed) based on multiple X-ray projection images (radiograms) recorded from different directions. The term tomography is related to the representation of 3D reconstructed volumes by using slices through the object, also used in other 3D imaging methods. Micro X-ray Computed Tomography (µXRCT) is directly based on XRCT but has a significantly higher resolution. Since the same basic principles apply, most of the µXRCT fundamentals presented below are transferable to XRCT, even though the term µXRCT is commonly used. µXRCT has many applications. It is used in medical diagnostics, industrial applications (quality assurance), and research throughout many fields [15, 55, 66, 73, 115, 116, 118, 126–128, 137, 144]. This section is structured according to the operating principle of the method. In detail, it addresses the items listed in Figure 2.1. The method is described in much more detail in different textbooks on which parts of the following are based. For instance, see Carmignato *et al.* [13] with a particular focus on industrial XRCT, Stock [128] with a focus on µXRCT in materials science, Hsieh [41] and Russo [114] with a focus on clinical XRCT, as well as Buzug [12] going deeper into the theory of signal processing without neglecting to discuss practical issues. Regarding the presentation of the µXRCT basics, it is tried to keep those as general as possible while enriching them by specific of the later shown established setup. The topic of image post-processing, which includes everything required for a subsequent quantification based on the output of µXRCT imaging, is only briefly addressed.
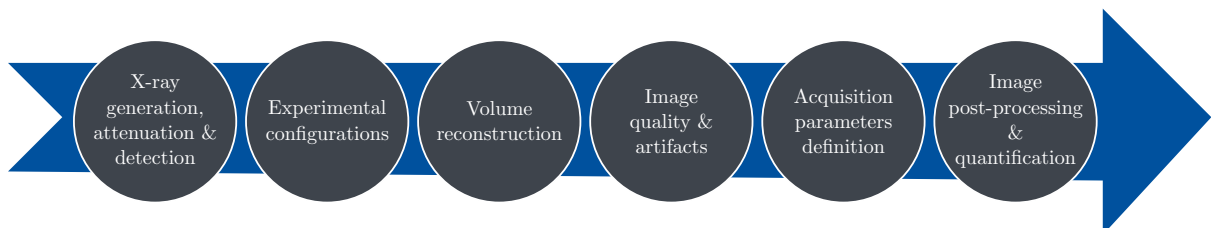

Figure 2.1: Organization of the µXRCT fundamentals within this section.

2.1.1   X-ray generation

X-rays are electromagnetic waves. They were discovered by the German mechanical engineer and physicist Wilhelm Röntgen in 1895, which is why they are also named Röntgen radiation in many languages [114]. Specific experimental observations of the interaction of X-rays with matter are much easier to explain when the radiation is described as a beam of photons instead of using the wave presentation. Photons are particles or quanta of energy with mass zero. The representation of radiation either as a wave or as a particle is called wave-particle duality [28]. The X-ray photon energy E is proportional to the frequency f and can be quantified by the Planck relation $E = hf = hc/\lambda$, where $h = 6.63 \times 10^{-34}\,\mathrm{J\,Hz^{-1}}$ is the Planck constant, λ the wavelength and $c = 3 \times 10^8\,\mathrm{m\,s^{-1}}$ the speed of light. The wavelength is in the range of $10\,\mathrm{pm}$ to $10\,\mathrm{nm}$. Depending on the wavelength, X-rays are classified as soft ($\lambda > 0.1\,\mathrm{nm}$) and hard X-rays ($\lambda < 0.1\,\mathrm{nm}$) [13].

There are different possibilities for generating X-rays. The common feature is that X-rays are generated when charged particles are accelerated or when electrons change atomic shells within an atom. An X-ray tube is employed for the generation in laboratory systems, which principle design is depicted in Figure 2.2. An X-ray tube is a vacuum tube that converts electrical input power into X-rays. It consists of a cathode and anode inserted in an evacuated housing. Usually, a thin tungsten filament connected to a low-voltage generator is used for the cathode. Due to the Joule effect, the filament is heated up, aiding the subsequent emission of electrons. A high-voltage power source connects the cathode and anode to accelerate the emitted electrons towards the anode, also called the target. The applied tube voltage and current govern the electron beam's intensity. Focusing and centering of the electron beam is achieved by magnetic lenses (coils).

From the interaction of the focused and centered electron beam with the target, X-rays are generated by three interaction types. (i) Deceleration of fast electrons in the atoms of the target material yielding to bremsstrahlung ("braking" radiation), Figure 2.3(b). By the interaction of the electron with the nucleus, its velocity increases and then decreases (brakes) as it moves away from the nucleus due to the electrostatic attraction of the nucleus. (ii) Collision of an accelerated electron with an atomic nucleus of the target, Figure 2.3(c). In this case, the total energy of the electron is transferred to bremsstrahlung. (iii)Photoelectric emission of X-rays from orbital electron transitions in
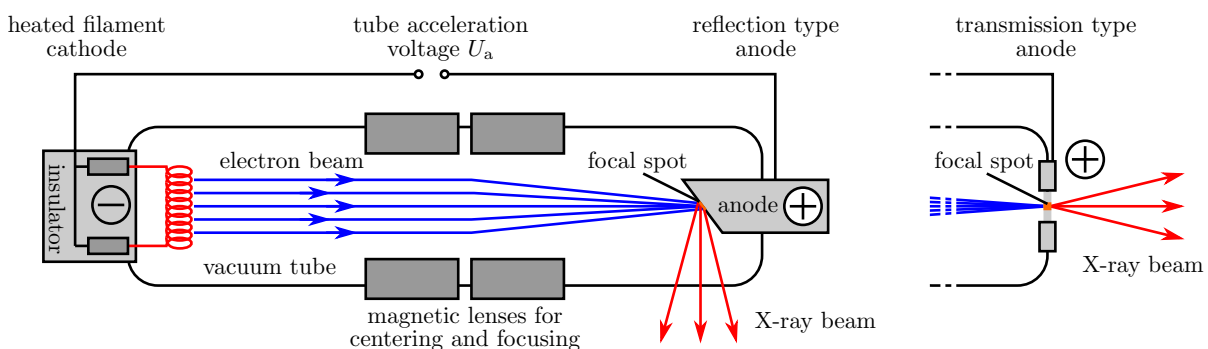

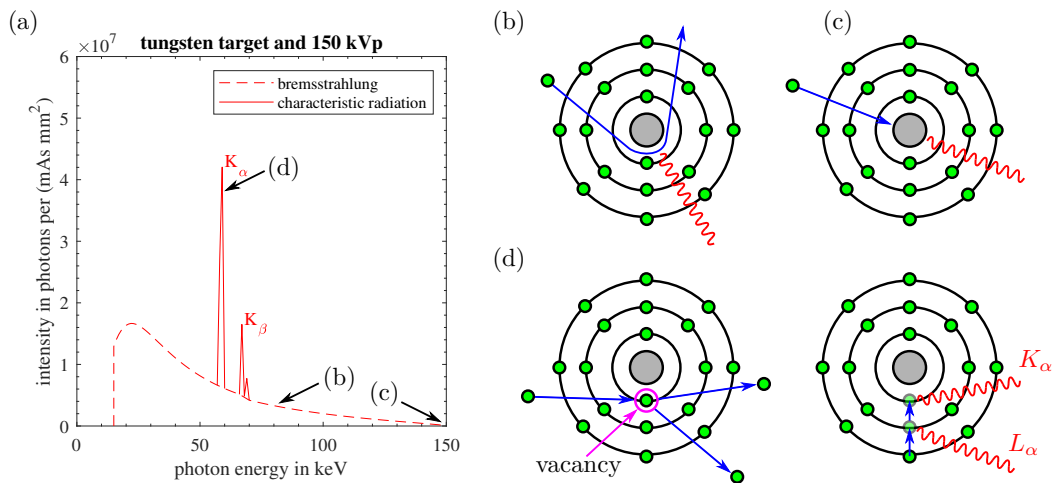**Figure 2.2:** Working principle of an X-ray tube.

Figure 2.3: Mechanisms of X-ray generation in an X-ray tube. (a) X-ray tube spectrum (created with SpekCalc [80]), (b) principle of bremsstrahlung generation, (c) direct interaction of an electron with the atomic nucleus, and (d) photoelectric emission yielding to characteristic radiation.

the target atoms, Figure 2.3(d). The resulting X-rays are named characteristic radiation. A typical resulting X-ray beam spectrum is illustrated in Figure 2.3(a).

X-ray tube characteristics The X-ray tube power P is given by the applied tube voltage U_a and the applied tube current I_a, $P = U_a I_a$. The maximum possible photon energy within the spectrum is given by $E_{max} = e\,U_a$, with the electric charge of an electron e. The range of possible tube voltage, current, and power, in combination with the focal spot size, are typical performance parameters of an X-ray tube, among others. Thereby, the maximum X-ray tube power P_{max} correlates with the focal spot size of the electron beam on the target. Too many electrons per area per time would otherwise vaporize the target. The maximum theoretical possible image resolution depends directly on the X-ray source's focal spot radius r_f. The smaller it is, the higher the possible image resolution, cf. Subsection 2.1.4. Therefore, X-ray sources are typically classified based on the size of their focal spot in conventional, micro-focus, and nano-focus X-ray sources. However, the smaller the focal spot, the smaller the maximum possible tube power. Modern micro- and nano-focus X-ray sources work with an adaptive focal spot size depending on the applied U_a and I_a to compensate for this problem. For illustrative purposes, in Figure 2.4, the defocusing characteristic of the employed 80 W micro-focus X-ray source is shown. The source offers a good compromise between high resolution (small focal spot) and high possible photon energy, respectively flux.

For a given polychromatic X-ray tube, the operator can influence the resulting spectrum by adjusting the tube voltage U_a and the tube current I_a, usually related to the focal spot size. Moreover, the spectrum can be manipulated using physical pre-filters, e.g., aluminum or copper sheets with a certain thickness. With this, the soft X-ray's portion of the spectrum can be reduced. The influences on the spectrum are illustrated in Figure 2.5 based on a simulation for an X-ray tube with a tungsten reflection target.
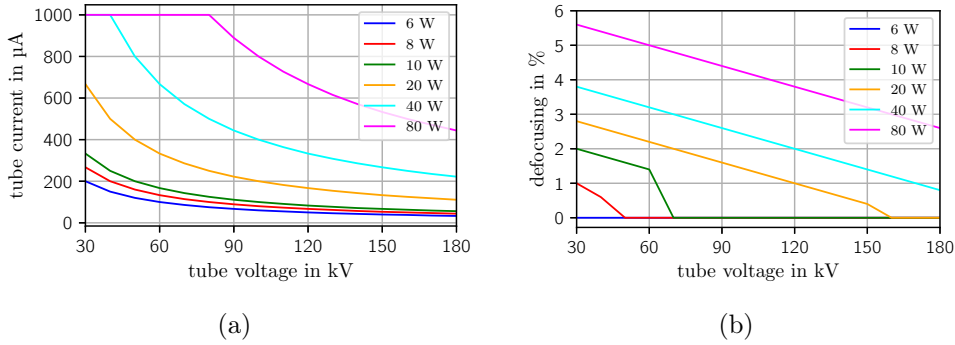
Figure 2.4: Employed micro-focus X-ray tube characteristic ($P_{max} = 80\,\text{W}$). (a) Tube power combinations. (b) Defocusing of the electron beam for different tube powers. 0.8 to 1.0 % of defocusing corresponds with 5 µm focal spot increase starting from a minimal focal spot size of about 3 µm.
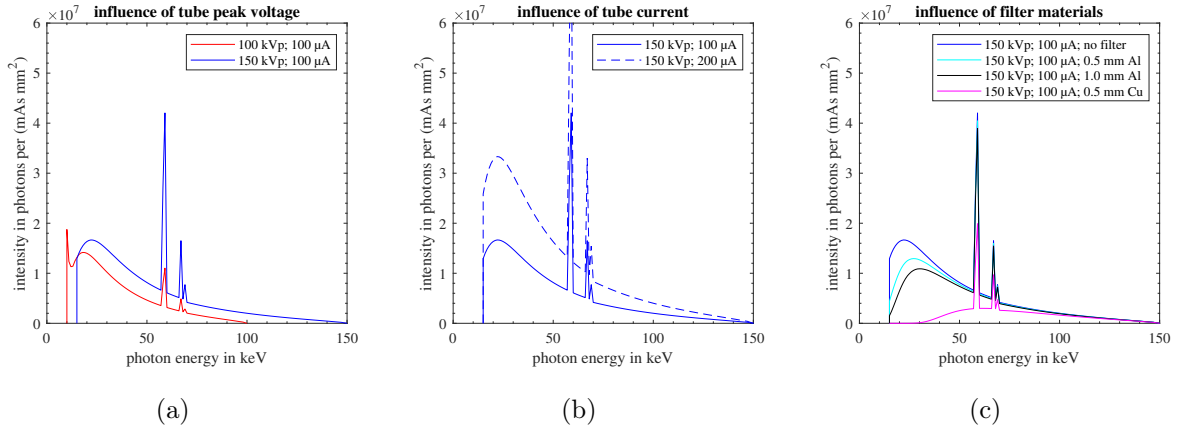
Figure 2.5: X-ray tube spectrum manipulation (created with SpekCalc [80]).

2.1.2   X-ray attenuation

The interaction of photons with matter is the basic physical principle leading to a non-uniform X-ray image (radiogram). It can be described on a macroscopic level, sufficient to understand the principles of X-ray imaging. However, for a better understanding, which is necessary, for example, to understand typical image artifacts, a more detailed view is necessary.

Macroscopic observation   Assuming a monochromatic X-ray beam, the radiant intensity (number of photons per area and time equivalent to power per area [W/m^2]) that emerges from a slice with a thickness d$\tilde{s}$ is reduced by

$$\mathrm{d}\tilde{I} = -\mu\tilde{I}\mathrm{d}\tilde{s} \tag{2.1}$$

with the intensity $\tilde{I}$ that entered where μ [m^{-1}] is the linear attenuation coefficient, whose numerical value is material and photon energy dependent. The solution of this
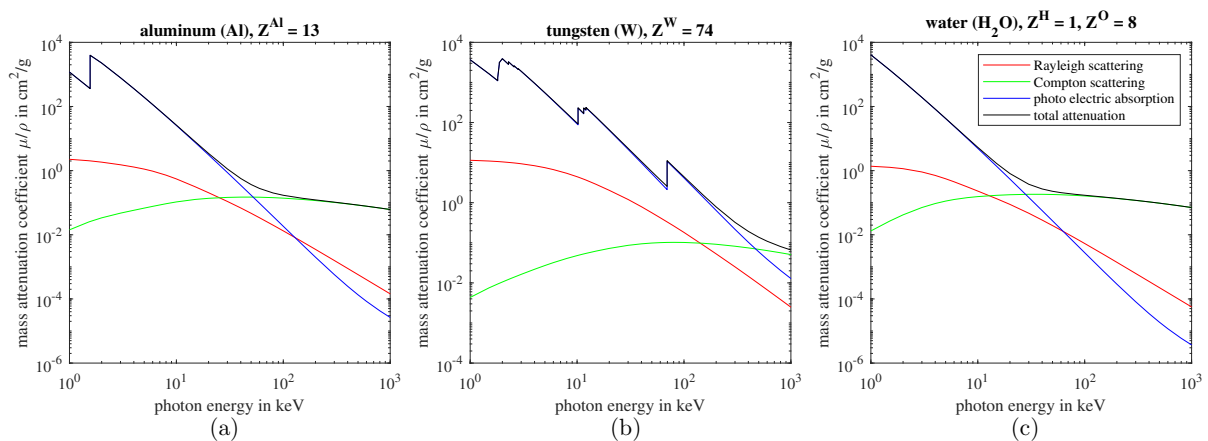
Figure 2.6: Total mass attenuation coefficients with their contributions in relation to photon energy for two elements (a,b) and one compound (c); legend in (c). Values are based on the National Institute of Standards and Technology (NIST) online database [7].

homogeneous differential equation of first order for X-rays passing through a slab of matter with thickness s is

$$I(s) = I_0 \, e^{-\int_0^s \mu(\tilde{s}) d\tilde{s}} \tag{2.2}$$

with the initial X-ray intensity I_0. This equation is named the Lambert-Beer law for a monochromatic X-ray beam. For a polychromatic X-ray beam, the energy dependency has to be taken into account leading to the Lambert-Beer law for a polychromatic X-ray beam

$$I(s) = \int_0^{E_{\max}} I_0(E) e^{-\int_0^s \mu(\tilde{s}, E) d\tilde{s}} dE \,. \tag{2.3}$$

The ratio $I(s)/I_0$ is the so-called transmission T. The attenuation A follows by $A = 1 - T$. Both intensities I_0 and $I(s)$, in front of the slab of matter and behind, are measurable and build the basis in attenuation-based X-ray imaging [72].

Mechanisms of attenuation The macroscopic observable exponential intensity reduction of an X-ray beam when passing through an object, called attenuation, consists of four primary interaction mechanisms: Rayleigh scattering also known as Thomson scattering, photoelectric absorption, Compton scattering, and pair production. The different interaction mechanisms depend strongly on the involved photon energy apart from the irradiated material properties: density ρ, atomic number Z, and absorption edges. The total attenuation coefficient is the sum of all four portions, $\mu = \mu_{\mathrm{ray}} + \mu_{\mathrm{pe}} + \mu_{\mathrm{compt}} + \mu_{\mathrm{pp}}$ [12, 13]. Exemplarily, in Figure 2.6, the mass attenuation (μ/ρ) over photon energy is depicted for two chemical elements and one compound.

The photoelectric absorption and the Compton scattering are relevant for X-ray energies used in µXRCT. The photoelectric effect is a phenomenon in which the incident photon with energy E is completely absorbed by an atom. In contrast, in Compton scattering, the photon only loses energy and changes its direction with the reduced energy E'. In both mechanisms, an electron is ejected due to the incident photon. The ejected electron is either a photoelectron with energy E_{pe} or a Compton electron with energy E_{compt}, cf.
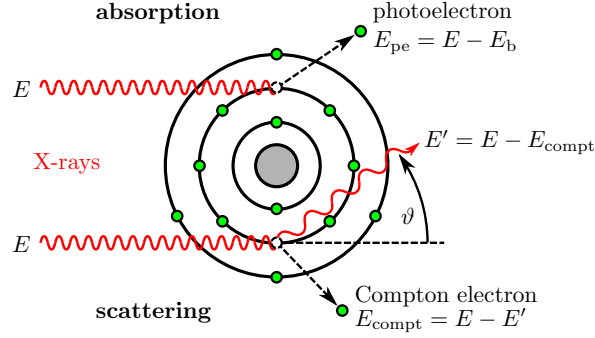
Figure 2.7: Illustration of photoelectric absorption and Compton scattering mechanism.

Figure 2.7. The higher the energy E of an incident photon related to the electron binding energy E_b, the higher the probability that the photon is not absorbed and continues to travel, in contrast to the photoelectric effect where it is absorbed. As a rule of thumb, for the attenuation coefficient due to the photoelectric effect

$$\mu_{pe} \propto Z^4 E^{-3} \tag{2.4}$$

holds [12]. The attenuation due to Compton scattering is given by

$$\mu_{compt} = \rho_e \, \sigma_{compt} \,. \tag{2.5}$$

Therein, ρ_e is the electron density, and σ_{compt} is the so-called cross-section for Compton scattering (i.e., the "likelihood" and angular distribution of photons scattered by a single electron). Latter can be derived from the Klein-Nishina equation and depends weakly on photon energy [12, 114]. As evident, Compton scattering depends on the electron density and scales only indirectly linear with the atomic number since $\rho_e = \rho \frac{Z}{m_a} N_A$, where m_a is the atomic mass, and N_A the Avogadro constant. Compared to photoelectric absorption, Compton scattering provides low-contrast information. However, the scattered photons lead to an undesirable background haze in the radiograms. Readers more interested in modern X-ray physics are referred to Ref. [3]. Figure 2.8 shows an illustrative comparison of attenuation coefficients of some materials used in the scope of this work. The transition at about 100 keV photon energy corresponds with the predominant mechanisms. Below 100 keV, the attenuation coefficient is dominated by photoelectric absorption and above primarily by Compton scattering.

2.1.3   X-ray detection and X-ray image

In modern X-ray imaging, the intensity of the transmitted X-rays is measured and converted into a digital X-ray image, a so-called radiogram. It is often referred to as a projection image in the context of µXRCT. For X-ray detection, X-ray detectors based on CCD, CMOS, and amorphous-Silicon (a-Si) sensor technology are applied [2, 64, 144, 149]. Therein, the transmitted photons are converted into an electrical signal, which is amplified, quantified, and finally digitized and represented as an image. Depending on the
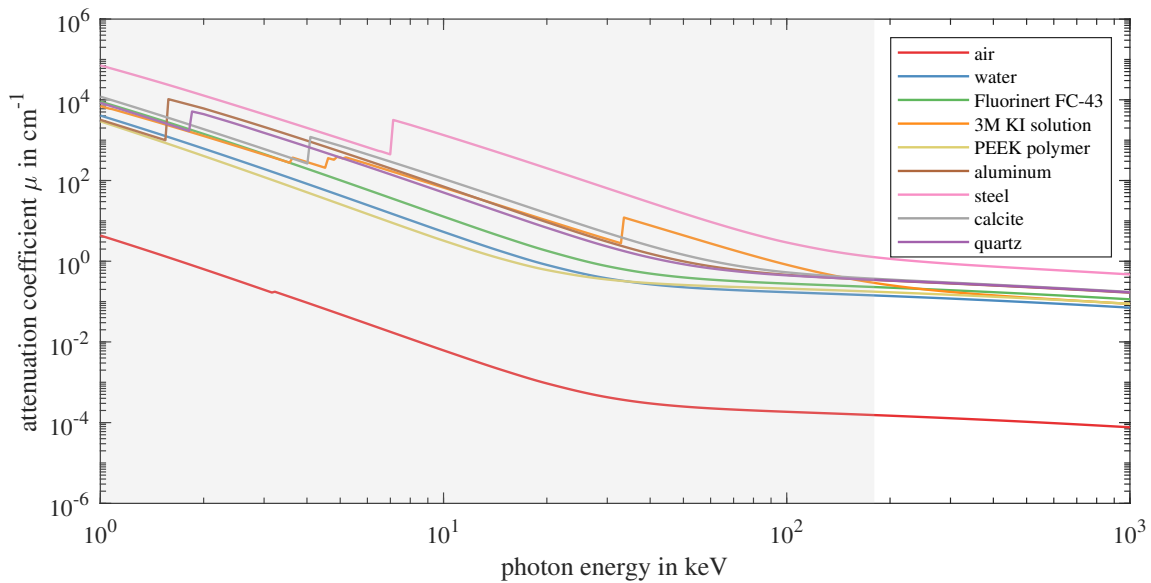
Figure 2.8: Comparison of photon energy-dependent attenuation coefficients of some materials used in the context of this work. Derived from the National Institute of Standards and Technology (NIST) online database [42]. The gray highlighted energy band shows the possible photon energies with the employed X-ray tube.

input for the conversion into an electrical signal, either X-ray photons or light photons, it is distinguished between direct and indirect converting detectors, respectively. For the latter, in an obligated pre-step, each X-ray photon is first converted into thousands of light photons by the use of a scintillator. This step is omitted for direct-conversion detectors, cf. Figure 2.9(a). They are the newest generation of detectors, partly combined with photon counting. They are quite promising due to different advantages, e.g., the unsharpness of the scintillation layer is removed, resulting in less blur in the image [142]. However, they are not yet widely used in laboratory systems.

The resulting projection image is usually displayed as a gray scale image. The higher the attenuation, or the lower the transmission, the darker the gray value of the corresponding pixel and vice versa. An example of a projection image is given in Figure 2.12(a), Subsection 2.1.5.

Detector characteristics The following refers to solid-state scintillator detectors, as used in the established system. In principle, solid-state scintillator detectors are available in different designs: single-row or multi-row, depending on the µXRCT setup, cf. Figure 2.10, both either flat or curved [13]. The resolution of a detector defines the number of columns and rows, which subdivide the X-ray-sensitive area into single pixels of a specific pixel size p_{size} as illustrated in Figure 2.9(b). The intensity $I(u, v)$ measured by one pixel at position (u, v) is the integral over the corresponding pixel area. The pixel bit-depth resolution defines how accurately the measured intensity values are resolved. The distance between adjacent pixel centers is the so-called pixel pitch that is identical to the pixel size in the ideal case. For quantification, the ratio of the usable detector sensor area
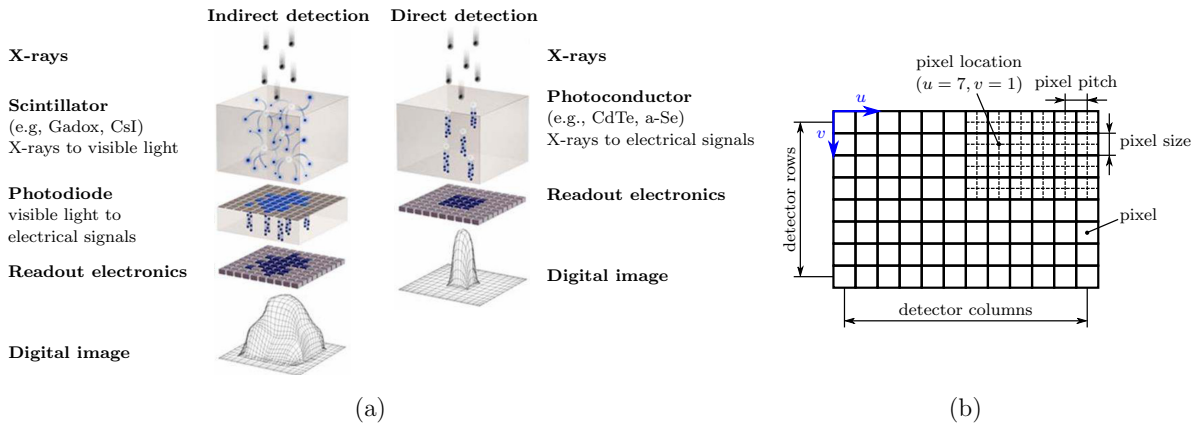
Figure 2.9: (a) Schematic of indirect versus direct X-ray detection based on Ref. [18]. (b) X-ray detector definitions.

over the total detector sensor area is usually used, also denoted as Geometric Detection Efficiency (GDE) [41]. Many different materials with specific pros and cons are used as scintillator. For an overview, see, e.g., Ref. [128]. In the context of this work, a detector with a Gadox scintillator and another with a CsI scintillator are used, see Chapter I. The scintillator's material and its thickness strongly influence the final image quality, quantified by the Modulation Transfer Function (MTF) and the Detective Quantum Efficiency (DQE), for details see Subsection 2.1.6. Furthermore, it defines the usable X-ray energy range (sensitivity).

The main parameter (in combination with the X-ray tube settings) which can be set is the exposure (integration) time, simply put, the time over which transmitted X-ray photons are collected. Between two exposures, also called frames, the data has to be read out and saved. Depending on how fast this can be done defines the maximum possible frame rate. The reciprocal value of the frame rate (minus the readout time) defines the corresponding minimal exposure time. A too long exposure time can result in an over-saturated projection image which strongly depends on the X-ray source settings. Another often available detector feature is binning. With this, also called hardware binning, it is possible to combine adjacent detector pixels into a single effective one, which can have different benefits like the increase of the Signal-to-Noise Ratio (SNR), cf. Subsection 2.1.6.

2.1.4   Experimental µXRCT configurations

So far, it has been explained how X-rays are generated, how they interact with matter, and how the transmitted X-ray intensity is measured by an X-ray detector leading to an X-ray image. However, many such projection images of the examined object from different directions are needed to back-calculate the object's internal structure. For this, a circular trajectory is usually used for the relative movement of the object and image acquisition system. For practical reasons, in materials science and related subjects, the object is usually rotated compared to medical applications, where the object is fixed, and the imaging setup is rotated. In the following, the former is always assumed.
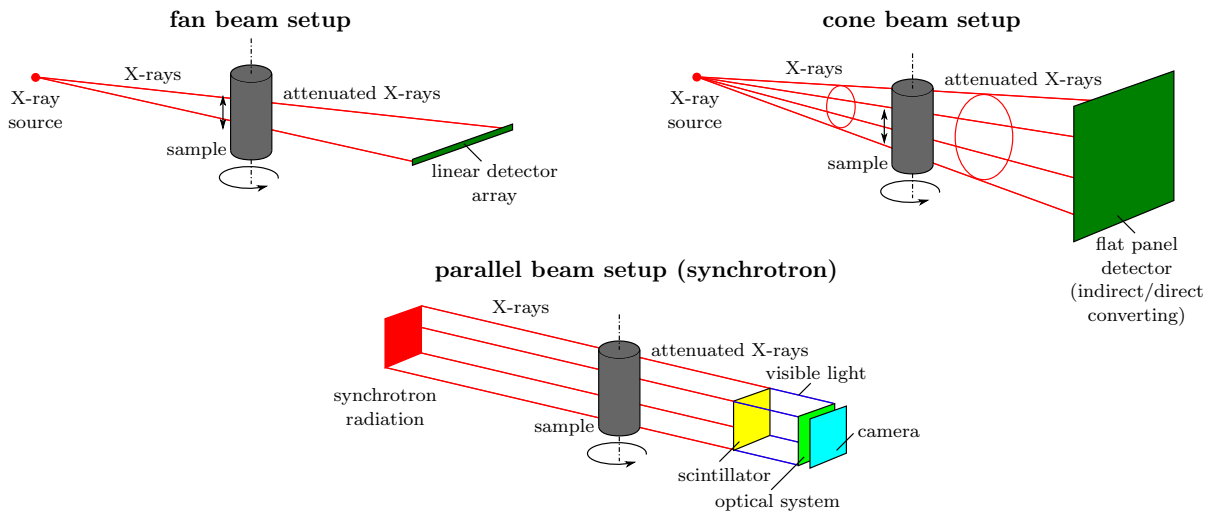
Figure 2.10: Different µXRCT configurations, cf. Refs. [13, 128].

In Figure 2.10, a typical fan and cone beam setup used in laboratory systems as well as a parallel beam setup as can be found at synchrotron radiation beamlines, is sketched. In the fan beam setup, the single line array detector scans one specific position of the sample in the rotation axis direction during a single 360° sample rotation. Thus, for sampling the object in the rotation axis direction, a 360° rotation is needed for each discrete position. A faster method is to move the object helical-like. The 3D data acquisition in the cone beam setup is generally much faster compared to fan beam scanning. This is due to the fact that during a single 360° rotation, enough data is acquired for the 3D reconstruction of the object. This is possible because the 3D cone beam is combined with a 2D detector array. In case of a field of interest that exceeds the size of the field of view determined by the 2D detector array, the object can be moved step-wise or in a helical manner through the X-ray beam, analogous to the procedure in fan beam scanning. Even though cone beam scanning is used in many µXRCT systems, it should be noted that more artifacts (cone beam artifacts) occur compared to fan beam scanning. Therefore, fan beam scanning is still often used in industrial and materials science applications [13].

In the case of a fan- and cone-shaped X-ray beam, the object's magnification is achieved by employing the concept of geometric magnification, illustrated in Figure 2.11. The geometric magnification M of the object onto the image plane is given by the ratio of the Source-Detector-Distance (SDD) to the Source-Object-Distance (SOD),

$$M = \frac{SDD}{SOD} = \frac{SOD + ODD}{SOD} \, , \tag{2.6}$$

where ODD is the Object-Detector-Distance. The sampling interval of the object, respectively voxel size, follows by

$$v_{\text{size}} = \frac{p_{\text{size}}}{M} \tag{2.7}$$

with the detector pixel size p_{size}. A voxel denotes a pixel in 3D, cf. Figure 2.17, Subsection 2.1.5.
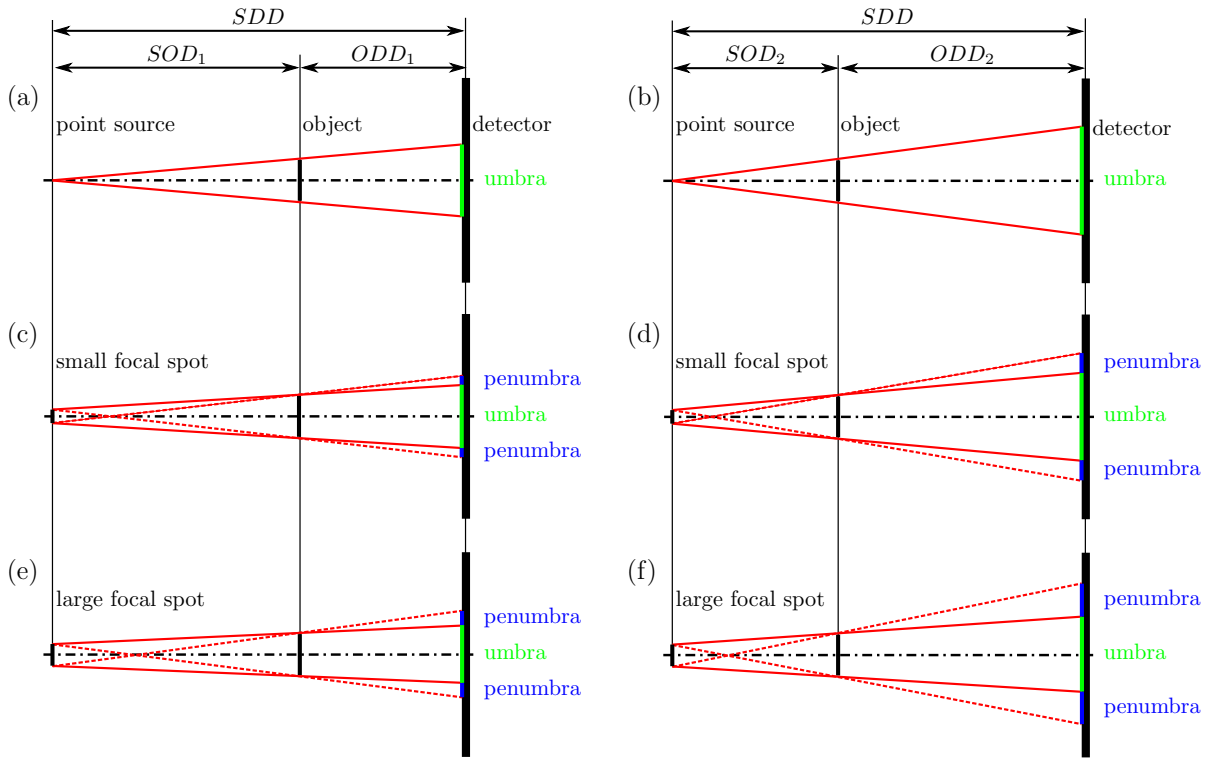
Figure 2.11: Illustration of the concept of geometric magnification and the influence of a finite source focal spot size.

It can be further distinguished between the fine-focus configuration ($SOD \ll SDD$) and the quasi-parallel configuration ($SOD > SDD/2$). In the fine-focus configuration, the detector pixel size and usually the SDD are fixed. To adjust the geometric magnification, the SOD is changed. Due to the finite size of the source's focal spot, so-called penumbra blurring occurs. That leads to blurred edges in the radiogram as depicted in Figure 2.11 for different focal spot radii r_f and values of M. The penumbra size P is related to r_f and M by

$$P = 2r_\mathrm{f}\frac{ODD}{SOD} = 2r_\mathrm{f}(M - 1)\,. \tag{2.8}$$

The overall maximum possible spatial resolution is limited by [137, 141]

$$R_\mathrm{max} = \underbrace{\frac{p_\mathrm{size}}{M}}_{=v_\mathrm{size}} + \underbrace{2r_\mathrm{f}\frac{M - 1}{M}}_{=P/M}\,. \tag{2.9}$$

That means, with increasing M, on the one side, it is zoomed in, and details are better resolved (decreasing v_size), but on the other side, edge blurring increases. Further, resolvable details cannot be smaller than the sampling interval, respectively v_size.

In the quasi-parallel configuration, the impact of penumbra blurring is reduced. In this configuration, the SOD is larger than the ODD, leading to $M < 2$. Consequently, the penumbra size is small and spatial resolutions smaller than the source focal spot size are possible. For the magnification of the object, an additional optical system between

the scintillator and the CCD/CMOS sensor is required, as in the parallel beam setup. This configuration has the intrinsic disadvantage that a lot of X-ray flux is wasted due to the low cone beam angle resulting in long scan times. Furthermore, it is technically significantly more complex than the fine-focus configuration. In the frame of this work, the fine-focus configuration is used. It is less complex, efficient, and sufficient for most upcoming research questions in the considered context.

At synchrotron radiation facilities, a nearly parallel and monochromatic X-ray beam is available. Due to the parallel nature, only a 180° rotation of the sample is required. The resulting 3D data sets have minor systematic artifacts (beam hardening and no cone beam artifacts) and, due to the high available X-ray intensity, by several orders of magnitude lower scan times, cf. Chapter 1. In this case, the object's magnification must be realized by an optical system (lenses) between the scintillator and the CCD/CMOS sensor, as in the quasi-parallel cone beam configuration.

2.1.5 Volume reconstruction

The aim of the volume reconstruction is to determine the spatial distribution of the attenuation value $\mu(\mathbf{x})$ for the scanned sample volume from the acquired projection images. The position vector $\mathbf{x} = (x, y, z)$ defines the position of each material point of the scanned volume in Cartesian coordinates (x, y, z). A short historical review shows how difficult this task used to be. After the introduction of the Radon and inverse Radon transformation by Johann Radon in 1917, it took more than 50 years until the first prototype scanner was built in 1971, and the very first reconstruction of a human head took place. Godfrey Hounsfield implemented the tomographic reconstruction algorithm based on the work of Allan Cormack in 1963, who created the mathematical framework for the practical implementation of tomographic reconstruction. In 1979, A. Cormack and G. Hounsfield received the Medicine Nobel Prize for this work.

In the following, some basic knowledge is provided to understand how the reconstruction works in general and how it is performed within this work. As usual, the expression $f(\mathbf{x})$ instead of $\mu(\mathbf{x})$ for the unknown object function is used. The following explanations are mainly based on Buzug [12] and Kak & Slaney [52]. Before starting with the actual reconstruction basics, some presteps are required, briefly described first.

Presteps: Normalization, linearization and sinogram space

The result of a scan is a set of projection images IM_n, $n \in \{1, \ldots, N_\theta\}$, of the object from N_θ different usually equidistant projection angles θ_n. The actual reconstruction is performed on the normalized (values in $[0, 1]$) and linearized projection images $\widetilde{IM}_n$. For normalization and linearization of the projection images IM_n, a current dark field image IM_{df} and open beam image IM_{ob} are needed. The dark field image, also called offset image, is acquired in absence of X-rays, while the open beam image, also called flat field image, is acquired in presence of X-rays but without the object itself. With these, a
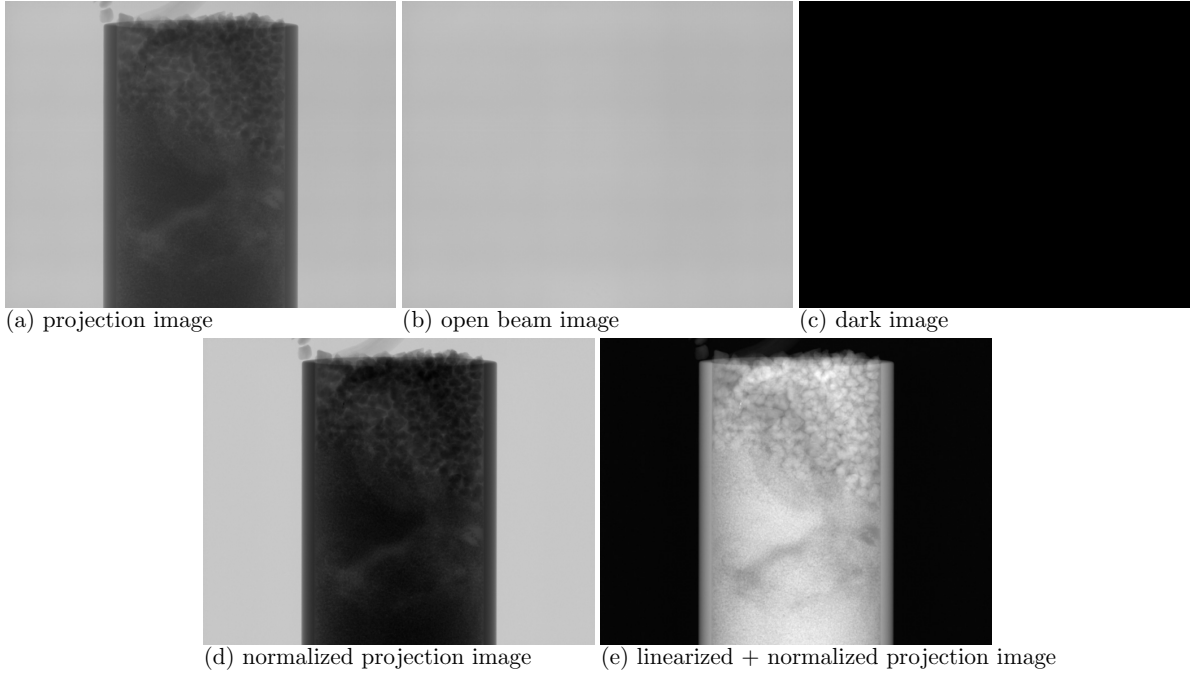
(a) projection image   (b) open beam image   (c) dark image

(d) normalized projection image   (e) linearized + normalized projection image

Figure 2.12: Illustration of the normalization and linearization step of projection images using the projection image of bean roots as an example.

normalization and linearization of each projection image is performed by

$$\widetilde{IM}_n = -\ln\left(\frac{IM_n - IM_{\mathrm{df}}}{IM_{\mathrm{ob}} - IM_{\mathrm{df}}}\right) . \tag{2.10}$$

Figure 2.12 shows exemplarily the different acquired images and the subsequent normalization and linearization steps.

From a comparison with the Lambert-Beer law for a monochromatic X-ray beam, Eq. (2.2), it is obvious that the nominator of the right side of Eq. (2.10) corresponds to the transmitted intensity I and the denominator to initial intensity I_0:

$$I(L) = I_0\,\mathrm{e}^{-\int_0^L \mu(\tilde{s})\mathrm{d}s} \qquad \longleftrightarrow \qquad -\ln\left(\frac{I(L)}{I_0}\right) = \int_0^L \mu(\tilde{s})\mathrm{d}\tilde{s} =: \tilde{p} \tag{2.11}$$

Each pixel value $\tilde{p}(u,v)$ of $\widetilde{IM}_n$ corresponds to the line integral of the unknown attenuation coefficients which belong to the respective X-ray path. The line integrals are sometimes referred to as the ray sum [72].

Before starting with the reconstruction of the unknown attenuation values based on $\widetilde{IM}_n$, it is advisable to perform additional intermediate steps to increase the image quality. Typical corrections include spot filtering, ring filtering, and corrections of geometrical misalignments of the setup. Transforming the projection image data $\widetilde{IM}_n$ into the sinogram space is also common. Thus, for each detector row, one sinogram is generated. Each sinogram contains all data that one specific detector row acquires during the rotation of the sample. Figure 2.13 shows an example of the transformation. The name sinogram is derived from the sinusoidal trajectory each feature performs over the projection angle θ.

(a) projection for $\theta = 0°$ (b) sinogram of the middle detector row   (c) corresponding tomogram
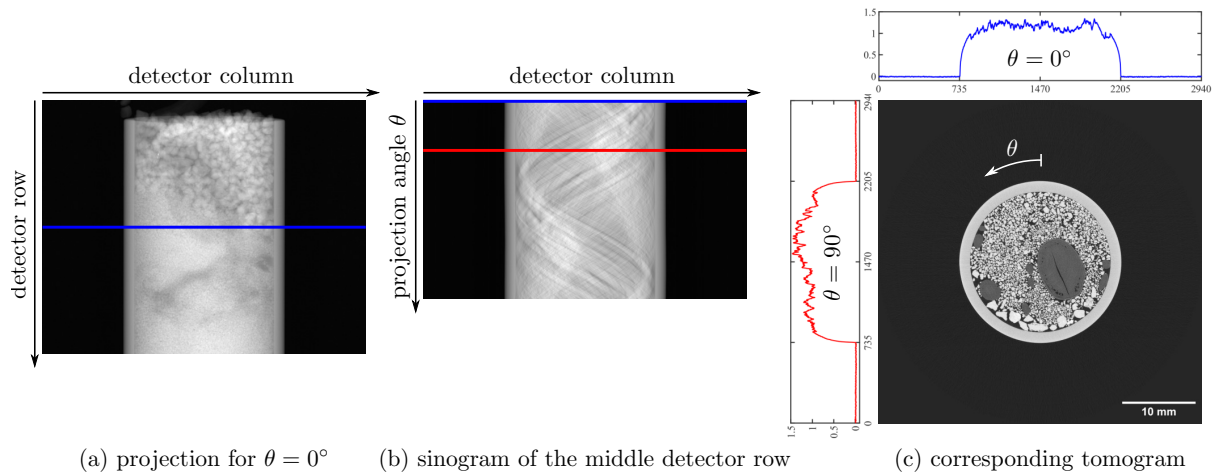
Figure 2.13: Transformation of normalized and linearized projection data into sinograms using the scan of bean roots as an example.

Radon transformation

The analytic reconstruction algorithm used depends on the shape of the X-ray beam, among other things. Before the applied FDK algorithm for cone beam X-ray sources in combination with a circular trajectory is considered, some essential basics are explained assuming a parallel beam and only 2D as illustrated in Figure 2.14.

In this case, the line integral $P_\theta(t)$ as function of t for projection angle θ is defined as

$$P_\theta(t) = \int\limits_{(\theta,t)\text{-line}} f(x,y)\mathrm{d}s \qquad (2.12)$$
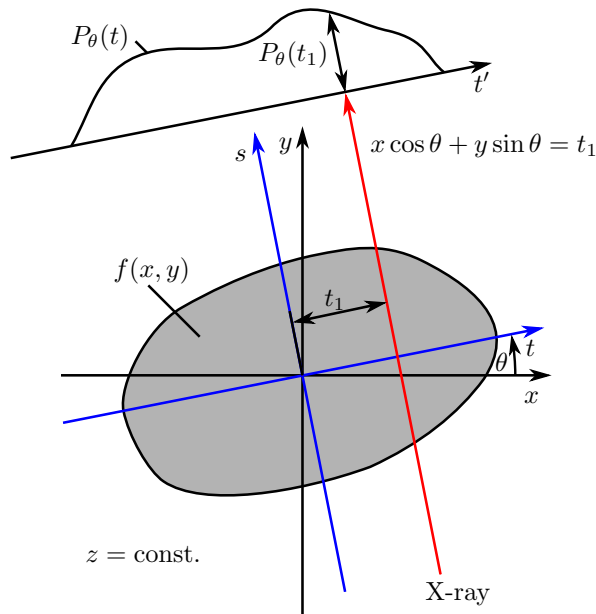
Figure 2.14: Object $f(x,y)$ and its projection $P_\theta(t)$ for a parallel beam scenario.

and known as the 2D Radon transform of the object function $f(x, y)$. Using the δ-function and the transformation $t = x \cos \theta + y \sin \theta$, Eq. (2.12) can also be written as

$$P_\theta(t) = \int_{-\infty}^{\infty} \int_{-\infty}^{\infty} f(x, y) \delta(x \cos \theta + y \sin \theta - t) \mathrm{d}x \mathrm{d}y. \tag{2.13}$$

A projection is formed by combining a set of line integrals. Since the available data are the measured projection data $P_\theta(t)$, the inverse problem needs to be solved. By applying the inverse Radon transformation on the projection data, the object function $f(x, y)$ is obtained. This is, however, connected to several mathematical challenges. Therefore, in practice, other approaches are used. One is the filtered back-projection.

Simple back-projection and filtered back-projection

To understand the filtered back-projection, we start with the simple back-projection. For reasons of simplicity, we still consider a parallel beam scenario in 2D. The basic idea of the simple back-projection is to smear out each measured line integral value (normalized and linearized detector pixel value) along the radiation path. The simple back-projection is mathematically defined as

$$g(x, y) = \int_0^\pi P_\theta(t) \mathrm{d}\theta = \int_0^\pi P_\theta(x \cos(\theta) + y \sin(\theta)) \mathrm{d}\theta \tag{2.14}$$

and illustrated in Figure 2.15 in the first row for different numbers of projection angles. As evident, the simple back-projection is not an acceptable reconstruction method since there is much blur in the reconstructed image (tomogram). This is indicated in Eq. (2.14) by using $g(x, y)$ instead of $f(x, y)$.
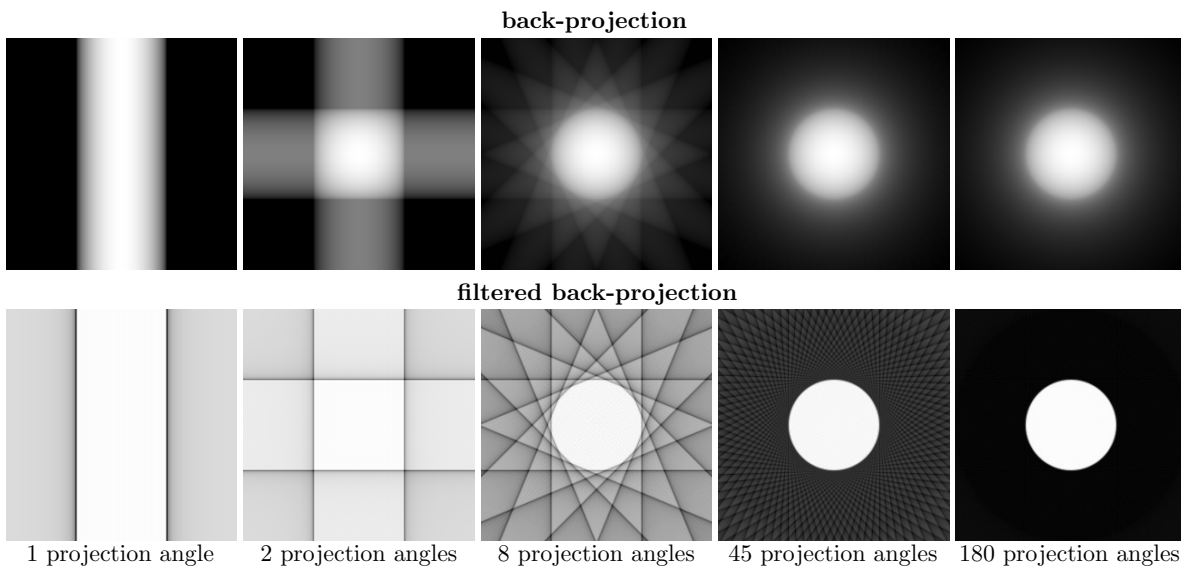

Figure 2.15: Simple back-projection versus filtered back-projection for different number of projection angles.

The blur is the basic motivation for the filtered back-projection. Thus, the Fourier transform $S_\theta(w) = \int_{-\infty}^{\infty} P_\theta(w)\mathrm{e}^{-j2\pi wt}\mathrm{d}t$ with frequency w of projection $P_\theta(t)$ is defined. With this the filtered projection

$$Q_\theta(t) = \int_{-\infty}^{\infty} S_\theta(w)|w|\mathrm{e}^{j2\pi wt}\mathrm{d}w \tag{2.15}$$

is determined. The filtered back-projection follows by

$$f(x,y) = \int_0^\pi Q_\theta(t)\mathrm{d}\theta = \int_0^\pi Q_\theta(x\cos(\theta) + y\sin(\theta))\mathrm{d}\theta\,. \tag{2.16}$$

As evident, Eq. (2.14) and Eq. (2.16) are almost identical. The crucial difference is that instead of smearing out the projection values $P_\theta(t)$, the filtered projection values $Q_\theta(t)$ are smeared out. The latter is illustrated in the second row of Figure 2.15. The high-pass filtering is performed in the frequency space. If $|w| := 1$, Eq. (2.16) would directly result in $P_\theta(t)$ ending up in the simple back-projection. The multiplication of $S_\theta(w)$ with $|w|$ leads to high-pass filtering, as the linearly increasing frequency variable results in a linear weighting of the spatial spectrum of $P_\theta(t)$. Alternatively, the filtering can be interpreted in the spatial domain by a convolution $Q_\theta(t) = P_\theta(t) * h(t)$ with the convolution kernel $h(t) = \int_{-\infty}^{\infty} |w|\mathrm{e}^{j2\pi wt}\mathrm{d}w$.

FDK cone beam reconstruction for planar detectors

Throughout this work, the so-called FDK algorithm is employed. The name of the FDK algorithm comes from the initials of the three developers, L. A. Feldkamp, L. C. Davis, and J. W. Kress, who proposed this algorithm in 1984 [20]. The algorithm is briefly summarized and discussed in the following, for more details, see Refs. [12, 20, 52].

The basic idea of this algorithm is to extend the 2D fan beam reconstruction algorithm for equally spaced collinear detectors by tilting the fan beam. The starting point is a set of normalized and linearized projections. The projection corresponding with the projection angle $\tilde{\theta}$ is given by $\tilde{P}_{\tilde{\theta}}(\eta', \zeta')$ where η' indicates the horizontal location and ζ' indicates the vertical location, cf. Figure 2.16. The algorithm requires that the planar detector system is projected on a planar plane containing the rotation axis, called virtual detector. Consequently, η' and ζ' have to be scaled with the applied geometric magnification M. It follows $\eta = \eta'/M$ and $\zeta = \zeta'/M$. After this initial step, each projection $\tilde{P}_{\tilde{\theta}}(\eta, \zeta)$ is weighted to obtain the weighted projection data

$$\tilde{P}'_{\tilde{\theta}}(\eta, \zeta) = \frac{SOD}{\sqrt{SOD^2 + \zeta^2 + \eta^2}}\tilde{P}_{\tilde{\theta}}(\eta, \zeta)\,. \tag{2.17}$$

Thus, it is considered that the titled fan for each elevation ζ changes the source-detector-distance and the angle increment $\mathrm{d}\tilde{\theta}$.

Secondly, the convolution of the weighted projection $\tilde{P}'_{\tilde{\theta}}(\eta, \zeta)$ with a ramp filter $h(\eta)/2$ by multiplying their Fourier transforms with respect to η is calculated

$$\tilde{Q}_{\tilde{\theta}}(\eta, \zeta) = \tilde{P}'_{\tilde{\theta}}(\eta, \zeta) * \frac{1}{2}h(\eta)\,. \tag{2.18}$$
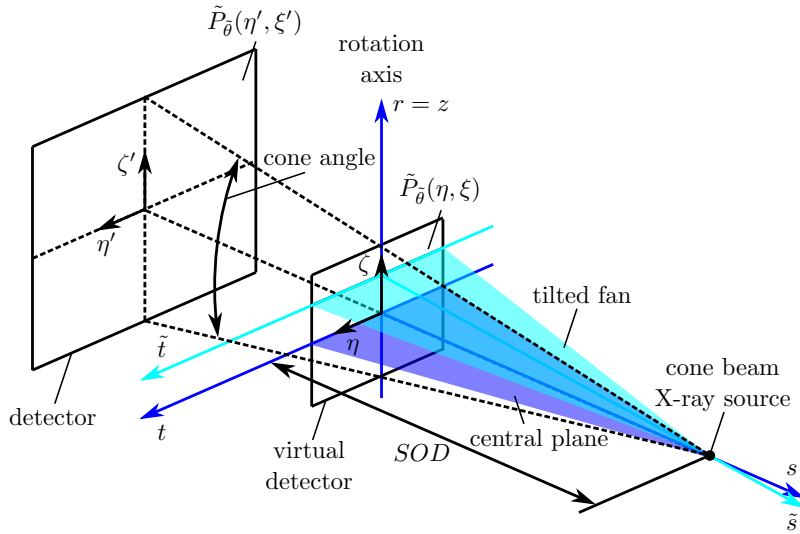
Figure 2.16: FDK cone beam reconstruction as extended 2D fan beam reconstruction. Geometrical definitions in the rotated coordinate system (t, s, r), rotated by projection angle $\tilde{\theta}$ against the fixed system (x, y, z) [52].

This convolution is performed independently for each elevation ζ.

In the last step, each weighted and filtered projection is back-projected over the 3D reconstruction grid

$$\tilde{f}(t, s, z) = \int_0^{2\pi} \frac{SOD^2}{(SOD - s)^2} \tilde{Q}_{\tilde{\theta}} \left(\frac{SOD\, t}{SOD - s}, \frac{SOD\, z}{SOD - s} \right) \mathrm{d}\tilde{\theta}. \tag{2.19}$$

The expression is simplified by using a rotated basic coordinate system. To end up in $f(x, y, z)$, $t = x \cos \beta + y \sin \beta$ and $s = -x \sin \beta + y \cos \beta$ are to be replaced. It has to be noted that $f(x, y, z)$ is an approximation and not an exact solution. The reason beyond is that with the commonly circular X-ray source orbit, so-called shadow zones occur in which no Radon data is available. The requirements of the so-called Tuy-Smith sufficiency condition [135] are not met.

The following remarks should be noted about the algorithm [52, 147]. (i) The reconstruction is exact for the central plane ($z = 0$) since the FDK algorithm is at this position identical to the equispatial fan beam reconstruction algorithm. The reconstruction error increases as the cone angle increases, such as when the reconstruction plane is further away from the central plane (increasing z), cf. Figure 2.18. (ii) The reconstruction is exact for objects homogeneous in the axial direction (z-direction), such as when $f(x, y, z) = f(x, y)$. (iii) The algorithm is perfectly suitable for GPU parallelization. For instance, the reconstruction of the whole volume can be segmented into several overlapping subvolumes in z-direction (projection parallelism scheme), and thus the computing process can be highly parallelized [74].

Algebraic reconstruction

Besides the analytic reconstruction methods, also called Fourier-based methods, to which the filtered back-projection and the FDK algorithm belong, other possibilities exist to perform the volume reconstruction. To mention is the group of algebraic reconstruction methods considering the reconstruction task as a linear system of equations. Thereby, the discrete nature or the practical implementation of µXRCT is considered from the beginning. The reconstruction problem formulation can be mathematically written as

$$\boldsymbol{W}\boldsymbol{v} = \boldsymbol{p} \tag{2.20}$$

whereas $\boldsymbol{W} \in \mathbb{R}^{m \times n}$ is the known projection matrix, $\boldsymbol{v} \in \mathbb{R}^n$ contains the unknown voxel data of all n voxels, representing the discretized unknown object function $f(\mathbf{x})$, and $\boldsymbol{p} \in \mathbb{R}^m$ includes all known projection data with the total number of all pixels m of all projections. The goal is to find $\boldsymbol{v} = \boldsymbol{W}^{-1}\boldsymbol{p}$. Since the projection matrix is generally not square and too large to invert algebraically, $\boldsymbol{W}^{-1}$ usually cannot be determined. An approach for solving this problem is to transfer it to an optimization problem formulation given by

$$\boldsymbol{v}^* = \underset{\boldsymbol{v} \in \mathbb{R}^n}{\arg\min} ||\boldsymbol{p} - \boldsymbol{W}\boldsymbol{v}||^2 \,, \tag{2.21}$$

which searches for the voxel vector $\boldsymbol{v}^* \in \mathbb{R}^n$ that minimizes the projection distance iteratively. Different algorithms to handle this optimization problem exist, e.g., the Algebraic Reconstruction Technique (ART), the Simultaneous Algebraic Reconstruction Technique (SART), the Simultaneous Iterative Reconstruction Technique (SIRT) [52], and Conjugate Gradient Least Squares (CGLS) [36, 77].

Algebraic reconstruction methods have several advantages compared to analytic ones. They are more potent and flexible since their application is not linked to particular geometric constraints of the underlying scan setup. Therefore, they are ideal for unconventional setups. Prior knowledge regarding the unknown object function can be exploited, and thus scan time can be saved. The main drawback of these methods is that they are computationally much more demanding compared to the analytical reconstruction methods, which, however, is increasingly fading into the background due to higher available computational power.

3D image presentation

The reconstructed 3D object $f(\mathbf{x})$ is visualized using a regular grid in 3D space. To each grid point belongs a voxel with a specific value resulting from the reconstruction process. The value correlates with the attenuation coefficient $\mu(\mathbf{x})$ of the considered physical volume element. From a mechanical perspective, each voxel can be interpreted as a discretized material point. For visualization, usually, a gray scale is used. The brighter the voxel gray value, the higher the material attenuation of the voxel and vice versa. As a rule of thumb, a higher attenuation can also be roughly interpreted as a higher material density. The reconstruction (FDK) is performed slice-/stack-wise in the direction of the rotation axis. Therefore, saving the data set as a stack of 2D gray value images (tomograms) is common. In the case of a panel detector with squared detector pixels,
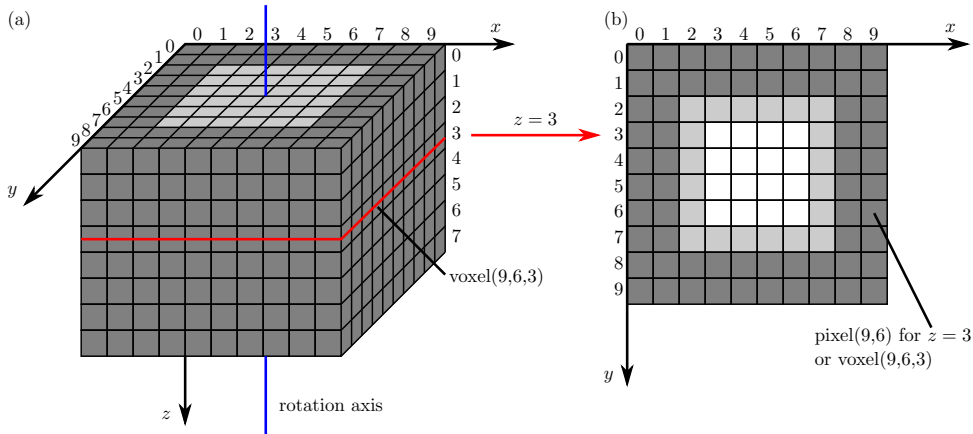
Figure 2.17: Reconstructed 3D object ($f(\mathbf{x}) \sim \mu(\mathbf{x})$) representation using a regular grid.

the voxels are cubes, which holds for the entire thesis. In Figure 2.17, an illustration is given with the coordinate system definition mainly applied within this work. Each voxel corresponds to a physical volume element. The physical volume element is related to the adjusted voxel edge size v_{size} given by Eq. (2.7).

The data size of a reconstructed data set follows from $\mathrm{NOE}_x \times \mathrm{NOE}_y \times \mathrm{NOE}_z \times 2^k$ where k is the voxel's bit-depth, typical 8-bit or 16-bit, and NOE the Number Of Elements.[1] Here NOE_x and NOE_y correspond to the number of detector columns and NOE_z to the number of detector rows. However, NOE_z is usually slightly lower since the slices with poor image quality in the edge region are cut off.

2.1.6   Image quality and artifacts in reconstructed volumes

Knowledge about image quality and artifacts are essential for correctly interpreting the reconstructed data sets and to properly define the scan settings influencing the image quality. Artifacts are referred to visual patterns in an image that does not physically belong to the imaging target. No knowledge of these can lead to misinterpretation of the data. This subsection addresses the topic of image quality and the most important artifacts. The latter is mainly shown by examples acquired on the built-up system.

Spatial resolution and Modulation Transfer Function

The spatial resolution is the smallest-spaced feature in an image that can be distinguished. Important to note is that the spatial resolution is not the same as the voxel size, but it can never be smaller, cf. Eq. (2.9). As a general guideline, to resolve a feature, at least 4–5 voxels are required for a sharp image.

Different possibilities exist to evaluate the spatial resolution of the complete imaging chain until the final reconstructed tomograms. One is the use of phantoms with an orthogonal combination of particular patterns of different sizes, e.g., bars, holes, fans, or the "Siemens

---

[1]For the two detectors used within in this work, $\mathrm{NOE}_x = \mathrm{NOE}_y = 2940\,(1944)$, and $\mathrm{NOE}_z = 2304\,(1536)$. Accordingly, the size of one reconstructed data set is up to $40\,(20)\,\mathrm{GB}$.

star". Another is the use of techniques to determine the so-called Modulation Transfer Function (MTF) curve, as described in the international standards DIN EN ISO 15708-3 [17] and ISO 12233 [46]. The MTF curve is a mathematical expression that describes the system's imaging quality with regard to spatial resolution. Related to this is the Michelson contrast of a gray value image IM given by

$$C = \frac{(IM_{\max} - IM_{\min})}{(IM_{\max} + IM_{\min})}, \tag{2.22}$$

which is the ratio of the image gray value variation interval around the mean value normalized by the mean value. For periodic functions, C is also called modulation. The MTF defines the ratio of the modulation of a transferred signal to the modulation of the input signal and can take values in $[0, 1]$. A value of 1 means that the considered imaging modality preserved the complete image contrast. The MTF curve of a imaging system quantifies the resolution of objects with a spatial frequency q (given in line pairs per millimeter [lp/mm]). It indicates how close two neighboring lines can get (increasing q) before they are no longer distinguishable due to the vanishing modulation of the transferred (measured) signal [12]. Examples of MTF curves can be found in Chapter I, Figure 7(c), as they were determined for the built-up system.

The MTF of the complete imaging process is the product of several contributions,

$$\mathrm{MTF}_{\text{μXRCT imaging}}(q) = \underbrace{\mathrm{MTF}_{\text{imaging hardware}}(q)}_{\mathrm{MTF}_{\text{X-ray source}}(q) \times \mathrm{MTF}_{\text{sampling}}(q)} \times \underbrace{\mathrm{MTF}_{\text{imaging software}}(q)}_{\mathrm{MTF}_{\text{interpolation}}(q) \times \mathrm{MTF}_{\text{filter kernel}}(q)} . \tag{2.23}$$

Each of the contributors can affect the final image resolution negatively. The contribution of the hardware ($\mathrm{MTF}_{\text{imaging hardware}}$) starts with the X-ray source (focal spot size), which determines the maximum physical possible resolution of the system ($\mathrm{MTF}_{\text{X-ray source}}$), see Eq. (2.9). In addition, it comprises the characteristics of the detector (detector blurring), the accurate alignment of all components, the accuracy of the sample rotation, as well as the chosen operator parameters (geometric magnification, voxel size, number of projections, signal-to-noise ratio, etc.), summarized as the influence of sampling ($\mathrm{MTF}_{\text{sampling}}$). The subsequent reconstruction also affects the final resolution. In the case of the FDK algorithm, the influence is given by the necessary interpolations ($\mathrm{MTF}_{\text{interpolation}}$) and the applied filter kernel ($\mathrm{MTF}_{\text{filter kernel}}$).

Noise, SNR and DQE

Noise affects the detectability of signals and is an ever-present problem in X-ray imaging. In systems using modern detectors, the image noise comes mainly from the shot noise, arising from finite photon statistics since X-ray matter interaction and detection are statistical events [114]. The random shot noise is governed by Poisson statistics. When a detector pixel records in average N_{p} photons, the uncertainty (noise) is given by $\sqrt{N_{\mathrm{p}}}$. Consequently, the Signal-to-Noise-Ratio (SNR) follows by

$$\mathrm{SNR}_{\text{detector}} = \frac{N_{\mathrm{p}}}{\sqrt{N_{\mathrm{p}}}} = \sqrt{N_{\mathrm{p}}}. \tag{2.24}$$

Related to the SNR is the Detective Quantum Efficiency (DQE) of the detector already briefly mentioned in Subsection 2.1.3. The DQE describes how effectively a detector can transfer the energy of the incident X-ray beam out of the detector [13, 41]. It is defined by

$$\mathrm{DQE} = \frac{(\mathrm{SNR}_{\text{detector output}})^2}{(\mathrm{SNR}_{\text{detector input}})^2} = \frac{N_{\text{p, detector output}}}{N_{\text{p, detector input}}} \, . \tag{2.25}$$

The DQE can reach a maximal value of 1 in the case of an ideal detector. For smaller values, it correspondingly degrades the SNR of the resulting projection images. Thus, the DQE is an essential property of the used detector.

In order to quantify the SNR in the reconstructed volume, which is related to the shot noise, the dose fractionation theorem [31, 69] is used. The dose fractionation theorem shows that tomographic reconstruction consistently integrates information from all projection angles. In a tomogram, each voxel has been traversed by many rays (one from each viewing angle). If it is supposed that a voxel attenuates N_{p} photons from all those rays, the uncertainty in the attenuation of the voxel is $\sqrt{N_{\text{p}}}$, and the SNR is again given by $\sqrt{N_{\text{p}}}$, equivalent to Eq. (2.24). Consequently, the number of photons passing through the sample is the governing factor in terms of SNR. The SNR within the tomograms increases with the square root of the acquisition time. Instead of increasing the acquisition time for a higher SNR value, detector binning can be a meaningful option. With the identical exposure time and number of projection angles, a 2×2 detector binning improves the SNR by a factor of $\sqrt{8}$. Alternatively, the same SNR value can be achieved in $8 \times$ less time by 2×2 detector binning ($8 \times$ fewer voxels).

Cone angle/Feldkamp artifacts

As already mentioned in the context of the FDK algorithm, cone beam µXRCT based on a circular trajectory cannot result in an exact solution for the entire 3D object since the so-called Tuy-Smith sufficiency condition [135] is not satisfied [12, 132]. In other words, the
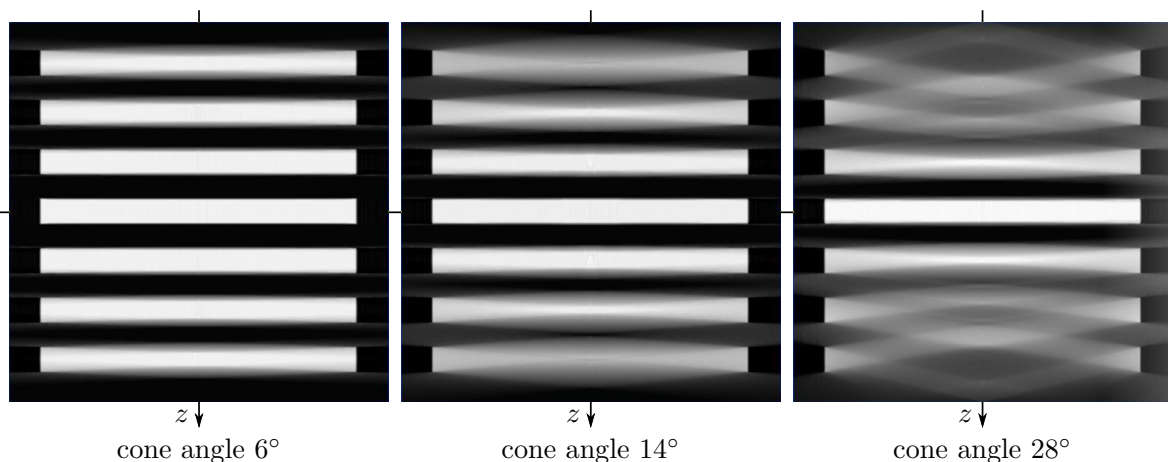

cone angle 6°   cone angle 14°   cone angle 28°

Figure 2.18: Cone angle/Feldkamp artifacts illustrated on a bar pattern object for different employed cone angles using the FDK reconstruction algorithm (based on Ref. [51]).

necessary data for an exact reconstruction in the 3D Radon space is not complete. That manifests in the reconstructed data sets as so-called cone angle or Feldkamp artifacts, as shown in Figure 2.18 on the reconstruction of an equidistant bar pattern sample. As can be observed, the extent of these artifacts is related to the cone angle given by the underlying system and the considered elevation (detector row). The smaller the cone angle, the less significant the resulting artifacts. In the setup presented, the maximum cone angle is 6.6°, consequently, this effect is small.

Beam hardening artifacts

Unlike a monochromatic X-ray beam, a polychromatic X-ray beam usually encounters the problem of beam hardening when traveling through an object. In general, low-energy X-rays are more strongly absorbed than high-energy X-rays. Consequently, the spectrum changes and the mean X-ray spectrum energy increases, which is called beam hardening. With higher absorption and higher object thickness, this effect is more significant.

The volume reconstruction sets up on the normalized and linearized projection values $\tilde{p}$ (ray sums) resulting from the Lambert-Beer law for a monochromatic X-ray beam, cf. Eqs. (2.2) and (2.11). However, for a polychromatic X-ray beam, actually the Lambert-Beer law for a polychromatic X-ray beam given by Eq. (2.3) would have to be used since μ depends on the photon energy E. However, the reconstruction is still performed based on the simplified and not correct assumption of a linear relation between $\tilde{p}$ and μ given by Eq. (2.11). Figure 2.19(a) illustrates the resulting cupping effect on a scanned biphasic sample. The effect is caused by the non-linear relation between the attenuation values and the projection values, which is not taken into account since the detector cannot distinguish between photons of different energy.

There are different hardware- and software-based possibilities to decrease this artifact. In a hardware-based way, a physical pre-filter is used to remove the low-energy X-ray photons from the beam spectrum, cf. Figure 2.5(c), which reduces the cupping effect. Linearization techniques represent a possibility of software-based correction. They have
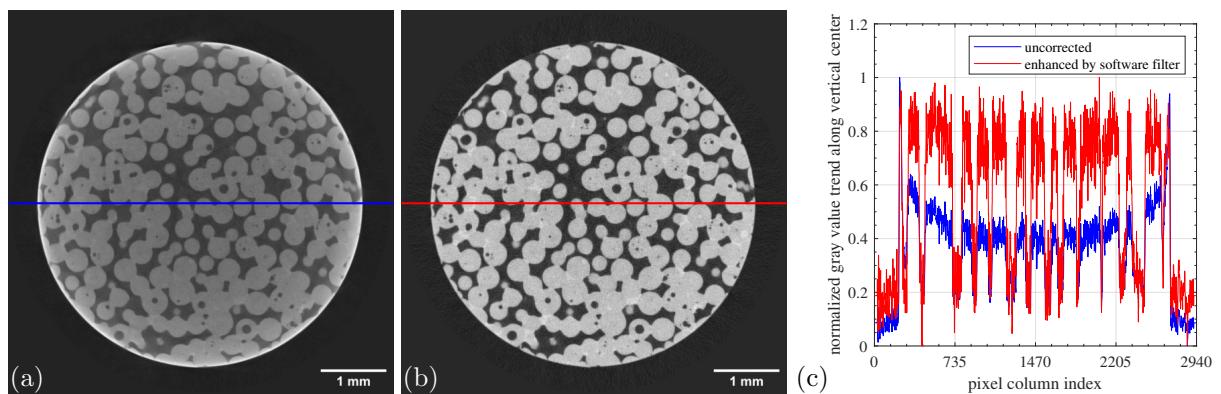

Figure 2.19: Beam hardening artifact (cupping effect) on a cylindrical 5 mm sintered bronze (CuSn10) sample with 39–43 % porosity. (a) uncorrected, (b) improved by simple beam hardening correction software filter, and (c) comparison for lines shown in (a,b).

been used in combination with hardware-based correction within this thesis. Linearization techniques are based on the idea that the measured polychromatic projection values are transformed into monochromatic values. Polynomial functions are usually used for this purpose, e.g., $\bar{p} = a(b + c\tilde{p} + d\tilde{p}^2 + e\tilde{p}^3 + f\tilde{p}^4)$ in which $\bar{p}$ represents the transformed values of the projection images used for the volume reconstruction [13]. The coefficients of the polynomial are adjusted to reduce the effect accordingly, as exemplified in Figure 2.19(b,c).

Cone angle (Feldkamp) and beam hardening artifacts are specific for cone beam μXRCT in combination with a circular trajectory and a polychromatic X-ray source. The artifact types in the following occur in any configuration, regardless of the shape of the X-ray beam and X-ray spectrum.

Detector/ring artifacts

The individual pixels of an X-ray detector always show slight differences concerning sensitivity, linearity, and spectral response and, therefore, are never exactly equal. It is also not uncommon that individual pixels or single rows/columns of pixels do not work at all. In this case, they deliver as signal output black pixels in the raw radiogram equivalent to a theoretically transmitted X-ray intensity of zero. Each detector pixel traces out a circular arc in the reconstruction, as illustrated in Figure 2.20(a). If the response of a pixel is too different from the neighboring pixels, visible rings appear in the reconstructed image. The smaller the arc, the stronger the effect, which is why the strongest ring artifacts are usually present in the area near the center of rotation, as shown in Figure 2.20(b). There are different techniques, hardware- and software-based, to reduce the creation of ring artifacts. A comparison of software-based ring artifact removal techniques can be found in,

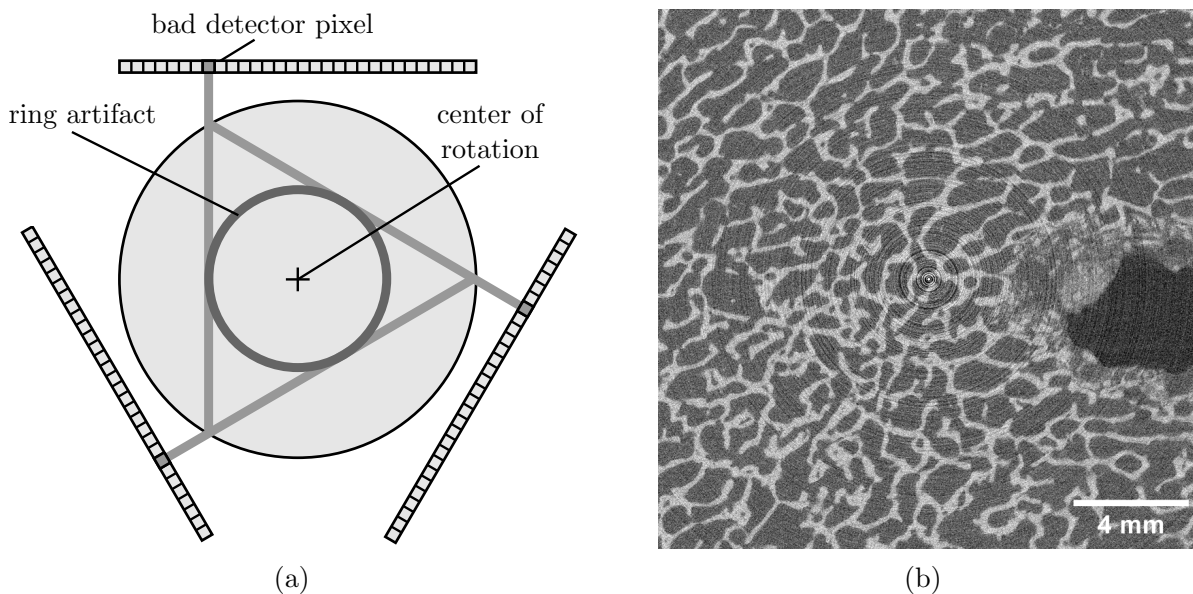(a)   (b)

Figure 2.20: (a) Creation of ring artifacts caused by the inequality of detector pixels. (b) Ring artifacts in a tomogram of a human femur head μXRCT scan without any correction. (For the data set with applied hardware and software correction, see Ref. [103].)
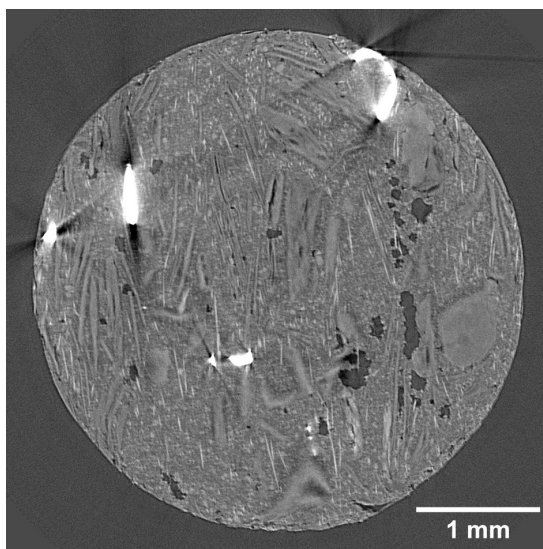
Figure 2.21: Moderate scattering artifacts due to metal chips in an expandable graphite tape.

e.g., Ref. [4]. For a hardware-based approach, see Chapter I II D and the example in Chapter I IV A.

Scatter and metal artifacts

Metal artifacts manifest themselves in the reconstructed data sets as dark stripes/streaks between the metal parts and glowing artifacts in the non-metallic areas. Although any metal yields artifacts, their impact depends on the size of the metal parts and on the chemical composition. The higher the atomic number (e.g., iron or steel), the more pronounced the artifacts, whereas, e.g. aluminum (low atomic number) is less problematic. In Figure 2.21, an example is given in which steel chips are included in an expandable graphite tape. The typical stripes and glowing artifacts are visible.

Center of rotation misalignment artifacts

One key element for the quality of the reconstructed data set is the software-based correction of underlying geometrical misalignments of a system, which can be hardware-based corrected only up to a certain level. Significant influence has the Center Of Rotation (COR) position and, related to this, the detector tilt angle in the image plane. Figure 2.22 shows how an incorrect COR value appears in the reconstructed tomograms. Typical signs are double edges and edge blur.

Considering one specific slice at vertical position z_j, the COR_j can be determined by reconstructing this slice with different values for the COR to find the optimal value [140]. However, in case of an additional detector tilt, the COR is only correct for the specific slice position (z_j-coordinate). A tilt correction must be performed to ensure the quality of all slides in z-direction. For the determination of the detector tilt angle, an interpolative approach has proven useful. For this purpose, the COR_j is determined for three different
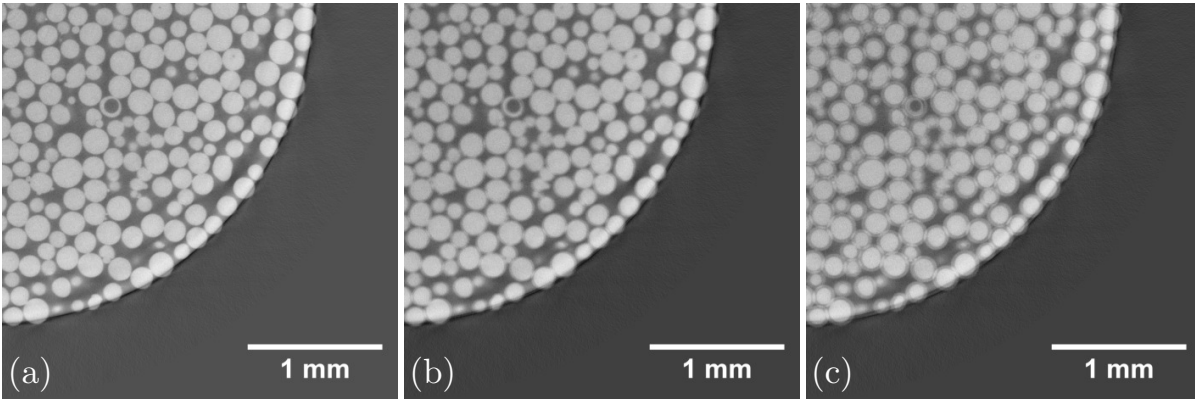
Figure 2.22: Center Of Rotation (COR) misalignment artifact. (a) COR correct, (b) COR 3 pixel off, and (c) COR 6 pixel off. (Zirconium dioxide (ZrO_2 68 %) beads of 0.1–0.2 mm diameter in a PEEK tube with 5 mm inner diameter.)

z_j positions (e.g., bottom, middle, and top). The angle searched for is then obtained by linear interpolation between z_j and COR_j.

Motion artifacts

If the sample remains not static during the scan, motion artifacts occur. That can happen if the sample is not fixed correctly on the sample holder or if the sample changes during the scan, apart from the movement of living objects. The change in the sample's microstructure during the imaging is particularly relevant for time-resolved in situ investigations. If the acquisition time of the scan is significantly slower than the process under investigation in uninterrupted time-lapse scanning mode, this can lead to the same type of artifacts. Also, intense relaxation or creep processes in interrupted time-lapse scanning mode can lead to motion artifacts. Depending on the origin, motion artifacts can lead to only slightly blurred edges or even smearing the image beyond recognition [128].

Undersampling artifacts

The theoretical number of required equidistant projection angles N_θ over 360° in a cone beam setup is determined by the number of involved detector columns $N_{columns}$ and defined by

$$N_\theta \geq \frac{\pi}{2} N_{columns} \tag{2.26}$$

based on the Nyquist–Shannon sampling theorem known from signal processing [12, 34]. In practice, since the number affects not only the scanning but also the reconstruction time and the required computational power, it is preferable to deal with the lowest possible number of projections providing an acceptable image quality [13]. Consequently, it is common to scan with significantly smaller N_θ than theoretically specified.[2] However, if

---

[2]In the case of the two employed detectors entirely covered by the sample, this would theoretically result in $N_\theta = \pi/2\,2940\,(1944) \approx 4619\,(3054)$. However, only 1800 (1440) projection angles are usually

the number is too low, this will result in artifacts, as seen in Figure 2.15 in the second row. For a recent systematic study of the influence on image quality, see Ref. [139].

2.1.7   Definition of acquisition parameters

Before an object or process can be scanned with a given µXRCT system, e.g., with the system described in Chapter I, the acquisition parameters have to be chosen. This is usually done according to the protocol depicted in Figure 2.23.
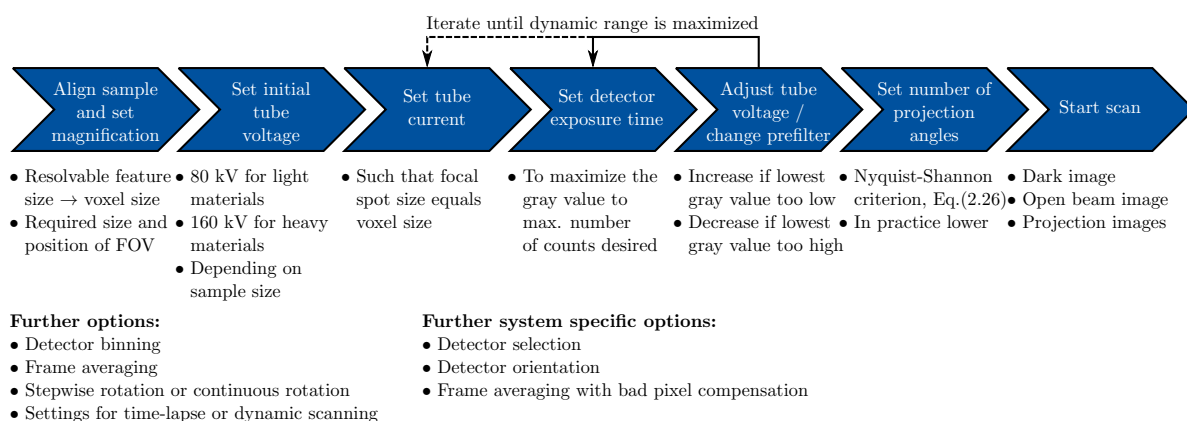

Figure 2.23: Protocol to determine the scan settings (extended based on Ref. [152]).

If the object is not yet geometrically determined, the protocol starts one step before with the definition of the size and shape of the sample. The representative volume size and the expected smallest feature of interest are considered. Ideally, the sample should be cylindrical and in radial direction not larger than the physical field of view to achieve optimal SNR and lowest artifacts. If no statement can be made about the representative volume size and the expected smallest feature, overview scans are performed beforehand.

During the selection process of the image acquisition settings, the necessary time per scan becomes an important quantity when experimental investigations are combined with in situ imaging. Theoretically, the time for one full scan in a perfect µXRCT system (neglecting all intermediate steps) is given by

$$\text{acquisition time} = \text{exposure time} \times \text{number of projections}. \qquad (2.27)$$

However, in the frequently used stepwise rotation protocol, a factor must be considered as the sample rotation is stopped at each projection angle position θ_n to avoid image blurring from the sample movement. According to Ref. [152], who compared different µXRCT studies performed on different commercial systems, this factor is 1.7 on average. This also holds approximately for the built-up system. If the scan time is particularly relevant, this value has to be optimized in the first step. Values close to 1 are possible by continuous sample rotation. In the next step, the acquisition time can only be reduced further by decreasing either the exposure time or the number of projections. Both harm the image

---

used, leading to sufficient good results.

quality, as described partly in the previous subsection, and can only be partially compensated by adapting other scan parameters. There will always be a trade-off between image quality and scan duration for a given hardware configuration. For a detailed discussion, it is referred to Ref. [152].

2.1.8   Image post-processing and quantification

The result of a reconstructed µXRCT scan is the back-calculated discretized distribution of $f(\mathbf{x}) \sim \mu(\mathbf{x})$ in the considered volume. For a quantitative analysis and other subsequent steps, the data set must be processed using image-processing methods [11, 45, 113, 117, 134]. Usually following main steps are involved: (i) denoising, (ii) segmentation, and (iii) quantification and possible geometry extraction.

Denoising

Due to the unavoidable noise in the data, the first step is noise reduction by using smoothing filters. It can be differentiated between global (e.g., mean, median, or Gaussian smoothing filter) and local smoothing techniques (e.g., anisotropic diffusion filter or total variation denoising) [32]. Compared to global techniques, local ones try to adapt the smoothing process in accordance with regional features and are more "edge preserving". Therefore, they are mostly preferred, however, significantly more computationally expensive.
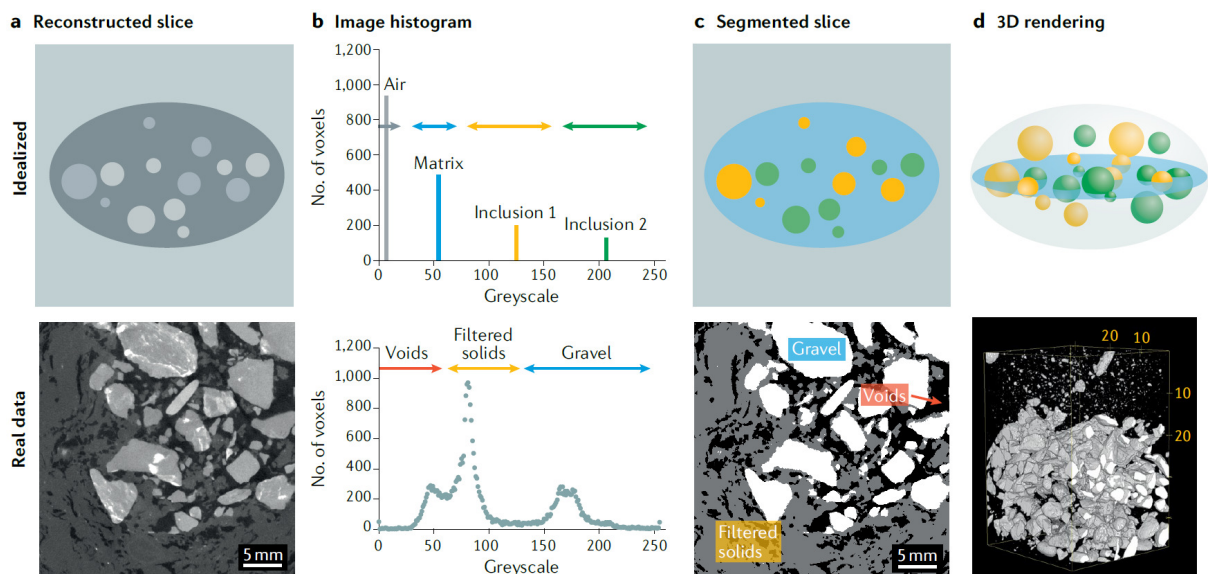

Figure 2.24: Segmentation processes for an idealized sample (row 1) and a real sample (row 2) on basis on a gravel filter pack (from Ref. [146]).

Segmentation

In the subsequent segmentation step, the object has to be separated into different regions, which are homogenous with respect to some characteristics. In Figure 2.24, the "threshold-based method" [76] is illustrated for an idealized and real example. Based on the gray value histogram of the whole volume, the different phases can be identified and thresholds defined. For details, it is referred to Ref. [146]. However, this method does not always lead to a satisfactory result, especially when the contrast between phases is low and the data set includes artifacts leading to over- or under-segmentation. Therefore, numerous other approaches like boundary-based and region-growing approaches [32] are used, up to machine/deep learning for the segmentation [146]. In traditional methods, morphological operations (dilation and erosion) or their combinations (closing and opening) [113] are usually applied in a subsequent step to improve segmentation results further. It is essential to mention that the segmentation result should always be critically questioned, as different methods can lead to different results. With regard to the quantification and other subsequent steps, measurement uncertainty must be taken into account.

Quantification and possible geometry extraction

Once the data set is segmented, many aspects can be quantified and analyzed, e.g., phase volumes and surfaces, population distributions, connectivity of phases, volume-averaged data, and much more. Based on the segmented data sets, the geometry or idealized geometry (graphs) can be extracted and used as input for different kinds of numerical simulations. For instance, the pore space can be extracted for direct numerical simulations to determine the sample's intrinsic permeability (tensor) [26, 75].

Temporal scan series

For temporally resolved scans, 3D images exist for different points in time. Those images can be treated separately according to the above-described approach with a subsequent comparison. In particular, for ex situ investigations, it may be necessary to transform the different frames into the same coordinate system, usually by using a rigid body transformation. This process is called image registration and can also be necessary for in situ investigations. The registration can be performed on the gray value images or based on the segmented ones. Related to this is the Digital Volume Correlation (DVC) [6, 122], also called Volumetric DIC or 3D-DIC [85], which is the extension of the well-known Digital Image Correlation (DIC) [83, 129]. It can be used to determine the displacement field between two 3D images.

2.2   Mechanical characterization and link to continuum mechanics

This section briefly overviews the employed mechanical and hydro-mechanical testing methods and motivates the link between imaging and continuum mechanics. While µXRCT imaging provides information on the micro scale, all the test methods considered here provide information on the macro (effective) scale. Information about deformation and other changes can be derived from a set of 3D images of an object under different loading conditions. In particular, deformations resulting from mechanical loading can be described by the concept of kinematics known from continuum mechanics [29, 38] and is a possibility to combine both scales.

2.2.1   Kinematics

Each material point $\mathcal{P}$ of a material body $\mathcal{B}$ can be identified in the reference configuration at time t_0 by the vector $\mathbf{X}$, and in the current (deformed) configuration at any time t by the vector $\mathbf{x}$, cf. Figure 2.25. The relation between the reference configuration and the current configuration is given by the Lagrangean placement function

$$\mathbf{x} = \chi(\mathbf{X}, t) \,. \tag{2.28}$$

To connect both configurations based on image data, it is more convenient to use the displacement vector defined as

$$\mathbf{u} = \mathbf{x}(\mathbf{X}, t) - \mathbf{X} \,. \tag{2.29}$$

A material line element $\mathrm{d}\mathbf{X}$ in the reference configuration and the corresponding line element $\mathrm{d}\mathbf{x}$ in the current configuration is considered to characterize the deformation.
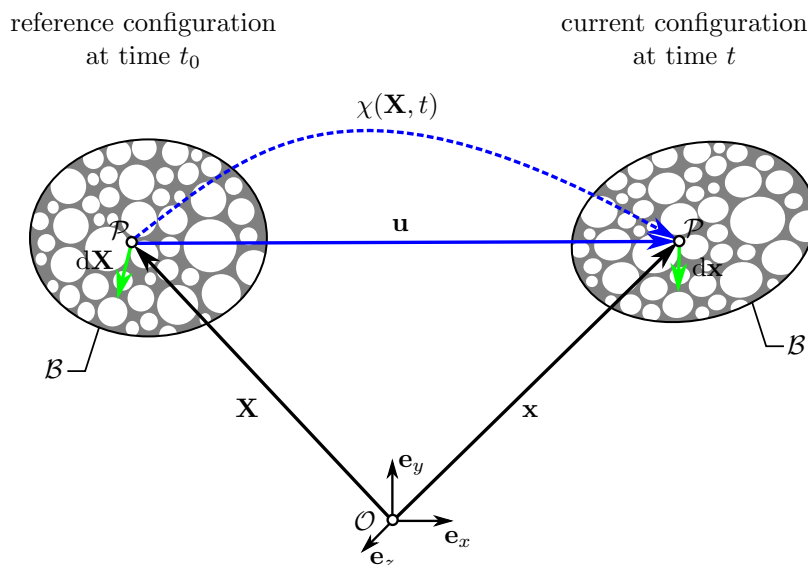

Figure 2.25: Reference and current configuration of a material body.

The line element in the current configuration is given by

$$\mathrm{d}\mathbf{x} = \mathbf{x}(\mathbf{X} + \mathrm{d}\mathbf{X}, t) - \mathbf{x}(\mathbf{X}, t) = \frac{\partial \mathbf{x}}{\partial \mathbf{X}} \cdot \mathrm{d}\mathbf{X} + \mathcal{O}\,. \tag{2.30}$$

Introducing the material deformation gradient $\mathbf{F} = \dfrac{\partial \mathbf{x}}{\partial \mathbf{X}} = \operatorname{Grad}\mathbf{x}$, and neglecting higher order terms, mapping relations for a material line, area and volume element in the reference $(\mathrm{d}\mathbf{X}, \mathrm{d}\mathbf{A}, \mathrm{d}V)$ and the deformed $(\mathrm{d}\mathbf{x}, \mathrm{d}\mathbf{a}, \mathrm{d}v)$ configuration can be found:

$$\mathrm{d}\mathbf{x} = \mathbf{F} \cdot \mathrm{d}\mathbf{X} \qquad \longleftrightarrow \qquad \mathrm{d}\mathbf{X} = \mathbf{F}^{-1} \cdot \mathrm{d}\mathbf{x} \tag{2.31}$$

$$\mathrm{d}\mathbf{a} = (\det \mathbf{F})\mathbf{F}^{-T} \cdot \mathrm{d}\mathbf{A} \qquad \longleftrightarrow \qquad \mathrm{d}\mathbf{A} = (\det \mathbf{F})^{-1}\mathbf{F}^{T} \cdot \mathrm{d}\mathbf{a} \tag{2.32}$$

$$\mathrm{d}v = (\det \mathbf{F})\mathrm{d}V \qquad \longleftrightarrow \qquad \mathrm{d}V = (\det \mathbf{F})^{-1}\mathrm{d}v \tag{2.33}$$

Alternatively, the material deformation gradient can also be formulated in terms of the displacement vector $\mathbf{u}$, yielding

$$\mathbf{F} = \frac{\partial \mathbf{x}}{\partial \mathbf{X}} = \frac{\partial(\mathbf{X} + \mathbf{u})}{\partial \mathbf{X}} = \mathbf{I} + \operatorname{Grad}\mathbf{u} \tag{2.34}$$

with the second-order unity tensor $\mathbf{I}$. The displacement field can be extracted from time-resolved 3D images by volumetric DVC [6, 85, 122], cf. Subsection 2.1.8. Knowing the displacement field enables calculating the deformation gradient $\mathbf{F}$ and all quantities based on it used in continuum mechanics. This allows, for instance, to analyze local deformation states.

Since the deformation gradient $\mathbf{F}$ consists of a rigid body rotation and a stretch, a polar decomposition via

$$\mathbf{F} = \mathbf{R} \cdot \mathbf{U} = \mathbf{V} \cdot \mathbf{R} \tag{2.35}$$

is meaningful to separate between a stretch followed by a rotation or vice versa. Therein, $\mathbf{R}$ denotes a proper orthogonal rotation tensor with the properties $\mathbf{R}^{-1} = \mathbf{R}^{T}$ and $\det \mathbf{R} = 1$. $\mathbf{U}$ is the right and $\mathbf{V}$ the left stretch tensor. Both are symmetric and positive definite. A rigid body motion is characterized by $\mathbf{U} = \mathbf{V} = \mathbf{I}$ and consequently $\mathbf{F} = \mathbf{R}$.

No stretch is associated with zero strain in engineering applications, which is why different strain tensors are defined. For instance, a measure of deformation is the difference between the squares of the differential line element in the undeformed configuration and the deformed configuration $(\mathrm{d}\mathbf{x}^2 - \mathrm{d}\mathbf{X}^2)$ which is the motivation for the Green-Lagrangean strain tensor

$$\mathbf{E} = \frac{1}{2}(\mathbf{F}^{T} \cdot \mathbf{F} - \mathbf{I})\,. \tag{2.36}$$

For small strains, also referred to as engineering strains, the geometric linearized Green-Lagrangean strain tensor

$$\boldsymbol{\varepsilon} = \operatorname{lin}(\mathbf{E}) = \frac{1}{2}(\operatorname{grad}\mathbf{u} + \operatorname{grad}^{T}\mathbf{u}) = \frac{1}{2}(\operatorname{Grad}\mathbf{u} + \operatorname{Grad}^{T}\mathbf{u}) \tag{2.37}$$

is used.

2.2.2   Mechanical and hydro-mechanical testing

Depending on the material class and the physical property of interest, numerous testing methods and protocols (often industry-specific) were developed and standardized in ASTM (American Society for Testing and Materials) and ISO (International Organization for Standardization) norms in order to guarantee comparability. In constitutive modeling of the mechanical material behavior, specific material properties are usually less interesting than the relationship between the deformation state and the applied loading condition over time. Basic load cases (tension, compression, shear, bending, torsion) and their combinations are usually experimentally applied to material samples to investigate this relationship. By introducing the stress tensor $\boldsymbol{\sigma}$, beside the strain tensor $\boldsymbol{\varepsilon}$, tests are performed either strain-controlled, $\varepsilon(t)$, or stress-controlled, $\sigma(t)$, over time t. In the case of strain control, the tested sample is subjected to time-dependent displacements (strains), causing resultant forces and torques (stresses) depending on the material response. Vice versa with stress control. Here the sample reacts to the loading of time-dependent forces and torques (stresses) with displacements corresponding to time-dependent states of strain [29]. In the following, a brief description of the tests used in the present work is given, illustrated in Figure 2.26.
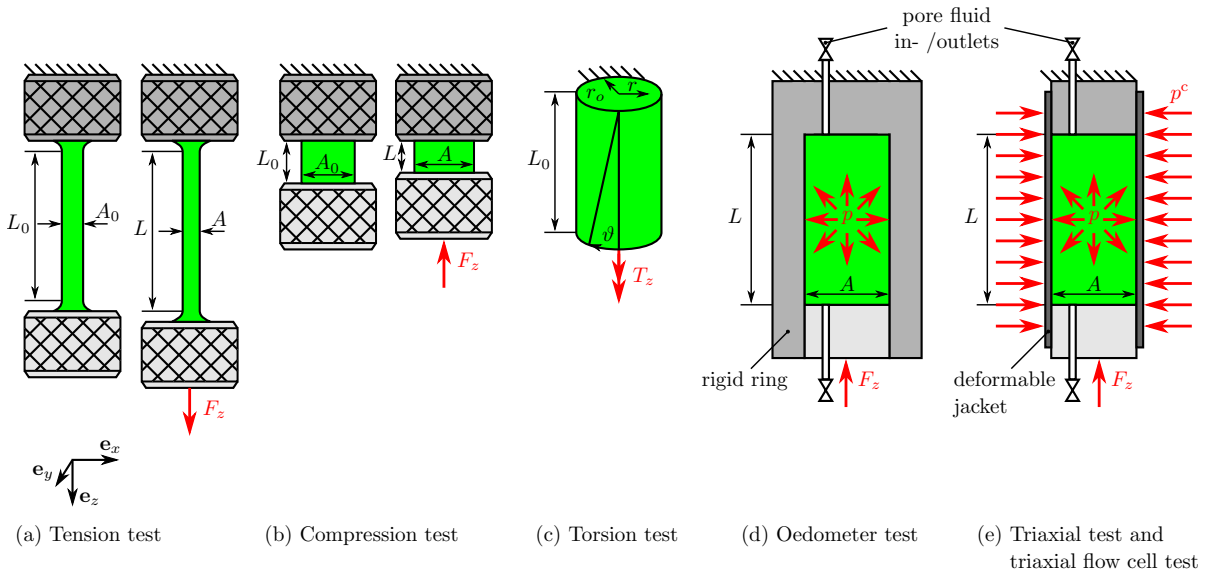

(a) Tension test   (b) Compression test   (c) Torsion test   (d) Oedometer test   (e) Triaxial test and triaxial flow cell test

Figure 2.26: Basic experimental tests used within this work.

In addition, acoustic wave propagation testing using the ultrasonic through-transmission technique is briefly described. As μXRCT, ultrasound investigations are non-destructive and allow determining the material's small-strain stiffness. This characterization method is employed alone and in combination with oedometer testing.

It is important to note that the concept of "engineering stress" and "engineering strain" is used in the material testing context. If required, the engineering stresses, also called 1st Piola-Kirchhoff or nominal stresses in the 3D generalization in continuum mechanics, can be converted into Cauchy stresses $\mathbf{T} = (\det \mathbf{F})^{-1}\mathbf{T}_{\mathrm{R}} \cdot \mathbf{F}^{T}$ where $\mathbf{T}_{\mathrm{R}}$ denotes the 1st Piola-Kirchhoff stress tensor [29, 38]. As common, a homogeneous stress distribution within

the sample is assumed. Information about the deformation state can be derived from the current position of the force/torque actuator if homogeneous sample deformation can be assumed and the machine/apparatus compliance is taken into account. In the case of non-homogeneous deformation, measurements must be performed locally. For this, strain gauges can be utilized. However, the strain gauges' positioning should consider the potential negative impact on imaging. In addition, larger deformations in relation to the spatial resolution of µXRCT imaging can be quantified based on the acquired images at each location as briefly motivated in Subsection 2.2.1.

Uniaxial tension testing

The uniaxial tensile test is one of the most important tests in destructive material testing. A sample with initial cross-section area A_0 and initial gauge section length L_0 in the unloaded state is uniformly loaded in the sample's longitudinal direction either in force- or displacement-controlled mode, cf. Figure 2.26(a). During the test, apart from the applied force F_z, the instantaneous gauge length L is measured. The engineering stress-strain curve is derived from the measured quantities to eliminate the specimen size influence. The engineering stress in loading direction is defined as

$$\sigma_{zz} = \frac{F_z}{A_0} \,, \tag{2.38}$$

and the corresponding engineering strain in loading direction is given by the sample elongation $\Delta L = L - L_0$ related to the original gauge section length L_0 of the sample

$$\varepsilon_{zz} = \frac{\Delta L}{L_0} \,. \tag{2.39}$$

In addition to the elongation of the sample in the longitudinal direction, a contraction perpendicular to the loading direction usually occurs described by the lateral strains $\varepsilon_{xx} = \varepsilon_{yy}$. Each material has a characteristic stress-strain profile, on the basis typical engineering quantities can be defined, such as Young's modulus, tensile strength, and proportional limit [40, 54, 57].

Uniaxial compression testing

The counterpart to the uniaxial tensile test is the uniaxial compression test, cf. Figure 2.26(b). A sample with initial cross-section A_0 and initial length L_0 is located and subsequently uniformly loaded between two stamps in force- or displacement-controlled mode. The uniaxial compression test is a crucial test to study building materials (e.g., rock, concrete, bricks, wood) but also to study metals when the focus is on the plastic stress-strain relationship at high strains since necking does not occur in contrast to uniaxial tensile testing. Important for the test is a moderate length-to-diameter ratio of the sample and a low friction coefficient in the contact zone between the sample and the stamps. The engineering stress and strain are defined analogously to the tensile test, Eq. (2.38) and (2.39). However, by convention, they are typically defined negatively. Usually, an expansion of the sample perpendicular to the loading direction occurs [40, 57].

Torsion testing

Another basic material test is the torsion test, cf. Figure 2.26(c). Starting from the unloaded state, the sample is twisted in torque or twist angle-controlled mode. The torque T_z and twist angle ϑ_z are measured during the test. Torsion tests have distinct advantages in comparison with tension and compression tests. It is, in particular, possible to study the stress-strain relationship over a large strain range since the necking and/or barreling (bulging), commonly seen in uniaxial tension or compression tests, does not occur [40, 148]. Usually, solid or hollow cylinders with a uniform cross-section are used as sample geometries. Therefore, defining the resulting stresses and strains in cylindrical coordinates (r, φ, z) for the radial, circumferential and axial direction is common. For solid and hollow cylindrical sample geometries, each material element deforms in pure shear under torsion loading. Between the twist angle ϑ_z and the shear angle $\gamma_{\varphi z} = 2\varepsilon_{\varphi z}$ following relation holds

$$\gamma_{\varphi z} = \frac{r\vartheta_z}{L_0} \tag{2.40}$$

where r is the radial position of the considered infinitesimal volume element and L_0 is the sample length. However, the calculation of the shear stress from the torque T_z is not unambiguously possible since the shear stress $\tau_{\varphi z}$ depends on $\gamma_{\varphi z}$ which varies with the radial position r. Without knowledge or an assumption for $\tau_{\varphi z}(r)$ the integration of the shear stress

$$T_z = 2\pi \int_{r_\mathrm{i}}^{r_\mathrm{o}} \tau_{\varphi z}(r) r^2 \mathrm{d}r \tag{2.41}$$

with the inner and outer radii r_i and r_o of the hollow cylinder (or solid cylinder $r_\mathrm{i} = 0$) cannot be performed. Vice versa, the shear stress cannot be computed from the measured torque T_z. Handbook equations for torsion testing quite often use the assumption of linear elasticity where $\tau_{\varphi z} = G\gamma_{\varphi z} = Gr\vartheta_z/L_0$ with the shear modulus G. Thus, the shear stress distribution is linear in radial direction, and from Eq. (2.41) follows

$$\tau_{\varphi z}(r) = \frac{2T_z\, r}{\pi(r_\mathrm{o}^4 - r_\mathrm{i}^4)} \tag{2.42}$$

with the maximum stress at the outer surface. If the material behaves not linear elastic, this equation no longer holds. For instance, in the case of perfect plastic material, the shear stress is uniformly distributed across the cross-section given by

$$\tau_{\varphi z} = \frac{3T_z}{2\pi(r_\mathrm{o}^3 - r_\mathrm{i}^3)} \,. \tag{2.43}$$

Consequently, deriving the stress-strain relationship from the experimentally measured torque-twist data can be difficult. Using a thin-walled tube as sample geometry can solve this problem, as the variation of stress and strain across the wall can be neglected. More interested readers are referred to Ref. [148] and therein cited literature. As before, the stress-strain response is a material characteristic based on which engineering quantities (e.g., shear modulus and torsional shear strength) can be derived.

Oedometer testing (confined uniaxial compression testing)

The oedometer test is a confined uniaxial compression test using an oedometer cell, cf. Figure 2.26(d). It is mainly used in soil mechanics but is also applied in other fields. During this test, a cylindrical sample (e.g., granular media like soil or powder) is enclosed in a stiff ring that prevents radial displacement ($\varepsilon_{rr} = 0$) and is loaded in the longitudinal direction by two stamps either in force- or displacement-controlled mode. The stamps are usually porous or equipped with a pore fluid port for potential sample drainage. Due to the stiff ring, the only non-zero strain is the longitudinal strain ε_{zz} equal to the volumetric strain. In different subject areas, individual definitions are used for the axial strain. The engineering strain definition is analog to the uniaxial tensile, respectively, compression test, given by Eq. (2.39). For the longitudinal stress σ_{zz}, Eq. (2.38) holds. Since the sample's radial expansion is impossible, a 3D stress state results. Different characteristic values, like the coefficient of volume compressibility, can be derived from the stress-strain curve [138].

Triaxial and triaxial flow cell testing

Triaxial testing of cylindrical samples using a Hoek triaxial cell design [37] is one of the most widespread and versatile tests used in rock and soil mechanics [47, 138]. With a triaxial cell, representative stress conditions can be imposed. Under these stress conditions, in addition to rock/soil failure parameters, other quantities, such as the sample's small-strain stiffness or intrinsic permeability with the appropriate equipment, can be determined.

The imposed mechanical boundary conditions are given by the axial load F_z and the confining fluid pressure p^c acting on a thin rubber sleeve confining the cylindrical sample's surface, cf. Figure 2.26(e). A homogeneous stress state results, given by

$$\sigma_{rr} = \sigma_{\varphi\varphi} = -p^c, \quad \sigma_{zz} = -|F_z|/A_0 \quad \text{and} \quad \tau_{r\varphi} = \tau_{rz} = \tau_{\varphi z} = 0 \tag{2.44}$$

using cylindrical coordinates [143]. Normal geomechanical stress definitions define positive stresses in compression compared to the definition applied in continuum mechanics used here. In addition to the confining and axial loading, it is usually possible to saturate the sample with a pore fluid with pressure p, $p < p^c$, and $p < |F_z|/A_0$. The corresponding cell is also called triaxial flow cell, but often just triaxial cell. By using the effective stress principle, from the total stress tensor $\boldsymbol{\sigma}$ the effective stress tensor $\boldsymbol{\sigma}_E$ can be derived by $\boldsymbol{\sigma}_E = \boldsymbol{\sigma} + \alpha\, p\, \mathbf{I}$ with Biot's coefficient α and the second-order unity tensor $\mathbf{I}$.

Usually, $\sigma_{zz} \leq \sigma_{rr} = \sigma_{\varphi\varphi}$ holds. In this case, the minimum principle stress (σ_3) corresponds to σ_{zz}, and the maximum and intermediate principal stresses (σ_1 and σ_2) are identical and correspond to $\sigma_{rr} = \sigma_{\varphi\varphi}$. The deviatoric stress σ_{dev} is given by $(\sigma_1 - \sigma_3)/2 = (\sigma_{rr} - \sigma_{zz})/2 = (|F_z|/A_0 - p^c)/2$, which corresponds to the magnitude of the maximum shear stress τ_{max}. The volumetric stress σ_{vol} corresponds to $(\sigma_{rr} + \sigma_{\varphi\varphi} + \sigma_{zz})/3 = -(2p^c + |F_z|/A_0)/3$. In Figure 2.27, volumetric and deviatoric stresses for different ratios of $(|F_z|/A_0)/p^c = \sigma_{zz}/\sigma_{rr}$ are visualized.

The engineering strain in the longitudinal direction ε_{zz} is given analogously to the uniaxial compressive or tensile test by Eq. (2.39). The sample's radial strain ε_{rr} can be back-
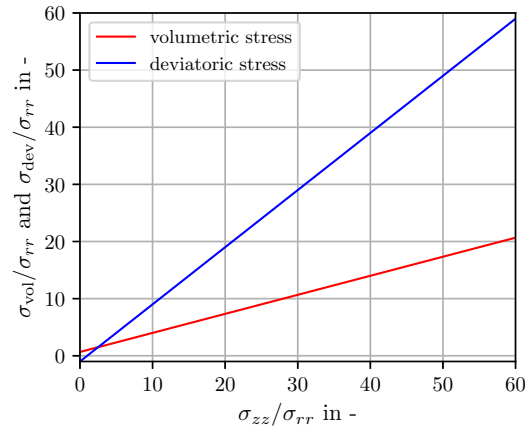
Figure 2.27: Resulting volumetric and deviatoric stresses in a triaxial (Hoek) cell for different ratios of axial ($\sigma_{zz} = -|F_z|/A_0$) and radial ($\sigma_{rr} = -p^c$) loading.

calculated from the injected confining fluid volume to establish p^c if the compliance of all involved components as well as the confining fluid compressibility is known. However, since the samples that are usually examined are relatively stiff, e.g., rock cores, the values are not very accurate. If the strains are of greater interest, it is recommended to use strain gauges.

A typical triaxial shear test consists of four steps: (i) sample and system preparation, (ii) saturation, (iii) consolidation, and (vi) shearing by increasing $|\sigma_{zz}| = |F_z|/A_0$. Depending on how the shearing is performed in combination with the drainage conditions, in geomechanics, different types of triaxial tests are distinguished [70, 71]. In addition to standardized test protocols, various investigations can be carried out within a triaxial flow cell. In particular, hydro-mechanically coupled phenomena and flow processes can be studied, for instance, the characterization of the load-depending intrinsic permeability. For this, the pore fluid inlet is connected to a syringe pump. The volume flux q or the pressure p_1 at the inlet is controlled, while the other is measured respectively. Furthermore, the back pressure p_2 at the outlet is measured or controlled. From this information, in combination with the pore fluid properties, the intrinsic permeability for single-phase flow can be derived under different stress states ($\sigma_{rr} = \sigma_{\varphi\varphi}$, σ_{zz}). Instead of using a triaxial flow cell to investigate transport phenomena, simpler cell designs are often used when hydro-mechanical coupling aspects are less relevant. For these cells, usually, only p^c can be prescribed [22], or no mechanical loading conditions can be imposed at all.

Acoustic wave propagation testing at ultrasonic frequencies

Acoustic wave propagation testing at ultrasonic frequencies is a standard non-destructive testing method often used to characterize the small-strain stiffness of materials. There are two types of waves in elastic solids. The first type are compressional (primary) waves, so-called P-waves, and the second type are shear (secondary) waves, so-called S-waves. P-waves are longitudinal waves since the propagating displacement field varies in the direction of the wave propagation. S-waves are transverse waves as the displacement
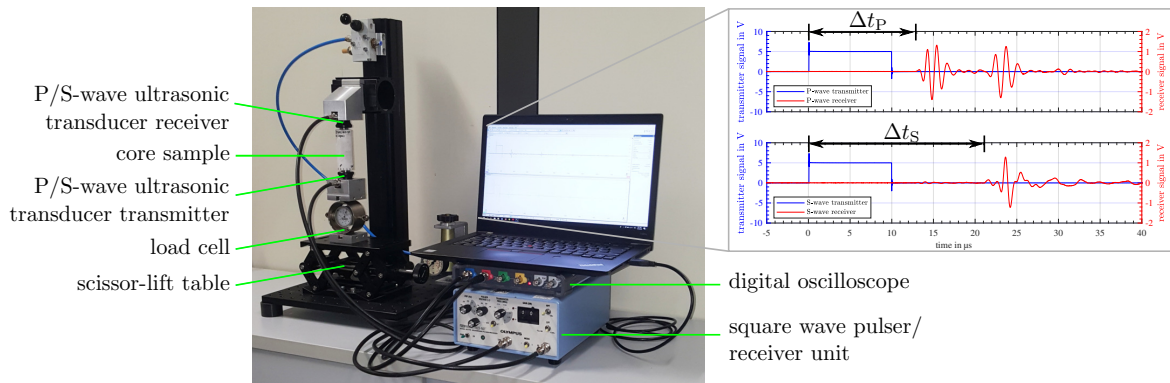
Figure 2.28: Ultrasonic through-transmission measurement setup.

field varies perpendicular to the wave propagation direction, cf., e.g., Ref. [125]. The propagation velocity of both waves v_P and v_S in a homogeneous, isotropic, elastic medium is directly related to the material's small-strain stiffness by

$$v_P = \sqrt{\frac{\tilde{M}}{\rho}} \quad \text{and} \quad v_S = \sqrt{\frac{G}{\rho}} \tag{2.45}$$

with the P-wave modulus $\tilde{M}$, the shear modulus modulus G and the bulk density ρ. The P-wave modulus is also called constrained modulus since the material expansion in lateral direction is prevented by neighboring material [1, 125]. By determining the waves' propagation velocity v_P and v_S through the sample, the sample small-strain moduli, also sometimes called dynamic moduli, can be derived.

To measure the waves' propagation velocities, different methods exist. One is the employed ultrasonic through-transmission technique using a pair of identical P-wave respectively S-wave piezoelectric ultrasonic transducers. A typical setup with the measured signals is shown in Figure 2.28. The sample of length L_0 is aligned between the respective transducer pair. A coupling gel between the sample and the transducers is used, and a specific contact pressure is imposed to ensure proper transmission. One ultrasonic transducer, connected to a square wave generator with an amplifier, emits a pulse. The other transducer on the opposite sample side is used as a receiver. An oscilloscope records the signals of both ultrasonic transducers. From the two signals, the travel time Δt of the pulse in the sample can be detected by determining the first arrival point of the wavefronts at the receiver transducer. In combination with the known sample length, the propagation velocities are given by $v_P = L_0/\Delta t_P$ and $v_S = L_0/\Delta t_S$. For more details about ultrasonic testing, it is referred to Ref. [56].

Chapter 3:
Summary and Outlook

3.1   Summary

In the context of the present work, "Experimental multi-scale characterization using micro X-ray computed tomography," the infrastructure to investigate a wide variety of physical phenomena from mechanics and beyond, combined on the macro (effective) scale and the micro scale (grain or pore scale), was set up.

For this purpose, a modular, open-designed, and thus very versatile µXRCT system was developed and established. It was intrinsically designed for in situ investigations of porous materials by its open and modular nature on each level. The system was presented in detail in the publication "An open, modular, and flexible micro X-ray computed tomography system for research," Chapter I. It has been employed in various collaborations to investigate different research questions, ending in numerous published articles and data set publications. Thereby, a particular focus was laid on the FAIR data principles throughout the work [145]. In this context, a workflow was established for publishing the data sets (image and measurement data) via DaRUS, including required metadata to make them more sustainable and usable by other researchers.

A specific research question dealt with understanding and characterizing the influence of different thermal treatments on Carrara marble core samples. This multi-scale problem was investigated in the publication "Effects of thermal treatment on acoustic waves in Carrara marble," Chapter II. Here, non-invasive µXRCT imaging was combined ex situ with non-destructive acoustic wave propagation measurements at ultrasound frequencies. Independent of the exact heat treatment protocol, the generated crack porosity could be identified as the significant microstructural parameter, and a corresponding model could be derived to predict the wave propagation evolution based on the crack porosity.

Many open questions from mechanics and, in particular, investigations of hydro-mechanically coupled phenomena of fluid-saturated porous materials require an in situ approach of experiment and imaging with potentially subsequent simulation. The built-up µXRCT system was extended by integrating a universal testing machine to make such experimental studies as simple and versatile as possible. This approach allows in situ compression/tension and torsion studies and their combinations (simultaneously or sequentially) in the complete range of possible geometric magnifications. By using the extended system, the quite challenging effect (from a modeling perspective) of load sequence behavior due to nonlinearities was illustrated on an open-cell reticulated PUR sample as part of the publication "A multifunctional mechanical testing stage for micro X-ray computed tomography," Chapter III. The spectrum of possible mechanical and hydro-mechanically coupled boundary value problems can be extended by employing special cell designs, as demonstrated by two further examples employing a customized oedometer cell and a triaxial flow cell. In both cases, the axial load is applied externally by the integrated universal

testing machine resulting in a straightforward cell design. An in situ fracture experiment of a rock sample within the triaxial flow cell was considered to show the possibilities of application in the context of fracture mechanics.

The effective stiffness behavior of granular mixtures consisting of stiff (glass) and soft (rubber) monodisperse particles has yet to be fully understood, as it cannot be explained with classical mixture theories. The workflow for investigating such multi-scale problems from the granular media field (solid-like state) was subsequently presented in detail in the publication "Multi-scale characterization of granular media by in situ laboratory X-ray computed tomography," Chapter IV. For the study, a customized oedometer cell with integrated ultrasonic P-wave transducers to characterize the sample's small-strain stiffness under different preloads was designed and integrated into the extended system. With the workflow presented and the corresponding data sets, the first step has been taken to investigate further and better understand the effective mixture stiffness behavior.

3.2   Outlook

The research potential offered by µXRCT imaging alone and especially in combination with mechanical and hydro-mechanical characterization is enormous. In particular, the laboratory-based possibilities will further increase. Thanks to the open and modular concept of the presented system, hardware and software adaptations and extensions are always possible. That offers optimization potential, especially with regard to the time resolution of in situ studies. For instance, continuous sample rotation respectively dynamic scanning should be considered. In addition, the optimization of data redundancy in the image acquisition process by software development can be a promising approach for faster scanning. Thus, a few projection images are sufficient to observe and characterize the temporal evolution of specific field functions, like the displacement field over time. This kind of approach is named projection-based digital volume correlation (DVC) [48, 60, 131] and should be considered in more detail. There is also potential for improvement in the calibration of the centrical alignment of the two rotary tables in the installed testing device, for instance, by integrating customized flexure elements [50, 120, 121].

The built-up system can be considered a versatile experimental platform, ready for more complex multi-physical problems by appropriate extensions. One recent example is the chemo-thermo-hydro-mechanical investigation of the influence of flow rate and temperature on the reaction rate of CO_2-saturated brine in fractured carbonate rock cores in the context of CO_2 storage. The integration of an environmental chamber could be an expedient extension. Recently, an in situ heating chamber for up to $1000\,°C$ has been proposed [151]. Such a chamber allows to investigate the crack initiation in the investigated Carrara marble samples not only after the cooling but during the crack initiation/opening at high temperatures.

Different multi-scale problems have been considered or at least motivated in the context of this work. The resulting data sets and the possibility to create corresponding complementary data sets offer the potential to further connect both scales by using and developing further different modeling approaches, not part of this thesis.

Bibliography

[1] Aki, K. & Richards, P. G.: *Quantitative Seismology*. University Science Books, Mill Valley, CA 2009.

[2] Allé, P.; Wenger, E.; Dahaoui, S.; Schaniel, D. & Lecomte, C.: Comparison of CCD, CMOS and Hybrid Pixel X-ray detectors: detection principle and data quality. *Physica Scripta* **91** (2016), 063001.

[3] Als-Nielsen, J. & McMorrow, D.: *Elements of modern X-Ray Physics*. Wiley, Chichester, England 2011.

[4] Anas, E. M. A.; Kim, J. G.; Lee, S. Y. & Hasan, M. K.: Comparison of ring artifact removal methods using flat panel detector based CT images. *BioMedical Engineering OnLine* **10** (2011), 72.

[5] Balcewicz, M.; Siegert, M.; Gurris, M.; Ruf, M.; Krach, D.; Steeb, H. & Saenger, E. H.: Digital rock physics: A geological driven workflow for the segmentation of anisotropic Ruhr sandstone. *Frontiers in Earth Science* **9** (2021), 673753.

[6] Bay, B. K.; Smith, T. S.; Fyhrie, D. P. & Saad, M.: Digital volume correlation: Three-dimensional strain mapping using X-ray tomography. *Experimental Mechanics* **39** (1999), 217–226.

[7] Berger, M. J.; Hubbell, J. H.; Seltzer, S. M.; Chang, J.; Coursey, J. S.; Sukumar, R.; Zucker, D. S. & Olsen, K.: XCOM: Photon cross sections database (version 1.5), NIST standard reference database 8 (XGAM) (2010), https://physics.nist.gov/xcom.

[8] Blumich, B.: *NMR Imaging of Materials*. Monographs on the Physics and Chemistry of Materials, Oxford University Press, London, England 2000.

[9] Boone, M. N.; Witte, Y. D.; Dierick, M.; Almeida, A. & Hoorebeke, L. V.: Improved signal-to-noise ratio in laboratory-based phase contrast tomography. *Microscopy and Microanalysis* **18** (2012), 399–405.

[10] Buffiere, J.-Y.; Maire, E.; Adrien, J.; Masse, J.-P. & Boller, E.: In situ experiments with X ray tomography: an attractive tool for experimental mechanics. *Experimental Mechanics* **50** (2010), 289–305.

[11] Burger, W. & Burge, M. J.: *Digital Image Processing*. Springer, London, England 2016.

[12] Buzug, T. M.: *Computed Tomography*. Springer, Berlin, Germany 2008.

[13] Carmignato, S.; Dewulf, W. & Leach, R. (eds.): *Industrial X-Ray Computed Tomography*. Springer International Publishing, Cham, Switzerland 2018.

[14] Chen, Y.; Steeb, H.; Erfani, H.; Karadimitriou, N. K.; Walczak, M. S.; Ruf, M.; Lee, D.; An, S.; Hasan, S.; Connolley, T.; Vo, N. T. & Niasar, V.: Nonuniqueness of hydrodynamic dispersion revealed using fast 4D synchrotron X-ray imaging. *Science Advances* **7** (2021), eabj0960.

[15] Cnudde, V. & Boone, M. N.: High-resolution X-ray computed tomography in geosciences: A review of the current technology and applications. *Earth-Science Reviews* **123** (2013), 1–17.

[16] Dewanckele, J.; Boone, M. A.; Coppens, F.; Van Loo, D. & Merkle, A. P.: Innovations in laboratory-based dynamic micro-CT to accelerate in situ research. *Journal of Microscopy* **277** (2020), 197–209.

[17] DIN EN ISO 15708-3: Non-destructive testing - Radiation methods for computed tomography - Part 3: Operation and interpretation, ISO 15708-3:2017 Standard (2019).

[18] Direct Conversion AB: Direct conversion vs indirect conversion (2016), https://directconversion.com/technology/, accessed 2022-10-02.

[19] Espes, E.; Andersson, T.; Björnsson, F.; Gratorp, C.; Hansson, B. A. M.; Hemberg, O.; Johansson, G.; Kronstedt, J.; Otendal, M.; Tuohimaa, T. & Takman, P.: Liquid-metal-jet X-ray tube technology and tomography applications. In Stock, S. R. (ed.): *SPIE Proceedings*, SPIE 2014.

[20] Feldkamp, L. A.; Davis, L. C. & Kress, J. W.: Practical cone-beam algorithm. *Journal of the Optical Society of America A* **1** (1984), 612.

[21] Francois, N.; Cruikshank, R.; Herring, A.; Kingston, A.; Webster, S.; Knackstedt, M. & Saadatfar, M.: A versatile microtomography system to study in situ the failure and fragmentation in geomaterials. *Review of Scientific Instruments* **93** (2022), 083704.

[22] Fusseis, F.; Steeb, H.; Xiao, X.; Zhu, W.; Butler, I. B.; Elphick, S. & Mäder, U.: A low-cost X-ray-transparent experimental cell for synchrotron-based X-ray microtomography studies under geological reservoir conditions. *Journal of Synchrotron Radiation* **21** (2014), 251–253.

[23] Gajjar, P.; Jørgensen, J. S.; Godinho, J. R. A.; Johnson, C. G.; Ramsey, A. & Withers, P. J.: New software protocols for enabling laboratory based temporal CT. *Review of Scientific Instruments* **89** (2018), 093702.

[24] Gao, Y.; Hu, W.; Xin, S. & Sun, L.: A review of applications of CT imaging on fiber reinforced composites. *Journal of Composite Materials* **56** (2021), 133–164.

[25] Garcea, S.; Wang, Y. & Withers, P.: X-ray computed tomography of polymer composites. *Composites Science and Technology* **156** (2018), 305–319.

[26] Gerke, K. M.; Vasilyev, R. V.; Khirevich, S.; Collins, D.; Karsanina, M. V.; Sizonenko, T. O.; Korost, D. V.; Lamontagne, S. & Mallants, D.: Finite-difference method Stokes solver (FDMSS) for 3D pore geometries: Software development, validation and case studies. *Computers & Geosciences* **114** (2018), 41–58.

[27] Gorshkov, V. A.; Kroening, M.; Anosov, Y. & Dorjgochoo, O.: X-ray scattering tomography. *Nondestructive Testing and Evaluation* **20** (2005), 147–157.

[28] Greiner, W.: *Quantum Mechanics – An Introduction*. Springer, Berlin, Germany 2000.

[29] Haupt, P.: *Continuum Mechanics and Theory of Materials*. Springer, Berlin, Germany 2002.

[30] Hawkes, P. W. & Spence, J. C. H. (eds.): *Springer Handbook of Microscopy*. Springer, Cham, Switzerland 2019.

[31] Hegerl, R. & Hoppe, W.: Influence of electron noise on three-dimensional image reconstruction. *Zeitschrift für Naturforschung A* **31** (1976), 1717–1721.

[32] Heinzl, C.; Amirkhanov, A. & Kastner, J.: Processing, analysis and visualization of CT data. In Carmignato, S.; Dewulf, W. & Leach, R. (eds.): *Industrial X-Ray Computed Tomography*. Springer International Publishing, Cham, Switzerland 2017, pp. 99–142.

[33] Hemberg, O.; Otendal, M. & Hertz, H. M.: Liquid-metal-jet anode electron-impact X-ray source. *Applied Physics Letters* **83** (2003), 1483–1485.

[34] Herman, G. T.: *Fundamentals of Computerized Tomography*. Springer London, London, England 2009.

[35] Hermann, S.; Schneider, M.; Flemisch, B.; Frey, S.; Iglezakis, D.; Ruf, M.; Schembera, B.; Seeland, A. & Steeb, H.: Datenmanagement im SFB 1313. *Bausteine Forschungsdatenmanagement* **1** (2020), 28–38.

[36] Hestenes, M. R. & Stiefel, E.: Methods of conjugate gradients for solving linear systems. *Journal of Research of the National Bureau of Standards* **49** (1952), 409–436.

[37] Hoek, E. & Franklin, J. A.: Simple triaxial cell for field or laboratory testing of rock. *Transactions of the Institution of Mining and Metallurgy* **77** (1968), A22–26.

[38] Holzapfel, G. A.: *Nonlinear Solid Mechanics: A Continuum Approach for Engineering*. John Wiley & Sons, Chichester, England 2000.

[39] Hommel, J.; Gehring, L.; Weinhardt, F.; Ruf, M. & Steeb, H.: Effects of enzymatically induced carbonate precipitation on capillary pressure-saturation relations. *Minerals* **12** (2022), 1186.

[40]   Hosford, W.: Mechanical testing. In *Solid Mechanics*. Cambridge University Press, Cambridge, England 2010, pp. 31–56.

[41]   Hsieh, J.: *Computed tomography principles, design, artifacts, and recent advances*. SPIE Press, Bellingham, WA 2009.

[42]   Hubbell, J. H. & Seltzer, S. M.: Tables of X-ray mass attenuation coefficients and mass energy-absorption coefficients (version 1.4), NIST standard reference database 126 (2004), https://physics.nist.gov/xaamdi.

[43]   Hunter, L. & Dewanckele, J.: Evolution of micro-CT: Moving from 3D to 4D. *Microscopy Today* **29** (2021), 28–34.

[44]   Hurley, R. C.; Hall, S. A. & Wright, J. P.: Multi-scale mechanics of granular solids from grain-resolved X-ray measurements. *Proceedings of the Royal Society A: Mathematical, Physical and Engineering Sciences* **473** (2017), 20170491.

[45]   Iassonov, P.; Gebrenegus, T. & Tuller, M.: Segmentation of X-ray computed tomography images of porous materials: A crucial step for characterization and quantitative analysis of pore structures. *Water Resources Research* **45** (2009), W09415.

[46]   ISO 12233: Photography — Electronic still picture imaging — Resolution and spatial frequency responses, ISO 12233:2017 Standard (2017).

[47]   Jaeger, J. C.; Cook, N. G. W. & Zimmerman, R. W.: *Fundamentals of Rock Mechanics*. Wiley-Blackwell, Chichester, England 2007.

[48]   Jailin, C.; Bouterf, A.; Poncelet, M. & Roux, S.: In situ CT-scan mechanical tests: Fast 4D mechanical identification. *Experimental Mechanics* **57** (2017), 1327–1340.

[49]   Jiang, H.: *Photoacoustic Tomography*. CRC Press, London, England 2014.

[50]   Jiao, C.; Wang, Z.; Lv, B.; Wang, G. & Yue, W.: Design and analysis of a novel flexure-based XY micropositioning stage. *Applied Sciences* **10** (2020), 8336.

[51]   Kachelrieß, M.: Fundamentals of cone-beam CT imaging (2015), https://www.yumpu.com/s/mWCujAHacrO5qUXh, accessed 2022-12-11.

[52]   Kak, A. C. & Slaney, M.: *Principles of Computerized Tomographic Imaging*, vol. 33 of *Classics in Applied Methematics*. Society for Industrial and Applied Mathematics, Philadelphia, PA 2001.

[53]   Khairi, M. T. M.; Ibrahim, S.; Yunus, M. A. M.; Faramarzi, M.; Sean, G. P.; Puspanathan, J. & Abid, A.: Ultrasound computed tomography for material inspection: Principles, design and applications. *Measurement* **146** (2019), 490–523.

[54]   Komvopoulos, K.: *Mechanical testing of engineering materials*. Cognella, San Diego, CA 2017.

[55] Kotwaliwale, N.; Singh, K.; Kalne, A.; Jha, S. N.; Seth, N. & Kar, A.: X-ray imaging methods for internal quality evaluation of agricultural produce. *Journal of Food Science and Technology* **51** (2011), 1–15.

[56] Krautkrämer, J. & Krautkrämer, H.: *Ultrasonic Testing of Materials.* Springer, Berlin, Germany 1990.

[57] Kuhn, H. & Medlin, D. (eds.): *ASM Handbook Volume 8: Mechanical Testing and Evaluation.* ASM Handbooks, ASM International, Russell Township, OH 2000.

[58] Larsson, D. H.; Vågberg, W.; Yaroshenko, A.; Önder Yildirim, A. & Hertz, H. M.: High-resolution short-exposure small-animal laboratory X-ray phase-contrast tomography. *Scientific Reports* **6** (2016), 39074.

[59] Leary, R. K. & Midgley, P. A.: Electron Tomography in Materials Science. In Hawkes, P. W. & Spence, J. C. H. (eds.): *Springer Handbook of Microscopy.* Springer International Publishing, Cham, Switzerland 2019, pp. 1279–1329.

[60] Leclerc, H.; Roux, S. & Hild, F.: Projection savings in CT-based digital volume correlation. *Experimental Mechanics* **55** (2014), 275–287.

[61] Lee, D.; Karadimitriou, N.; Ruf, M. & Steeb, H.: Detecting micro fractures: a comprehensive comparison of conventional and machine-learning-based segmentation methods. *Solid Earth* **13** (2022), 1475–1494.

[62] Lissa, S.; Ruf, M.; Steeb, H. & Quintal, B.: Effects of crack roughness on attenuation caused by squirt flow in Carrara marble. In *SEG Technical Program Expanded Abstracts 2020*, Society of Exploration Geophysicists 2020, pp. 2439–2443.

[63] Lissa, S.; Ruf, M.; Steeb, H. & Quintal, B.: Digital rock physics applied to squirt flow. *Geophysics* **86** (2021), MR235–MR245.

[64] Luo, Z.; Moch, J. G.; Johnson, S. S. & Chen, C. C.: A review on X-ray detection using nanomaterials. *Current Nanoscience* **13** (2017), 364–372.

[65] Maire, E.; Bourlot, C. L.; Adrien, J.; Mortensen, A. & Mokso, R.: 20 Hz X-ray tomography during an in situ tensile test. *International Journal of Fracture* **200** (2016), 3–12.

[66] Maire, E.; Buffière, J. Y.; Salvo, L.; Blandin, J. J.; Ludwig, W. & Létang, J. M.: On the application of X-ray microtomography in the field of materials science. *Advanced Engineering Materials* **3** (2001), 539.

[67] Mantouvalou, I.; Malzer, W. & Kanngießer, B.: Quantification for 3D micro X-ray fluorescence. *Spectrochimica Acta Part B: Atomic Spectroscopy* **77** (2012), 9–18.

[68] Mayo, S. C.; Stevenson, A. W. & Wilkins, S. W.: In-line phase-contrast X-ray imaging and tomography for materials science. *Materials* **5** (2012), 937–965.

[69] McEwen, B. F.; Downing, K. H. & Glaeser, R. M.: The relevance of dose-fractionation in tomography of radiation-sensitive specimens. *Ultramicroscopy* **60** (1995), 357–373.

[70] McPhee, C.; Reed, J. & Zubizarreta, I.: Chapter 12 - Geomechanics tests. In McPhee, C.; Reed, J. & Zubizarreta, I. (eds.): *Core Analysis: A Best Practice Guide*. Elsevier, Amsterdam, Netherlands 2015, Developments in Petroleum Science, pp. 671–779.

[71] McPhee, C.; Reed, J. & Zubizarreta, I.: *Core Analysis: A Best Practice Guide*. Developments in Petroleum Science, Elsevier, Amsterdam, Netherlands 2015.

[72] Menk, R. H.: Basic physics of X-ray interactions in matter. In Russo, P. (ed.): *Handbook of X-ray Imaging: Physics and Technology*. CRC Press, Boca Raton, FL 2018, pp. 3–52.

[73] Mizutani, R. & Suzuki, Y.: X-ray microtomography in biology. *Micron* **43** (2012), 104–115.

[74] Okitsu, Y.; Ino, F. & Hagihara, K.: High-performance cone beam reconstruction using CUDA compatible GPUs. *Parallel Computing* **36** (2010), 129–141.

[75] Osorno, M.; Uribe, D.; Ruiz, O. E. & Steeb, H.: Finite difference calculations of permeability in large domains in a wide porosity range. *Archive of Applied Mechanics* **85** (2015), 1043–1054.

[76] Otsu, N.: A threshold selection method from gray-level histograms. *IEEE Transactions on Systems, Man, and Cybernetics* **9** (1979), 62–66.

[77] Paige, C. C. & Saunders, M. A.: LSQR: An algorithm for sparse linear equations and sparse least squares. *ACM Transactions on Mathematical Software* **8** (1982), 43–71.

[78] Pfeiffer, F.; Weitkamp, T.; Bunk, O. & David, C.: Phase retrieval and differential phase-contrast imaging with low-brilliance X-ray sources. *Nature Physics* **2** (2006), 258–261.

[79] du Plessis, A. & Broeckhoven, C.: Looking deep into nature: A review of micro-computed tomography in biomimicry. *Acta Biomaterialia* **85** (2019), 27–40.

[80] Poludniowski, G.; Landry, G.; DeBlois, F.; Evans, P. & Verhaegen, F.: SpekCalc: a program to calculate photon spectra from tungsten anode X-ray tubes. *Physics in Medicine and Biology* **54** (2009), N433–N438.

[81] Poulsen, H.: *Three-Dimensional X-Ray Diffraction Microscopy*. Springer, Berlin, Germany 2004.

[82] Rahimabadi, P. S.; Khodaei, M. & Koswattage, K. R.: Review on applications of synchrotron-based X-ray techniques in materials characterization. *X-Ray Spectrometry* **49** (2020), 348–373.

[83] Rastogi, P. & Hack, E. (eds.): *Optical methods for solid mechanics.* Wiley-VCH Verlag, Weinheim, Germany 2012.

[84] Renard, F.; Cordonnier, B.; Dysthe, D. K.; Boller, E.; Tafforeau, P. & Rack, A.: A deformation rig for synchrotron microtomography studies of geomaterials under conditions down to 10 km depth in the earth. *Journal of Synchrotron Radiation* **23** (2016), 1030–1034.

[85] Roux, S.; Hild, F.; Viot, P. & Bernard, D.: Three-dimensional image correlation from X-ray computed tomography of solid foam. *Composites Part A: Applied Science and Manufacturing* **39** (2008), 1253–1265.

[86] Ruf, M.; Balcewicz, M.; Saenger, E. H. & Steeb, H.: Digital rock physics: A geological driven workflow for the segmentation of anisotropic Ruhr sandstone: micro-XRCT data set (2021), https://doi.org/10.18419/darus-1152.

[87] Ruf, M.; Hommel, J. & Steeb, H.: Enzymatically induced carbonate precipitation and its effect on capillary pressure-saturation relations of porous media - micro-XRCT dataset of high column (sample 4) (2022), https://doi.org/10.18419/darus-2907.

[88] Ruf, M.; Hommel, J. & Steeb, H.: Enzymatically induced carbonate precipitation and its effect on capillary pressure-saturation relations of porous media - micro-XRCT dataset of low column (sample 10) (2022), https://doi.org/10.18419/darus-2908.

[89] Ruf, M.; Hommel, J. & Steeb, H.: Enzymatically induced carbonate precipitation and its effect on capillary pressure-saturation relations of porous media - micro-XRCT dataset of medium column (sample 3) (2022), https://doi.org/10.18419/darus-2906.

[90] Ruf, M.; Lee, D.; Piotrowski, J.; Huisman, J. A. & Steeb, H.: micro-XRCT data sets of subflorescent salt crusts from evaporation of MgSO4 solution with 0.32 mol/L initial concentration (2021), https://doi.org/10.18419/darus-2002.

[91] Ruf, M.; Lee, D.; Piotrowski, J.; Huisman, J. A. & Steeb, H.: micro-XRCT data sets of subflorescent salt crusts from evaporation of MgSO4 solution with 0.64 mol/L initial concentration (2021), https://doi.org/10.18419/darus-1848.

[92] Ruf, M.; Lee, D.; Piotrowski, J.; Huisman, J. A. & Steeb, H.: micro-XRCT data sets of subflorescent salt crusts from evaporation of MgSO4 solution with 0.96 mol/L initial concentration (2021), https://doi.org/10.18419/darus-2003.

[93] Ruf, M.; Lee, D. & Steeb, H.: In situ performed fracturing experiment of a limestone sample using an X-ray transparent triaxial cell: micro-XRCT data sets and measurement data (2023), https://doi.org/10.18419/darus-3106.

[94] Ruf, M.; Lee, D. & Steeb, H.: A multifunctional mechanical testing stage for micro X-ray computed tomography. *Review of Scientific Instruments* **94** (2023), 085115.

[95] Ruf, M. & Steeb, H.: micro-XRCT data set of an in-situ flow experiment with an X-ray transparent flow cell (2020), https://doi.org/10.18419/darus-691.

[96] Ruf, M. & Steeb, H.: micro-XRCT data set of Carrara marble with artificially created crack network: fast cooling down from 600°C (2020), https://doi.org/10.18419/darus-682.

[97] Ruf, M. & Steeb, H.: micro-XRCT data set of Carrara marble with artificially created crack network: slow cooling down from 600°C (2020), https://doi.org/10.18419/darus-754.

[98] Ruf, M. & Steeb, H.: micro-XRCT data set of open-pored asphalt concrete (2020), https://doi.org/10.18419/darus-639.

[99] Ruf, M. & Steeb, H.: An open, modular, and flexible micro X-ray computed tomography system for research. *Review of Scientific Instruments* **91** (2020), 113102.

[100] Ruf, M. & Steeb, H.: Effects of thermal treatment on acoustic waves in Carrara marble: measurement data (2021), https://doi.org/10.18419/DARUS-1862.

[101] Ruf, M. & Steeb, H.: Effects of thermal treatment on acoustic waves in Carrara marble. *International Journal of Rock Mechanics and Mining Sciences* **159** (2022), 105205.

[102] Ruf, M. & Steeb, H.: In situ micro-XRCT data sets of an open-cell polyurethane foam sample under combined loading conditions (compression + torsion, tension) (2023), https://doi.org/10.18419/DARUS-2834.

[103] Ruf, M.; Steeb, H.; Gebert, J.; Schneider, R. & Helwig, P.: Sample 1 of human femoral heads: micro-XRCT data sets (2021), https://doi.org/10.18419/DARUS-1177.

[104] Ruf, M.; Steeb, H. & Karadimitriou, N.: Visualization of the uniaxial compression of open-cell foams. In Médici, E. F. & Otero, A. D. (eds.): *Album of Porous Media*. Springer International Publishing, Cham, Switzerland 2023, pp. 117–117.

[105] Ruf, M.; Taghizadeh, K. & Steeb, H.: micro-XRCT data sets and in situ measured ultrasonic wave propagation of a pre-stressed monodisperse rubber and glass particle mixture with 50% volume rubber content (2021), https://doi.org/10.18419/darus-2208.

[106] Ruf, M.; Taghizadeh, K. & Steeb, H.: micro-XRCT data sets and in situ measured ultrasonic wave propagation of a pre-stressed monodisperse rubber and glass particle mixture with 30% volume rubber content (2022), https://doi.org/10.18419/DARUS-2833.

[107] Ruf, M.; Taghizadeh, K. & Steeb, H.: Multi-scale characterization of granular media by in situ laboratory X-ray computed tomography. *GAMM-Mitteilungen* **45** (2022), e20220001.

[108] Ruf, M.; Taghizadeh, K. & Steeb, H.: micro-XRCT data sets and in situ measured ultrasonic wave propagation of pre-stressed monodisperse rubber and glass particle mixtures with 10%, 20%, 40%, and 60% volume rubber content: sample 1 (2023), https://doi.org/10.18419/DARUS-3436.

[109] Ruf, M.; Taghizadeh, K. & Steeb, H.: micro-XRCT data sets and in situ measured ultrasonic wave propagation of pre-stressed monodisperse rubber and glass particle mixtures with 10%, 20%, and 30% volume rubber content: samples 2 and 3 (2023), https://doi.org/10.18419/DARUS-3437.

[110] Ruf, M.; Teutsch, T.; Alber, S.; Steeb, H. & Ressel, W.: micro-XRCT data sets of a stone mastic asphalt drill core before and after a uniaxial compression test (sample 2): sample 2-1 (2021), https://doi.org/10.18419/darus-1641.

[111] Ruf, M.; Teutsch, T.; Alber, S.; Steeb, H. & Ressel, W.: micro-XRCT data sets of a stone mastic asphalt drill core before and after a uniaxial compression test (sample 2): sample 2-2 (2021), https://doi.org/10.18419/darus-1833.

[112] Ruf, M.; Teutsch, T.; Alber, S.; Steeb, H. & Ressel, W.: micro-XRCT data sets of a stone mastic asphalt drill core before and after a uniaxial compression test (sample 2): sample 2-3 (2021), https://doi.org/10.18419/darus-1834.

[113] Russ, J. C. & Neal, F. B.: *The Image Processing Handbook*. CRC Press, Boca Raton, FL 2016.

[114] Russo, P. (ed.): *Handbook of X-ray Imaging: Physics and Technology*. CRC Press, Boca Raton, FL 2018.

[115] Salvo, L.; Cloetens, P.; Maire, E.; Zabler, S.; Blandin, J.; Buffière, J.; Ludwig, W.; Boller, E.; Bellet, D. & Josserond, C.: X-ray micro-tomography an attractive characterisation technique in materials science. *Nuclear Instruments and Methods in Physics Research Section B: Beam Interactions with Materials and Atoms* **200** (2003), 273–286.

[116] Salvo, L.; Suéry, M.; Marmottant, A.; Limodin, N. & Bernard, D.: 3D imaging in material science: application of X-ray tomography. *Comptes Rendus Physique* **11** (2010), 641–649.

[117] Schlüter, S.; Sheppard, A.; Brown, K. & Wildenschild, D.: Image processing of multiphase images obtained via X-ray microtomography: A review. *Water Resources Research* **50** (2014), 3615–3639.

[118] Schoeman, L.; Williams, P.; du Plessis, A. & Manley, M.: X-ray micro-computed tomography (µCT) for non-destructive characterisation of food microstructure. *Trends in Food Science & Technology* **47** (2016), 10–24.

[119] Schuck, B.; Teutsch, T.; Alber, S.; Ressel, W.; Steeb, H. & Ruf, M.: Study of air void topology of asphalt with focus on air void constrictions – a review and research approach. *Road Materials and Pavement Design* **22** (2021), 1–19.

[120] Shade, P. A.; Blank, B.; Schuren, J. C.; Turner, T. J.; Kenesei, P.; Goetze, K.; Suter, R. M.; Bernier, J. V.; Li, S. F.; Lind, J.; Lienert, U. & Almer, J.: A rotational and axial motion system load frame insert for in situ high energy X-ray studies. *Review of Scientific Instruments* **86** (2015), 093902.

[121] Smith, S. T.: *Flexures*. CRC Press, Boca Raton, FL 2000.

[122] Smith, T. S.; Bay, B. K. & Rashid, M. M.: Digital volume correlation including rotational degrees of freedom during minimization. *Experimental Mechanics* **42** (2002), 272–278.

[123] Stampanoni, M.; Groso, A.; Isenegger, A.; Mikuljan, G.; Chen, Q.; Bertrand, A.; Henein, S.; Betemps, R.; Frommherz, U.; Böhler, P.; Meister, D.; Lange, M. & Abela, R.: Trends in synchrotron-based tomographic imaging: the SLS experience. In Bonse, U. (ed.): *SPIE Proceedings*, SPIE 2006.

[124] Staron, P.; Schreyer, A.; Clemens, H. & Mayer, S. (eds.): *Neutrons and Synchrotron Radiation in Engineering Materials Science*. Wiley-VCH Verlag, Weinheim, Germany 2017.

[125] Stein, S. & Wysession, M.: *An Introduction to Seismology, Earthquakes, and Earth Structure*. Blackwell Publishing, Malden, MA 1991.

[126] Stock, S. R.: X-ray microtomography of materials. *International Materials Reviews* **44** (1999), 141–164.

[127] Stock, S. R.: Recent advances in X-ray microtomography applied to materials. *International Materials Reviews* **53** (2008), 129–181.

[128] Stock, S. R.: *MicroComputed Tomography: Methodology and Applications*. CRC Press, Boca Raton, FL 2019.

[129] Sutton, M. A.; Orteu, J.-J. & Schreier, H.: *Image correlation for shape, motion and deformation measurements*. Springer, New York, NY 2009.

[130] Taghizadeh, K.; Ruf, M.; Luding, S. & Steeb, H.: X-ray 3D imaging–based microunderstanding of granular mixtures: Stiffness enhancement by adding small fractions of soft particles. *Proceedings of the National Academy of Sciences* **120** (2023), e2219999120.

[131] Taillandier-Thomas, T.; Roux, S. & Hild, F.: Soft route to 4D tomography. *Physical Review Letters* **117** (2016), 025501.

[132] Tang, X.; Krupinski, E. A.; Xie, H. & Stillman, A. E.: On the data acquisition, image reconstruction, cone beam artifacts, and their suppression in axial MDCT and CBCT - A review. *Medical Physics* **45** (2018), e761–e782.

[133] Teutsch, T.; Gönninger, L.; Ruf, M.; Steeb, H. & Ressel, W.: Microstructural characterisation and analysis of coarse aggregates in asphalt drill cores. *Road Materials and Pavement Design* **24** (2023), 2714–2736.

[134] Tuller, M.; Kulkarni, R. & Fink, W.: Segmentation of X-ray CT data of porous materials: A review of global and locally adaptive algorithms. In Anderson, S. H. & Hopmans, J. W. (eds.): *Soil–Water–Root Processes: Advances in Tomography and Imaging.* American Society of Agronomy and Soil Science Society of America 2013, chap. 8, pp. 157–182.

[135] Tuy, H. K.: An inversion formula for cone-beam reconstruction. *SIAM Journal on Applied Mathematics* **43** (1983), 546–552.

[136] Vahid Dastjerdi, S.; Steeb, H.; Ruf, M.; Lee, D.; Weinhardt, F.; Karadimitriou, N. & Class, H.: micro-XRCT dataset of enzymatically induced calcite precipitation (EICP) in a microfluidic cell (2021), https://doi.org/10.18419/DARUS-866.

[137] Vásárhelyi, L.; Kónya, Z.; Kukovecz, Á. & Vajtai, R.: Microcomputed tomography–based characterization of advanced materials: A review. *Materials Today Advances* **8** (2020), 100084.

[138] Verruijt, A.: *An Introduction to Soil Mechanics*, vol. 30 of *Theory and Applications of Transport in Porous Media.* Springer, Cham, Switzerland 2018.

[139] Villarraga-Gómez, H. & Smith, S. T.: Effect of the number of projections on dimensional measurements with X-ray computed tomography. *Precision Engineering* **66** (2020), 445–456.

[140] Vlassenbroeck, J.; Dierick, M.; Masschaele, B.; Cnudde, V.; Hoorebeke, L. V. & Jacobs, P.: Software tools for quantification of X-ray microtomography at the UGCT. *Nuclear Instruments and Methods in Physics Research Section A: Accelerators, Spectrometers, Detectors and Associated Equipment* **580** (2007), 442–445.

[141] Vlassenbroeck, Jelle: *Advances in laboratory-based X-ray microtomography.* Ph.D. thesis, Ghent University, Ghent, Belgium (2009).

[142] Walter, D.; Zscherpel, U. & Ewert, U.: Photon counting and energy discriminating X-ray detectors - benefits and applications. 19th World Conference on Non-Destructive Testing (WCNDT 2016), 13-17 June 2016 in Munich, Germany. *e-Journal of Nondestructive Testing* **21** (2016), 19252.

[143] Wei, X. X.: Analytical solutions for finite cylinders compressed between platens and the strain effect on the valence-band structure of Si1-xGex alloy. *International Journal of Solids and Structures* **44** (2007), 7906–7923.

[144] Wildenschild, D. & Sheppard, A. P.: X-ray imaging and analysis techniques for quantifying pore-scale structure and processes in subsurface porous medium systems. *Advances in Water Resources* **51** (2013), 217–246.

[145] Wilkinson, M. D.; Dumontier, M.; Aalbersberg, I. J.; Appleton, G.; Axton, M.; Baak, A.; Blomberg, N.; Boiten, J.-W.; da Silva Santos, L. B.; Bourne, P. E.; Bouwman, J.; Brookes, A. J.; Clark, T.; Crosas, M.; Dillo, I.; Dumon, O.; Edmunds, S.; Evelo, C. T.; Finkers, R.; Gonzalez-Beltran, A.; Gray, A. J.; Groth, P.; Goble,

C.; Grethe, J. S.; Heringa, J.; 't Hoen, P. A.; Hooft, R.; Kuhn, T.; Kok, R.; Kok, J.; Lusher, S. J.; Martone, M. E.; Mons, A.; Packer, A. L.; Persson, B.; Rocca-Serra, P.; Roos, M.; van Schaik, R.; Sansone, S.-A.; Schultes, E.; Sengstag, T.; Slater, T.; Strawn, G.; Swertz, M. A.; Thompson, M.; van der Lei, J.; van Mulligen, E.; Velterop, J.; Waagmeester, A.; Wittenburg, P.; Wolstencroft, K.; Zhao, J. & Mons, B.: The FAIR Guiding Principles for scientific data management and stewardship. *Scientific Data* **3** (2016), 160018.

[146] Withers, P. J.; Bouman, C.; Carmignato, S.; Cnudde, V.; Grimaldi, D.; Hagen, C. K.; Maire, E.; Manley, M.; Plessis, A. D. & Stock, S. R.: X-ray computed tomography. *Nature Reviews Methods Primers* **1** (2021).

[147] Yang, K.: X-ray cone beam computed tomography. In Russo, P. (ed.): *Handbook of X-ray Imaging: Physics and Technology*. CRC Press, Boca Raton, FL 2018, pp. 713–747.

[148] Yang, Z. X.; Li, X. S. & Yang, J.: Interpretation of torsional shear results for non-linear stress–strain relationship. *International Journal for Numerical and Analytical Methods in Geomechanics* **32** (2008), 1247–1266.

[149] Zentai, G.: Comparison of CMOS and a-Si flat panel imagers for X-ray imaging. In *2011 IEEE International Conference on Imaging Systems and Techniques*, IEEE 2011, pp. 194–200.

[150] Zhang, L. & Wang, S.: Correlation of materials property and performance with internal structures evolvement revealed by laboratory X-ray tomography. *Materials* **11** (2018), 1795.

[151] Zhu, R.; Qu, Z.; Yang, S. & Fang, D.: An in situ microtomography apparatus with a laboratory x-ray source for elevated temperatures of up to 1000°C. *Review of Scientific Instruments* **92** (2021), 033704.

[152] Zwanenburg, E.; Williams, M. & Warnett, J.: Review of high-speed imaging with lab-based x-ray computed tomography. *Measurement Science and Technology* **33** (2021), 012003.

List of Figures

Publications

Chapter I:
An Open, Modular, and Flexible Micro X-ray Computed Tomography System for Research

An open, modular, and flexible micro X-ray computed tomography system for research

View Online   Export Citation   CrossMark

Matthias Ruf[1,a] (iD) and Holger Steeb[1,2,a] (iD)

AFFILIATIONS

[1] University of Stuttgart, Institute of Applied Mechanics (CE), Pfaffenwaldring 7, D-70569 Stuttgart, Germany
[2] University of Stuttgart, SC SimTech, D-70569 Stuttgart, Germany

[a] Authors to whom correspondence should be addressed: matthias.ruf@mechbau.uni-stuttgart.de and holger.steeb@mechbau.uni-stuttgart.de

ABSTRACT

In this paper, a modular and open micro X-ray Computed Tomography (μXRCT) system is presented, which was set up during the last years at the Institute of Applied Mechanics (CE) of the University of Stuttgart and earlier at the Institute of Computational Engineering of Ruhr-University Bochum. The system is characterized by its intrinsic flexibility resulting from the modular and open design on each level and the opportunity to implement advanced experimental *in situ* setups. On the one hand, the presented work is intended to support researchers interested in setting up an experimental XRCT system for the microstructural characterization of materials. On the other hand, it aims to support scientists confronted with the decision to set up a system on their own or to buy a commercial scanner. In addition to the presentation of the various hardware components and the applied modular software concept, the technical opportunities of the open and modular hard- and software design are demonstrated by implementing a simple and reliable method for the compensation of bad detector pixels to enhance the raw data quality of the projections. A detailed investigation of the performance of the presented system with regard to the achievable spatial resolution is presented. XRCT datasets of three different applications are finally shown and discussed, demonstrating the wide scope of options of the presented system.

Published under license by AIP Publishing. https://doi.org/10.1063/5.0019541

I. INTRODUCTION AND MOTIVATION

The capability that micro X-ray Computed Tomography (μXRCT) as a non-destructive imaging technique offers is well known in many research domains, and it is becoming more and more a routine microscopy technique, cf. Maire and Withers (2013), Landis and Keane (2010), Stock, 2008a; 2008b, Cnudde and Boone (2013), Schoeman *et al.* (2016), Mizutani and Suzuki (2012), and Kotwaliwale *et al.* (2011). Various companies are selling complete bench-top and free-standing laboratory μXRCT systems, designed for special use cases that differ mainly in the available X-ray power and equipment. This limits mostly the usable sample size in combination with the range of the adjustable magnification as well as the maximum attainable spatial resolution. Free-standing systems in the same power range as the system presented in this manuscript are, for instance, the *phoenix nanotom m* and the *Phoenix V|tome|x S240* from Waygate Technologies, a Baker Hughes business (former GE Inspection Technologies), or the *XT H 225* from Nikon Corporation. In contrast, the *SKYSCAN 1273* offered by Bruker Corporation shows a typical example of a bench-top system. Most systems can be used directly out of the box and therefore are pretty user-friendly. At the same time, a predominant number of systems are so-called full protection XRCT devices, which means that they already have an inherent X-ray protection that reduces the entry-level even further. For most users, this is a huge benefit that explains why most researchers use commercially available systems. However, this can also mean a strong limitation. Extending such a system is not possible if the manufacturer does not support an upgrade. The used controlling software is not open-source, which means that it is not possible to include other arbitrary hardware components. The latter is even more relevant in the event of system failures as components cannot be flexibly replaced, which, in the worst case, can result in long breakdown periods of the entire system. Moreover, the working space is limited according to the acquired system and cannot be

enlarged, which is, in particular, a strong limitation for experimental *in situ* setups. Especially in research, this can be adverse. It is mostly unknown that which kinds of experiments must be performed in the future, and the investment costs to buy a suitable system are high, making it impossible to buy new devices each time. It is desirable in research to have an open and modular system where modifications can be done on each level.

At the Institute of Applied Mechanics (CE) of the University of Stuttgart, the research focus lies among others on porous media on different scale levels. Motivated by overcoming the limitations of commercial µXRCT systems, over the last years, a system was built up in-house, starting with the acquisition of the needed hardware components. In opposition to other research groups that also built up open and modular scanners for special research applications, for instance, the Centre for X-ray Tomography at Ghent University (Dierick *et al.*, 2014; Masschaele *et al.*, 2013), the aim is not pushing the limits of µXRCT systems. The focus is on having a flexible and modular system where changes can be done on each level, which means on the hardware as well as on the software side. Only this enables a free integration of any hardware components and results in independence from the manufacturer. In addition, to prepare and test, for instance, *in situ* setups for investigations in synchrotron radiation facilities, the working space should be as large as possible, which resulted in an accessible lead shielded cabin surrounding the system.

Although the basics of µXRCT systems are well known and documented in the literature (Carmignato *et al.*, 2018; Stock, 2008a) and the advantages of an open, modular, and flexible system are obvious, it is hard to decide to build such a system from scratch. To help other

groups who are also considering building such a system themselves, in the following, a technical description of the current state of our system as well as the system performance is given. To demonstrate the advantage of an open system, as an example, the implementation of a method to enhance the dataset quality by the reduction of bad detector pixels is presented. Finally, some selected application examples are shown to demonstrate the capability of the system. The datasets (projection images and reconstructed datasets) of the presented examples are open access published.

II. MATERIALS AND METHODS

In this section, first, the used hardware components, their assembly, and the calibration of the system are described. Afterward, the software concept to control all hardware components to record a scan dataset is explained, which is followed by a brief discussion of the typical system maintenance work and breakdowns. Finally, an implemented method is presented to compensate for bad detector pixels to enhance the image data quality. The latter should exemplarily show the benefit of an open and modular system.

A. Hardware

In Fig. 1, an overview of the system is given, which consists of three main components: the X-ray source ("1"); the sample positioning mechanics ("2"), highlighted in Fig. 2; and the detector ("3a" or "3b"). Additionally, two coordinate systems are defined ($\mathbf{e}_i$- and $\hat{\mathbf{e}}_i$-coordinate systems), and the possible motorized degrees of freedom of the different components are visualized by green arrows.

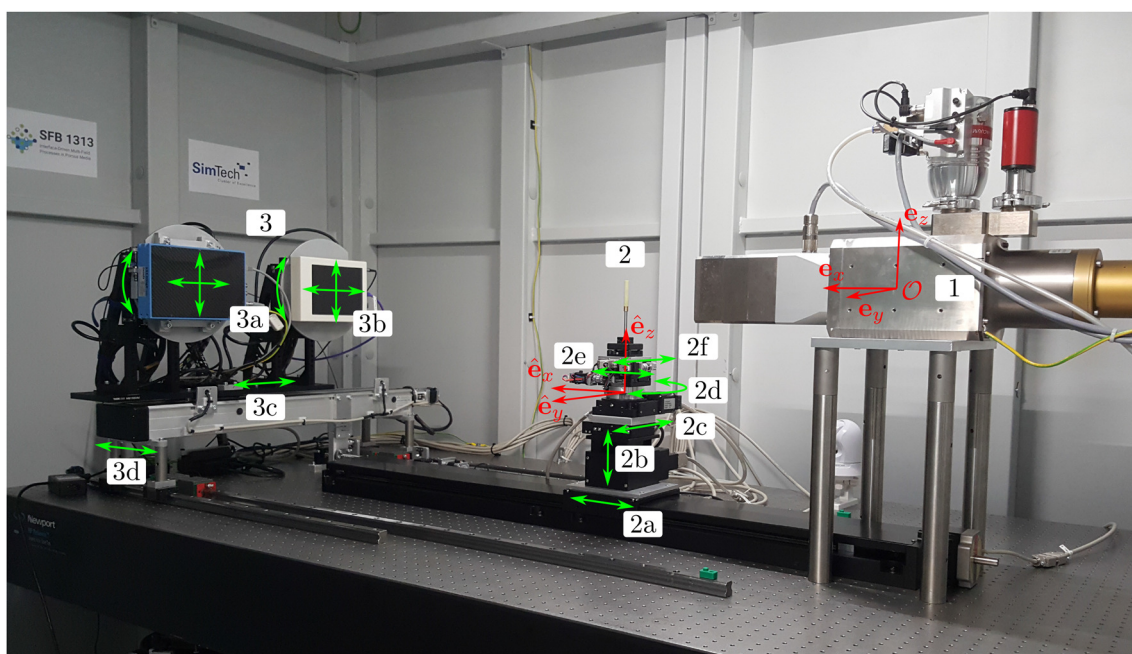**FIG. 1**. Arrangement of the components on the optical table located in a lead shielded accessible cabin. Possible moving directions of the motorized positioners are illustrated by green arrows and are related to the defined coordinate systems. The coordinate system $\mathbf{e}_x$, $\mathbf{e}_y$, $\mathbf{e}_z$ is the base system, and $\hat{\mathbf{e}}_x$, $\hat{\mathbf{e}}_y$, $\hat{\mathbf{e}}_z$ moves with the sample.
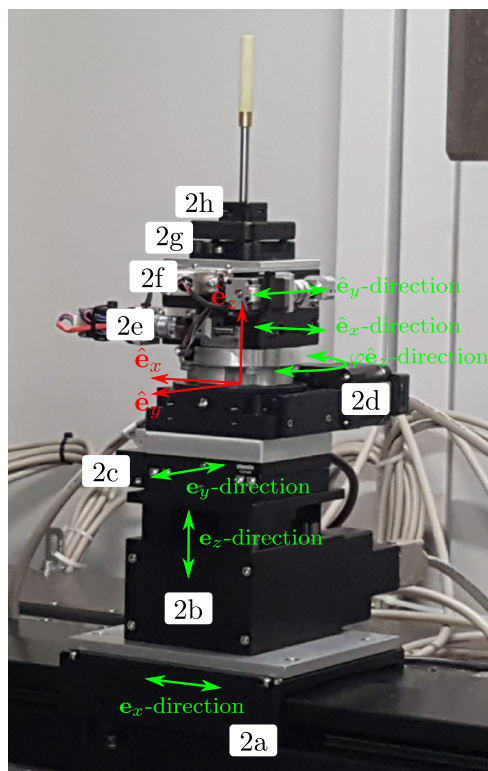
FIG. 2. Detailed view of the sample positioning stack, cf. Fig. 1 ("2").

As in most industrial XRCT systems, the sample is rotated and the remaining components are fixed. In the following, the employed hardware components, grouped in the X-ray source, detector(s), motorized stages, and controllers, and the assembly including the calibration are presented. For a summary of the hardware components presented in the following, see Appendix, Table V.

1. X-ray source

As the X-ray source, the open micro-focus tube *FineTec FORE 180.01C TT* with a tungsten transmission target from FineTec Fine-Focus Technologies GmbH, Germany, is used; cf. Fig. 1 ("1"). The X-ray tube provides a maximum power of up to 80 W and at the same time a focal spot size down to <3 μm by moderate power levels, which is a unique feature of this X-ray source. The X-ray tube can be operated with an acceleration voltage in the range of 30 kV–180 kV and an acceleration flux of 10 μA–1000 μA. The selected open design of the X-ray tube offers several advantages over a sealed design. The biggest advantage is that almost all maintenance work can be done on-site and all wearing parts, for instance, the cathode filament, can be replaced easily. After a manufacturer training, all maintenance work can even be carried out by the customer himself. In the long term, this saves a lot of costs. The system downtime as a criticism of an open source vs a sealed one during maintenance is usually insignificant in the field of research. From time to time, it is necessary to influence the X-ray spectrum that is realized by mounting appropriate filter materials

(metal sheets with a defined thickness) directly in front of the X-ray source.

2. Detector(s)

In the presented state of our setup, two different indirect conversion flat panel detectors with CMOS image sensor technology are available, which can be operated in the whole X-ray spectrum range that the X-ray source provides. On the one side, a *Dexela 1512NDT* with GOS-based DRZ Standard scintillator option from PerkinElmer, Inc., Waltham, MA, USA, cf. Fig. 1 ("3a"), can be used, which has a sensitive area of 145.4 × 114.9 mm² by a pixel size of 74.8 μm, which means a resolution of 1944 × 1536 pixels. On the other side, a *Shad-o-Box 6K HS* from Teledyne DALSA, Inc., Waterloo, ON, Canada, cf. Fig. 1 ("3b"), with an active area of 146 × 114 mm² and a pixel size of 49.5 μm that produces projection images of 2940 × 2304 pixels is available. For the scintillator option in opposition to the Dexela 1512 detector, CsI was chosen. Initially, the system was operated exclusively with the Dexela 1512NDT detector. The GOS-based DRZ Standard scintillator option for the Dexela 1512NDT detector was chosen for its longevity, and the sensor resolution was chosen in order to be able to handle the resulting datasets without too high hardware requirements. The Shad-o-Box 6K HS detector was purchased afterward to expand the capabilities of the system toward slightly higher spatial resolution and a significantly larger field of view for the same voxel size, which explains the selected CsI scintillator and the significantly higher sensor resolution for nearly the same active sensor area. Since the datasets, meaning the projection images as well as the reconstructed volume datasets, using the Shad-o-Box 6K HS detector are markedly bigger, the reconstruction process and, in particular, all further post-processing steps are much more time consuming, and in addition, the needed hardware requirements for these jobs are considerably higher. This will be discussed in detail in Sec. III. Depending on the performed scan, the more suitable detector is selected, which can be done without a recalibration of the system. The communication and the data transfer of the 14 bit depth image output of the detectors are done via GigE Vision interfaces using direct individual Ethernet connections to the controlling computer.

3. Stages and controllers

As depicted by the green arrows in Fig. 1, there is a high flexibility in the positioning of the sample ("2"), shown in detail in Fig. 2, and the detector(s) ("3a" and "3b"). The description of the underlying concept as well as the selection of the used hardware components is split according to this separation and given in the following.

a. Sample positioning. The movement and positioning of the sample are realized by five motorized translation stages and one rotation stage in total. In Table I, the employed stages are summarized as well as the related moving directions according to the two coordinate systems defined in Fig. 1 and depicted in detail in Fig. 2. Furthermore, the available travel ranges, the bidirectional repeatability (if available), and the resolution for one full step of the employed stepper motors are given, although microstepping is usually used. With the stage ("2a") to set up the position in the $\mathbf{e}_x$-direction, the geometric magnification, M, given by the relation of the source–detector distance SDD to the source–object distance SOD, $M = SDD/SOD$,

TABLE I. Overview of the employed motorized stages.

Component to be moved	Direction	Travel range	Repeatability (bidirectional)	Resolution (per full step)	Manufacturer	Model/description
	$\mathbf{e}_x$	1000 mm	<3 μm	25 μm	OWIS GmbH	LIMES 170-1000-3HSM
	$\mathbf{e}_y$	25 mm	<2.7 μm	1.25 μm	Standa Ltd.	8MT167-25LS-MEn1
	$\mathbf{e}_z$	30 mm	<6 μm	2.5 μm	OWIS GmbH	HVM 100-30-HSM-MS
Sample	$\hat{\mathbf{e}}_x$	25 mm	N/A	1.25 μm	Newport Corp. and Nanotec Electronic GmbH & Co. KG	M423 stage mechanic and ST2018L0804-A actuator
	$\hat{\mathbf{e}}_y$	25 mm	N/A	1.25 μm	Newport Corp. and Nanotec Electronic GmbH & Co. KG	M423 stage mechanic and ST2018L0804-A actuator
	$\varphi\,\mathbf{e}_z = \varphi\,\hat{\mathbf{e}}_z$[a]	Endless	<1.5 arcmin	0.6 arcmin	Standa Ltd.	8MR190-2-28-MEn1
Detector rack	$\mathbf{e}_x$	250 mm	N/A	25 μm	Self-made; see text	
	$\mathbf{e}_y$	535 mm	N/A	6.25 μm	isel Germany AG	2 346 110 079 with Vexta PK245M-01B stepper motor
Detector 1 and detector 2	$\mathbf{e}_y$	75 mm	<5.0 μm	2.5 μm	Standa Ltd.	8MTF-75XX-MEn1
	$\mathbf{e}_z$	75 mm	<5.0 μm	2.5 μm		
	$\eta\mathbf{e}_x$[a]	10°	N/A	N/A	Self-made; see text	

[a]$\varphi\,\hat{\mathbf{e}}_z = \varphi\,\mathbf{e}_z$ and $\eta\mathbf{e}_x$ are rotation vectors with the rotation axes given by the basis vectors and the rotation angle given by φ and η.

can be adjusted in a wide range that means $M \in [\approx 1.25, \approx 50.0]$, which of course also depends on the sample size. After testing different drive concepts, we use exclusively stepper motors to drive the different sample positioning stages in the presented setup. The reason for this is that already without any additional instrumentation and control (open-loop mode), precise positioning and repeatability of movement can be achieved. For instance, the latter stage provides a repeatability (bidirectional) of less than 3 μm and a positioning error of less than 10 μm per 100 mm (complete travel range of 1000 mm) according to the manufacturer's product information in the open-loop mode using a direct driven preloaded ball screw with a spindle pitch of 5 mm and a bipolar stepper with 200 steps/revolution. The stage ("2b") is primarily used for the fine adjustment of the relative sample position compared to the optical axis in the $\mathbf{e}_z$-direction, which explains the limited range of only 30 mm to ensure a very low pitch and yaw angles as well as lateral deviation. With a repeatability (bidirectional) of <6 μm, it can also be used for helical cone beam scans.

On top of the elevator stage, we have the translation stage ("2c") for the fine adjustment of the rotation axis position in the $\mathbf{e}_y$-direction related to the optical axis. The stage is mainly used for the alignment of the system, cf. Sec. II A 4 b, but offers, in principle, the possibility for performing translational laminography scans. Therefore, this stage is additionally equipped with an encoder and can be operated in the closed-loop mode. The next component in the sample positioning stack is the rotation stage ("2d"), which is the only component in standard cone beam scanning that moves during the whole scan with a possible duration of several hours. For the selection, high stability combined with a low wobble and eccentricity are the dominating factors besides high repeatability and a low position error. To ensure the last two points, the stage is equipped with an encoder system and operated in the closed-loop mode. The two

translation stages ("2e" and "2f") on top of the rotation table that are perpendicular to each other ($\hat{\mathbf{e}}_x$- and $\hat{\mathbf{e}}_y$-directions) and rotate with the sample are used for fine adjustment of the sample's rotation center. Using two additional stages offers the flexibility to compensate for eccentric fixed samples on the sample holder or, for instance, to define flexibly the region of interest of a larger sample that is to be scanned.

To easily mount and remove a sample on top of the sample positioning stack, magnetic kinematic bases from Newport's *BK Series* are employed (Newport Corp., Irvine, CA, USA). The bottom plate of Newport's *M-BK-2A* model with a base size of 50.5×62.23 mm² is firmly screwed down on top of the sample positioning stack; cf. Fig. 2 ("2g"). Depending on the weight, size, and geometry of the sample, different kinds of sample holders are employed and mounted on the top plate of Newport's *M-BK-2A* model. For small and light samples, as in the case of the sample shown in Figs. 1 and 2, Newport's *M-BK-1A* model with a base size of only 25.4×25.4 mm² is used, cf. Fig. 2 ("2h"), using an adapter to mount it on the fixed installed *M-BK-2A* bottom plate. The maximum sample weight (inclusive holder) is limited by the weakest element in the sample positioning stack, which is the rotation stage ("2d") with a maximum load capacity of 100 N and a residual load capacity of about 90 N. It should be noted that with regard to the resulting sample size, the sample mass of about 9 kg is not the limiting factor in the overall system. Rather, it is the maximum power of the X-ray source that limits the sample size (maximum diameter in the X-ray direction). The latter strongly depends on the sample material, making it hard to quantify this. In addition, the choice of the geometric magnifications also limits the sample size in several respects: on the one hand, by the physical required distance between the sample and the X-ray source and, on the other hand, by the sensor size of the detector, if the sample is to be scanned over the entire

diameter. From this point of view, the corresponding sample diameters are in the range of 116 mm–3 mm, depending on the applied geometric magnifications of $M \in [\approx 1.25, \approx 50.0]$, assuming that the X-ray power is high enough and no artificial sensor enlargement is employed.

b. Detector positioning. In addition to the positioning of the sample, also the position of the detector(s) ("3a" and "3b") is motorized and controlled. On the one hand, this simplifies the calibration of the system, and on the other hand, it permits a lot of advanced possibilities. As all stages of the sample positioning stack, all employed stages of the detector positioning system are also summarized in Table I with the related moving directions, travel ranges, and further specifications.

Depending on the scan performed, the more suitable of the two detectors is used without having to recalibrate the system. This is achieved by mounting both detectors on a motorized translation stage with a travel range of 535 mm in the $\mathbf{e}_y$-direction, which is direct driven with a stepper motor; cf. Fig. 1 ("3c"). By means of this stage, it is also possible to increase the field of view in the $\mathbf{e}_y$-direction, otherwise limited by the sensitive area of the detector, by moving the respective detector out of the middle position and combining the resulting projections from different detector positions to a single one. Herewith, wider samples can also be scanned. This technique is, for instance, also applied in the research scanner *Nanowood* at Ghent University (Dierick *et al.*, 2014). The translation stage for selecting the detector is mounted on linear rails and is direct driven with a stepper motor via a ball screw spindle (16 mm diameter and 5 mm pitch) with appropriate bearing supports and hall-effect sensors as limit switches to adjust the source–detector distance; cf. Fig. 1 ("3d"). Both detectors are mounted on XY-stages primarily designed for microscopy applications where a high accuracy and repeatability are mandatory. With these stages, precise positioning of the detectors in the direction of $\mathbf{e}_y$ and $\mathbf{e}_z$ is possible. On the one hand, this allows a fine alignment of the detector with regard to the optical axis, and on the other hand, this offers further possibilities, for instance, the compensation of so-called bad detector pixels or artificial sensor resolution enhancement techniques. A crucial factor for the last two points is the repeatability of the stages that explains the selection. To prevent any potential step losses, they are equipped with encoders and operated exclusively in the closed-loop mode when using such advanced options. The XY-stages are fixed on self-made rotation tables that enable the adjustment of the in-plane detector orientation $\eta \mathbf{e}_x$, needed to calibrate the system. This can be done remotely by using the two linear actuators *N-470.420 (PiezoMike)* from Physik Instrumente (PI), Germany, which offer high accuracy and self-locking at rest. Besides, the self-made rotation tables offer the possibility to switch with ease from horizontal, as shown in Fig. 1, to vertical detector orientation. However, the use of this option requires a corresponding system recalibration.

c. Controller. For the motion control of the stages, we use the *Standa 8SMC4-Ethernet/RS232-B19x3-8* (8 channels) and the *Standa 8SMC5-Ethernet/RS232-B19x3-12* (12 channels) multi-axis motion controllers from Standa Ltd., Lithuania, with the software package *XILab (Version 1.14.12)* running on a Windows operating system. The controllers can be used in combination with a high variety of different drive concepts. They support stepping motors, DC motors as well as brushless DC (BLDC) motors in combination

with differential or single-ended encoders and various kinds of limit switches. The operation of stepper motors can also be done without an encoder and in case an encoder is used, in open- as well as in closed-loop modes. Furthermore, microstep modes down to 1/256 of one full step are provided for high precision tasks, to mention only a few features. As a result of using identical controller(s) whenever possible for all stages, an identical software interface is established that makes it very easy to integrate other stages in the scan loop. In the presented setup, 12 of the 20 channels are in use, making it possible to extend or change the setup with ease. Whenever possible, stages are employed that can be used in combination with the multi-axis motion controllers for the mentioned reasons. If this is not possible, for instance, for the employed *N-470.420 (PiezoMike)* actuators from Physik Instrumente (PI), which are used for the detector rotation adjustment during the system calibration procedure, appropriate controllers of the corresponding manufacturer are employed.

4. Assembly

a. Base and shielding. To arrange and mount all components and uncouple the whole setup from potential environmental vibrations, an optical breadboard vibration isolation table is employed. This ensures a high level of flexibility combined with a simple arrangement of the components. For this, the *Newport RP Reliance sealed hole table top*, 1200 × 2400 × 203 mm,[3] with four pneumatic vibration isolators with automatic re-leveling (*Newport S-2000A-428-TC*) in combination with a tie-bar system (*Newport M-TB-48*) is installed. The latter improves the mobility of the whole system, for instance, when maintenance operation must be done. To protect the environment from the x rays, the whole setup is housed in an accessible cabin with a length of 3 m, a width of 2.3 m, and a height of 2.4 m with a lead shielding from the same manufacturer as the X-ray source (FineTec FineFocus Technologies GmbH, Germany). The accessible space that could be used for an experimental setup is significantly larger than in commercially available inherent full protection XRCT devices.

As in a lot of systems, the distance between the X-ray source and the detector is set to 1000 mm (40 in.). The fine adjustment of the distance can be done by the motorized translation stage that moves the traverse both detectors are mounted on; cf. Fig. 1 ("3d"). With the presented standard setup in addition to cone beam scanning, helical cone beam scanning as well as coplanar translational laminography for flat objects can theoretically be performed.

b. Calibration. The image quality of an XRCT system is mainly influenced by its calibration. Systematical geometrical misalignments of the relative position and orientation of the presented major components (the X-ray source, the rotation stage, and the detector) lead to unwanted errors and artifacts and should be reduced as far as possible. For this, a lot of different methods with the aim to determine the system misalignments from projection images of test phantoms were developed; cf. Ferrucci *et al.* (2015). One group of methods assumes an ideal rotation of the stage, which we also suppose in our system. Additionally, we suppose that the detector has no out-of-plane rotation, meaning that the detector is perpendicular to the optical axis, also called the magnification axis, whose direction is identical to the basis vector $\mathbf{e}_x$ in Fig. 1.

This may be justified because slight detector out-of-plane rotational deviations have a negligible error in the 3D dataset (Yang *et al.*, 2006). In addition, before the respective calibration, all components are pre-aligned as accurate as possible on the optical table. Therefore, the assumption of only slight misalignments of the detector's out-of-plane orientation is ensured. For a better comprehension of the calibration procedure and the assumptions made, all terms used are depicted in Fig. 3 using an illustration of the perfectly aligned system.

For calibration, a single point marker object, consisting of a highly accurate small steel ball with a diameter of 30 μm fixed with dental wax on the tip of a glass rod, is employed. The significant higher X-ray attenuation of the steel ball against the glass rod and the dental wax makes it simple to segment the steel ball in the projection images and subsequently to determine its center of mass. The latter is used afterward to describe the position of the point marker object in the projection images. The used size of the steel ball is arbitrary but should provide a good compromise to be used in a wide range of different geometric magnifications. Furthermore, the *QRM-MicroCT-Bar pattern* from QRM Quality Assurance in Radiology and Medicine GmbH, Germany, is used for the calibration of the scale.

The following basic steps are conducted and repeated if necessary:

1. The point marker object is centered so that it coincides with the rotation axis by adjusting its positions in $\hat{\mathbf{e}}_x$- and $\hat{\mathbf{e}}_y$-directions. This can be achieved by using at least two projections of the point marker at a rotation angle of $\varphi = 0°$ and $\varphi = 180°$ for finding the position in direction of $\hat{\mathbf{e}}_y$ and, respectively, at $\varphi = 90°$ and $\varphi = 270°$ for the $\hat{\mathbf{e}}_x$-direction.
2. The point marker is positioned so that it coincides with the magnification axis by adjusting the position in the $\mathbf{e}_y$- and $\mathbf{e}_z$-directions of the rotation axis. This is done by using two projections that were acquired at two different geometric magnifications (positions in direction of $\mathbf{e}_x$).

3. The intersection of the magnification axis with the detector, called the principal point, enables the compensation for the detector's offsets in $\mathbf{e}_y$- and $\mathbf{e}_z$-directions, which are adjusted to zero ($u_{0y} = u_{0z} = 0$).
4. Moving the point marker out of the rotation axis, for instance, in the direction of $\hat{\mathbf{e}}_x$, and performing projections for different rotation angles φ validates the correct execution of the previous steps if all projections of the point marker lie on a straight line. From the tilt of the line, the detector in-plane rotation angle η is determined and corrected via the motorized rotatable mounting of the detector. An offset shift of the sample's rotation table can also be detected from the marker positions at $\varphi = 0°$ and $\varphi = 180°$ rotation angles.
5. After the fine adjustment of all components, the relation between the sample position in the $\mathbf{e}_x$-direction and the resulting voxel size is determined by using the *QRM-MicroCT-Bar pattern.* At least three different sample positions are considered. Because of the linear relationship between the voxel size and the coordinate in the direction of $\mathbf{e}_x$, a mathematical formulation by linear regression can be found. By extrapolation, the source–detector distance (*SDD*) is given by the distance between the coordinates in the direction of $\mathbf{e}_x$ where the voxel size is equal to the detector's pixel size and where the voxel size theoretically is zero. In addition, the source–object distance (*SOD*) can be derived from the current distance between the sample position's coordinate and the coordinate where the voxel size theoretically is zero. With these two values, the geometrical magnification $M = SDD/SOD$ can be calculated.

Smaller misalignments are detected during the setup of the 3D reconstruction and are subsequently compensated during the same. Up to now, the commercial software *Octopus Reconstruction* (Vlassenbroeck *et al.*, 2007) in the newest version is employed for this purpose.

B. Software

To control the scan loop, the scripting language *MATLAB* from The MathWorks, Inc., is used. The communication between *MATLAB* and the different hardware controllers (X-ray source, detectors, and stages) is realized by socket programming. For this purpose, special interface programs in the library language that is supported by the used hardware controllers are applied. Basically, this approach enables one to use any script language to control the whole scan process. The benefit of this method is that it is highly flexible and each hardware component can be integrated. Hence, each hardware component can be replaced with ease in the case of a defect without depending on a specific manufacturer.

For the classical cone beam setup, the tomographic reconstruction based on the projection images as well as beam profile and dark images is performed by the commercial software *Octopus Reconstruction* (Version 8.9.4-64 bit) developed at Ghent University (Vlassenbroeck *et al.*, 2007) with the Multiple-Graphics Processing Units (Multi-GPU) package. The software is able to correct smaller geometrical misalignments of the system. As an alternative to *Octopus Reconstruction*, first steps with the open-source library *ASTRA Toolbox* (van Aarle *et al.*, 2016) were carried out, which provides next to analytical also algebraic reconstruction methods. A not yet tested open-source software alternative for fast circular cone
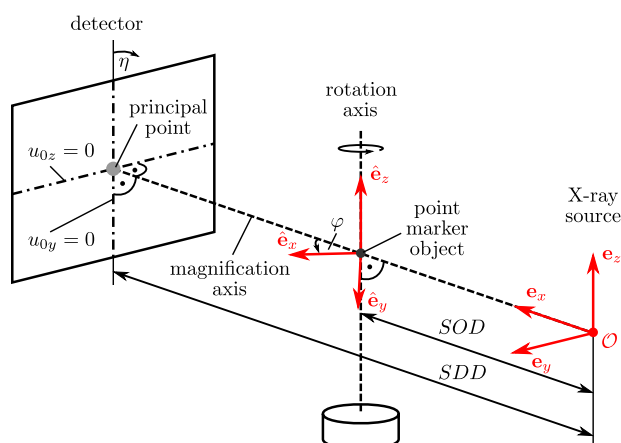

FIG. 3. Illustration of the aligned (calibrated) system and the used terms. For the possible moving directions of the components, cf. Figs. 1 and 2.

beam CT reconstruction might also be the *Reconstruction Toolkit (RTK)* (Rit *et al.*, 2014) based on the open-source software package *Insight Toolkit (ITK)*. To evaluate the captured image stacks, the open-source software *ImageJ* (Schindelin *et al.*, 2015; Schneider *et al.*, 2012), especially the distribution *Fiji* (Schindelin *et al.*, 2012), is used on each level. Next to *ImageJ*, the commercial software *Avizo* in the newest version from Thermo Fisher Scientific, Inc., for post-processing steps such as image segmentation is employed. Alternatives for image processing and three-dimensional visualization are, for instance, open-source software tools based on the open-source packages *ITK* and the *Visualization ToolKit (VTK)* such as *3DSlicer* or other commercial software such as *Dragonfly* from Object Research Systems (ORS), Inc., which is freely available for academic users. A summary of the above-mentioned software is given in Appendix, Table V.

C. System maintenance and breakdowns

In this section, we briefly want to address the system maintenance as well as the reaction on system breakdowns. In principle, the maintenance of the system is not time consuming and mainly limited to the maintenance of the X-ray source. As explained in Sec. II A 1, an open-tube X-ray source is employed, which allows the maintenance to be carried out by the user and on-site after a training provided by the manufacturer of the source. Besides annual all-inclusive maintenance of the X-ray source, which takes 1–2 days, some of the maintenance steps have to be repeated every 3–6 months, depending on the number of operating hours, for instance, renewal of the high voltage electrical contact grease or replacement of the cathode filament. After the annual maintenance, recalibration of the system is subsequently performed, which takes another 1–2 days. As part of the system recalibration, detector pixel maps are regularly (re-)created, representing aging of the detectors, and are required for the method presented in Sec. II D.

System failures related to hardware defects can usually be resolved within some days to a few weeks as most components are modular and therefore can be replaced quickly with comparable available components, which of course requires mostly recalibration of the system. For example, the use of two detectors offers a certain redundancy for potential (detector) failures in addition to the extension of the general possibilities. Thus, longer system failures can mostly be avoided, which is a further big advantage of the presented system concept. Longer system breakdowns usually only occur during major reconstruction measures and modifications that are planned in advance.

D. Compensation of bad detector pixels

It is commonly known that each detector has so-called *hot* and *cold* pixels (Gureyev and Nesterets, 2018). These pixels distinguish from average ones by working better or worse; in extreme cases, they do not work at all (dead pixels) and lead to unwanted ring artifacts in the 3D datasets. There are different possibilities to handle such pixels. One way is to use software-based ring artifact reduction techniques that can be classified into approaches based on the sinogram processing, also known as pre-processing techniques, and approaches based on the processing of the reconstructed images recognized as post-processing techniques (Anas *et al.*, 2011). Another approach that could be integrated into our system later on due to the modular and open concept and therefore shall serve as an example of the same is to improve the projection data by themselves by reducing the number of bad pixels, which is referred to as *projection data based approach* in this work. For this, several projections from slightly different detector positions (shift of multiple pixels) are captured and combined afterward to one single enhanced projection image. Alternatively, if the detector cannot be moved, the sample could be moved within the plane defined by the normal vector $\mathbf{n} = \mathbf{e}_x$ by using the vertical and the lateral linear translation stages to achieve the same effect. However, in the latter approach, it is more difficult to ensure that the resulting projections are shifted by pixel multiples due to the relation to the employed geometric magnification. In both cases, highly accurate motorized linear stages are required. The combination of the projections for one projection angle can be performed randomly, for instance, as in Jenneson *et al.* (2003) or as in our case with the help of a pixel map of the detector created in advance. The main disadvantage of this method is the increasing scan time due to which this approach is not appropriate when the sample is sensitive to the radiation dose from X rays. If the scan time can be disregarded and a high-quality scan is wished, this is a suitable approach, especially in combination with the software-based techniques. Concerning a high signal-to-noise ratio (SNR), the increasing scan time is even beneficial since it is always advisable to have a high number of X-ray photons that pass the sample during the whole scan (Gureyev and Nesterets, 2018).

1. Pixel map creation

One of the essential steps in the projection data based approach is the combination of the different projections for the respective angle. For this, a pixel map (visualized logical matrix) is employed that marks the good and the bad pixels of the detector. Since the pixel behavior of the detector depends on the X-ray beam characteristics, several open beam images for different tube voltages are taken (see Table II). The tube flux and the detector exposure time were set to ensure that no oversaturation takes place. To reduce noise impact, five images were captured for each parameter set and subsequently averaged.

With the resulting averaged open beam images, one final pixel map is created that is a pragmatic compromise solution to an otherwise large number of pixel maps for different settings. For this purpose, all detector pixels form the pixel set P that consists of the good pixel set P_{good} and the bad pixel set P_{bad}; $P = P_{\text{good}} \cup P_{\text{bad}}$ holds. For each of the J contributing averaged open beam images of the different parameter combinations, the gray values in the range

TABLE II. Underlying settings of the detector pixel maps.

Detector	Dexela 1512	Shad-o-Box 6K HS
Tube voltage (kV)	30, 60, 90, 120, 150, 180	
Tube flux (μA)	50	100
Detector exposure time (ms)	500	1000
Number of averaged images (-)	5	

$\{0, \ldots, 16\,383\}$ of the pixel set P_j are known and the bad pixel set P_{bad_j} with $j = 1, \ldots, J$ is determined as follows:

1. All pixels of P_j that have a gray value of zero represent defect pixels and are assigned to the set P_{bad_j}.

2. The gray values (GV) of the remaining pixel set $P_j \backslash P_{\text{bad}_j}$ are assumed to be normally distributed with the mean value μ_{GV_j} and the standard deviation σ_{GV_j}. Good pixels are defined in the range of $\mu_{\text{GV}_j} \pm 3\,\sigma_{\text{GV}_j}$, corresponding to $9\,999\,966\,\%$ of the remaining pixels, and form the set P_{good_j}. The pixels outside this range are declared to be bad pixels and are added to the set P_{bad_j}. The used approach assumes a uniform illumination of the detector. If this cannot be assumed, the criterion should be adapted. Otherwise, too many pixels are declared as bad ones, especially in the outer region. This could be achieved, for example, by a prior correction of the gray values according to the determined illumination profile.

For the final detector pixel map, the bad pixels are given by the union set $P_{\text{bad}} = \bigcup\limits_{j=1}^{J} P_{\text{bad}_j}$ of all bad pixel sets resulting from the J open beam images. Subsequently, the good pixel set is given by the set difference $P_{\text{good}} = P \backslash P_{\text{bad}}$. In Fig. 4, the pixel maps of the two detectors used in the presented system are shown. Yellow represents the good pixels (logical value 1), and red represents the bad ones (logical value 0). An additional benefit of using a pixel map is seeing the change in the detector over time when always the same procedure is applied and repeated after a specified time.

2. Detector moving pattern

The next step is to find a suitable moving pattern for the respective detector that minimizes the number of bad pixels in the final combined projection for the particular projection angle. The detector translation for position i can be described by the translation vector $\boldsymbol{u}_i = u_{ix}\mathbf{e}_x + u_{iy}\mathbf{e}_y + u_{iz}\mathbf{e}_z$. For the default (centered) detector position, the translation vector is given by $\boldsymbol{u}_0 = \mathbf{0}$, which means $u_{0x} = u_{0y} = u_{0z} = 0$. Since the value $u_{ix} = 0$ holds for all positions, it is omitted in the following. It is assumed that the final projection image has identical dimensions (resolution) as the input ones. In order to compensate bad pixels that are located in one row and one column, a vertical and a horizontal detector shift (in $\mathbf{e}_z$- and $\mathbf{e}_y$-directions) are needed. This leads to at least three detector positions to satisfy the mentioned requirements. As explained above, a higher number of projections always lead to enhanced image quality, which is why the number of different detector positions I is chosen to be $I = 5$ when the scan is not time-critical. The unknown detector translations are given by $\boldsymbol{u}_i$ with $i = 1, \ldots, 5$. This leads to a mathematical optimization problem with the object function to minimize the number of bad pixels in the final image. To simplify the problem, two further constraints are inserted: First, the first unknown detector position is set to the default position, $\boldsymbol{u}_1 := \boldsymbol{u}_0$, and second, axial symmetry in both directions with the same value is supposed. In this case, the set of 10 unknowns $\{(u_{1y}, u_{1z}), (u_{2y}, u_{2z}), [u_{3y}, u_{3z}), (u_{4y}, u_{4z}), (u_{5y}, u_{5z})\}$ is reduced to $n_p l_p \{(0, 0), (1, 1), (1, -1), (-1, -1), (-1, 1)\}$ with the unknown number of pixels n_p and the detector specific pixel pitch l_p, identical pixel pitch in vertical and horizontal directions, assumed. Hence, only one parameter is left and must be determined, which is performed by calculating the relative number of

(a)
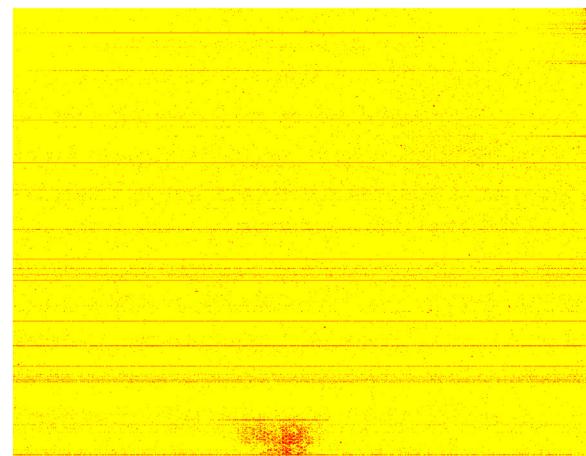
(b)

FIG. 4. Detector pixel maps based on the presented approach. Yellow corresponds to good pixels (P_{good}). Red corresponds to bad pixels (P_{bad}). (a) Dexela 1512 detector. (b) Shad-o-Box 6K HS detector.

bad pixels for varied values of n_p. In Fig. 5, the results for different applied pixel shifts for the determined pixel maps (cf. Fig. 4) are given under the assumption that the maximal allowed shift is $n_p = 100$. For the Dexela 1512 detector, the smallest shift with the lowest relative number of bad pixels is $n_p = 35$ [cf. Fig. 5(a)], and for the Shad-o-Box 6K HS, $n_p = 33$ [cf. Fig. 5(b)]. Without detector shifting, both detectors have a relative number of bad pixels about 10^{-2}. With the defined moving pattern, this can be reduced to 10^{-10} for the Dexela 1512 detector and to 10^{-5} for the Shad-o-Box 6K HS. A demonstration of the influence of the presented method on the image quality of a real sample is depicted in Fig. 10 in the scope of the first shown application example, Subsection IV A.

Concerning the implementation, there are at least two possibilities to perform the scan loop. The first way is to capture all $I = 5$
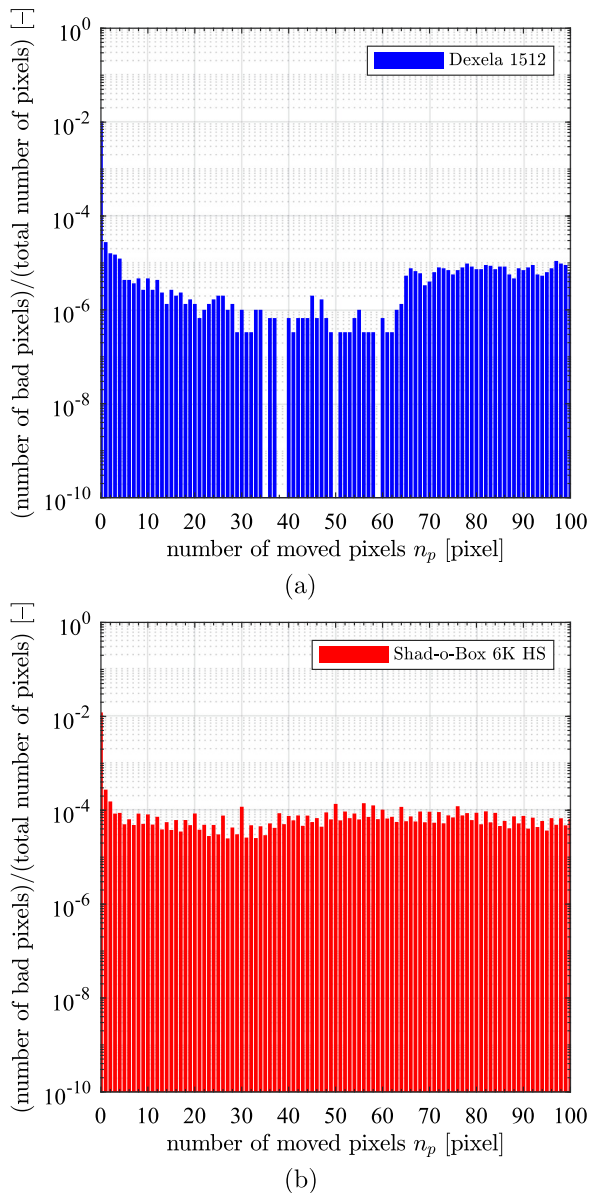
FIG. 5. Determination of the detector shift to minimize the number of bad pixels in the final projection for the supposed detector moving pattern. (a) Dexela 1512 detector. (b) Shad-o-Box 6K HS detector.

projections for one projection angle and go to the next angle position afterward. The advantage is that the stitching process can be started already during the scan, but the detector must be shifted very often. This leads to the second possibility where the detector is not moved to the position u_{i+1} until all angle projections for the detector position u_i are recorded. In this case, the overall required number of detector shifts corresponds to the number of employed detector positions I. Although the stitching process can only be started at the end or during the last sample rotation, this method is still less time consuming than the first one. Additionally, the latter one is

also preferable regarding the position error of the detector since the position error is identical for all projection angles for the respective detector positions u_i. Consequently, the second method is applied in our scan loop.

III. SYSTEM PERFORMANCE

A. Spatial resolution

To study the system performance and the behavior concerning spatial resolution, in particular, as a function of the two available detectors, the concept of modulation transfer function (Rossmann, 1969) based on CT scans of a cylindrical phantom according to the international standard DIN EN ISO 15708-3 (2019) is applied. Therefore, a cylindrical test phantom was manufactured, which consists of a stepped brass (CuZn39Pb3) cylinder with diameters of 1 mm, 2 mm, 3 mm, 4 mm, and 5 mm with a manufacturing tolerance of ±1 μm, which was coated afterward with cold polymerizing polyester resin (*Technovit 4002 IQ* from Kulzer GmbH, Germany) and lathed to an outer diameter of 10 mm [see Fig. 6(a)]. The different diameters of the transition zone between the brass and the polyester resin phase enable us to use the phantom in a wide range of geometric magnifications.

To evaluate the system with regard to the two detectors, the same geometric magnifications of 4.95, 16.5, 24.75, and 33.02 were investigated. The resulting voxel sizes, as well as the corresponding sampling frequencies given by the appropriate reciprocal voxel sizes, and the critical Nyquist frequencies that are half of the appropriate sampling frequency (Marshall and Monnin, 2018) are summarized in Table III. For all scans, the phantom was positioned so that the transition between the 2 mm and the 3 mm diameter section is always in the middle of the field of view and coincides with the principal point of the detector. The X-ray source was operated with a tube voltage of 100 kV (120 kV) and a tube current of 100 μA (120 μA) for the Dexela 1512 (Shad-o-Box 6K HS) detector, which ensures the minimal achievable focal spot size of the source in both cases. Since the Shad-o-Box 6K HS detector is less sensitive than the Dexela 1512 detector, the X-ray beam spectrum has to be adjusted

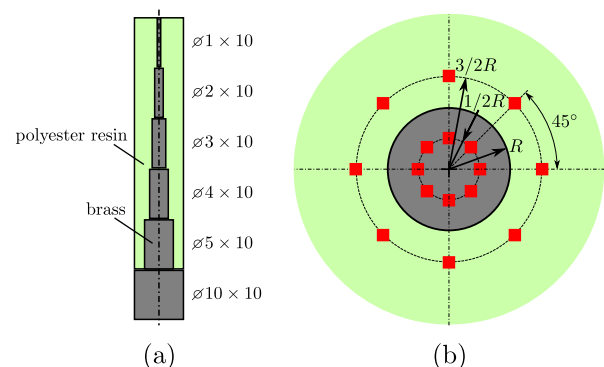
FIG. 6. Cylindrical test phantom for the determination of the modulation transfer functions and noise measurements. (a) Composition and dimensions. (b) Arbitrary cross section extraction with red markers to show the noise measurement regions.

TABLE III. Investigated geometric magnifications and corresponding voxel size, sampling frequency, and Nyquist frequency.

Geometric magnification (-)	4.95	16.50	24.75	33.02
Dexela 1512 detector				
Voxel size (μm)	15.11	4.53	3.02	2.27
Sampling frequency (mm^{-1})	66.2	220.6	330.9	441.4
Nyquist frequency (mm^{-1})	33.1	110.3	165.5	220.7
Shad-o-Box 6K HS detector				
Voxel size (μm)	10.0	3.0	2.0	1.5
Sampling frequency (mm^{-1})	100.0	333.3	500.0	666.8
Nyquist frequency (mm^{-1})	50.0	166.7	250.0	333.4

accordingly, and it is not possible to set identical parameters. Furthermore, for both detectors, an exposure time of 1000 ms was used, and the projection based compensation approach for bad detector pixels is described in Subsection II D. The signal-to-noise ratio was positively affected by capturing two projection images each time and averaging the same subsequently. Starting with the theoretical number of required projection angles and comparing the results with the results that were achieved by using the empirical number of 1440 (1800) projection angles for the Dexela 1512 (Shad-o-Box 6K HS) detector showed that they are nonsensitive for this investigation that why these numbers were used for all scans. The 3D reconstruction was performed with Octopus Reconstruction (Version 8.9.4-64 bit) using the Filtered Back Projection (FBP) method. To avoid an influence on the results, a minimum of possible software filters were used, especially no noise filtering. To compensate for beam hardening, the simple beam hardening correction was set with appropriate parameters.

From the single slices of the 3D datasets, the respective Modulation Transfer Function (MTF) can be calculated. For this, the first step is to determine the center of the inner (brass) cylinder with sub-pixel-accuracy. Beginning in the determined center and going outside in an arbitrary radial direction leads to the Edge Response Function (ERF) at the transition from the inner phase (brass phase) to the outer phase (polyester resin phase). Using a cylinder has the advantage that the image noise that also occurs in the ERF can be reduced by using different directions for the ERF and averaging the resulting profiles. Here, always 360 equidistant angles were used. Besides, it is possible to reduce noise further by averaging several slices of the stack before the calculation. In this case, it must be ensured that all employed slices are coaxial (Friedman et al., 2013). The negative derivation of the ERF according to the radial coordinate r leads to the Line Response Function (LRF). Performing a Fourier transform for the LRF and a subsequent normalization finally leads to the Modulation Transfer Function (MTF).

All calculations were performed in *MATLAB R2018b*, and for the steps from the ERF to the MTF, the algorithm of Granton (2010) was adapted. As expected, no difference in the results for different diameters of the transition between both material phases could be detected. In Fig. 7, the steps from the ERF to the MTF for both detectors for a geometric magnification of 24.75 are represented. To be able to compare the results, they were normalized. In the final representation of the MTFs [Fig. 7(c)], it can be seen that the Shad-o-Box 6K HS detector provides a higher spatial resolution corresponding to the number of line pairs per length for all possible MTF values for the examined geometric magnification.

To get a single number for the spatial resolution, it is customary to specify the spatial frequency at which the modulation transfer has dropped to 10% (Du et al., 2007; Weiß et al., 2012); cf. Fig. 7(c). From the results of the spatial resolution for each slice of one stack at 10% MTF, without taking into account the transition zones between the sections of different diameters, the mean value, as well as the

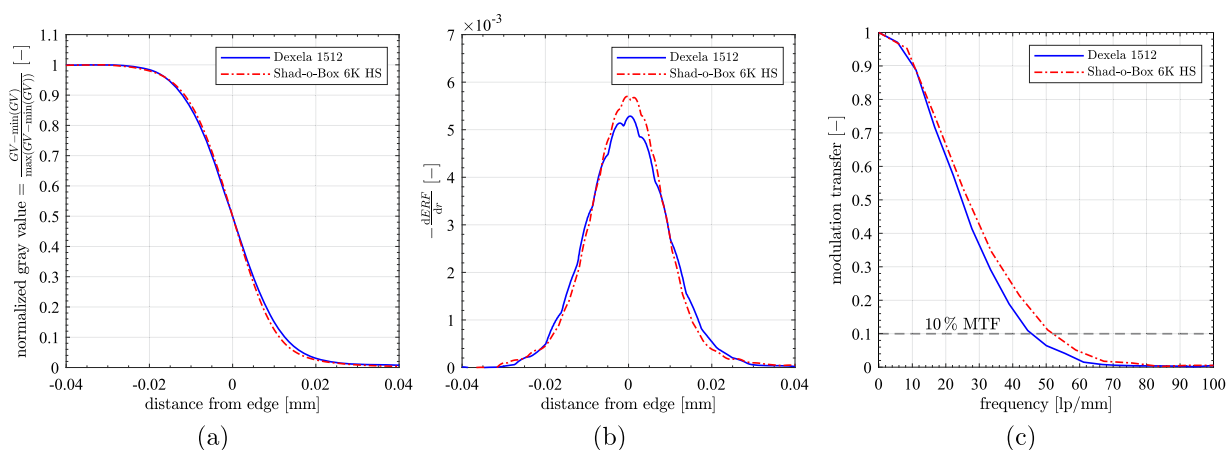**FIG. 7**. Illustration of the determination of the modulation transfer function to evaluate the system's spatial resolution based on 25 averaged slices to reduce image noise from the 3 mm sections of the two respective reconstructed datasets at a geometric magnification of 24.75 for both detectors. (a) Edge Response Function (ERF). (b) Line Response Function (LRF). (c) Modulation Transfer Function (MTF).

standard deviation, can be calculated. No significant distinction could be observed concerning the used number of slices to be averaged to reduce image noise. Hence, it was abstained from slice averaging, and each slice was separately evaluated.

Performing this for all eight executed scans leads to the plots shown in Fig. 8(a) where the error bars indicate the standard deviation and the numbers next to the data points are related to the corresponding voxel size; cf. Table III. The maximum of the red line indicates the maximal achievable spatial resolution in the case of the Shad-o-Box 6K HS detector, which is about 50.6 lp/mm. A further increase in the geometric magnification even declines the spatial resolution, which can be explained with the penumbra blurring effect that counteracts the positive effect on the spatial resolution of the geometric magnification; cf. Russo (2018) and Carmignato *et al.* (2018). Therefore, it is counterproductive to go to lower voxel sizes than 2.0 μm when using the Shad-o-Box 6K HS detector, also regarding the decreasing size of the field of view, which is plotted over the voxel size in Fig. 8(b). Considering the Dexela 1512 detector, this point is not yet attained due to the still increasing spatial resolution for the examined geometric magnifications. Since the size of the penumbra blurring should be identical in both cases, this observation is unexpected and shows that there are influences on the spatial resolution that are hard to separate. Going to higher geometric magnification, it is expected that the same effect can be observed. This would mean that a relationship with the voxel size exists that cannot be explained by the sampling frequency since in all cases the Nyquist criterion (Marshall and Monnin, 2018) is more than fulfilled (see Table III). Another influence could be the slightly different settings of the X-ray source also when in both cases the focal spot size should be basically identical.

Nevertheless, from this investigation, it can be concluded that the highest achievable spatial resolution of the system is about 50 lp/mm, which means a minimum representable feature size of about 10 μm at 10% MTF. This value could be qualitatively validated by a scan of a bar pattern phantom. Moreover, for the same geometric magnification, the setup with the Shad-o-Box 6K HS detector provides a higher spatial resolution in all meaningful cases, except for the highest magnification, than the setup with the Dexela 1512 detector. Since the geometrical sensor dimensions of both detectors are nearly identical, it follows that the resulting field of view size is nearly the same. However, for the same field of view, using the Shad-o-Box 6K HS detector provides a higher spatial resolution, which follows from the combined consideration of Figs. 8(a) and 8(b) and also confirms the characteristic of the underlying scintillator options of both detectors.

B. Signal, noise, signal-to-noise ratio, contrast, and contrast-to-noise ratio

According to DIN EN ISO 15708-3 (2019), the signal and the noise for a homogeneous area of a reconstructed image are characterized by the mean value μ and the standard deviation σ of the pixel gray values that belong to this area. With these two quantities, the signal-to-noise ratio is given by

$$\text{SNR} = \mu/\sigma. \tag{1}$$

As recommended in DIN EN ISO 15708-3 (2019), the reconstructed datasets of the cylindrical phantom employed for the investigation of the system's spatial resolution are used to determine these quantities. Since there are two almost homogeneous material phases, also the contrast, as well as the contrast-to-noise ratio (CNR) between them, is defined by

$$\text{contrast} = \frac{|\mu_{brass} - \mu_{resin}|}{\mu_{resin}} \quad \text{and} \quad \text{CNR} = \frac{|\mu_{brass} - \mu_{resin}|}{\sigma_{resin}}, \tag{2}$$

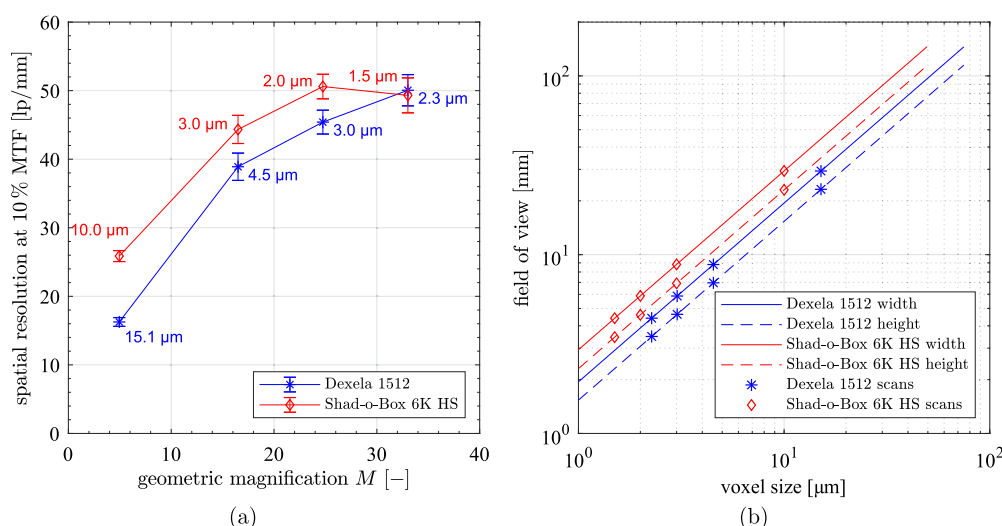with the polyester resin phase serving as background material.

FIG. 8. (a) Comparison of the achievable spatial resolution for different geometric magnifications and the corresponding voxel sizes for the two detector options. Error bars indicate the standard deviation. (b) Field of view size in relation to the voxel size of the employed detectors.

TABLE IV. Signal, noise, signal-to-noise, contrast, and contrast-to-noise results of the two material phases for two radial coordinates based on an XRCT scan of the cylindrical phantom with both detector options. Settings: geometric magnification of 24.75 (24.75); corresponding voxel size of 3.0 μm (2.0 μm); X-ray tube voltage of 100 kV (120 kV) and tube flux of 100 μA (120 μA); detector option Dexela 1512 (Shad-o-Box 6K HS) with an exposure time of 1000 ms (1000 ms); and 1440 (1800) projection angles with detector stitching according to Subsection II D, each projection based on two averaged images.

Detector	Dexela 1512		Shad-o-Box 6K HS	
Section (diameter)	2 mm	3 mm	2 mm	3 mm
Slices	500 (58–557)	700 (783–1482)	800 (85–884)	1000 (1224–2223)
μ_{brass}	0.4832 ± 0.0024	0.4718 ± 0.0014	0.5729 ± 0.0004	0.5671 ± 0.0004
σ_{brass}	0.0184 ± 0.0009	0.0298 ± 0.0013	0.0153 ± 0.0004	0.0231 ± 0.0012
SNR_{brass}	26.3730 ± 1.1158	15.8737 ± 0.6459	37.3803 ± 1.0004	24.5742 ± 1.3444
μ_{resin}	0.1229 ± 0.0002	0.1207 ± 0.0002	0.3588 ± 0.0001	0.3581 ± 0.0001
σ_{resin}	0.0106 ± 0.0005	0.0171 ± 0.0009	0.0088 ± 0.0002	0.0132 ± 0.0007
SNR_{resin}	11.6641 ± 0.0196	7.0669 ± 0.3351	40.8675 ± 0.9263	27.1949 ± 1.4662
Contrast	2.9313 ± 0.0196	2.9100 ± 0.0113	0.5965 ± 0.0013	0.5836 ± 0.0011
CNR	34.1821 ± 1.4252	20.5643 ± 0.9641	24.3799 ± 0.5887	15.8707 ± 0.8466

For examination, eight squared areas with a respective edge length of 200 μm were specified for each phase corresponding to the red squares in Fig. 6(b). The radial locations are defined in relation to the transition radius R between the two material phases. The examination is based on the datasets for a geometric magnification of 24.75, which corresponds to a voxel size of about 3.0 μm for the Dexela 1512 detector and 2.0 μm for the Shad-o-Box 6K HS detector, and leads to a size of 67 pixel × 67 pixel and 100 pixel × 100 pixel for the squared areas, respectively. The signal μ, the noise σ, and the SNR values, as well as the contrast and the CNR, were calculated for each 16-bit gray value (interval [0, 1]) slice of the 2 mm and 3 mm sections of the phantom. The resulting mean values and their standard deviations are summarized in Table IV. In all cases, the influence on the mean value μ for the two examined radial locations of each phase is negligible, which is evidence that beam hardening was successfully compensated. However, it is obvious that all noise measurements σ increase in the radial direction, which is a consequence of the reduced number of projection angles against the required theoretical numbers. This also explains why the SNR values are not identical for the same material phase for different radial positions. It can be observed that the Shad-o-Box 6K HS detector provides overall a higher SNR. Since the SNR grows as the square root of the number of photons, the lower power, as well as the lower number of projection angles that were used for the Dexela 1512 detector, may have an influence (Carmignato *et al.*, 2018; Russo, 2018; and Stock, 2008a). However, as already explained, it is not possible to perform scans with identical settings due to the different sensitivities of the detectors. In return, the contrast and the CNR are significantly higher for the Dexela 1512 detector. The latter is a direct consequence of the higher contrast, which is again influenced by the applied source settings. It has to be mentioned that the presented results are material specific and cannot be considered as absolute quantities of the XRCT system. However, they complement the spatial resolution investigations and are useful to understand the different detector characteristics.

C. Discussion

The spatial resolution together with the additionally presented quantities is only one part for evaluating the performance and capability of an XRCT system. Besides, the presented values cannot be considered as absolute quantities of the system because there are various dependencies that start with the investigated material combination of the phantom and the employed scanning settings. However, the performed study offers a very good indication of what is generally possible with regard to the maximum achievable resolution at moderate power levels and how the behavior of the setup differs with regard to the two available detectors. Moreover, there are a lot of other factors, for instance, the scan time and the size of the recorded datasets that are crucial quantities for a user of such a system or the recipient of the datasets. In particular, the size of the datasets is not irrelevant since it affects the needed hardware for post-processing steps. For instance, a complete reconstructed dataset that is acquired with the Shad-o-Box 6K HS detector and saved in 16-bit TIFF image format has a size up to 39.8 GB, whereas it only has a size of 11.6 GB when the Dexela 1512 detector is employed. Therefore, even if it seems that the performance of the system in combination with the Shad-o-Box 6K HS detector is more beneficial in regard to spatial resolution combined with the size of field of view, there are a lot of cases where these requirements are not decisive and using the system with the Dexela 1512 detector is preferred. Furthermore, a detector with a higher resolution always requires more projection angles, which is adverse for the necessary scan time, especially for time critical scans. So far, unmentioned and not further considered in the presented performance study is the possibility of detector binning. Detector binning is a simple solution to increase the SNR and the detector's maximum possible frame rate; if not, all of the sensor resolution is needed. For this, the Shad-o-Box 6K HS detector provides the possibility to apply a 2 × 2 pixel binning. In contrast, the Dexela detector provides pixel binning up to 4 × 4 pixels in various, also rectangular, combinations. Consequently, the Dexela detector

offers much more flexibility in this respect, which should not remain unmentioned.

IV. EXAMPLES

In the following, datasets of three typical application examples of the XRCT system are presented. The examples were chosen in a way to demonstrate the broad spectrum of the device. All scans were performed using the classical cone beam configuration. The reconstructed datasets, as well as the underlying projection images of the three subsequent examples including the metadata of the scanning parameters, are open access published in Ruf and Steeb, 2020c; 2020b; and 2020a.

A. Open-pored asphalt concrete

A widely used construction material with a high economic impact is open-pored asphalt concrete. Current research projects deal, for instance, with the study of effective mechanical properties (Schüler *et al.*, 2016; Alber *et al.*, 2018) or the sound absorption behavior (Wang *et al.*, 2016). For experimental investigations, core samples are often used. Due to the physical dimensions of such drill cores, this is an appropriate example for a large sample. The investigated core has a diameter of 100 mm and a height of 50 mm and was positioned in the device to achieve a geometric magnification of 3.0

by employing the Dexela 1512 detector. This corresponds to a voxel size of 25.0 μm. With these settings, the complete sample is not in the field of view which is regarded in the reconstruction process. The X-ray tube was set to a voltage of 140 kV by a flux of 400 μA. 1440 projection angle positions (angle increment 0.25°) and 5 projections in accord with the moving pattern of Subsection II D for each angle by a detector exposure time of 2500 ms were recorded. The whole elapsed scan time with these settings was 05:36 h. The reconstruction was done with Octopus Reconstruction (Version 8.9.4-64 bit) using the Filtered Back Projection (FBP) method with the required Region Of Interest (ROI) filter. In Fig. 9, an orthogonal view of the dataset (Ruf and Steeb, 2020c) is exhibited where the mineral aggregate is represented by the bright gray value, the bituminous binder between the particles is represented by the medium gray value, and the void space (air) is represented by the dark gray (black) areas.

We always employ the projection data based approach in non-time critical scans to reduce ring artifacts, which was introduced in Subsection II D, to improve the quality of the resulting datasets. To demonstrate the enhanced image quality, the scan of the asphalt core was repeated with exactly the same scan settings but without movement of the detector. In this case, five images were recorded and subsequently averaged, but the detector was always fixed in the middle/default position. We refer to this scan as a usual scan. In Fig. 10,
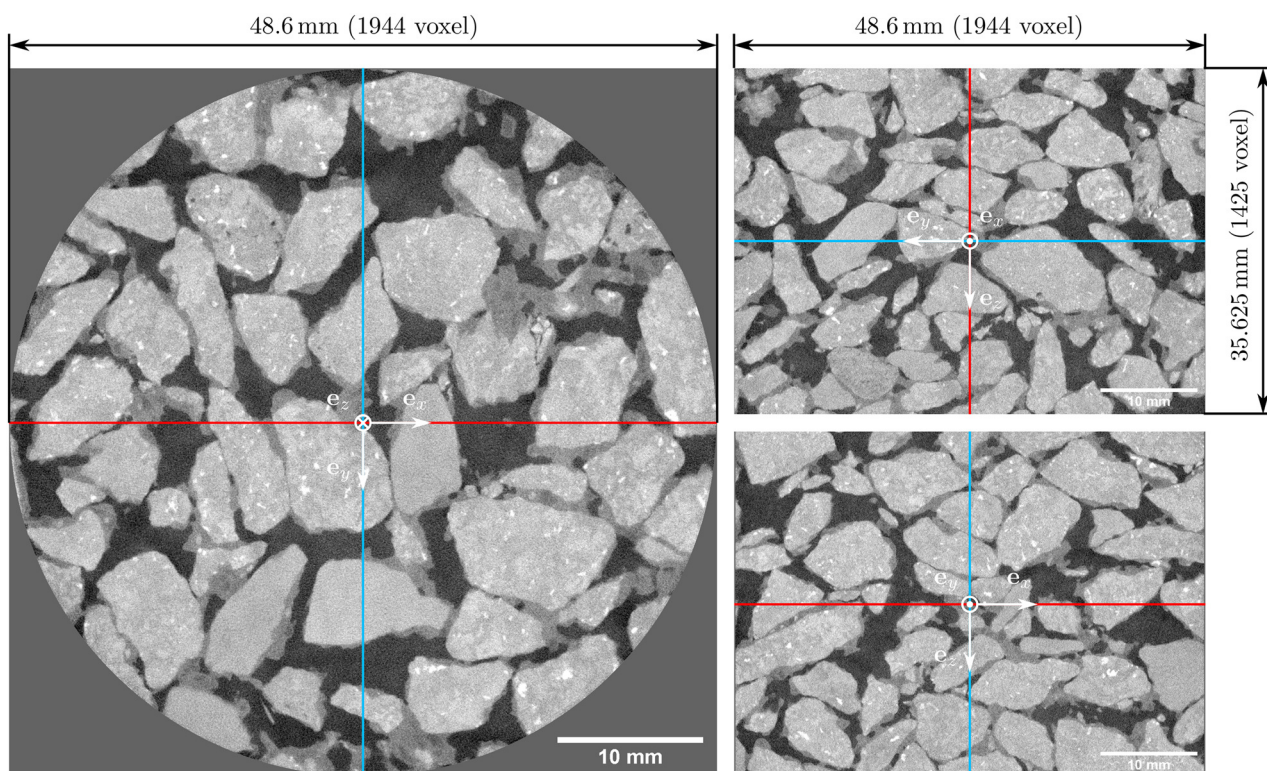
FIG. 9. Region of interest XRCT scan of an open-pored asphalt concrete core. The underlying dataset can be found in Ruf and Steeb (2020c), https://doi.org/10.18419/darus-639; licensed under a Creative Commons Attribution (CC BY) license. Settings: geometric magnification of 3.0; corresponding voxel size of 25.0 μm; X-ray tube voltage of 140 kV and tube flux of 400 μA; detector option Dexela 1512 with an exposure time of 2500 ms; 1440 projection angles with detector stitching according to Subsection II D.
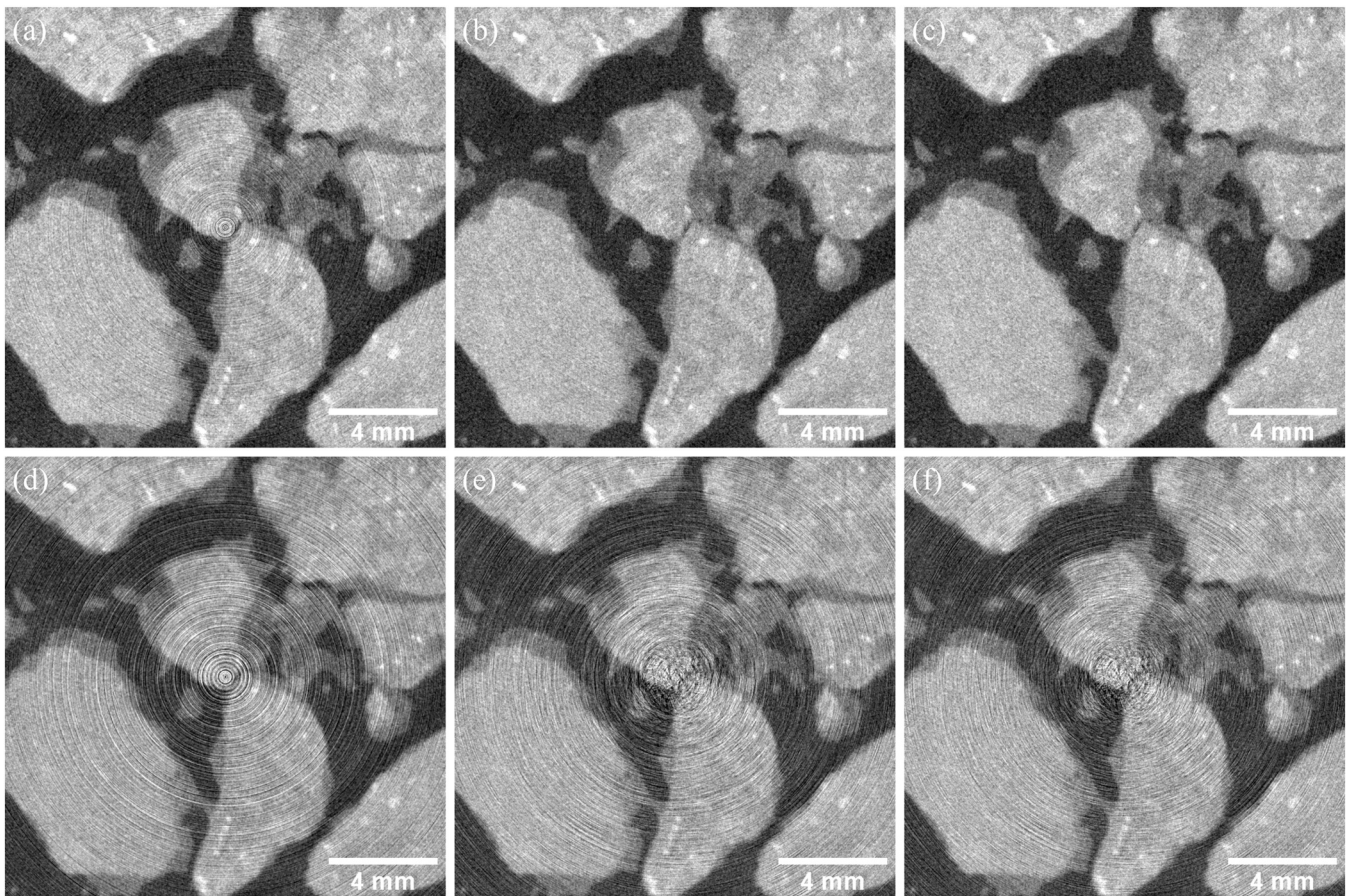
FIG. 10. Demonstration of the projection data based approach described in Subsection II D to reduce ring artifacts. (a)–(c) refer to the projection data based approach and (d)–(f) refer to a usual scan without any compensation. The reconstruction was performed in Octopus Reconstruction with the FBP method and a ROI filter. In (a) and (d), no spot and ring filters were used. In (b) and (e), pre-processing filters (spot and ring filters) in automode were applied. In (c) and (f), an additionally post-processing ring filter was applied (minimum arc length of 270° and maximum ring width of 10 pixel).

an extraction of 648 pixel × 648 pixel of the center of one representative reconstructed slice for both cases and different ring filter techniques is shown. The first row [(a)–(c)] of Fig. 10 is related to the projection based approach, and the second row [(d)–(f)] is related to the usual scan. Using Octopus Reconstruction (FBP) with no spot and ring filters at all leads to the results given in (a) and (d). In both cases, ring artifacts are visible, but in (d), they are significantly more distinctive. The application of a pre-processing spot and ring filter in automode leads to the results given in (b) and (e). The image quality in (b) compared to that in (a) could be improved further, and nearly no ring artifacts are visible anymore. An additional applied post-processing ring filter leads to (c) and (f). In the case of the projection based approach, the last ring artifacts could be removed successfully, and finally, a high-quality dataset was created. The pre- and post-processing filters were also able to improve the image quality of the reconstructed data of the usual scan but not as powerful as in the projection based approach, and moreover, partly new artifacts were created. As a result, it is always advisable to improve the

projection data as far as possible and combine this approach with other ring artifact reduction techniques to achieve high-quality XRCT datasets.

B. Carrara marble with artificially created crack network

An example that requires a high spatial resolution is the visualization of micro-cracks in tight (crystalline) rocks to study the influence on hydro-mechanical coupling, which is strongly affected by the deformation of fluid-saturated fractures (Vinci *et al.*, 2014). For this, Carrara marble is often used due to its high mineral purity and generally low anisotropy and homogeneity, which makes it a very reproducible material for rock deformation tests from both the mechanical and microstructural points of view (Delle Piane *et al.*, 2015; Sarout *et al.*, 2017). For the creation of micro-cracks, a thermal treatment was applied. Starting from a Carrara marble block with a thickness of 80 mm, a cylindrical sample with a diameter

of 30 mm and a final length of 75 mm was drilled out using a water-cooled diamond drill. The core was subjected to a thermal treatment starting at room temperature (20 °C) and heating up with 3 K min^{-1} to 600 °C. This temperature was held for 2 h. Due to the anisotropic thermal expansion of the grains during the heat-up period, micro-cracks are initiated along the grain boundaries. Quenching the sample in water at room temperature amplifies the creation of micro-cracks because of the temperature gradient difference between the core and the outer region. To achieve a high spatial resolution, a small cylindrical core with a diameter of 5 mm and a length of 10 mm was drilled out of the primary sample, as suggested in Delle Piane *et al.* (2015), using again a water-cooled diamond drill.

For the XRCT scan, the Shad-o-Box 6K HS detector with an exposure time of 3000 ms was employed. Totally, 1800 projection angle positions (angle increment of 0.2°) and 5 projections in accord with the moving pattern of Subsection II D for each angle were set. The X-ray tube voltage was set to 80 kV, and the flux was set to 100 µA. Additionally, an aluminum filter with a thickness of 0.5 mm was mounted directly in front of the X-ray source to reduce the weak X-ray radiation. The geometric magnification was set 24.76, which means a voxel size of 2 µm and corresponds to the highest achievable spatial resolution of the system; cf. Fig. 8(a). This results in a field of view of 5.88 mm in the horizontal direction and 4.61 mm in the vertical direction. Hence, the sample can be scanned over the whole diameter of 5 mm. The scan needed 15:45 h. In Fig. 11, the reconstructed dataset (Ruf and Steeb, 2020b) is shown. Due to the

thermal treatment, a homogeneous crack network evolved between the single grains of the crystalline rock, which cannot be observed in a virgin sample that was not subjected to a thermal treatment. As can be observed, for the most part, there is a very high aspect ratio between the length of the cracks, in the order of millimeters, and their aperture which is partly in the order of micrometers. The requirements for the definition of an appropriate Representative Volume Element (RVE) for further hydro-mechanical investigations are about 10 features in thickness direction, resulting in an RVE size of about 2 mm, assuming a mean grain diameter of about 200 µm. Moreover, to evaluate the choice of the RVE, it is essential to have a comparative region. All together explains the challenge and illustrates why a high spatial resolution and a large field of view are needed, which are given in the presented setup in combination with the Shad-o-Box 6K HS detector, cf. Fig. 8, as demonstrated in Fig. 11.

C. *In situ* experiment with an X-ray transparent flow cell

Finally, an example is shown that demonstrates an *in situ* experiment with an X-ray transparent flow cell, shown in Fig. 12, for a possible subsequent application in synchrotron radiation facilities. Applying such a cell, it is possible to study materials *in situ* under geological reservoir conditions (high confining and fluid pressure and high temperatures). The cell is designed and made in-house. The conceptual design was presented in Fusseis *et al.* (2014) and offers

(a)

(b)
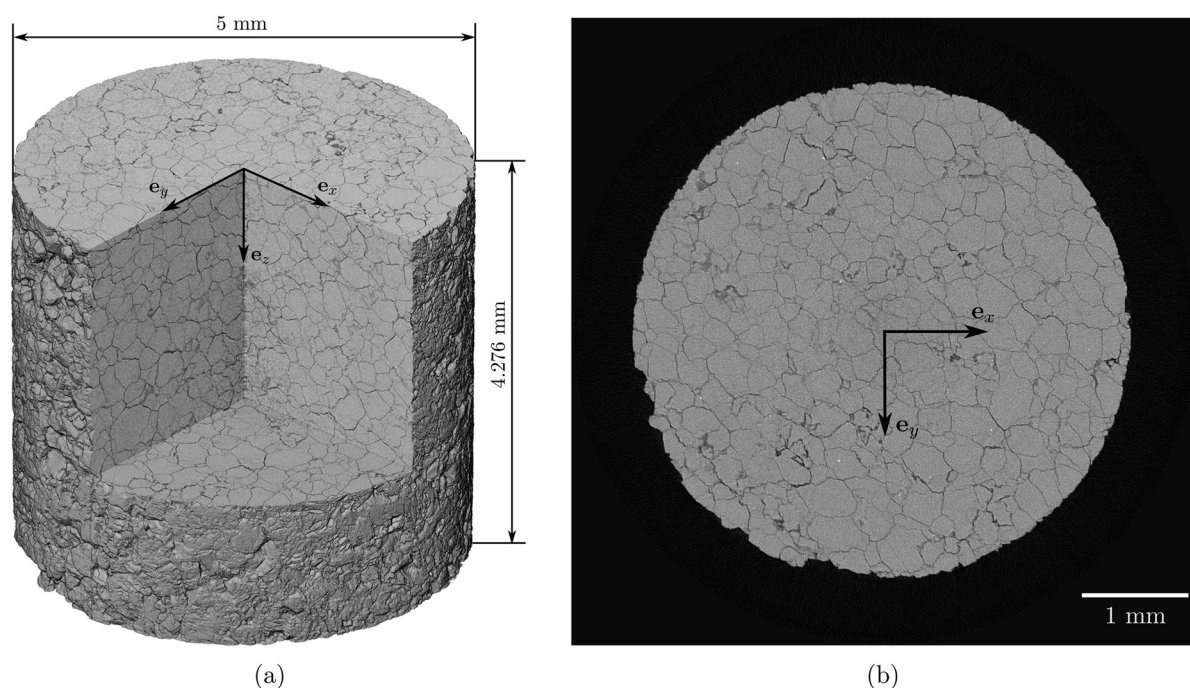
FIG. 11. High resolution XRCT scan of a Carrara marble core with micro-cracks along the grain boundaries initiated by thermal treatment. The underlying dataset can be found in Ruf and Steeb (2020b), https://doi.org/10.18419/darus-682; licensed under a Creative Commons Attribution (CC BY) license. (a) 3D volume with extraction. (b) Single slice (slice 1410). Settings: geometric magnification of 24.76; corresponding voxel size of 2 µm; X-ray tube voltage of 80 kV and tube flux 100 µA with a 0.5 mm thick Al-filter; detector option Shad-o-Box 6K HS with an exposure time of 3000 ms; 1800 projection angles with detector stitching according to Subsection II D.

FIG. 12. *In situ* setup of the X-ray transparent flow cell installed in the presented XRCT system: (a) overview and (b) detailed view of the flow cell with tubings.

the possibility to apply a confining pressure and to inject a pore fluid against a backpressure under X-ray radiation. Due to the space available inside the lead shielded cabin and on the optical table of our system, which is comparable with the environmental conditions in a synchrotron radiation facility, all additionally needed hardware can be located close to the experimental cell as it would be the case in a synchrotron radiation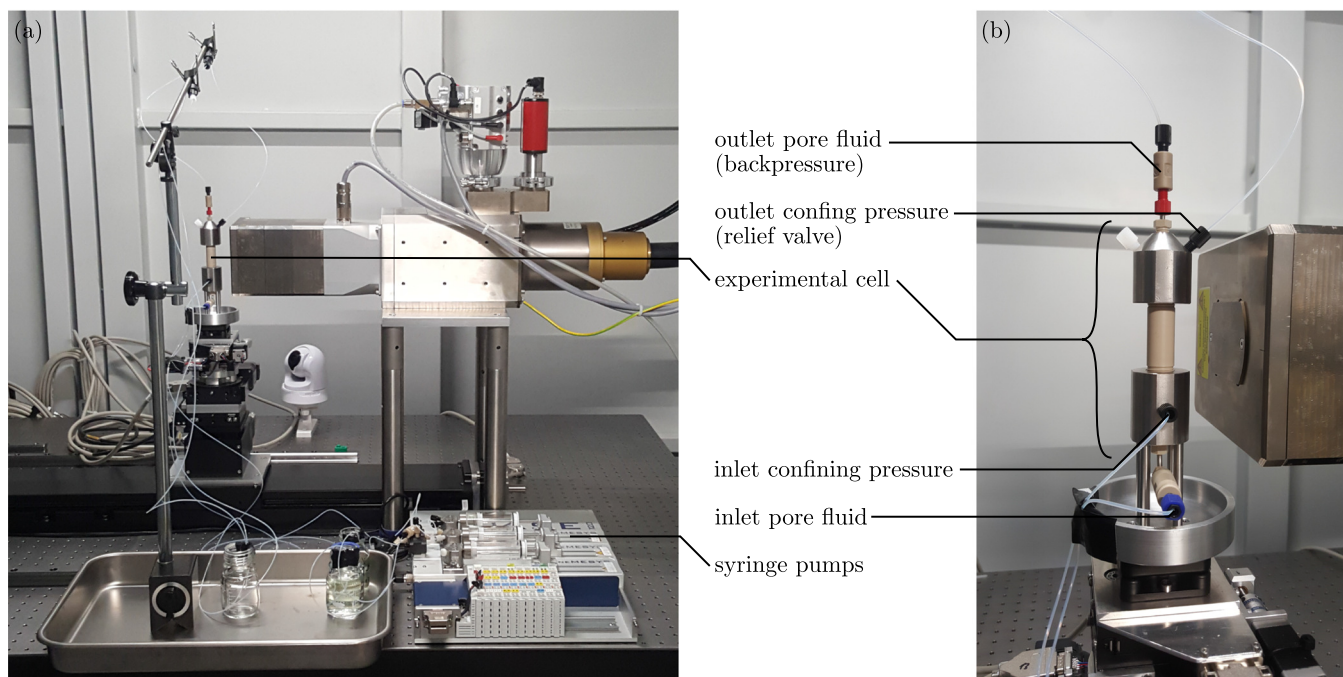 facility; cf. Fig. 12(a). This allows a quasi-static preliminary test and the preparation of experimental setups before using them finally in a synchrotron radiation facility where transient physical processes can be studied.

To demonstrate this, we use as a porous medium a cylindrical sandstone core with a diameter of 3 mm and a length of 9 mm extracted from a sandstone block from the County of Bentheim. From previous investigations on this material, it is known that the sandstone has an effective porosity of about 21.47% and an intrinsic permeability of about 2.05×10^{-12} m^2 (Musialak, 2013). To apply a confining pressure on the sample's cylindrical surface, the sample is jacketed by a silicon and a shrink tube that seal it against the fluid used for the confining pressure; cf. Fusseis *et al.* (2014) and the supplementary material. Besides a preliminary test of the flow cell, the *in situ* experiment aims to figure out how good the sample can be saturated with distilled water. For this purpose, two scans were executed without changing the position of the sample. The first scan was performed from the unsaturated sample, and the second one was performed after the *in situ* saturation process. Both scans were performed under an identical confining pressure of $p^c = 0.6$ MPa, which was applied to the cylindrical surface of the sample using distilled water and a syringe pump (*mid-pressure syringe pump neMESYS 1000N* from CETONI GmbH, Germany). For the

saturation of the sample, 3M KI solution that means 3 mol of potassium iodide dissolved in 1 l distilled water was used to get a higher contrast between the water phase and the potential remaining empty pore spaces. For the saturation of the sample, a total volume of about 25 ml under a constant flow of 100 μl s^{-1} against a backpressure of $p^b = 0.28$ MPa (40 psi pressure relief valve) was injected with a second syringe pump of the same type. To counteract the creation of hydrogen as a consequence of the X-rays, a constant flow of 0.5 μl s^{-1} against the same backpressure ($p^b = 0.28$ MPa) was sustained during the whole second scan. For both scans, the following identical scan settings were used: an X-ray tube voltage of 110 kV with a tube flux of 110 μA. For the detector option, the Shad-o-Box 6K HS with an exposure time of 2000 ms was chosen. Furthermore, 1800 projections from five different detector positions, according to Subsection II D, were acquired. The geometrical magnification was set to 24.75, resulting in a voxel size of 2 μm. Each scan needed about 10:40 h. The complete installed setup with all tubings and the employed syringe pumps is depicted in Fig. 12(a). The required 360° rotation of the cell is split in ±180° to avoid winding of the tubes.

In Figs. 13(a) and 13(b), one slice of each of the two reconstructed datasets (Ruf and Steeb, 2020a) of exactly the same location before and after the saturation with 3M KI solution is shown. In Fig. 13(a), the skeleton of the sandstone can be seen given by the bright gray areas, surrounded by a silicon tube and an additional shrink tube to seal the sample from the fluid (distilled water) used to apply the confining pressure on the sample. The pore space is given by the dark gray area in between the sandstone grains and mainly filled with air. After the saturation of the sample, the prior air-filled pore space is nearly fully saturated with the 3M KI solution. This can
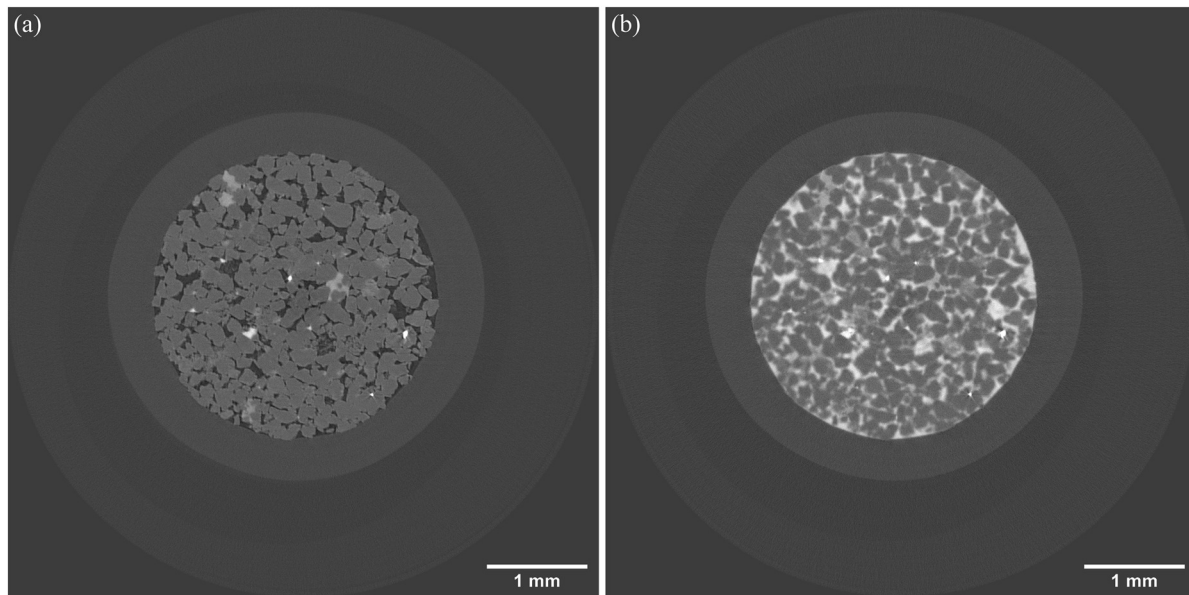
FIG. 13. Illustration of the *in situ* study using slice 720 of the underlying reconstructed datasets that can be found in Ruf and Steeb (2020a), https://doi.org/10.18419/darus-691; licensed under a Creative Commons Attribution (CC BY) license: (a) before the saturation and (b) after the saturation with 3M KI solution. Settings: geometric magnification of 24.75; corresponding voxel size of 2 μm; X-ray tube voltage of 110 kV and tube flux of 110 μA; detector option Shad-o-Box 6K HS with an exposure time of 2000 ms; and 1800 projection angles with detector stitching according to Subsection II D.

be observed in Fig. 13(b) by the almost white color of the KI solution, which is the most attenuating component.

V. SUMMARY AND CONCLUSION

A modular and flexible designed µXRCT system that is open to changes at every level was presented. For this, first of all, the used hardware components, the assembly of the same including the employed system calibration algorithm, and the software concept were summarized. To show the benefit of a modular and open system on the hardware as well as on the software side, a simple projection data based method to reduce ring artifacts was presented, which results in a significantly enhanced dataset quality. Within the first application example, the method was compared with software-based ring filter reduction techniques, whereas the best result could be achieved by the combination of different methods. After a systematic study to evaluate the performance of the system in respect of the attainable spatial resolution for an exemplary material combination, three different example datasets were presented, which demonstrate the wide scope of options of the presented µXRCT system. In particular, the last example that showed an *in situ* experiment in a flow cell should display how crucial a sufficient space for *in situ* studies is. Although such a system cannot be used to investigate transient processes, it is possible to prepare and test setups for future investigation in synchrotron radiation facilities. The datasets of the three examples and the associated projection images where the reconstructed datasets are based on, as well as the related metadata, are separately open access published in Ruf and Steeb, 2020c; 2020b; and 2020a. The presented work should be a motivation and an aid for researchers thinking about building such a system themselves or

have already decided to do so. Furthermore, it shows what kind of dataset quality can be expected. Altogether, the benefits that an open, modular, and flexible µXRCT system concept in the research area can offer are pointed out and illustrated in the presented work.

APPENDIX: COMPONENTS OVERVIEW

Table V summarizes the essential components according to their mentioning in the text. The individual components are divided into groups for a rough indication of the associated hardware acquisition costs that might be of interest to specific readers. The costs for the X-ray source (No. 1) were ~80 000 €; for the two detectors (Nos. 2 and 3) were ~48 000 € and ~55 000 €, respectively; for the sample positioning mechanics (No. 4) were ~12 000 €; for the detectors positioning mechanics (No. 5) were ~7000 €; for the employed motion controllers (No. 6) were ~12 000 €; for the X-ray protection (No. 7) were ~50 000 €; and for the optical table (No. 8) were ~6500 €. The costs for the other components (No. 9) amounted to ~3000 €. Thus, the total costs for the pure hardware were about 275 000 €. All costs are without sales taxes and related to the date of purchase.

TABLE V. Summary of the presented hardware and software. For details, see the corresponding text.

Nos.	Function	Component	Supplier/manufacturer
		Hardware	
1	X-ray source	FineTec FORE 180.01C TT	FineTec FineFocus Technologies GmbH, Germany
2	Detector 1	Dexela 1512NDT with a GOS-based DRZ Standard scintillator	PerkinElmer, Inc., Waltham, MA, USA
3	Detector 2	Shad-o-Box 6K HS with a CsI scintillator	Teledyne DALSA, Inc., Waterloo, ON, Canada
4	Sample $\mathbf{e}_x$-axis stage	OWIS LIMES 170-1000-3HSM	OWIS GmbH, Germany
	Sample $\mathbf{e}_y$-axis stage	Standa MT167-25LS-MEn1	Standa Ltd., Lithuania
	Sample $\mathbf{e}_z$-axis stage	OWIS HVM 100-30-HSM-MS	OWIS GmbH, Germany
	Sample $\hat{\mathbf{e}}_x$-axis stage	Newport M423 stage mechanic with a Nanotec ST2018L0804-A actuator	Newport Corp., Irvine, CA, USA, and Nanotec Electronic GmbH & Co., Germany
	Sample $\hat{\mathbf{e}}_y$-axis stage	Newport M423 stage mechanic with a Nanotec ST2018L0804-A actuator	Newport Corp., Irvine, CA, USA, and Nanotec Electronic GmbH & Co., Germany
	Sample $\varphi\mathbf{e}_z$-axis stage	Standa 8MR190-2-28-MEn1	Standa Ltd., Lithuania
	Sample holder	Newport M-BK-2A and Newport M-BK-1A	Newport Corp., Irvine, CA, USA
5	Detector rack $\mathbf{e}_x$-axis stage		Self-made
	Detector rack $\mathbf{e}_y$-axis stage	isel 234 611 0079 with a Vexta PK245M-01B stepper motor	isel Germany AG, Germany, and Oriental Motor Europa GmbH, Germany
	Detector $\mathbf{e}_y$/$\mathbf{e}_z$-axis stages (2x)	Standa 8MTF-75XX-MEn1	Standa Ltd., Lithuania
	Detector $\eta\mathbf{e}_x$-axis (2x)		Self-made
6	Motion controller/driver 1	Standa 8SMC4-Ethernet/RS232-B19x3-8	Standa Ltd., Lithuania
	Motion controller/driver 2	Standa 8SMC5-Ethernet/RS232-B19x3-12	Standa Ltd., Lithuania
7	X-ray protection	Lead shielded, accessible cabin (3 m length, 2.3 m width, and 2.4 m height)	FineTec FineFocus Technologies GmbH, Germany
8	Optical table	Newport RP Reliance sealed hole table top (2400 mm length, 1200 mm width, and 203 mm thickness) with Newport S-2000A-428-TC and Newport M-TB-48	Newport Corp., Irvine, CA, USA
9	Miscellaneous optomechanics	Breadboards, optical post assemblies, etc.	Thorlabs, Inc., Newton, NJ, USA
	Calibration phantom	QRM-MicroCT-Bar pattern	QRM Quality Assurance in Radiology and Medicine GmbH, Germany
		Software	
10	Scan controlling	MATLAB[a]	The MathWorks, Inc., Natick, MA, USA
11	Reconstruction	Octopus Reconstruction[a] (not available anymore)	XRE NV, Belgium
		ASTRA Toolbox[b]	imec-Vision Lab, http://www.astra-toolbox.com
		Alternative: Reconstruction Toolkit (RTK)[b]	https://www.openrtk.org
12	Image processing	ImageJ/Fiji[b]	https://imagej.net; https://fiji.sc
		Avizo[b]	Thermo Fisher Scientific, Inc., Waltham, MA, USA
		Alternative(s): Dragonfly[c]	Object Research Systems (ORS), Inc., Montreal, QC, Canada

TABLE V. Summary of the presented hardware and software. For details, see the corresponding text.

Nos.	Function	Component	Supplier/manufacturer
		Packages based on the Insight Toolkit (ITK)[b] and the Visualization ToolKit (VTK),[b] e.g., 3DSlicer[b]	https://www.itk.org; https://www.vtk.org; https://www.slicer.org

[a]Commercial software.
[b]Open-source software.
[c]Commercial software but free for academic use.

DATA AVAILABILITY

The image data of all application examples (reconstructed datasets, projection datasets, and metadata) that support the findings of this study are openly available in the data repository of the University of Stuttgart (DaRUS) at https://doi.org/10.18419/DARUS-639 (Ruf and Steeb, 2020c), https://doi.org/10.18419/DARUS-682 (Ruf and Steeb, 2020b), and https://doi.org/10.18419/DARUS-691 (Ruf and Steeb, 2020a).

REFERENCES

Alber, S., Ressel, W., Liu, P., Hu, J., Wang, D., Oeser, M., Uribe, D., and Steeb, H., "Investigation of microstructure characteristics of porous asphalt with relevance to acoustic pavement performance," Int. J. Transp. Sci. Technol. **7**, 199–207 (2018).

Anas, E. M. A., Kim, J. G., Lee, S. Y., and Hasan, M. K., "Comparison of ring artifact removal methods using flat panel detector based CT images," Biomed. Eng. Online **10**, 72 (2011).

Industrial X-Ray Computed Tomography, edited by Carmignato, S., Dewulf, W., and Leach, R. (Springer International Publishing, 2018).

Cnudde, V. and Boone, M. N., "High-resolution X-ray computed tomography in geosciences: A review of the current technology and applications," Earth-Sci. Rev. **123**, 1–17 (2013).

Delle Piane, C., Arena, A., Sarout, J., Esteban, L., and Cazes, E., "Micro-crack enhanced permeability in tight rocks: An experimental and microstructural study," Tectonophysics **665**, 149–156 (2015).

Dierick, M., Van Loo, D., Masschaele, B., Van den Bulcke, J., Van Acker, J., Cnudde, V., and Van Hoorebeke, L., "Recent micro-CT scanner developments at UGCT," Nucl. Instrum. Methods Phys. Res., Sect. B **324**, 35–40 (2014).

DIN EN ISO 15708-3, Non-destructive testing—Radiation methods for computed tomography—Part 3: Operation and interpretation, ISO 15708-3:2017 Standard, 2019.

Du, L. Y., Umoh, J., Nikolov, H. N., Pollmann, S. I., Lee, T.-Y., and Holdsworth, D. W., "A quality assurance phantom for the performance evaluation of volumetric micro-CT systems," Phys. Med. Biol. **52**, 7087–7108 (2007).

Ferrucci, M., Leach, R. K., Giusca, C., Carmignato, S., and Dewulf, W., "Towards geometrical calibration of X-ray computed tomography systems—A review," Meas. Sci. Technol. **26**, 092003 (2015).

Friedman, S. N., Fung, G. S. K., Siewerdsen, J. H., and Tsui, B. M. W., "A simple approach to measure computed tomography (CT) modulation transfer function (MTF) and noise-power spectrum (NPS) using the American college of radiology (ACR) accreditation phantom," Med. Phys. **40**, 051907-1–051907-9 (2013).

Fusseis, F., Steeb, H., Xiao, X., Zhu, W.-l., Butler, I. B., Elphick, S., and Mäder, U., "A low-cost X-ray-transparent experimental cell for synchrotron-based X-ray microtomography studies under geological reservoir conditions," J. Synchrotron Radiat. **21**, 251–253 (2014).

Granton, P., "Slant edge script," https://de.mathworks.com/matlabcentral/file exchange/28631-slant-edge-script (2010), retrieved November 19, 2019.

Gureyev, T. E. and Nesterets, Y. I., "Image quality in attenuation-based and phase-contrast-based X-ray imaging," in *Handbook of X-Ray Imaging: Physics and Technology*, Series in Medical Physics and Biomedical Engineering (CRC Press, 2018), pp. 275–307.

Jenneson, P. M., Gilboy, W. B., Morton, E. J., and Gregory, P. J., "An X-ray microtomography system optimised for the low-dose study of living organisms," Appl. Radiat. Isot. **58**, 177–181 (2003).

Kotwaliwale, N., Singh, K., Kalne, A., Jha, S. N., Seth, N., and Kar, A., "X-ray imaging methods for internal quality evaluation of agricultural produce," J. Food Sci. Technol. **51**, 1–15 (2011).

Landis, E. N. and Keane, D. T., "X-ray microtomography," Mater. Charact. **61**, 1305–1316 (2010).

Maire, E. and Withers, P. J., "Quantitative X-ray tomography," Int. Mater. Rev. **59**, 1–43 (2013).

Marshall, N. W. and Monnin, P., "Physical image quality evaluation of X-ray detectors for digital radiography and mammography," in *Handbook of X-Ray Imaging: Physics and Technology*, Series in Medical Physics and Biomedical Engineering (CRC Press, 2018), pp. 469–506.

Masschaele, B., Dierick, M., Loo, D. V., Boone, M. N., Brabant, L., Pauwels, E., Cnudde, V., and Hoorebeke, L. V., "HECTOR: A 240 kV micro-CT setup optimized for research," J. Phys.: Conf. Ser. **463**, 012012 (2013).

Mizutani, R. and Suzuki, Y., "X-ray microtomography in biology," Micron **43**, 104–115 (2012).

Musialak, J., "Experimentelle untersuchungen des mechanischen verhaltens heterogen gesättigter speichergesteine," M.S. thesis, Ruhr-Universität Bochum, Institute of Computational Engineering, Chair of Continuum Mechanics, 2013.

Rit, S., Oliva, M. V., Brousmiche, S., Labarbe, R., Sarrut, D., and Sharp, G. C., "The reconstruction toolkit (RTK), an open-source cone-beam CT reconstruction toolkit based on the insight toolkit (ITK)," J. Phys.: Conf. Ser. **489**, 012079 (2014).

Rossmann, K., "Point spread-function, line spread-function, and modulation transfer function," Radiology **93**, 257–272 (1969).

Ruf, M. and Steeb, H. (2020a), "micro-XRCT data set of an *in-situ* flow experiment with an X-ray transparent flow cell," DaRUS, https://doi.org/10.18419/DARUS-691.

Ruf, M. and Steeb, H. (2020b), "micro-XRCT data set of Carrara marble with artificially created crack network: fast cooling down from 600 °C," DaRUS, https://doi.org/10.18419/DARUS-682.

Ruf, M. and Steeb, H. (2020c), "micro-XRCT data set of open-pored asphalt concrete," DaRUS, https://doi.org/10.18419/DARUS-639.

Handbook of X-Ray Imaging: Physics and Technology, Series in Medical Physics and Biomedical Engineering, edited by Russo, P. (CRC Press, 2018).

Sarout, J., Cazes, E., Delle Piane, C., Arena, A., and Esteban, L., "Stress-dependent permeability and wave dispersion in tight cracked rocks: Experimental validation of simple effective medium models," J. Geophys. Res.: Solid Earth **122**, 6180–6201, https://doi.org/10.1002/2017jb014147 (2017).

Schindelin, J., Arganda-Carreras, I., Frise, E., Kaynig, V., Longair, M., Pietzsch, T., Preibisch, S., Rueden, C., Saalfeld, S., Schmid, B., Tinevez, J.-Y., White, D. J., Hartenstein, V., Eliceiri, K., Tomancak, P., and Cardona, A., "Fiji: An

open-source platform for biological-image analysis," Nat. Methods **9**, 676–682 (2012).

Schindelin, J., Rueden, C. T., Hiner, M. C., and Eliceiri, K. W., "The ImageJ ecosystem: An open platform for biomedical image analysis," Mol. Reprod. Dev. **82**, 518–529 (2015).

Schneider, C. A., Rasband, W. S., and Eliceiri, K. W., "NIH image to ImageJ: 25 years of image analysis," Nat. Methods **9**, 671–675 (2012).

Schoeman, L., Williams, P., du Plessis, A., and Manley, M., "X-ray micro-computed tomography (μCT) for non-destructive characterisation of food microstructure," Trends Food Sci. Technol. **47**, 10–24 (2016).

Schüler, T., Jänicke, R., and Steeb, H., "Nonlinear modeling and computational homogenization of asphalt concrete on the basis of XRCT scans," Constr. Build. Mater. **109**, 96–108 (2016).

Stock, S. R., *MicroComputed Tomography: Methodology and Applications* (CRC Press, 2008a).

Stock, S. R., "Recent advances in X-ray microtomography applied to materials," Int. Mater. Rev. **53**, 129–181 (2008b).

van Aarle, W., Palenstijn, W. J., Cant, J., Janssens, E., Bleichrodt, F., Dabravolski, A., De Beenhouwer, J., Batenburg, K. J., and Sijbers, J., "Fast and flexible X-ray tomography using the ASTRA toolbox," Opt. Express **24**, 25129 (2016).

Vinci, C., Renner, J., and Steeb, H., "On attenuation of seismic waves associated with flow in fractures," Geophys. Res. Lett. **41**, 7515–7523, https://doi.org/10.1002/2014gl061634 (2014).

Vlassenbroeck, J., Dierick, M., Masschaele, B., Cnudde, V., Van Hoorebeke, L., and Jacobs, P., "Software tools for quantification of X-ray microtomography at the UGCT," Nucl. Instrum. Methods Phys. Res., Sect. A **580**, 442–445 (2007).

Wang, H., Ding, Y., Liao, G., and Ai, C., "Modeling and optimization of acoustic absorption for porous asphalt concrete," J. Eng. Mech. **142**, 04016002 (2016).

Weiß, D., Shi, Q., and Kuhn, C., "Measuring the 3D resolution of a micro-focus X-ray CT setup," in 4th Conference on Industrial Computed Tomography (iCT), Wels, Austria, 19–21 September 2012.

Yang, K., Kwan, A. L. C., Miller, D. F., and Boone, J. M., "A geometric calibration method for cone beam CT systems," Med. Phys. **33**, 1695–1706 (2006).

Chapter II:
Effects of Thermal Treatment on Acoustic Waves in Carrara Marble

Effects of thermal treatment on acoustic waves in Carrara marble☆

Matthias Ruf [a,*], Holger Steeb [a,b]

[a] *University of Stuttgart, Institute of Applied Mechanics (CE), Pfaffenwaldring 7, Stuttgart, D-70569, Germany*
[b] *University of Stuttgart, SC SimTech, Pfaffenwaldring 5a, Stuttgart, D-70569, Germany*

A B S T R A C T

Many physical processes in the field of rock physics are influenced by the presence of fractures and microcracks. Therefore, intact rock samples are often used for reproducible experimental studies, and cracks are artificially created by various methods. For this, one possibility is the use of thermal treatments. In this work, twelve different thermal treatments are experimentally studied for dry Bianco Carrara marble under ambient conditions. The focus is primarily on the influence of the cooling rate (slow versus fast cooling) in combination with different applied maximum temperatures. This also raises the question of the influence of the specimen size, which has never been systematically investigated in this context before. Therefore, three sizes of cylindrical core samples are investigated to identify a potential specimen size effect. As effective quantities on the core-scale, the bulk volume, the bulk density, and the P- and S-wave velocities, including shear wave splitting, are examined. To obtain a three-dimensional insight into the mechanisms occurring on the micro-scale level, micro X-ray Computed Tomography (μXRCT) imaging is employed. For both cooling conditions, with increasing maximum temperature, the bulk volume increases, the propagation velocities significantly drop, and shear wave splitting increases. This behavior is amplified for fast cooling. The bulk volume increase is related to the initiated crack volume as μXRCT shows. Based on comprehensive measurements, a logarithmic relationship between the relative bulk volume change and the relative change of the ultrasound velocities can be observed. Although there is a size effect for fast cooling, the relationship found is independent of the specimen size. Also the cooling protocol has almost no influence. A model is derived which predicts the relative change of the ultrasound velocities depending on the initiated relative bulk volume change.

1. Introduction

Bianco Carrara marble is a popular crystalline rock and frequently used in experimental rock physics to study different physical phenomena, cf. e.g. Refs. 2–12. Reasons are its high mineral purity, consisting of 98% calcite,[4] the low porosity of 0.7%,[13] combined with its almost isotropic and homogeneous mechanical behavior on the macroscopic level. All resulting in a very reproducible material for experimental rock studies which was already suggested in 1964 based on a petrofabric analysis of Carrara marble.[14]

Carrara marble is not only used in its virgin state under ambient conditions but often modified in its microstructure by mechanical or thermal treatments. Both with the aim to initiate microfractures (microcracks). The terms microfractures and microcracks will here be used synonymously as in Refs. 15, 16. The low porosity combined with the nearly mono-mineral composition allows the almost pure study of how microcracks affect the mechanical and hydro-mechanical properties on the macro-scale. Besides the initiation of microcracks by

a mechanical load, used, for instance, for the experimental verification of Hudson's theory,[2] the second possibility is to subject the specimens to a thermal treatment.[3,9,12] Here, in the simplest case, the specimens are heated-up to a specific maximum temperature, which is held for a certain period until a uniform temperature distribution is ensured. Afterward, the specimens are cooled back to room temperature. In principle, various cooling protocols are available. However, the two extreme cases are to perform the cooling very slowly, for instance, in the switched-off but still closed oven, or very fast, for instance, by quenching the sample in water. For the latter, the term thermal shock is frequently used.[17] In both cases, the creation of microcracks can be observed. Recent developments and new investigation methods in the field of experimental rock physics have led to a renewed interest in thermal treatments for the initiation of cracks in Carrara marble.[9,12,18] Also in other research areas dealing with the physical weathering of Carrara marble, artificially aging by thermal treatment cycles is still of interest.[19–21] In a recent work,[18] among other crustal rocks, Carrara

---

marble was investigated in regard to its elastic and electrical properties in relation to a varying degree of microfracturing. The microfracturing was achieved by applying different heat protocols (different maximum temperatures) and a slow cooling down (overnight) inside the oven. The effect of rapid cooling instead of slow cooling was not studied and no statistics were considered. Since also thermal shock is a frequently used cooling method,[9,12] the question arise how the nature of the initiated cracks and their effect on the macroscopic properties differs. Although recent studies exist for other rock types, e.g., granite[22–24] and the therein cited literature, a systematic investigation for marble, in particular Carrara marble, does not exist.

The presented research explores, for the first time, as far as the authors know, the different effects of a slow cooling procedure compared to a fast cooling for dry Carrara marble under ambient conditions in a systematic approach. As maximum temperatures the range from $100\,°C$ to $600\,°C$ in $100\,K$ increments is investigated. Further, the influence of the specimen size is taken into account to see if a size effect exists. For this, cylindrical core samples of three different sizes but with the same aspect ratio are investigated. To quantify how the samples are affected by the corresponding thermal treatment on the macro-scale, the bulk volume, the bulk density, as well as P- and S-wave velocity changes are related to the properties before the thermal treatment was applied. For S-wave propagation, shear wave splitting is taken into account to see if a possible anisotropy is caused by the thermal treatments. The results are linked to the changes on the micro-scale in a phenomenological qualitative manner by employing micro X-ray Computed Tomography (μXRCT) scans of sub-volumes of selected samples. This allows a three-dimensional (3d) insight into the modified microstructure. From the numerous characterizations, it can be followed that almost independent of the applied cooling procedure and independent of the sample size a logarithm relationship between the relative bulk volume change and the relative change of the ultrasonic velocities exists. This result is the basis of a new model predicting evolving acoustic velocities based on relative bulk volume changes. Moreover, it is discussed how the different thermal treatments are related to each other.

2. Materials and methods

2.1. Thermal treatments and samples preparation

As main geometry, cylindrical core samples with a diameter $d = 29\,mm$ and a length $l = 72.5\,mm$ were used. To study a potential size effect, two further specimen sizes were considered. The second sample size has a diameter of $d = 12\,mm$ and a length of $l = 30\,mm$ and the third one has a diameter of $d = 48\,mm$ and a length of $l = 120\,mm$. Thus, all three sample geometries have an identical aspect ratio of $l/d = 2.5$. The specimen sizes were defined with the consideration that all samples can be examined with identical ultrasonic transducers (same frequency). On the one hand, this limits the minimal sample diameter, and on the other, the maximal possible sample length. The medium-sized samples were extracted from two Carrara marble blocks with a thickness of $80\,mm$ and the small ones from one block with a thickness of $40\,mm$ by water-cooled diamond drilling. Drilling orientation of all samples was chosen identical. The large samples were taken from another block with a thickness of $125\,mm$. Again by water-cooled diamond drilling but with a different drilling orientation compared to the other ones. To ensure a perfect cylindrical geometry, the samples were reworked to the final size specified above employing a lathe.

After the initial characterization of the untreated cores, the samples were subjected to different thermal treatments. Treatments involve three steps: (1) Heating-up from room temperature to the maximum temperature T_{max} with a constant, relatively low heating rate to avoid bigger temperature gradients inside the samples. (2) Holding of T_{max} for a certain period to achieve a uniform temperature distribution inside the samples. (3) Cooling the samples back to room temperature ($\approx 20\,°C$) with a certain cooling protocol.

To cover the entire temperature range from room temperature up to a temperature of $600\,°C$ where the decomposition of calcite significantly begins,[25] we used as maximum temperatures T_{max} in our study $100\,°C$, $200\,°C$, $300\,°C$, $400\,°C$, $500\,°C$ and $600\,°C$. For the cooling procedures, we distinguish between the two extremes of "slow" and "fast" cooling. Slow cooling was performed in the switched-off but still closed oven and fast cooling by quenching the samples in a big water basin filled with water at room temperature ($\approx 20\,°C$). All remaining parameters were set constant. The heating rate was set to $3\,K\,min^{-1}$ and the subsequent holding time for T_{max} was set to $120\,min$ as in Refs. [9, 12]. The latter ensures a uniform temperature distribution in the whole sample. It is noted, that this is a conservative value and almost after a significantly shorter holding period a uniform temperature distribution is achieved as can be shown, for instance, by a vague estimation of the characteristic thermal diffusion time. The resulting 12 different thermal treatment profiles, based on the temperature inside the furnace chamber, are shown in Fig. 1. They are grouped in slow (a) and fast cooling (b) treatments. The cooling profile of slow cooling depends on the furnace insulation. At least, if the cooling rate cannot be controlled, as in our case, in the employed laboratory chamber furnace *Carbolite CWF 11/5 + 301 Controller* from Carbolite Gero GmbH & Co. KG, Germany. The highest maximum cooling gradient in amounts occurs directly after switching-off and is about $6.13\,K\,min^{-1}$ for $T_{max} = 600\,°C$. However, compared to the cooling gradient emerging in water quenching which is several orders of magnitude higher, this is extremely low, cf. Fig. 8. In the following, we use the value of T_{max} in degree Celsius followed by the term "slow" or "fast", indicating the applied cooling procedure, to refer to the different thermal treatments. It should be mentioned, that a temperature overshot after the transition from the heating-up to the holding phase can be observed, cf. Fig. 1. After few oscillations, the setpoint of T_{max} is finally reached. This could slightly influence the results of the samples subjected to lower maximum temperatures ($100\,°C$ and $200\,°C$) since the relative influence is here more significant.

To obtain statistical significance, three samples per thermal treatment for the medium-sized sample geometry were analyzed resulting in 36 samples. Besides, three additional samples were left untreated, which may be used for future reference purposes. For the small and large sample geometry, statistics were not taken into account and only one sample per thermal treatment was prepared, resulting in 12 samples for all thermal treatments. One more sample was left untreated for the same reason as for the medium-sized ones. To refer to the different samples, we use the following key: the thermal treatment, cf. Fig. 1, the value of the nominal diameter in millimeter, and a continuous sample number for the specific thermal treatment. All samples were investigated in the dry state and under ambient (laboratory) conditions. Further, classical oven drying was deliberately not done to avoid any potential influence. Instead, all samples were dried for several days under ambient conditions between the different steps of the measurement workflow.

2.2. Experimental characterization

To systematically study the effects of the different thermal treatments, each sample was characterized before and after the respective thermal treatment. As properties, the bulk volume, the bulk density, and the P- & S-wave propagation velocities in axial direction were determined based on direct measurements of the sample diameter, length, and mass, as well as ultrasonic signal data. In addition, selected samples were scanned by μXRCT imaging. All measurements were performed under ambient (laboratory) conditions. To distinguish between the moment of the measurements, we introduce the superscript "(0)" for the measurements before the thermal treatment, and the superscript "(1)" for the measurements after. The measurement procedures and the calculation of the used derived physical quantities are described briefly in the following. For further details see Appendix A.
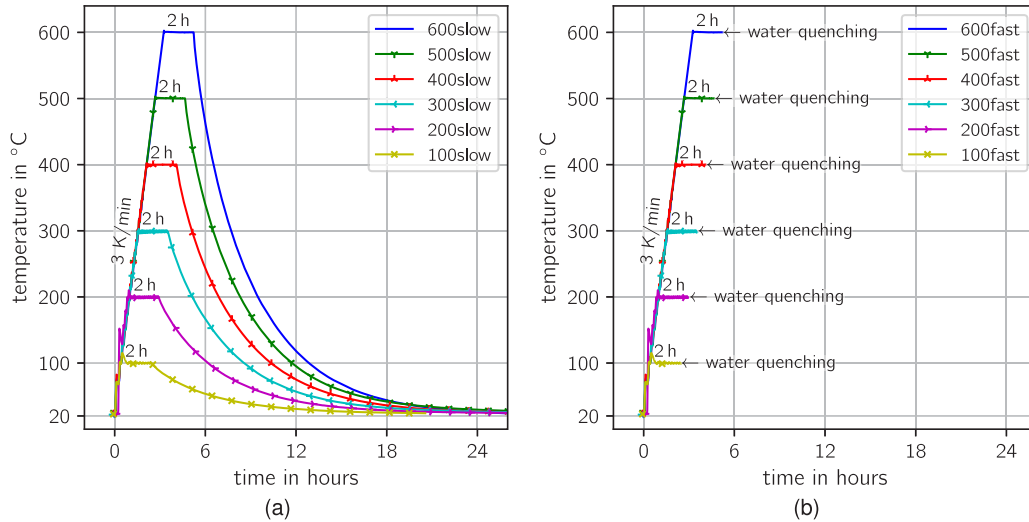
Fig. 1. Illustration of the 12 studied thermal treatments based on the logged oven temperature. Investigated maximum temperatures $100\,°C$, $200\,°C$, $300\,°C$, $400\,°C$, $500\,°C$ and $600\,°C$. Identical heating rate of $3\,K\,min^{-1}$ and holding time of $120\,min$ at maximum temperature. (a) Slow cooling. (b) Fast cooling.

For the determination of the bulk volume V and the bulk density ρ, a perfect cylindrical shape of the samples was assumed. This allows to use the sample diameter d and length l to calculate the bulk volume given by $V = (\pi/4)d^2l$. Together with the sample mass m, the bulk density follows by $\rho = m/V$. The underlying diameter and length were measured with micrometer calipers having a precision of $0.001\,mm$ except the length of the large samples which was measured with a caliper of $0.01\,mm$ precision. For measuring the mass of the medium-sized and large samples, a balance with a precision of $0.1\,g$ was employed. The mass of the small ones was measured with a balance having a precision of $0.001\,g$. All measurements were repeated three times and the subsequent steps were performed with the respective mean values.

The P- and S-wave velocities v_P and v_S in axial sample direction were determined using the ultrasonic through-transmission method. For measuring the P-wave velocities, two *Karl Deutsch S 12 HB 1* ultrasonic contact transducers were used, and for the S-wave velocities, a pair of *Olympus V153-RB* ones. Both transducer pairs are designed for an operating frequency of $1.0\,MHz$. The corresponding wavelengths are given by the ratio of the measured ultrasonic speeds (v_P or v_S) and the transducer frequency. For expected velocities between $6000\,m\,s^{-1}$ to $1000\,m\,s^{-1}$, the wavelengths should be in the range of $6\,mm$ to $1\,mm$. Compared to the mean grain size diameter of Carrara marble in the range of $150\,\mu m$ to $230\,\mu m$,[4,26] hence, we are in the large wavelength regime. Since the focus of this work is on the comparative characterization of different thermal treatments, velocity dispersion is not studied.

To identify a possible induced anisotropy, shear wave splitting was taken into account as done, for instance, in Refs. [2, 27]. This means, that by polar measurements a potentially existing shear wave splitting was identified, and in the positive case, the velocities $v_{S,1}$ and $v_{S,2}$ of the faster and the slower traveling S-wave determined. To quantify the state of anisotropy, Thomsens's anisotropy parameter

$$\gamma = \frac{1}{2}\left(\frac{v_{S,1}^2}{v_{S,2}^2} - 1\right) \tag{1}$$

is introduced[28] and used in the same manner as in Ref. [27]. If no variation of the velocity v_{S_i} over the polarization angle φ_i can be observed, it follows $\gamma = 0$. This is typically for an isotropic homogeneous medium where no shear wave splitting occurs. Since the anisotropy effects of the reference samples (virgin state) were insignificant ($v_{S,1} \approx v_{S,2}$), isotropy was assumed in this state. Hence, for all remaining samples

in the untreated state, the S-wave velocity was determined under an arbitrary angle.

To get an understanding how the microstructure is affected by the different thermal treatments, and in particular to observe the resulting differences between the slow and the fast cooling, μXRCT imaging was performed. The following three extreme conditions were considered: virgin state, 600slow, and 600fast. Since we are interested in expected small features, also the samples must be small enough to achieve suitable results. For this, from twin samples (diameter $d = 30\,mm$, length $l = 80\,mm$) which were subjected to exactly the same thermal treatment, core samples with a diameter of $5\,mm$ and a length of about $10\,mm$ were extracted and scanned. For the scans, the μXRCT system presented in Ref. 29 was employed. Further details about the scan settings can be found in A.2 of the Appendix. The resulting reconstructed data sets display physical volumes of $5.88\,mm \times 5.88\,mm \times 4.278\,mm$ using a uniform voxel size of $2.0\,\mu m$ ($2940 \times 2940 \times 2139$ voxel). Hence, the extracted samples were be scanned over the entire diameter. In axial direction, it was focused on the middle part of the $10\,mm$ long subsamples.

3. Results

The results of the absolute values for the determined density ρ, the P-wave velocity v_P as well as the S-wave velocity v_S, rather $v_{S,1}$ and $v_{S,2}$, of each sample, before and after the respective thermal treatment, can be found in Appendix C. Table 2 contains the results for the medium-sized samples, Table 3 for the small ones, and Table 4 for the large samples. From the descriptive statistic of the properties of the untreated samples, classified according to the used raw material blocks, it can be followed that they show only a slight variation within one block, cf. Table 5. Consequently, the four investigated Carrara marble blocks can be considered almost homogeneous. This substantiates the macroscopic homogeneous properties of Carrara marble listed in the introduction. Also, the variation in between the different used blocks is minor. Thus, the requirements of the aimed investigation are given.

To examine the influence of the different employed thermal treatments, in the following, the results are mainly presented as relative changes. This means that the absolute measured value differences between the two sample states are related to the corresponding measured values in the untreated sample. This eliminates the effect of minor variations in the absolute quantities. For details about the definition of the relative changes, see Appendix B. For the medium-sized sample
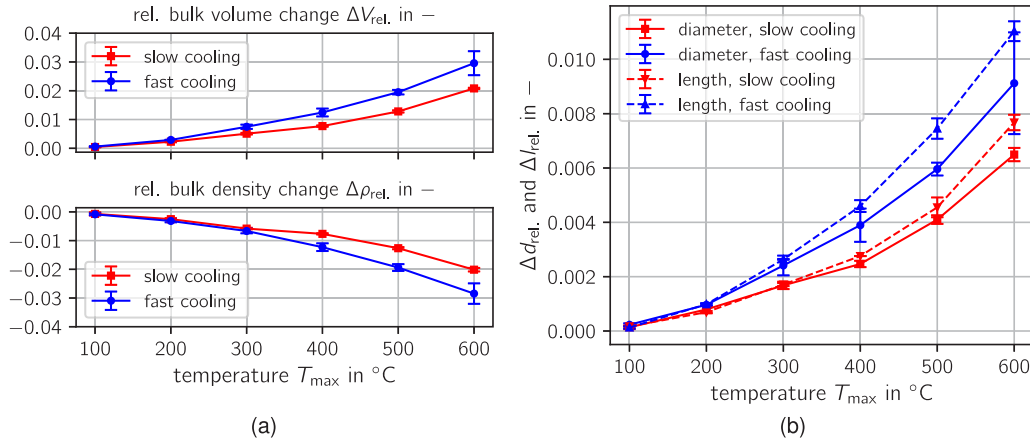
Fig. 2. Remaining deformation under ambient conditions for the medium-sized samples after the applied thermal treatments. (a) Bulk volume and bulk density change. (b) Length and diameter change.
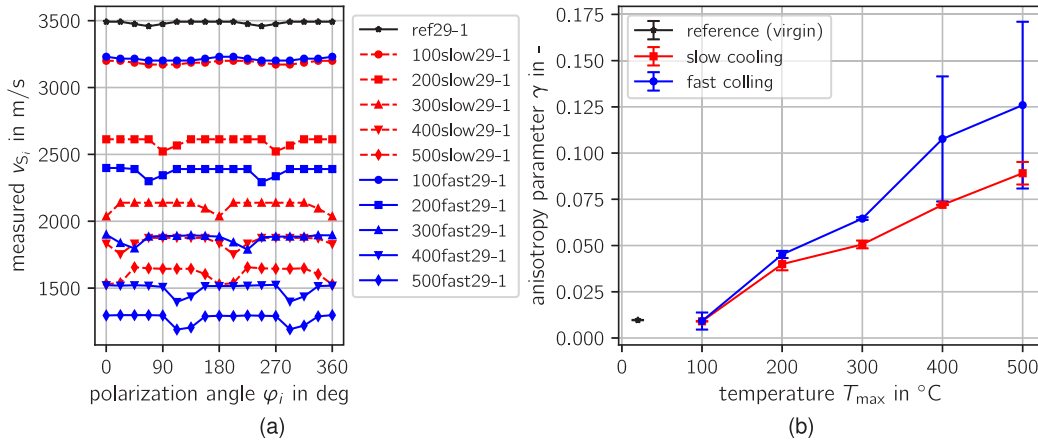

Fig. 3. Influence of the applied thermal treatment on the shear wave velocity and the related shear wave splitting for the medium-sized samples. (a) Polar shear wave velocity measurements to determine the fast and the slow shear wave velocities. (b) Thomsen's anisotropy parameter γ based on the shear wave split.

geometry, the mean value and the standard deviation of the underlying three samples per thermal treatment are used as descriptive statistic measures. In all plots following, we employ red lines to refer to the slow cooling treatments and blue lines to refer to the fast cooling treatments. We start with the results of the medium-sized samples, since for these, with three specimens per thermal treatment, statistic deviations were considered, represented as standard deviations in the plots.

3.1. Medium-sized samples

3.1.1. Bulk volume and bulk density change

In Fig. 2(a) the relative change of the bulk volume and bulk density based on the underlying diameter, length, and mass measurements for the different thermal treatments is presented. For both groups of thermal treatments, a remaining bulk volume increase with an increasing peak temperature of the respective thermal treatment can be observed. The bulk volume increase is equivalent to a reduction of the bulk density. It already occurs significantly for the slow cooling and is strengthened in case of a fast cooling procedure. The error bars illustrate a greater variation of the results for the fast cooling procedure compared to the slow cooling procedure. This can be explained by the manual performed quenching protocol. The relationship just described also applies to the underlying relative changes of the diameter and length, shown in Fig. 2(b). However, it is unexpected that the relative change of the length is systematically greater than the relative change of the diameter. Moreover, the difference increases with the maximum temperature.

3.1.2. Elastic wave propagation

Before considering the relative velocity changes, the possible anisotropic mechanical behavior perpendicular to the wave propagation direction is quantified. For this, for all samples, the shear wave speed under different polarization angles was measured, cf. Section 2.2 and Appendix A.1 in Appendix. The absolute measuring results against the polarization angle are exemplarily shown for one sample of each thermal treatment in Fig. 3(a). There is a clear connection between the considered polarization angle and the resultant shear wave speed. Already the untreated sample shows slightly this behavior. This is evidence that the raw material is slightly anisotropic perpendicular to the wave propagation direction. Since the anisotropy in the virgin state is comparatively low, this was neglected for the rest of the samples in the initial measurements. From the polar representation, we obtain the propagation velocities of the fast and the slow S-wave, $v_{S,1}$ and $v_{S,2}$, which are used to determine Thomsen's anisotropy parameter according to Eq. (1). The results are shown in Fig. 3(b). Although the absolute difference between $v_{S,1}^{(1)}$ and $v_{S,2}^{(1)}$ does not increase significantly above a temperature of about 300 °C, cf. the corresponding maxima and minima in Fig. 3(a), Thomsen's anisotropy parameter increases almost linearly over the entire temperature range. This is a result of the strong decrease of the wave velocities with the maximum applied temperature. Consequently, the almost isotropic mechanical properties of Carrara marble in the virgin state are not preserved after a thermal treatment with peak temperatures over 100 °C.

In Fig. 4(a) the results of the relative P-wave velocity changes $v_{P,rel.}$ as well as the S-wave velocity changes $v_{S,1,rel.}$ and $v_{S,2,rel.}$ are
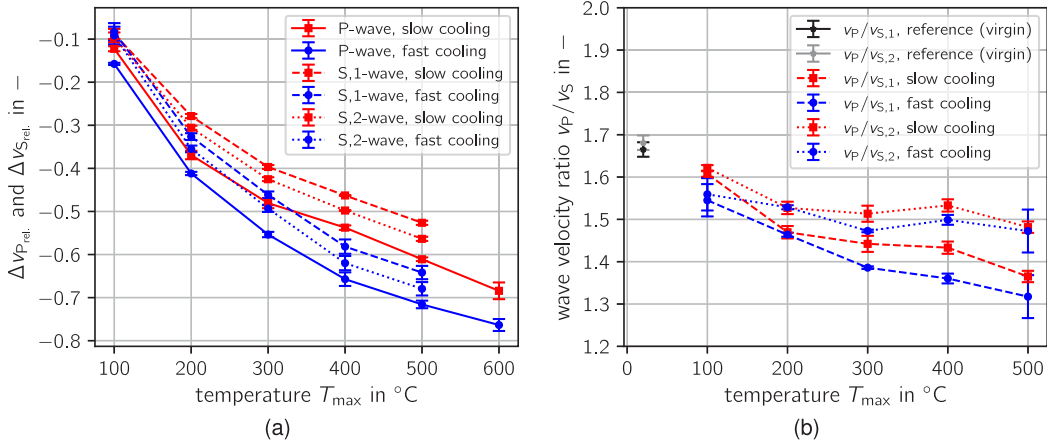
Fig. 4. Influence of the applied thermal treatment on the P- and S-wave velocity for the medium-sized samples.
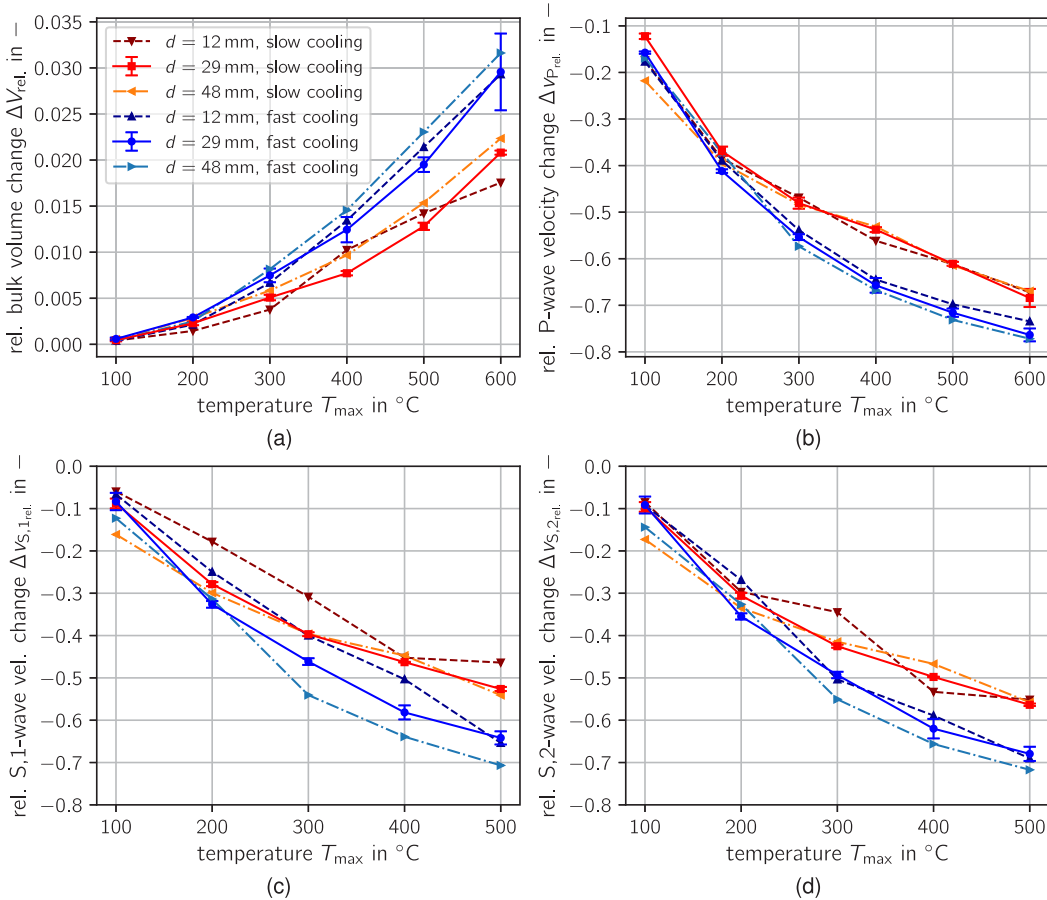

Fig. 5. Comparison of the specimen size influence on the effective properties for the different thermal treatments. (a) Relative bulk volume change. (b) Relative P-wave velocity change. (c) Relative S,1-wave velocity change. (d) Relative S,2-wave velocity change. (For interpretation of the references to color in this figure legend, the reader is referred to the web version of this article.)

presented. As already observed for the bulk volume/density change, there is a directly nonlinear correlation with the applied maximum temperature of the thermal treatment. Here, the greater the applied maximum temperature, the greater the reduction of the wave velocities. Over the entire temperature range, the P-wave propagation velocity decrease is slightly greater than the S-wave propagation velocity. For the highest applied temperature of 600 °C the P-wave speed reduction is about 76% (68%) in average for the fast cooling (slow cooling) method. This means that the absolute P-wave speed of about 5.8 km s^{-1} in the virgin sample drastically dropped to 1.4 km s^{-1} (1.8 km s^{-1}) after the

corresponding heat treatment. The difference of the relative changes between the cooling methods is up to 350 °C depending on the peak temperature and above more or less constant. In Fig. 4(b) the ratio of $v_P^{(1)}/v_{S,1}^{(1)}$ and $v_P^{(1)}/v_{S,2}^{(1)}$ over the maximum temperature is plotted. With increasing temperature, the ratio decreases for both groups and both velocity ratios. However, the decline over the temperature depends on the considered shear wave velocity. For the fast shear wave, the decline is significantly stronger. Since the ratio decreases with higher maximum temperature, it is increasingly more difficult and even impossible to determine reliably the arrival time of the shear waves. This explains

Table 1

Identified model parameters for the fits shown in Fig. 6 based on Eq. (2).

P-wave fits	m_P	b_P	c_P	R_P^2	MSE_P
3PM – slow cooling data	−0.335073	−1.239423	0.000200	0.9810	3.49×10^{-4}
3PM – fast cooling data	−0.375262	−1.345326	0.000260	0.9922	1.98×10^{-4}
3PM – all data	−0.360492	−1.304903	0.000240	0.9826	7.12×10^{-4}
Lin. regression – all data; no (0,0)	−0.326427	−1.243458	0.000000	0.9794	7.72×10^{-4}
S,1-wave fits	$m_{S,1}$	$b_{S,1}$	$c_{S,1}$	$R_{S,1}^2$	$MSE_{S,1}$
3PM – slow cooling data	−0.377876	−1.231739	0.000550	0.9799	3.49×10^{-4}
3PM – fast cooling data	−0.469200	−1.448040	0.000820	0.9754	1.98×10^{-4}
3PM – all data	−0.444088	−1.385192	0.000760	0.9701	7.12×10^{-4}
Lin. regression – all data; no (0,0)	−0.319990	−1.142914	0.000000	0.9511	1.13×10^{-3}
S,2-wave fits	$m_{S,2}$	$b_{S,2}$	$c_{S,2}$	$R_{S,2}^2$	$MSE_{S,2}$
3PM – slow cooling data	−0.371451	−1.258185	0.000410	0.9798	2.15×10^{-4}
3PM – fast cooling data	−0.478441	−1.506486	0.000710	0.9852	2.66×10^{-4}
3PM – all data	−0.442816	−1.423507	0.000610	0.9759	6.50×10^{-4}
Lin. regression – all data; no (0,0)	−0.335447	−1.212718	0.000000	0.9617	9.59×10^{-4}

why quantities utilizing the S-wave propagation velocities are only presented up to a maximum of 500 °C. In all cases, the standard deviation is low and for the slow cooled down samples again significantly less than for the fast cooled ones. The reasons are the same as already mentioned. The wavelengths are in the virgin state about 5.9 mm and 3.5 mm for the P-wave and the S-wave, respectively. Considering the extremes after the thermal treatments, they are reduced to 1.3 mm and 1.1 mm. For the higher peak temperatures, a signal gain of up to 40 dB for the P-wave measurements was required indicating a distinctive attenuation of the wave propagation. However, this observation is not investigated further within this work.

3.2. Influence of specimen size

Up to now, all shown results were based on measurements of the medium-sized samples. To identify a potential size effect, in Fig. 5 a comparison of the relative bulk volume change 5(a), the relative P-wave velocity change 5(b) as well as the relative S-wave velocity changes 5(c) and (d) for all three sample sizes is shown. The solid lines refer to the medium-sized samples ($d = 29$ mm), the dashed lines to the small ones ($d = 12$ mm), and the dash-dot lines to the large samples ($d = 48$ mm). All lines that refer to a slow cooling (fast cooling) protocol are visualized in red tones (blue tones).

The courses of all lines largely coincide with the results of the medium-sized samples. The highest differences can be observed for the relative S-wave velocity changes of the small samples. It is noted again that no statistics were considered for the small and large samples, and thus, only one sample per thermal treatment was investigated. Hence, the data of the small and large samples are not as smooth as for the medium-sized ones for which always the mean value of three samples is given. The comparison of the relative bulk volume change does not allow any conclusions to be drawn regarding a size effect. However, a clear distinction can be observed for the P-wave velocity measurements for values of T_{max} above 200 °C. For the slow cooling procedure, we obtain nearly the same results, independent of the specimen size. All dark-red/red/orange colored lines are almost on top of each other. A dependency on the specimen size occurs with fast cooling. With increasing specimen size, the P-wave velocity change is increasing, which corresponds with the brightness increase of the blue lines in the plot. The same can be observed for the S-wave velocity changes comparing the results of the large with the medium-sized samples ($d = 48$ mm versus $d = 29$ mm). In total, only two outliers (100slow and 200fast) of the large samples can be identified. In contrast, for the small samples, a systematic can only be found for the P-wave velocity changes. On the whole, it can be stated that there is an influence of the specimen size for a fast cooling protocol, while no influence is present in the case of a slow cooling protocol.

3.3. Correlation of ultrasound velocities with bulk volume changes

So far, the measurement results of the ultrasonic velocity changes and the bulk volume changes were studied separately in dependency of the applied maximum temperature of the corresponding thermal treatment. To find out if there is a relationship between the bulk volume change and the wave velocity change, in Fig. 6 all results are merged. Fig. 6(a) and (b) display the relationship for the P-wave, Fig. 6(c) and (d) for the S,1-wave and Fig. 6(e) and (f) for the S,2-wave velocities, respectively. In this representation also the influence of the observed overshot for the two lowest maximum temperatures is eliminated, cf. Fig. 1. From Fig. 6(a), (c) and (e) follows, that there might exist a logarithmic relationship in all cases. To verify this, in Fig. 6(b), (d) and (f) a semi-log scale for the bulk volume change is employed. Obviously, in all cases, all data points lie approximately on a straight line as indicated by a linear regression fit in the semi-log representation. This is evidence that regardless of the thermal treatment and the specimen size, the relative wave propagation change is significantly driven by the initiated bulk volume change. This motivates to establish a model predicting the evolution of the acoustic velocity changes based on the bulk volume changes. The fact that all data points in the semi-log plots lie approximately on a straight line motivates to employ a logarithmic model approach. Therefore, we propose for the relative P-wave and S-wave velocity changes $\Delta v_{i_{rel.}}$ with $i = \{P, S, 1, S, 2\}$, as a function of the relative bulk volume change $\Delta V_{rel.}$, following approach:

$$\Delta v_{i_{rel.}}(\Delta V_{rel.}) = m_i \log(\Delta V_{rel.} + c_i) + b_i \qquad \text{with} \qquad i = \{P, S, 1, S, 2\} \qquad (2)$$

The parameters m_i, c_i and b_i are corresponding fit parameters. Therefore, we refer to this model as the 3-Parameter Model (3PM). The parameter c_i is needed to incorporate the untreated (virgin) sample state in the logarithmic formulation since no thermal treatment corresponds to no changes of the bulk volume and the ultrasonic velocities. This known data point cannot be incorporated in the pure linear regression fit in the semi-log space. However, to take into account the entire range starting at zero bulk volume change, the consideration of this point is essential. Otherwise, the model prediction for low bulk volume changes would lead to unexpected results. The parameter m_i describes the slope of the resulting straight line in the semi-log representation when shifted by c_i and the parameter b_i the interception point with the vertical axis. The parameter identification was consequently constrained by the requirement to include the fixed point $(0,0)$. For higher bulk volume changes a slightly but systemically separation of the data points depending on the cooling procedure can be observed, cf. Fig. 6. Therefore, several fits were performed employing the following data sets: slow cooling, fast cooling, and all data points. The model parameters were determined using a classical least-squares approach. The resulting parameters together with the coefficients of determination R_i^2, as well as the Mean Squared Error MSE_i for the different regressions are
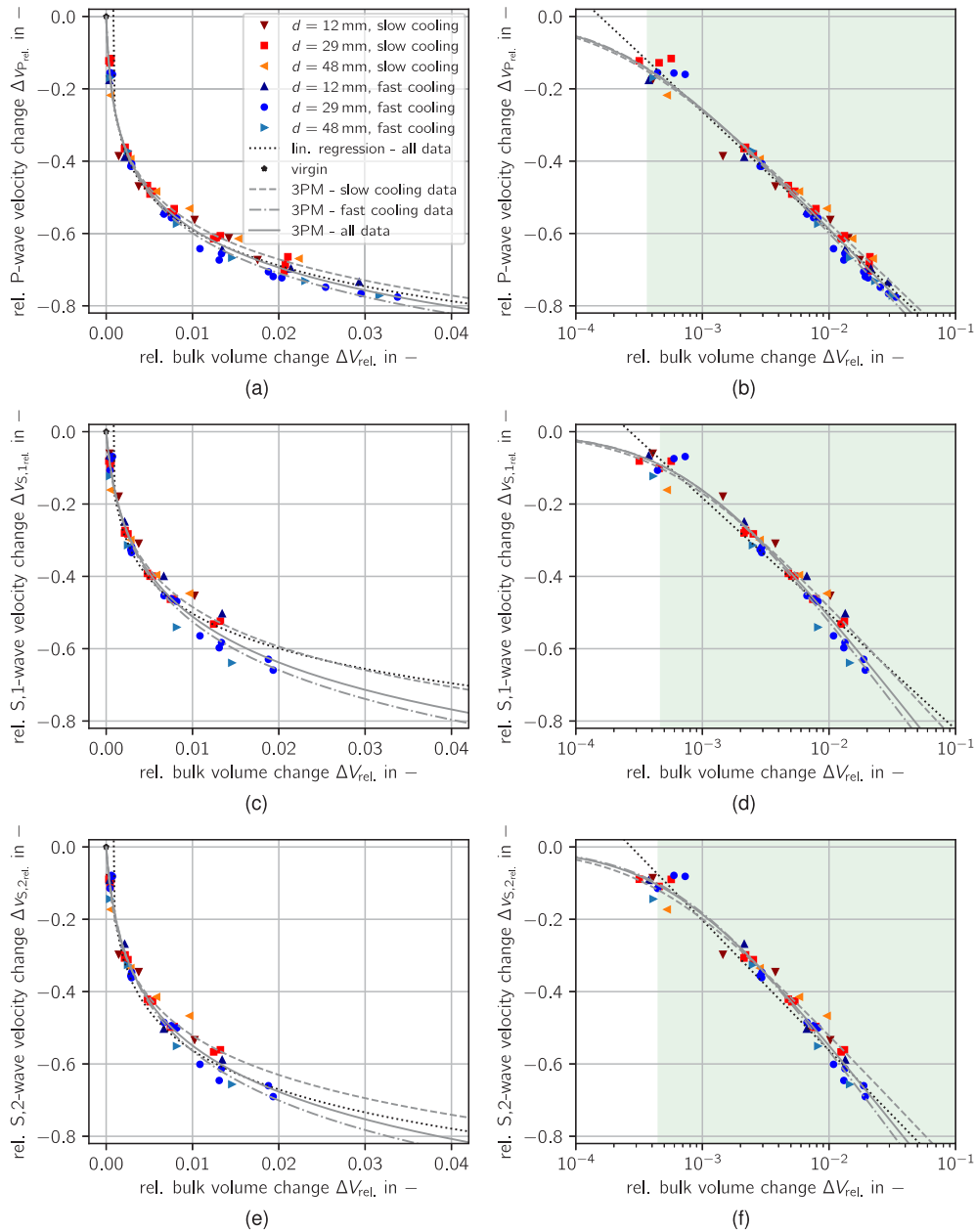
Fig. 6. Relative wave propagation velocity change as a function of the relative bulk volume change and fitted models. (a), (b) Relative P-wave velocity change. (c), (d) Relative S,1-wave velocity change. (e), (f) Relative S,2-wave velocity change. The green area indicates the area, where the error between the "3PM – all data" and the "Lin. regression – all data" is less than 15%. (For interpretation of the references to color in this figure legend, the reader is referred to the web version of this article.)

summarized in Table 1. Also the determined parameters of the linear regression fits in the semi-log space are listed where the parameter c_i vanishes ($c_i = 0$).

As can be followed from Fig. 6 in combination with the coefficients of determination, the optimized models can reproduce the underlying data well. Using the specific data sets results in a slightly improved fit than employing all data points. This can be observed in the plots as well as in the related coefficients of determination. Up to a bulk volume change of about 0.5%, there is no significant difference of the fits in between the cooling procedures. For the border data points in terms of the maximum bulk volume change, the relative error by using the model fitted for all data points instead of the specif one is less than 2.9% for the P-wave model and less than 4.7% for the S,1/S,2-wave models. In Fig. 6(b), (d) and (f) the region is highlighted, where the relative error between the 3PM and the linear regression is less than 15%. This

corresponds to relative bulk volume changes greater than 3.7×10^{-4} (0.037%) for the P-wave velocity changes and 4.7×10^{-4} (0.047%) for the S-wave velocity changes. For reasons of simplicity, in this regime also a prediction based on the linear regression fit can be justifiable. In Appendix D we present an alternative model approach also having just two fitting parameters but which can be used for the whole range of investigated relative bulk volume changes with just slightly worse metrics than the here presented 3-parameter model.

Based on the models given by Eq. (2) and the related optimized parameters in Table 1, the absolute values of the corresponding P- and S-wave velocities $v_P^{(1)}$ as well as $v_{S,1}^{(1)}$ and $v_{S,2}^{(2)}$ (abbreviated $v_{S,1/2}^{(1)}$) can be determined by

$$v_P^{(1)}(\Delta V_{rel.}) = v_P^{(0)} \left[m_P \log(\Delta V_{rel.} + c_P) + b_P + 1 \right] \qquad \text{and} \qquad (3)$$

$$v_{S,1/2}^{(1)}(\Delta V_{rel.}) = v_S^{(0)} \left[m_{S,1/2} \log(\Delta V_{rel.} + c_{S,1/2}) + b_{S,1/2} + 1 \right], \qquad (4)$$
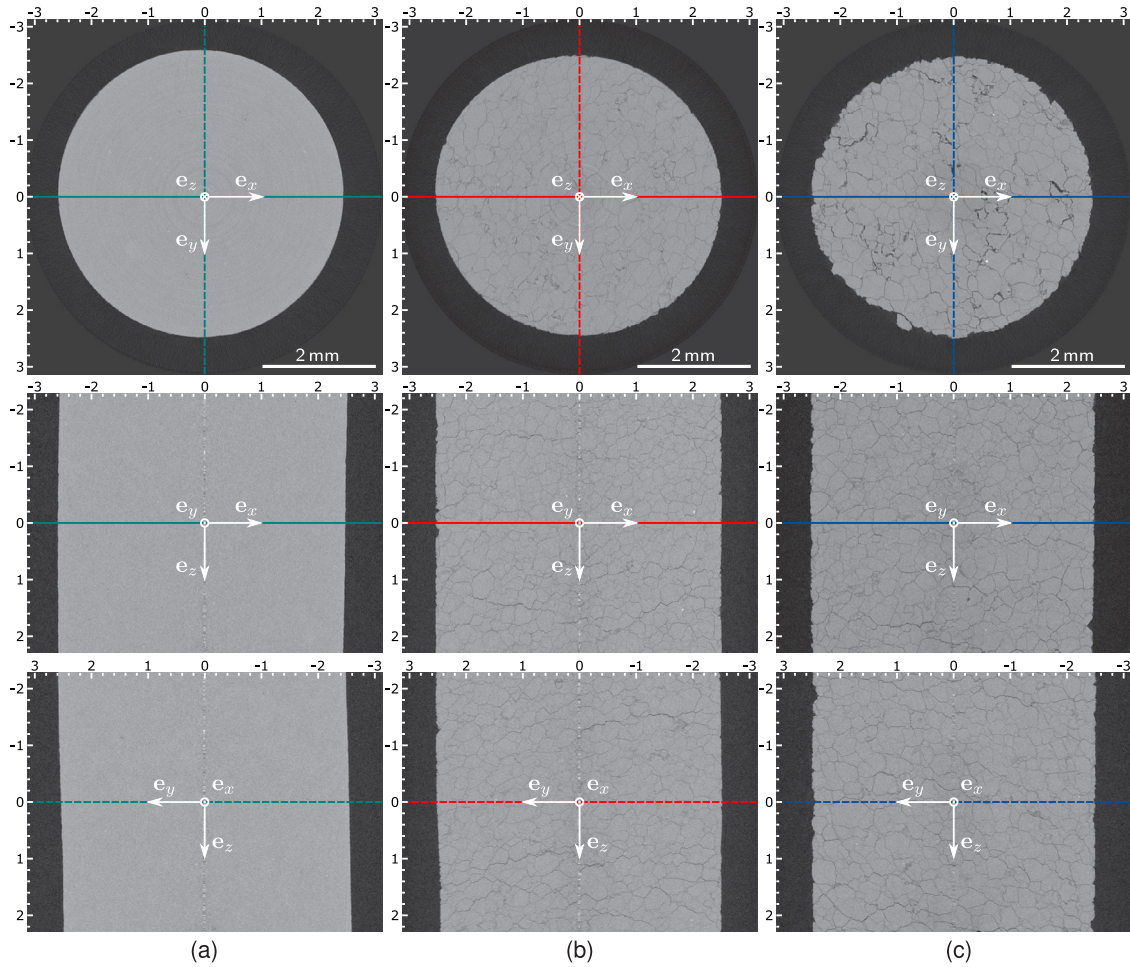
Fig. 7. Representative images (xy-, zx- and yz-section plane) from three different μXRCT data sets showing the inner structure of Carrara marble in different conditions. Coordinate units given in millimeter. (a) Virgin state. (b) $T_{\max} = 600\,°C$ and slow cooling (c) $T_{\max} = 600\,°C$ and fast cooling. The underlying data sets of (b) and (c) can be found in Refs. 31, 32; https://doi.org/10.18419/darus-754 and https://doi.org/10.18419/darus-682; licensed under a Creative Commons Attribution (CC BY) license.

employing the ultrasound velocities of the untreated samples and the relative bulk volume change. In combination with the associated modified bulk volume density

$$\rho^{(1)}(\Delta V_{\text{rel.}}) = \frac{\rho^{(0)}}{\Delta V_{\text{rel.}} + 1},\qquad(5)$$

an estimation of the dynamic elastic moduli can be done, cf. e.g. Ref. 30. The required underlying quantities in the untreated state needed for this are given by $v_{\mathrm{P}}^{(0)} = 5862\,\mathrm{m\,s^{-1}}$, $v_{\mathrm{S}}^{(0)} = 3495\,\mathrm{m\,s^{-1}}$ and $\rho^{(0)} = 2699\,\mathrm{kg\,m^{-3}}$ using the mean values of all investigated samples, cf. Table 5. Fig. 9(b,d) of Appendix C demonstrates this, showing the absolute values of the derived P-wave modulus $M = \rho\,v_{\mathrm{P}}^2$ and S-wave modulus $\mu = \rho\,v_{\mathrm{S}}^2$ for the medium-sized samples. Since the relation between the wave propagation velocities and other dynamic elastic moduli, e.g. bulk modulus, Young's modulus, Poisson's ratio, etc., is typically based on an isotropic material behavior, their application must be treated with caution. Further, only one wave propagation direction was evaluated and consequently, no statement over the overall anisotropic material behavior can be made.

3.4. Change of microstructure

In Fig. 7 the acquired μXRCT data sets of the three extreme cases are condensed by the use of three different representative cutting planes (xy-, zx- and yz-plane). The full 3d data sets of the slow, Fig. 7(b), and the fast, Fig. 7(c), cooled down samples can be found in Refs. 31, 32. In all cases, the bright gray area represents the calcite phase of

the Carrara marble. The surrounding dark gray represents air. In all scans some usual ring artifacts in the center are present. Fig. 7(a) exhibits the extremely homogeneous properties of Carrara marble in the virgin state. Apart from few inclusions and few very small pores the whole sample appears completely homogeneous. No microcracks or similar signs of damage can be identified. Due to the underlying physical principle, it is not possible to detect grain boundaries, as they do not show any difference in the attenuation coefficient. Fig. 7(b) and (c) exhibit the inner structure after the thermal treatment at the highest investigated maximum temperature of 600 °C and a subsequent slow and fast cooling. In both cases, a nearly homogeneous crack-network can be seen that crosses the entire data sets. The contrast of the crack network in Fig. 7(c) is higher, which is a result of the greater mean crack aperture in combination with the given spatial resolution of the employed system. Even if the crack networks seem to be homogeneous, individual cracks can be identified which exhibit a lager aperture than the average ones. This can be observed especially in the zx- and the yz-section plane.

4. Discussion

The μXRCT data sets in Fig. 7 show clearly the effects of the thermal treatments on the microstructure. Independent of the applied cooling method, a crack network was formed crossing the whole sample. The strictly monotonous and smooth curves in Fig. 2 in combination with the μXRCT images signal clearly that the bulk volume increase for both thermal treatments is the result of the newly created crack volume
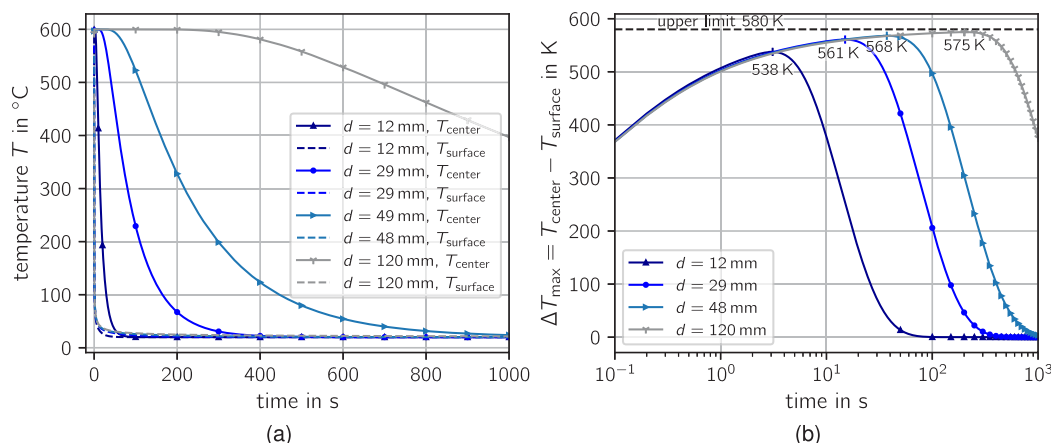
Fig. 8. Illustration of the influence of the specimen size (diameter) on the resulting temperature distribution during fast cooling. Estimation based on the analytical solution for an endless cylinder geometry with Robin boundary conditions, cf. e.g. Ref. 35. Initial temperature $T_0 = 600\,°C$, environment temperature (water basin) $T_\infty = 20\,°C$, heat transfer coefficient $h = 8000\,\text{W}\,\text{m}^{-2}\,\text{K}^{-1}$.[36] Underlying (averaged) material properties for Carrara marble: thermal conductivity $k = 1.5\,\text{W}\,\text{m}^{-1}\,\text{K}^{-1}$, density $\rho = 2700\,\text{kg}\,\text{m}^{-3}$, and specific heat capacity $c_p = 1000\,\text{J}\,\text{kg}^{-1}\,\text{K}^{-1}$, cf. Ref. 37.

and not of irreversible phase transformations. Ref. 18 inferred the same based on their investigations on thermally treated Carrara marble slowly cooled down. In this work, additionally, the bulk volume change was compared with the pore volume change (effective porosity) based on pycnometer measurements of the whole samples. Good agreement was shown for maximum temperatures up to 400 °C. For higher temperatures, a non-systematical variation could be observed. This could be due to the examination of only one sample per thermal treatment. Also the results from Ref. 33 investigating Ormea Black Marble with a comparable composition (almost pure calcite with a medium crystal size about 0.6 mm) confirm this. Therefore, we suppose that no additional remaining phase transformations occur (calcite to aragonite or vaterite, cf. e.g. Ref. 34), and the bulk volume increase is identical to the increase of the total porosity which is equal to the formed crack volume.

When we qualitatively compare Fig. 7(b) with (c), the density of cracks, meaning the crack length per unit area in 2d,[16,38] respectively the crack area per unit volume in 3d, is roughly the same. However, the mean crack aspect-ratio, defined by the ratio of the crack aperture to the crack length, in Fig. 7(c) is obviously greater. This explains the bulk volume difference of about 0.9 percent point in Fig. 2(a) for $T_{\max} = 600\,°C$, which is about 42% greater in case of the fast cooling. Consequently, there have to be two different mechanisms affecting the resulting crack volume. The question could arise why the μXRCT data sets are only evaluated in a qualitatively way and not further quantified, for instance, to determine the crack density and the mean crack aperture. This is because, even if the cracks are easy to recognize visually, it is still extremely difficult to reliably segment them, cf. Ref. 39. To exclude this kind of error source, it was deliberately avoided in this work. In μXRCT imaging it is generally challenging to resolve features with an extreme length/width aspect ratio which is typically for microcracks. On the one side, a high spatial system resolution is required to achieve accurate information about the crack aperture. On the other side, a large field of view is mandatory to have a representative volume. Especially the crack aperture in the range of a few micrometers cannot quantitatively be determined in a reliable way since the gray-scale contrast is too low due to the limited spatial resolution of the employed system. If the cracks are completely closed or have a very small aperture, it is expected that they should not be visible at all due to the typical noise in the scan data sets. This is also a further reason why samples for the μXRCT scans were used, which were treated with the highest maximum temperatures. The problem mentioned is also causal, why samples treated by lower maximum temperature were not scanned. For these, the crack opening is too small to obtain reliable information. To further investigate the influence of

the crack density and crack aspect ratio leading to the same total crack porosity, it is advisable to employ also other methods such as classical microscopy, but with the disadvantage of obtaining only 2d information and having the risk of changing the crack network during the sample preparation.

From investigations on the physical weathering of Carrara marble in the lower temperature range ($T_{\max.} \leq 80\,°C$), it is known that the anisotropic thermal expansion of the randomly oriented calcite grains and the resulting misfit strains are responsible for the initiation of cracks during the heating-up process.[21,40] If the crack closure is hindered during the cooling process, further cracks can be formed[40] or existing ones remain open. This becomes understandable if the thermal expansion of calcite is considered in more detail. Calcite has a trigonal crystal system and exhibits a temperature depending positive thermal expansion coefficient $\alpha_\parallel$ along and a negative thermal expansion coefficient $\alpha_\perp$ perpendicular to the optic axis.[41–43] In Ref. 42 equations for the thermal expansion coefficients for the temperature range from 28 °C to 524 °C were derived from experimental measurements. According to this, $\alpha_\parallel$ is in the range of $25.16 \times 10^{-6}\,\text{K}^{-1}$ to $32.40 \times 10^{-6}\,\text{K}^{-1}$, and $\alpha_\perp$ in the range of $-3.68 \times 10^{-6}\,\text{K}^{-1}$ to $-4.95 \times 10^{-6}\,\text{K}^{-1}$, which points out, that high stresses between differently oriented grains during the heating-up phase are inevitable. Since the difference between $\alpha_\parallel$ and $\alpha_\perp$ is increasing with the temperature, the mechanism known from physical weathering of Carrara marble is even heightened for higher peak temperatures as already supposed in 1934.[44] For a more detailed illustration of the mechanisms of thermal induced microcracks it is referred to Refs. 45–47. Since the calcite grain boundaries cannot be visualized by the employed imaging method, it is unclear whether the formed cracks are inter- or intragranular ones. Based on the crack initiation mechanism and the known typical mean grain sizes of Carrara marble from the literature, in the range of $\approx 150\,\mu\text{m}^4$ to $\approx 230\,\mu\text{m}$,[26] it is supposed that the major ones are intergranular cracks. However, this depends strongly on the grain-boundary toughness and the relation to other rock fabric properties as investigated by Ref. 40 for temperatures between ±50 °C. Therefore, this remains an open question. The crack initiation mechanism as a result of the anisotropy thermal expansion of the calcite grains, also explains the correlation with the applied maximum temperature and is in accordance with the results of Ref. 18, and other studies of thermally treated calcite marbles, for instance, Refs. 33, 44, 48. The resulting remaining deformation is also known as residual strain and occurs even for temperature changes of only 20 K to 50 K, cf. Ref. 21 and the therein cited literature. This explains why already for the lowest considered maximum temperature of 100 °C a relatively small bulk volume increase results in a significant change of the ultrasonic velocity. The detected difference between the

relative diameter and length change in Fig. 2(b) can only be the result of an underlying preferential oriented texture, which in general should be weak or non-existent for Carrara marble[21] but is not uncommon.[49]

The mechanism described above explains the crack initiation process in the case of both groups of thermal treatments since it is in principle independent of the cooling procedure. However, in the case of a subsequent fast cooling, there is a second mechanism that amplifies the first one in terms of the generated crack volume as obvious from the bulk volume measurements. The underlying mechanism is well known as thermal shock and frequently happens, for instance, as an undesired effect in ceramics, cf. Ref. 50. Here, the rapid cooling results in temperature gradients leading to a non-uniform strain distribution within the sample. If the local resulting stresses exceed the material strength, cracks are formed or existing ones are propagating or opened. Whereas the first mechanism depends strongly on the material and the underlying microstructure, the second one is always present and can also be used to initiate cracks in non-crystalline materials like borosilicate glass.[51,52] The effect of thermal quenching correlates with the difference between the maximum employed temperature and the temperature of the water basin. This explains the increasing difference in terms of the bulk volume or density with increasing maximum temperature for the two different thermal treatment groups. Further, this effect depends on the specimen size since this affects the achievable temperature gradients within the sample.[50,53]

For better understanding of the specimen size effect, we roughly estimate the maximum resulting temperature difference $\Delta T_{\max}$ within the three employed specimen sizes (diameter $d = \{12, 29, 48\}$ mm), as well as for a theoretical diameter of $d = 120$ mm, hence, one order of magnitude higher than the smallest investigated sample. The maximum possible temperature difference occurring during cooling is given by the difference between the temperature in the center of the core T_{center} and on the surface T_{surface}, $\Delta T_{\max} = T_{\text{center}} - T_{\text{surface}}$ holds.[36] The maximum temperature difference within the sample gives an estimation about the maximum possible tensile stresses to expect at the sample surface. From the sample surface, typically cracks start to propagate.[17] This becomes immediately clear when we look at the one-dimensional case. Here, the maximum possible tensile stress $\sigma_{\max}$ is given by $\sigma_{\max} = E\alpha \left(T_{\text{center}} - T_{\text{surface}} \right) = E\alpha \Delta T_{\max}$ where E denotes the Young's modulus and α the thermal expansion coefficient, cf. e.g. Ref. 17. If we assume E and α are independent of the specimen size, the higher $\Delta T_{\max}$ the higher the resulting tensile stress $\sigma_{\max}$ or the underlying tensile strain $\varepsilon_{\max} = \alpha \Delta T_{\max}$. Therefore, in the further illustration, we focus on $\Delta T_{\max}$. For reasons of simplicity, we consider an endless cylinder with Robin boundary conditions during the non-stationary cooling and neglect the effects on the sample tips. To solve the initial boundary value problem, we use the analytical solution in cylindrical coordinates, cf. e.g. Ref. 35. We examine the cooling from the initial sample temperature $T_0 = 600$ °C in a water basin with temperature $T_\infty = 20$ °C and employ as heat transfer coefficient $h = 8000$ W m^{-2} K^{-1}.[36] For the required material properties, we employ average values for Carrara marble covering the examined temperature range, which are in general depending on the temperature. For the density $\rho = 2700$ kg m^{-3}, for the specific heat capacity $c_p = 1000$ J kg^{-1} K^{-1}, and for the thermal conductivity $k = 1.5$ W m^{-1} K^{-1} are set, cf. Ref. 37. The evolving temperatures (T_{center} and T_{surface}) over time are shown in Fig. 8(a) and the resulting maximum temperature difference $\Delta T_{\max}$ in Fig. 8(b). It is obvious, that the resulting maximum temperature difference $\Delta T_{\max}$ is increasing with the underlying cylinder diameter, as the given peak values in Fig. 8(b) illustrate. Consequently, higher strain differences arise, and potentially, more cracks are created, or existing ones are opened. Both explain the increasing reduction of the P-wave velocities with increasing specimen size in Fig. 5(b). The same explanation holds for the S-wave velocities in Fig. 5(c,d) (observable for the large versus medium-sized samples). The size effect cannot be identified in terms of the relative bulk volume variation, cf. Fig. 5(a). There are several possible reasons for. Firstly, it is difficult to measure the geometry with high accuracy, which

is exacerbated as the specimen size becomes smaller. This explains well the unsystematic variation of the small samples compared to the medium-sized samples. The same holds for the S-wave measurements. Secondly, for the large samples compared to the medium-sized and small samples, the drilling orientation was chosen differently. This leads to the fact that compared to the other two sample geometries, the relative diameter change is greater than the relative length change, cf. Fig. 2. Since the diameter is squared in the calculation of the bulk volume, the overall bulk volume increase is systematically larger regardless of the cooling protocol. This would explain why the orange line is not congruent with the red one in Fig. 5(a). It can be concluded that using a slow cooling protocol, the results are not affected by the specimen size. In contrast, the specimen size has a not to be neglected influence on the results in case of a fast cooling protocol. However, the effect decreases with increasing specimen size as obvious from Fig. 8(b) and observable in Fig. 5(b). It ends up when the maximum possible difference of $\Delta T_{\max} = T_0 - T_\infty = 600$ °C $- 20$ °C $= 580$ K is more or less reached.

In general, the reliable determination of the S-wave velocity becomes more difficult with increasing crack porosity. The reason for this is the almost linear decreasing P- to S-wave velocity ratio with increasing maximum temperature of the subsequent thermal treatment, cf. Fig. 4(b). The same behavior was also observed for Valdieri marble by Ref. 48. Since the transmitted pulse of the S-wave transducer always includes P-wave portions, the first arrival of the S-wave is superimposed more and more by parts of the P-wave arriving before. For a physical interpretation of the velocity ratio v_P/v_S, we consider the ideal case of isotropic material behavior. In this case, the ratio of the compression modulus K and the shear modulus μ is given by $K/\mu = (v_P/v_S)^2 - 4/3$, cf. e.g. Ref. 30. Consequently, a reduction of v_P/v_S means that the compressive stiffness decreases proportionally more than the shear stiffness. This statement also holds for the thermally treated samples, although they cannot be considered as isotropic material. From the S-wave measurements, it can be concluded that a low to non-existent elastic anisotropy in the untreated sample state will be amplified or initiated by thermal treatments and may need attention. In particular, the application of theories based on assumptions about isotropic material behavior must be used with caution, e.g. the conversation from wave propagation velocities to dynamic elastic moduli. Employing Thomsen's anisotropy parameter for the quantification of the elastic anisotropy in one direction, an approximately linear increase with the used maximum temperature results, which is steeper for the fast cooling. That implicates that the crack aspect ratio has a strong influence on the anisotropy. Due to the increasing rate of anisotropy with the maximum temperature, it is advisable to consider not only one direction for the characterization.

The necessary amplification of the receiver transducer signal of up to 40 dB for the medium-sized samples and even 59 dB for the large samples treated at higher maximum temperatures is evident that a drastic wave attenuation occurs. From the 3d microstructure visualization, it is obvious that scattering on the crack surfaces and absorption due to friction should be the causal mechanisms. The different required signal gain for the P-wave (up to 40 dB) and the S-wave (up to 20 dB) measurements with increasing relative bulk volume change (e.g. for the medium-sized samples) agrees with the observed sensitivity of the P-wave and the S-wave velocity change, cf. Fig. 6. This can be explained by the underlying difference in the kinematics of the two waves.

Independent of the specimen size as well as the underlying thermal treatment, Fig. 6 shows a clearly logarithmic correlation between the relative bulk volume increase, identical to the initiated crack porosity, and the relative change of the wave propagation velocities. The drastic drop of the velocities already arise for comparable small crack porosities of less than one percent initiated by thermal treatments with less than 400 °C maximum temperature. Even a moderate temperature of 100 °C creates already numerous irreversible microcracks within the sample, as the wave velocity reduction shows. As mentioned in

Section 3.3, for higher relative bulk volume changes a separation of the underlying data points of the slow and the fast cooled down samples can be observed. This means that for an identical crack porosity the velocities are systematically slightly different. This can be well observed, for instance, on the samples that have a crack porosity of approximately 2.0% after the respective thermal treatment. To obtain this crack porosity, either heating to 600 °C has to be performed, followed by slow cooling or heating up to 500 °C with subsequent fast cooling. Since the crack porosity is nearly identical, the different effect on the velocity change can only be explained with different values of the crack density and the mean crack aspect ratio. Coming back to the example, it is supposed that the slowly cooled down sample has a higher crack density but a lower mean crack aspect ratio since a higher maximum temperature was employed. This hypothesis is based on the consideration that the heating-up phase is primarily responsible for the crack initiation and the fast cooling just holds the cracks more or less open. The latter is to be understood in such a way that due to the nonuniform strain field as a result of the fast cooling, the mismatch between the individual grains is amplified. Besides, it is supposed that in a sample that already contains numerous cracks, it is difficult to build up stresses by thermal shock large enough to initiate completely new cracks. Therefore, probably crack propagation is the dominating mechanism. However, since the differences are minor, in a good approximation the crack porosity can be employed as characterizing and simply measurable macroscopic quantity to estimate how the wave propagation is affected. The porosity already present in the untreated Carrara marble (about 0.57%, measured by mercury porosimetry) is also present after thermal treatment. Therefore, the proposed model approach in Eq. (2) does not incorporate the total porosity but only the newly resulting crack porosity. This is contrary to models frequently used in literature[30,54] and must be taken into account. Due to the completely different morphology of the pores in the virgin rock state, compared to the thermally induced crack pore space, and their different influences on effective properties, differentiation seems to be advisable, see also Appendix D.

In micro-mechanics, the challenge is to find appropriate microstructural parameters that determine the value of the effective physical properties, cf. Refs. 55, 56. For dry Carrara marble with cracks initiated by thermal treatments, the increase of the crack porosity, which is the same as the relative bulk volume increase, is an appropriate microstructural parameter to predict the wave velocity change under ambient conditions. In other words, the observed stiffness decrease, cf. Fig. 9, correlating with the reduction of the wave propagation velocities with increasing crack volume contains the information about the generated microcracks. Consequently, the measured effective properties may be interpreted as a mixture of the calcite grain phase with unchanged properties (identical to the effective properties in the untreated state) and the stiffness of the cracks.

5. Summary and conclusions

A systematic study and comparison about the effects of two groups of thermal treatments, distinguishing in the cooling conditions, slow and fast cooling, was carried out for Bianco Carrara marble. As effective properties, the bulk volume, the bulk density, and the P- and S-wave ultrasonic velocities before and after the thermal treatment were determined. For the latter, also shear wave splitting was taken into account. For all measurements, an increase of the bulk volume corresponding with a decrease of the bulk density and a decrease of the wave velocities with increasing maximum temperature of the employed thermal treatments could be observed. Growing shear wave splitting with the employed maximum temperature indicated an increase of anisotropy. For the samples which were subjected to fast cooling, the results were systematically amplified compared to the slowly cooled samples. Moreover, an influence of the specimen size could be identified in the case of fast cooling protocol, while the results were independent of the

specimen size for a slow cooling procedure. Based on μXRCT scans, the microstructure changes as a result of the employed thermal treatments compared to the virgin state were visualized for the extreme cases. For both, a nearly homogeneous network of microcracks was formed, which explains the bulk volume increase. Therefore, the relative increase of the bulk volume is supposed to be identical to the initiated crack porosity. From the μXRCT scans, it was obvious that the generated crack network mainly differs in the mean crack aspect-ratio. Following the literature, it could be shown that the dominating microfracture generation happens already during the heating-up phase due to anisotropic thermal expansion of the calcite grains. If fast cooling instead of slow cooling is applied, the crack porosity can be significantly increased. It is supposed that mainly the mean crack aspect-ratio is influenced by the fast cooling and not the crack density. It could be shown, that a logarithm relationship between the relative change of the ultrasonic velocities and the relative bulk volume increase exists. The latter is identical to the initiated crack porosity by thermal treatment. This relationship also explains why the fast cooling compared to the slow cooling, holding all other factors fixed, had only a minor influence on the wave propagation velocity but a major on the bulk volume. From the resulting data base, models were derived by employing a logarithm model approach with three parameters. The parameters were determined using least squares method. An alternative model approach with just two fitting parameters but almost the same good metrics is given in Appendix D. A slightly systematic difference dependent on the cooling method could be identified. Here it was supposed that for the same crack porosity, a different composition of the crack density and the mean crack aspect ratio is causal. Since the impact on the relative change of the wave velocities is insignificant, the macroscopical measurable relative bulk volume increase after a thermal treatment can be used to predict the relative change of the wave velocities. The proposed model approach should be applicable in general for Carrara marble with slightly customized parameters as they are influenced by the exact rock fabric. This could even be proven by the fact that the different underlying marble blocks came from different orders (used for large samples). If values of the absolute quantities of the ultrasonic velocities in the virgin sample state exist, a prediction of the absolute quantities after the thermal treatment based on the relative bulk volume increase can be performed. The resulting ultrasonic velocities can be used to derive other quantities as, for instance, the dynamic moduli. However, attention must be paid on potential initiated elastic anisotropy as a result of the thermal treatment. In this case, theories that assume isotropic material behavior are no longer valid or restricted.

To initiate the same crack porosity, both thermal treatments are capable up to a certain maximum crack porosity with approximately the same influence on the macroscopic properties. Using slow cooling is more advisable since no dependency on the specimen size exists. Further, slow cooling shows significantly less variation in the resulting measurement data and is, therefore, more deterministic. The only reason to employ a fast cooling for Carrara marble is when a higher crack porosity is required than can be realized by slow cooling. Depending on the microstructure, there are materials where no fracturing during the heating up occurs. For these kinds of materials, fast cooling (thermal shock) is the only possibility to initiate microcracks by a thermal treatment. We suppose that the qualitative results found are also transferable to other crystalline rocks within certain limits.

Declaration of competing interest

The authors declare that they have no known competing financial interests or personal relationships that could have appeared to influence the work reported in this paper.

Acknowledgments

Appendix A. Experimental characterization details

A.1. Ultrasonic velocities

In the through-transmission technique, there are two probes, one on either side of the sample, whereby one transmits a pulse while the other receives the pulse after a certain travel time. With the current sample length l (here $l^{(0)}$ or $l^{(1)}$) and the related travel time Δt_s of the pulse within the sample, the wave propagation velocities

$$v_{\mathrm{P}} = \frac{l}{\Delta t_{s,\mathrm{P}}} \qquad \text{and} \qquad v_{\mathrm{S}} = \frac{l}{\Delta t_{s,\mathrm{S}}} \tag{6}$$

can be derived. For the coupling of the transducers to the sample surface, an adequate couplant was used. All measurements were performed under an identical contact pressure of $0.25\,\mathrm{MPa}$. The related force was adjusted using a scissors-lift table and a mechanical load cell. As ultrasonic square wave pulser/receiver, the *Olympus-Panametrics 5077PR* unit in combination with the PC oscilloscope *PicoScope 5444B* was employed. For all samples an amplified square wave of $100\,\mathrm{V}$ with a repetition frequency of $100\,\mathrm{Hz}$ was set. The signals were recorded with a resolution of $15\,\mathrm{bit}$ and a sampling rate of $125\,\mathrm{MS/s}$. To reduce random noise, stacking of 32 signals was consequently performed. No additional signal gain was needed for all measurements before the thermal treatments. In contrast, for the thermally treated samples, especially at higher max. temperatures ($\geq 400\,°\mathrm{C}$), an additional signal gain was indispensable. This was set as low as possible. To determine the respective first arrival points of the emitted pulses, a similar systematic approach as in Ref. [58] was used. This involves following steps: (1) Low pass filtering of the raw signal for noise reduction. (2) Vertical signal offset correction. (3) Determination of the local signal minima and maxima. (4) Search for the first signal peak which also satisfies absolute or/and relative criteria. (5) Definition of two points at 20% and 80% of the first peak amplitude which are used to reconstruct a secant line. (6) Intersection of the secant line with the time axis gives the first arrival point.

The resulting time Δt is larger by the system time $\Delta t_{\mathrm{sys.}}$ than the pure travel time within the sample Δt_s, $\Delta t_s = \Delta t - \Delta t_{\mathrm{sys.}}$ holds. The system times $\Delta t_{\mathrm{sys.}}$ were experimentally determined for the two setups using two aluminum standards with a different length (l_1 and l_2) made out of the same semi-finished product. Since in both standards the speed of sound must be equal, the system time follows from the two measured time periods Δt_1 and Δt_2:

$$\frac{l_1}{\Delta t_1 - \Delta t_{\mathrm{sys.}}} = \frac{l_2}{\Delta t_2 - \Delta t_{\mathrm{sys.}}} \qquad \rightsquigarrow \qquad \Delta t_{\mathrm{sys.}} = \frac{l_2 \Delta t_1 - l_1 \Delta t_2}{l_2 - l_1} \tag{7}$$

To achieve a plane wave approximation, the basic requirement of ultrasonic measurement is that the sample diameter is much larger than the transducer diameter.[59] It is noted, that this is fulfilled for the medium-sized and large sample geometry, however, not for the small one. For the latter, the size ratio is about 1.0. Ref. [59] studied experimentally the influence of different sample and transducer size ratios on longitudinal waves for ceramic samples. For the here given ratio of ≈ 1.0, the influence was minor. For the relative changes we are mainly interested in, the impact should be even smaller.

For measuring the velocity $v_{\mathrm{S,1}}$ and $v_{\mathrm{S,2}}$, the opposite S-wave transducers were aligned and fixed according to their polarization direction. Subsequently, the sample was examined with respect to the polarization direction given by the orientation of the transducers. This was done by rotating the sample to different angle positions φ_i. The acquired receiver transducer signal is equal to the vector sum of the two shear waves in the direction of its orientation. If the polarization of the transducers is parallel to one of the two directions of the split shear waves, the shear wave is not split. A plot of the corresponding velocities v_{S_i} over the examined angles φ_i should result in a smooth $\cos(2\,\varphi_i)$ curve if the angle increments $\Delta \varphi$ are chosen small enough. Based on this, the propagation velocities of the two split shear waves are given by $v_{\mathrm{S,1}} = \max(v_{\mathrm{S}_i})$ and $v_{\mathrm{S,2}} = \min(v_{\mathrm{S}_i})$ with the corresponding polarization angles $\varphi_{0,1}$ and $\varphi_{0,2}$, whereas $\varphi_{0,2} = \varphi_{0,1} + \pi/2$ holds. It is important to note that the value pairs in between the maximum and the minimum velocities have no physical meaning. Since one full period corresponds to the range $\varphi = \pi$, investigating the interval $[0°, 180°]$ for the polarization angle φ_i is sufficient. However, to cross-check the velocities, we measured the medium-sized samples over the entire circumference, $\varphi_i \in [0°, 360°]$ in increments of $\Delta \varphi = 22.5°$. The small and large samples were measured for $\varphi_i \in [0°, 180°]$ in identical increments of $\Delta \varphi = 22.5°$.

A.2. Micro X-ray computed tomography imaging

For the µXRCT scans, an in-house modular built-up cone beam µXRCT system with a maximum spatial resolution of about $50\,\mathrm{lp/mm}$ at 10% of Modulation Transfer Function (MTF) was employed. A detailed description of the system used can be found in Ref. [29]. All scans were performed using the same geometric magnification of about 24.75. The X-ray tube voltage was set to $80\,\mathrm{kV}$ with a tube flux of $100\,\mathrm{µA}$. The beam spectrum was additionally modified by a $0.5\,\mathrm{mm}$ thick Al-filter. As detector a Shad-o-Box 6K HS with a CsI scintillator option from Teledyne DALSA Inc., Waterloo, Ontario, Canada was used. In total, 1800 projections from 5 different slightly shifted detector positions with an exposure time of $3000\,\mathrm{µs}$ were recorded and stitched to final 1800 enhanced projections as explained in Ref. [29]. The reconstruction was performed using the filtered back projection algorithm within the commercial software Octopus Reconstruction, Version 8.9.4-64 bit.[60] The corresponding voxel size of the reconstructed data sets is in all three cases about $2.0\,\mathrm{µm}$. The resulting volumes have a dimension of $2940 \times 2940 \times 2139$ voxel corresponding to $5.88\,\mathrm{mm} \times 5.88\,\mathrm{mm} \times 4.278\,\mathrm{mm}$. In the presented data sets noise reduction filtering was deliberately not applied yet. Compared to classical optical microscopy or scanning electron microscope providing only a 2d information, µXRCT makes possible to visualize the internal 3d structure in a noninvasive way. However, the underlying physical principle only allows a feature detection if there is a distinction in the attenuation coefficient.[61,62] The brighter the shade of gray in the reconstructed volumes, the higher the X-ray attenuation which correlates with the material density and vice versa.

Appendix B. Definition of relative changes

The relative change of the sample diameter d, length l and bulk volume V is defined by

$$\Delta d_{\mathrm{rel.}} = \frac{d^{(1)}}{d^{(0)}} - 1, \qquad \Delta l_{\mathrm{rel.}} = \frac{l^{(1)}}{l^{(0)}} - 1, \qquad \text{and}$$

$$\Delta V_{\mathrm{rel.}} = \frac{V^{(1)}}{V^{(0)}} - 1 = \frac{l^{(1)} d^{(1)2}}{l^{(0)} d^{(0)2}} - 1. \tag{8}$$

The relative change of the bulk density ρ follows by

$$\Delta \rho_{\mathrm{rel.}} = \frac{\rho^{(1)}}{\rho^{(0)}} - 1 = \frac{m^{(1)}}{V^{(1)}} \frac{V^{(0)}}{m^{(0)}} - 1 \tag{9}$$

Table 2
Absolute measured properties of dry, medium-sized samples (diameter $d = 29\,\text{mm}$, length $l = 72.5\,\text{mm}$). Measurements performed under ambient conditions.

Sample name	$\rho^{(0)}$ [g/cm³]	$\rho^{(1)}$ [g/cm³]	$v_{\text{P}}^{(0)}$ [m/s]	$v_{\text{P}}^{(1)}$ [m/s]	$v_{\text{S},1}^{(0)}$ [m/s]	$v_{\text{S},2}^{(0)}$ [m/s]	$v_{\text{S},1}^{(1)}$ [m/s]	$v_{\text{S},2}^{(1)}$ [m/s]
Slowly cooled samples								
100slow29-1	2.706	2.704	5924	5165	3560		3200	3172
100slow29-2	2.699	2.698	5972	5239	3560		3272	3242
100slow29-3	2.705	2.702	5975	5280	3579		3288	3258
200slow29-1	2.704	2.698	6072	3876	3595		2613	2522
200slow29-2	2.704	2.697	6020	3731	3577		2566	2462
200slow29-3	2.706	2.698	5972	3791	3577		2576	2479
300slow29-1	2.704	2.688	5978	3043	3561		2139	2037
300slow29-2	2.705	2.688	5972	3085	3560		2138	2042
300slow29-3	2.706	2.691	5972	3180	3578		2177	2071
400slow29-1	2.702	2.681	5805	2719	3486		1876	1754
400slow29-2	2.702	2.682	5808	2668	3484		1870	1749
400slow29-3	2.698	2.677	5805	2667	3493		1874	1752
500slow29-1	2.701	2.665	5790	2279	3479		1656	1527
500slow29-2	2.700	2.667	5787	2231	3482		1630	1508
500slow29-3	2.701	2.667	5806	2254	3499		1669	1529
600slow29-1	2.701	2.645	5831	1956	3509		–	–
600slow29-2	2.701	2.646	5805	1830	3487		–	–
600slow29-3	2.697	2.644	5662	1679	3454		–	–
Fast cooled samples								
100fast29-1	2.707	2.704	6077	5132	3616		3230	3202
100fast29-2	2.705	2.703	6024	5059	3579		3333	3288
100fast29-3	2.705	2.703	6078	5126	3622		3353	3337
200fast29-1	2.707	2.699	5973	3500	3561		2398	2292
200fast29-2	2.705	2.697	5972	3499	3578		2382	2285
200fast29-3	2.706	2.696	6020	3567	3577		2438	2336
300fast29-1	2.705	2.688	5973	2640	3578		1900	1788
300fast29-2	2.705	2.689	5973	2709	3578		1956	1842
300fast29-3	2.706	2.686	5974	2650	3561		1916	1802
400fast29-1	2.699	2.670	5808	2079	3500		1525	1396
400fast29-2	2.700	2.664	5799	1995	3492		1456	1351
400fast29-3	2.698	2.663	5762	1881	3468		1396	1229
500fast29-1	2.700	2.650	5783	1701	3503		1298	1190
500fast29-2	2.698	2.647	5779	1623	3474		1184	1076
500fast29-3	2.696	2.640	5767	1599	3467		1259	1081
600fast29-1	2.691	2.624	5789	1455	3480		–	–
600fast29-2	2.698	2.612	5728	1284	3435		–	–
600fast29-3	2.696	2.619	5767	1348	3468		–	–
Thermally untreated reference samples								
ref29-1	2.698	–	5774	–	3492	3459	–	–
ref29-2	2.699	–	5825	–	3458	3425	–	–
ref29-3	2.701	–	5840	–	3524	3490	–	–

Table 3
Absolute measured properties of dry, small samples (diameter $d = 12\,\text{mm}$, length $l = 30\,\text{mm}$). Measurements performed under ambient conditions.

Sample name	$\rho^{(0)}$ [g/cm³]	$\rho^{(1)}$ [g/cm³]	$v_{\text{P}}^{(0)}$ [m/s]	$v_{\text{P}}^{(1)}$ [m/s]	$v_{\text{S},1}^{(0)}$ [m/s]	$v_{\text{S},2}^{(0)}$ [m/s]	$v_{\text{S},1}^{(1)}$ [m/s]	$v_{\text{S},2}^{(1)}$ [m/s]
Slowly cooled samples								
100slow12-1	2.692	2.690	6019	4972	3540		3330	3240
200slow12-1	2.696	2.691	5802	3568	3432		2820	2413
300slow12-1	2.695	2.683	5737	3049	3452		2388	2262
400slow12-1	2.697	2.670	5838	2560	3504		1919	1637
500slow12-1	2.691	2.653	5927	2301	3554		1905	1594
600slow12-1	2.690	2.642	5847	1916	3523		–	–
Fast cooled samples								
100fast12-1	2.694	2.692	5916	4870	3522		3288	3197
200fast12-1	2.697	2.690	5884	3593	3491		2620	2553
300fast12-1	2.697	2.680	5903	2723	3488		2093	1731
400fast12-1	2.693	2.656	5604	1991	3416		1697	1404
500fast12-1	2.696	2.638	5705	1724	3443		1192	1066
600fast12-1	2.693	2.612	5838	1550	3508		–	–
Thermally untreated reference sample								
ref12-1	2.691	–	5846	–	3598	3526	–	–

Table 4
Absolute measured properties of dry, large samples (diameter $d = 48\,\text{mm}$, length $l = 120\,\text{mm}$). Measurements performed under ambient conditions.

Sample name	$\rho^{(0)}$ [g/cm³]	$\rho^{(1)}$ [g/cm³]	$v_{\text{P}}^{(0)}$ [m/s]	$v_{\text{P}}^{(1)}$ [m/s]	$v_{\text{S},1}^{(0)}$ [m/s]	$v_{\text{S},2}^{(0)}$ [m/s]	$v_{\text{S},1}^{(1)}$ [m/s]	$v_{\text{S},2}^{(1)}$ [m/s]
Slowly cooled samples								
100slow48-1	2.698	2696	5810	4544	3391		2845	2805
200slow48-1	2.697	2689	5696	3451	3333		2336	2217
300slow48-1	2.699	2683	6022	3109	3474		2098	2034
400slow48-1	2.698	2672	5700	2674	3355		1855	1789
500slow48-1	2.698	2658	5881	2268	3410		1566	1509
600slow48-1	2.698	2639	5760	1903	3352		1304	1231
Fast cooled samples								
100fast48-1	2.697	2696	5772	4793	3366		2952	2881
200fast48-1	2.697	2690	5706	3582	3376		2316	2275
300fast48-1	2.698	2676	5873	2506	3414		1568	1534
400fast48-1	2.699	2660	5926	1971	3450		1245	1186
500fast48-1	2.695	2635	5964	1602	3439		1008	972
600fast48-1	2.696	2613	5893	1345	3436		838	795
Thermally untreated reference sample								
ref48-1	2.698	–	5722	–	3384	3361	–	–

If isotropy in the virgin state is assumed ($v_{\text{S},1}^{(0)} \approx v_{\text{S},2}^{(0)}$), then $v_{\text{S},1}^{(0)}$ and $v_{\text{S},2}^{(0)}$ are respectively replaced by $v_{\text{S}}^{(0)}$.

Appendix C. Absolute measurement data

The absolute determined quantities for bulk density as well as velocities are given in Table 2 for the medium-sized samples, in Table 3 for the small ones, and in Table 4 for the large ones. For the measurements before the thermal treatment, the superscript "(0)" and after the thermal treatment the superscript "(1)" is used. The descriptive statistics of the samples in the virgin state, classified according to the used raw material blocks, are given in Table 5.

For simplicity to readers more familiar with elastic parameters than wave velocities, we visualized the corresponding absolute P-wave moduli M and S-wave moduli μ for the medium-sized samples in Fig. 9. They were derived from the measurements given in Table 2. Since the samples were made from two different Carrara marble blocks, smaller differences in the absolute properties are noticeable in the absolute representation. For comparison, the predicted results based on the proposed "3PM — all data" approach are shown in Fig. 9(b,d).

with the sample mass m. Due to the conservation of mass, the mass should be identical for both sample states, $m = m^{(0)} = m^{(1)}$. If this is fulfilled, verified accordingly by measuring twice, the relations

$$\Delta\rho_{\text{rel.}} = \frac{V^{(0)}}{V^{(1)}} - 1 \quad \text{and} \quad \Delta V_{\text{rel.}} = \frac{\rho^{(0)}}{\rho^{(1)}} - 1 \tag{10}$$

hold. Therefore, with the absolute quantities for the density given in Tables 2–4 the relative change of the density $\Delta\rho_{\text{rel.}}$ and the relative change of the bulk volume $\Delta V_{\text{rel.}}$ can be determined.

The relative changes for the P- and S-wave velocities are defined as

$$\Delta v_{\text{P}_{\text{rel.}}} = \frac{v_{\text{P}}^{(1)}}{v_{\text{P}}^{(0)}} - 1 \quad \text{and} \quad \Delta v_{\text{S}_{\text{rel.}}} = \frac{v_{\text{S}}^{(1)}}{v_{\text{S}}^{(0)}} - 1 \,. \tag{11}$$

In case of shear wave splitting, the relative changes of the velocity of the faster and the slower shear waves are consequently defined by

$$\Delta v_{\text{S},1_{\text{rel.}}} = \frac{v_{\text{S},1}^{(1)}}{v_{\text{S},1}^{(0)}} - 1 \quad \text{and} \quad \Delta v_{\text{S},2_{\text{rel.}}} = \frac{v_{\text{S},2}^{(1)}}{v_{\text{S},2}^{(0)}} - 1 \,. \tag{12}$$

Table 5
Descriptive statistic properties (mean value and standard deviation) of the dry, untreated samples, classified according to the used raw material blocks. Measurements performed under ambient conditions.

Block	Samples	$\rho^{(0)}$ [g/cm^3]	$v_{\mathrm{P}}^{(0)}$ [m/s]	$v_{\mathrm{S}}^{(0)}$ [m/s]
80 mm block a	100x29-x, 200x29-x, 300x29-x	2.705 ± 0.0018	5995 ± 42.0	3578 ± 17.6
80 mm block b	400x29-x, 500x29-x, 600x29-x, ref-x	2.699 ± 0.0024	5787 ± 37.4.6	3483 ± 19.8
40 mm block	xx12-1	2.694 ± 0.0024	5836 ± 102.8	3498 ± 50.1
125 mm block	xx48-1	2.697 ± 0.0011	5825 ± 104.8	3399 ± 41.1
All blocks	All	2.699 ± 0.0044	5862 ± 111.5	3495 ± 69.7
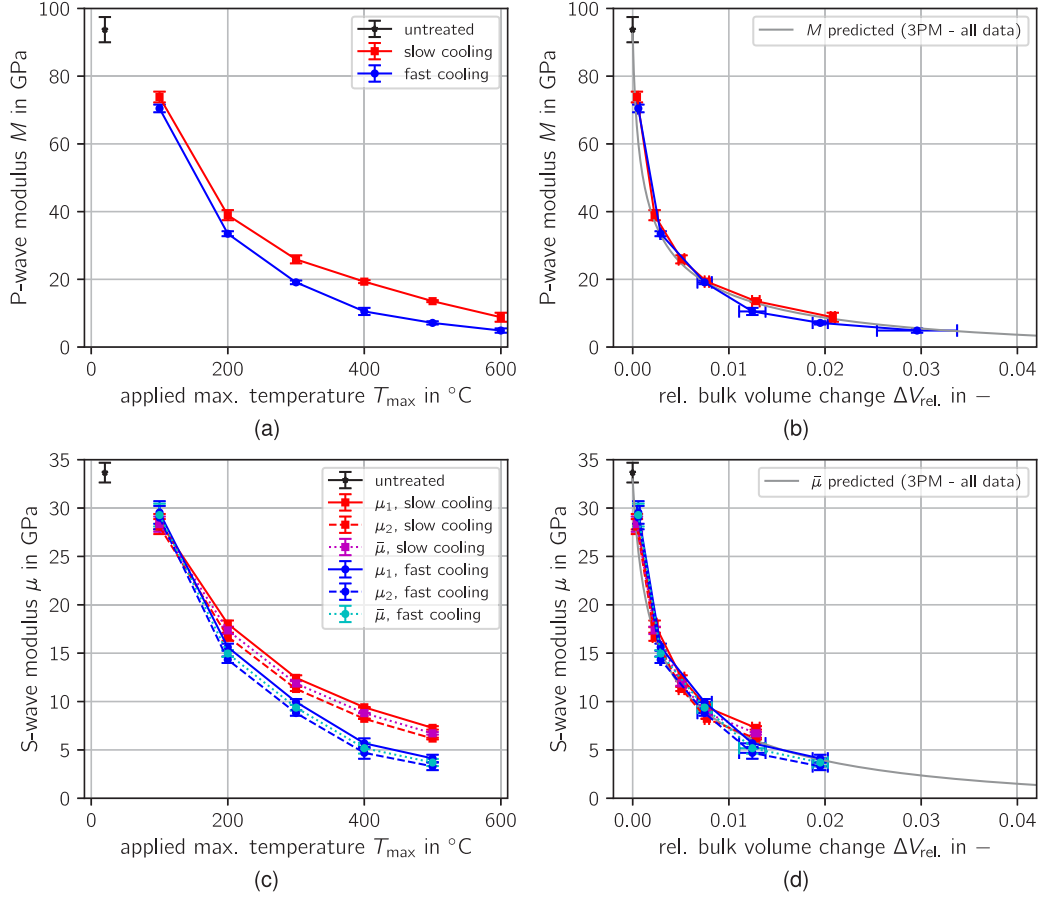
Fig. 9. Absolute derived elastic wave moduli of dry, medium-sized samples (diameter $d = 29$ mm, length $l = 72.5$ mm). Measurements performed under ambient conditions. (a,b) P-wave modulus $M = \rho\,v_{\mathrm{P}}^2$. (c,d) S-wave modulus $\mu = \rho\,v_{\mathrm{S}}^2$. $\square_1$ and $\square_2$ indicate the used shear wave velocity $v_{\mathrm{S},1}$ (fast) or $v_{\mathrm{S},2}$ (slow), as well as $\overline{\square}$ in case of arithmetic mean value of $v_{\mathrm{S},1}$ and $v_{\mathrm{S},2}$.

Appendix D. Alternative model to the 3PM approach for predicting the wave velocity evolution

The proposed 3-parameter model in Eq. (2) is based on the distribution of the N determined data points ($\Delta V_{\mathrm{rel.},n}$, $\Delta v_{i_{\mathrm{rel.},n}}$) in the semi-log representation. The parameter c_i was purely motivated by the prescription that no change of the relative bulk volume change ($\Delta V_{\mathrm{rel.}} = 0$) leads to no relative acoustic velocity change ($\Delta v_{i_{\mathrm{rel.}}} = 0$).

Another mathematically enhanced approach would be to use a function whose formulation intrinsically satisfies this prediction. That could be an exponential expression of the form

$$\Delta v_{i_{\mathrm{rel.}}}(\Delta V_{\mathrm{rel.}}) = \exp\left(-d_i \Delta V_{\mathrm{rel.}}\right) - 1 \qquad \text{with} \qquad i = \{\mathrm{P, S}\} \tag{13}$$

and the fit parameter d_i. This formulation is derived from a common approach used in rock mechanics of the form $v_i(\phi) = A_i F_i(\phi)$ to predict

the absolute acoustic velocity v_i from the total porosity ϕ.[54] Thereby, A_i represents the velocity of the elastic wave in the rock mineral, and $F_i(\phi)$ is a function depending on the rock porosity ϕ. For the function $F_i(\phi)$ phenomenological exponential functions of the form $F_i(\phi) = \exp\left(-d_i\phi\right)$ were proposed.[54] With this it follows:

$$v_i(\phi) = A_i \exp\left(-d_i\phi\right) \qquad \text{with} \qquad i = \{\mathrm{P, S}\}. \tag{14}$$

If the relative change of the wave velocity is considered, cf. Eq. (11), and the fact that $\phi = \phi_0 + \Delta V_{\mathrm{rel.}}$ holds, where ϕ_0 denotes the porosity in the untreated sample state, Eq. (13) can be derived. For this, we are using Eq. (14) and define the absolute wave velocity before $v_{\mathrm{i}}^{(0)}$, and after $v_{\mathrm{i}}^{(1)}$ the respective thermal treatment by

$$v_{\mathrm{i}}^{(0)} = A_i \exp\left(-d_i\phi_0\right) \qquad \text{and} \qquad v_{\mathrm{i}}^{(1)}(\Delta V_{\mathrm{rel.}}) = A_i \exp\left(-d_i\left(\phi_0 + \Delta V_{\mathrm{rel.}}\right)\right)$$
$$\text{with} \qquad i = \{\mathrm{P, S}\}. \tag{15}$$

Table 6

Identified model parameters, R_i^2, and MSE_i values for the model presented in Eq. (17). For comparison, R_i^2 and MSE_i values for the 3-parameter model presented in Eq. (2) with the identified fitting parameters in Table 1 are given in brackets.

P-wave fits	d_P	e_P	R_P^2		MSE_P	
2PM – slow cooling data	6.499 767	0.443 420	0.9724	[0.9810]	5.08×10^{-4}	[3.49×10^{-4}]
2PM – fast cooling data	8.101 392	0.476 191	0.9884	[0.9922]	2.98×10^{-4}	[1.98×10^{-4}]
2PM – all data	7.471 553	0.465 418	0.9772	[0.9826]	9.34×10^{-4}	[7.12×10^{-4}]
S,1-wave fits	$d_\text{S,1}$	$e_\text{S,1}$	$R_\text{S,1}^2$		$\text{MSE}_\text{S,1}$	
2PM – slow cooling data	8.576 916	0.551 530	0.9723	[0.9799]	2.65×10^{-4}	[1.92×10^{-4}]
2PM – fast cooling data	11.687 244	0.599 270	0.9703	[0.9754]	4.83×10^{-4}	[4.00×10^{-4}]
2PM – all data	10.727 748	0.587 914	0.9663	[0.9701]	8.32×10^{-4}	[7.38×10^{-4}]
S,2-wave fits	$d_\text{S,2}$	$e_\text{S,2}$	$R_\text{S,2}^2$		$\text{MSE}_\text{S,2}$	
2PM – slow cooling data	8.613 052	0.528 986	0.9717	[0.9798]	3.01×10^{-4}	[2.15×10^{-4}]
2PM – fast cooling data	13.012 297	0.598 397	0.9806	[0.9852]	3.48×10^{-4}	[2.66×10^{-4}]
2PM – all data	11.306 728	0.575 288	0.9721	[0.9759]	7.52×10^{-4}	[6.50×10^{-4}]

We set these in Eq. (11) to calculate the relative acoustic velocity change:

$$
\begin{aligned}
\Delta v_{i_\text{rel.}}(\Delta V_\text{rel.}) &= \frac{v_i^{(1)}(\Delta V_\text{rel.})}{v_i^{(0)}} - 1 \\
&= \frac{A_i \exp\left(-d_i\left(\phi_0 + \Delta V_\text{rel.}\right)\right)}{A_i \exp\left(-d_i \phi_0\right)} - 1 \\
&= \exp\left(-d_i \Delta V_\text{rel.}\right) - 1 \quad \text{with} \quad i = \{\text{P, S}\}
\end{aligned} \tag{16}
$$

Consequently, A_i and ϕ_0 vanish and just the fitting parameter d_i remains. Further, the relative wave velocity change is only governed by $\Delta V_\text{rel.}$. However, with the single fitting parameter d_i, no adequate fit of the data points is possible.

Therefore, we propose to introduce a second fitting parameter e_i that exponentiates the relative bulk volume change $\Delta V_\text{rel.}$. Following alternative model results

$$
\Delta v_{i_\text{rel.}}(\Delta V_\text{rel.}) = \exp\left(-d_i\left(\Delta V_\text{rel.}\right)^{e_i}\right) - 1 \quad \text{with} \quad i = \{\text{P, S, 1, S, 2}\} \tag{17}
$$

and the two fitting parameters d_i and e_i.

In Table 6 the two fitting parameters together with the two metrics R_i^2, and MSE_i are provided. The MSE_i is in the same order of magnitude and just slightly higher compared to the proposed 3PM approach, Eq. (2). Likewise, the coefficient of determination is almost equally good. In conclusion, this approach is potentially a good alternative from a mathematical point of few with just two fitting parameters. To predict the absolute wave velocities based on the known wave velocities in the untreated Carrara marble state we substitute equation Eq. (17) into equation Eq. (11) and solve for $v_i^{(1)}$:

$$
v_i^{(1)}(\Delta V_\text{rel.}) = v_i^{(0)} \exp\left(-d_i\left(\Delta V_\text{rel.}\right)^{e_i}\right) \quad \text{with} \quad i = \{\text{P, S, 1, S, 2}\}. \tag{18}
$$

References

1. Ruf M, Steeb H. Effects of thermal treatment on acoustic waves in Carrara marble [preprint]. 2021 http://dx.doi.org/10.1002/essoar.10507938.2, https://essoar.org (2021).
2. Peacock S, McCann C, Sothcott J, Astin T. Seismic velocities in fractured rocks: An experimental verification of Hudson's theory. *Geophys Prospect*. 1994;42(1):27–80. http://dx.doi.org/10.1111/j.1365-2478.1994.tb00193.x.
3. Mahmutoglu Y. Mechanical behaviour of cyclically heated fine grained rock. *Rock Mech Rock Eng*. 1998;31(3):169–179. http://dx.doi.org/10.1007/s006030050017.
4. Pieri M, Burlini L, Kunze K, Stretton I, Olgaard DL. Rheological and microstructural evolution of carrara marble with high shear strain: Results from high temperature torsion experiments. *J Struct Geol*. 2001;23(9):1393–1413. http://dx.doi.org/10.1016/S0191-8141(01)00006-2.
5. Schubnel A, Walker E, Thompson BD, Fortin J, Guéguen Y, Young RP. Transient creep, aseismic damage and slow failure in carrara marble deformed across the brittle-ductile transition. *Geophys Res Lett*. 2006;33(17). http://dx.doi.org/10.1029/2006gl026619.
6. Schubnel A, Benson PM, Thompson BD, Hazzard JF, Young RP. Quantifying damage, saturation and anisotropy in cracked rocks by inverting elastic wave velocities. *Pure Appl Geophys*. 2006;163(5–6):947–973. http://dx.doi.org/10.1007/s00024-006-0061-y.
7. Delle Piane C, Burlini L. Influence of strain history on the mechanical and microfabric evolution of calcite rocks: Insights from torsion experiments. *Swiss J Geosci*. 2008;101(2):361–375. http://dx.doi.org/10.1007/s00015-008-1257-1.
8. Arena A, Delle Piane C, Sarout J. A new computational approach to cracks quantification from 2D image analysis: Application to micro-cracks description in rocks. *Comput Geosci*. 2014;66:106–120. http://dx.doi.org/10.1016/j.cageo.2014.01.007.
9. Delle Piane C, Arena A, Sarout J, Esteban L, Cazes E. Micro-crack enhanced permeability in tight rocks: An experimental and microstructural study. *Tectonophysics*. 2015;665:149–156. http://dx.doi.org/10.1016/j.tecto.2015.10.001.
10. Kandula N, Cordonnier B, Boller E, Weiss J, Dysthe DK, Renard F. Dynamics of microscale precursors during brittle compressive failure in carrara marble. *J Geophys Res: Solid Earth*. 2019;124(6):6121–6139. http://dx.doi.org/10.1029/2019jb017381.
11. Lissa S, Ruf M, Steeb H, Quintal B. Digital rock physics applied to squirt flow. *Geophysics*. 2021:1–40. http://dx.doi.org/10.1190/geo2020-0731.1.
12. Sarout J, Cazes E, Delle Piane C, Arena A, Esteban L. Stress-dependent permeability and wave dispersion in tight cracked rocks: Experimental validation of simple effective medium models. *J Geophys Res: Solid Earth*. 2017;122(8):6180–6201. http://dx.doi.org/10.1002/2017jb014147.
13. Howarth DF, Adamson WR, Berndt JR. Correlation of model tunnel boring and drilling machine performances with rock properties. *Int J Rock Mech Min Sci Geomech Abstr*. 1986;23(2):171–175. http://dx.doi.org/10.1016/0148-9062(86)90344-x.
14. Ramez MRH, Murrell SAF. A petrofabric analysis of carrara marble. *Int J Rock Mech Min Sci Geomech Abstr*. 1964;1(2):217–229. http://dx.doi.org/10.1016/0148-9062(64)90028-2.
15. Anders MH, Laubach SE, Scholz CH. Microfractures: A review. *J Struct Geol*. 2014;69:377–394. http://dx.doi.org/10.1016/j.jsg.2014.05.011.
16. Kranz RL. Microcracks in rocks: A review. *Tectonophysics*. 1983;100(1–3):449–480. http://dx.doi.org/10.1016/0040-1951(83)90198-1.
17. Kim K, Kemeny J, Nickerson M. Effect of rapid thermal cooling on mechanical rock properties. *Rock Mech Rock Eng*. 2013;47(6):2005–2019. http://dx.doi.org/10.1007/s00603-013-0523-3.
18. Pimienta L, Orellana LF, Violay M. Variations in elastic and electrical properties of crustal rocks with varying degree of microfracturation. *J Geophys Res: Solid Earth*. 2019;124(7):6376–6396. http://dx.doi.org/10.1029/2019jb017339.
19. El Boudani M, Wilkie-Chancellier N, Martinez L, Hébert R, Rolland O, Forst S, Vergès-Belmin V, Serfaty S. Marble characterization by ultrasonic methods. *Procedia Earth Planet Sci*. 2015;15:249–256. http://dx.doi.org/10.1016/j.proeps.2015.08.061.
20. El Boudani M, Wilkie-Chancellier N, Martinez L, Hébert R, Rolland O, Forst S, Vergès-Belmin V, Serfaty S. Marble ageing characterization by acoustic waves. *Physics Procedia*. 2015;70:222–226. http://dx.doi.org/10.1016/j.phpro.2015.08.140.
21. Siegesmund S, Ullemeyer K, Weiss T, Tschegg EK. Physical weathering of marbles caused by anisotropic thermal expansion. *Int J Earth Sci*. 2000;89(1):170–182. http://dx.doi.org/10.1007/s005310050324.
22. Gao J, Fan L, Xi Y, Du X. Effects of cooling thermal shock on the P-wave velocity of granite and its microstructure analysis under immersion in water, half immersion in water, and near-water cooling conditions. *Bull Eng Geol Environ*. 2021;81(1). http://dx.doi.org/10.1007/s10064-021-02505-x.
23. Fan L, Li H, Xi Y. Investigation of three different cooling treatments on dynamic mechanical properties and fragmentation characteristics of granite subjected to thermal cycling. *Undergr Space*. 2022. http://dx.doi.org/10.1016/j.undsp.2021.12.010.
24. Shao S, Wasantha P, Ranjith P, Chen B. Effect of cooling rate on the mechanical behavior of heated strathbogie granite with different grain sizes. *Int J Rock Mech Min Sci*. 2014;70:381–387. http://dx.doi.org/10.1016/j.ijrmms.2014.04.003.

25. Rodriguez-Navarro C, Ruiz-Agudo E, Luque A, Rodriguez-Navarro AB, Ortega-Huertas M. Thermal decomposition of calcite: Mechanisms of formation and textural evolution of CaO nanocrystals. *Am Mineral*. 2009;94(4):578–593. http://dx.doi.org/10.2138/am.2009.3021.

26. Fredrich JT, Evans B, Wong T. Effect of grain size on brittle and semibrittle strength: Implications for micromechanical modelling of failure in compression. *J Geophys Res*. 1990;95(B7):10907. http://dx.doi.org/10.1029/jb095ib07p10907.

27. de Figueiredo JJS, Schleicher J, Stewart RR, Dayur N, Omoboya B, Wiley R, William A. Shear wave anisotropy from aligned inclusions: Ultrasonic frequency dependence of velocity and attenuation. *Geophys J Int*. 2013;193(1):475–488. http://dx.doi.org/10.1093/gji/ggs130.

28. Thomsen L. Weak elastic anisotropy. *Geophysics*. 1986;51(10):1954–1966. http://dx.doi.org/10.1190/1.1442051.

29. Ruf M, Steeb H. An open, modular, and flexible micro X-ray computed tomography system for research. *Rev Sci Instrum*. 2020;91(11):113102. http://dx.doi.org/10.1063/5.0019541.

30. Mavko G, Mukerji T, Dvorkin J. *The Rock Physics Handbook – Tools for Seismic Analysis of Porous Media*. 2nd ed. Cambridge University Press; 2009.

31. Ruf M, Steeb H. micro-XRCT data set of Carrara marble with artificially created crack network: slow cooling down from 600°C. 2020. http://dx.doi.org/10.18419/darus-754.

32. Ruf M, Steeb H. micro-XRCT data set of carrara marble with artificially created crack network: fast cooling down from 600°C. 2020. http://dx.doi.org/10.18419/darus-682.

33. Ferrero AM, Marini P. Experimental studies on the mechanical behaviour of two thermal cracked marbles. *Rock Mech Rock Eng*. 2001;34(1):57–66. http://dx.doi.org/10.1007/s006030170026.

34. Ševčík R, Šašek P, Viani A. Physical and nanomechanical properties of the synthetic anhydrous crystalline CaCO3 polymorphs: vaterite, aragonite and calcite. *J Mater Sci*. 2017;53(6):4022–4033. http://dx.doi.org/10.1007/s10853-017-1884-x.

35. Marek R, Nitsche K. *Praxis Der Wärmeübertragung*. Hanser Fachbuchverlag; 2019.

36. Stevens J. Thermal gradients from quenching. 2014 Accessed 2021-06-08 http://heat-transfer-thermodynamics.blogspot.com/2014/03/thermal-gradients-from-quenching.html.

37. Merriman JD, Hofmeister AM, Roy DJ, Whittington AG. Temperature-dependent thermal transport properties of carbonate minerals and rocks. *Geosphere*. 2018;14(4):1961–1987. http://dx.doi.org/10.1130/ges01581.1.

38. Moore D, Lockner D. The role of microcracking in shear-fracture propagation in granite. *J Struct Geol*. 1995;17(1):95–114. http://dx.doi.org/10.1016/0191-8141(94)e0018-t.

39. Lee D, Karadimitriou N, Ruf M, Steeb H. Detecting micro fractures with X-ray computed tomography. 2021 arXiv:2103.12821.

40. Shushakova V, Fuller ER, Siegesmund S. Microcracking in calcite and dolomite marble: microstructural influences and effects on properties. *Environ Earth Sci*. 2012;69(4):1263–1279. http://dx.doi.org/10.1007/s12665-012-1995-2.

41. Srinivasan R. The thermal expansion of calcite from room temperature up to 400°C. *Proc Indian Acad Sci A*. 1955;42(2):81–85. http://dx.doi.org/10.1007/bf03053495.

42. Rao KVK, Naidu SVN, Murthy KS. Precision lattice parameters and thermal expansion of calcite. *J Phys Chem Solids*. 1968;29(2):245–248. http://dx.doi.org/10.1016/0022-3697(68)90068-1.

43. Dove MT, Swainson IP, Powell BM, Tennant DC. Neutron powder diffraction study of the orientational order–disorder phase transition in calcite, CaCO3. *Phys Chem Min*. 2005;32(7):493–503. http://dx.doi.org/10.1007/s00269-005-0026-1.

44. Rayleigh L. The bending of marble. *Proc R Soc Lond Ser A Math Phys Eng Sci*. 1934;144(852):266–279. http://dx.doi.org/10.1098/rspa.1934.0048.

45. Clarke DR. Microfracture in brittle solids resulting from anisotropic shape changes. *Acta Metall*. 1980;28(7):913–924. http://dx.doi.org/10.1016/0001-6160(80)90107-8.

46. Evans AG, Clarke DR. Residual stresses and microcracking induced by thermal contraction inhomogeneity. In: *Thermal Stresses in Severe Environments*. Springer US; 1980:629–648. http://dx.doi.org/10.1007/978-1-4613-3156-8_39.

47. Fredrich JT, Wong T. Micromechanics of thermally induced cracking in three crustal rocks. *J Geophys Res: Solid Earth*. 1986;91(B12):12743–12764. http://dx.doi.org/10.1029/jb091ib12p12743.

48. Vagnon F, Colombero C, Colombo F, Comina C, Ferrero AM, Mandrone G, Vinciguerra SC. Effects of thermal treatment on physical and mechanical properties of valdieri marble - NW Italy. *Int J Rock Mech Min Sci*. 2019;116:75–86. http://dx.doi.org/10.1016/j.ijrmms.2019.03.006.

49. Sheremeti-Kabashi F, Snethlage R. Determination of structural anisotropy of carrara marble with ultrasonic measurements. In: *Proceedings of the 9th International Congress on Deterioration and Conservation of Stone*. Elsevier; 2000:247–253. http://dx.doi.org/10.1016/b978-044450517-0/50106-9.

50. Kingery WD. Factors affecting thermal stress resistance of ceramic materials. *J Am Ceram Soc*. 1955;38(1):3–15. http://dx.doi.org/10.1111/j.1151-2916.1955.tb14545.x.

51. Ougier-Simonin A, Fortin J, Guéguen Y, Schubnel A, Bouyer F. Cracks in glass under triaxial conditions. *Internat J Engrg Sci*. 2010;49(1):105–121. http://dx.doi.org/10.1016/j.ijengsci.2010.06.026.

52. Ougier-Simonin A, Guéguen Y, Fortin J, Schubnel A, Bouyer F. Permeability and elastic properties of cracked glass under pressure. *J Geophys Res*. 2011;116(B7). http://dx.doi.org/10.1029/2010jb008077.

53. Becher PF, Warwick WH. Factors influencing the thermal shock behavior of ceramics. In: *Thermal Shock and Thermal Fatigue Behavior of Advanced Ceramics*. Springer Netherlands; 1993:37–48. http://dx.doi.org/10.1007/978-94-015-8200-1_4.

54. Musso G, Cosentini RM, Foti S, Comina C, Capasso G. Assessment of the structural representativeness of sample data sets for the mechanical characterization of deep formations. *Geophysics*. 2015;80(5):D441–D457. http://dx.doi.org/10.1190/geo2014-0351.1.

55. Guéguen Y, Kachanov M. Effective elastic properties of cracked rocks – an overview. In: *Mechanics of Crustal Rocks*. Springer Vienna; 2011:73–125. http://dx.doi.org/10.1007/978-3-7091-0939-7_3.

56. Kachanov M, Sevostianov I eds, *Effective Properties of Heterogeneous Materials*. Springer Netherlands; 2013. http://dx.doi.org/10.1007/978-94-007-5715-8.

57. Ruf M, Steeb H. Effects of thermal treatment on acoustic waves in Carrara marble: measurement data. 2021. http://dx.doi.org/10.18419/darus-1862.

58. Jacobsson L, Kjell G. *Measurement of p- and s-wave velocity in material using ultrasonics*. Tech. Rep. RISE Report 2017:48; RISE Research Institutes of Sweden; 2017.

59. Zhang R, Jiang B, Cao W. Influence of sample size on ultrasonic phase velocity measurements in piezoelectric ceramics. *J Appl Phys*. 2002;91(12):10194. http://dx.doi.org/10.1063/1.1479754.

60. Vlassenbroeck J, Dierick M, Masschaele B, Cnudde V, Van Hoorebeke L, Jacobs P. Software tools for quantification of X-ray microtomography at the UGCT. *Nucl Instrum Methods Phys Res A*. 2007;580(1):442–445. http://dx.doi.org/10.1016/j.nima.2007.05.073.

61. Carmignato S, Dewulf W, Leach R eds, *Industrial X-Ray Computed Tomography*. Springer International Publishing; 2018. http://dx.doi.org/10.1007/978-3-319-59573-3.

62. Stock SR. *MicroComputed Tomography: Methodology and Applications*. CRC Press; 2008.

Chapter III:
A Multifunctional Mechanical Testing Stage for Micro X-Ray Computed Tomography

A multifunctional mechanical testing stage for micro x-ray computed tomography Ⓕ

View Online   Export Citation   CrossMark

Matthias Ruf,[1,a] 🔾 Dongwon Lee,[1] 🔾 and Holger Steeb[1,2,a] 🔾

AFFILIATIONS

[1] University of Stuttgart, Institute of Applied Mechanics (CE), Pfaffenwaldring 7, D-70569 Stuttgart, Germany
[2] University of Stuttgart, SC SimTech, D-70569 Stuttgart, Germany

[a]Authors to whom correspondence should be addressed: matthias.ruf@mechbau.uni-stuttgart.de
and holger.steeb@mechbau.uni-stuttgart.de

ABSTRACT

An existing open and modular designed micro X-Ray Computed Tomography (µXRCT) system is extended by a test rig in order to combine mechanical and hydro-mechanical experiments with µXRCT characterization. The aim of the system is to cover the complete resolution range of the underlying µXRCT system in combination with a broad load capacity range. A characteristic feature of the developed setup is that it consists mainly of standard components. This makes the shown test rig potentially interesting for other researchers considering extending an existing µXRCT system with an apparatus for mechanical and hydro-mechanical *in situ* testing. For the load frame, an uniaxial 10 kN universal testing machine with a digital control system was employed, which was extended by two aligned rotational stages. The uniaxial load capacity is ±3.1 kN and can be combined with torque moments of up to ±15 N m both limited by the used rotational stages. The setup is designed in such a way that different x-ray transparent cells (flow cells, oedometer cells, triaxial cells, etc.) can be integrated to generate three-dimensional stress/strain states as required for porous media research. Three applications demonstrate the possible versatile use of the system. As part of these examples, we show how corresponding x-ray transparent cells are designed and implemented. Finally, we discuss the presented approach's technical advantages and disadvantages and suggest improvements.

Published under an exclusive license by AIP Publishing. https://doi.org/10.1063/5.0153042

I. INTRODUCTION AND MOTIVATION

To characterize and understand the morphology of materials and components, micro X-Ray Computed Tomography (µXRCT) imaging has become a standard three-dimensional (3D) imaging method in numerous research fields.[1–12] For various classes of materials, it is well known that the inherent morphology is tremendously changed if the material deforms. Prominent examples are (soft) cellular materials, such as polymer foams,[13] where morphological properties, such as intrinsic porosity, strongly depend on the state of deformation. µXRCT-based characterization of the evolution of morphological properties at different deformation states provides novel and important insight and understanding of the material's behavior. Additionally, it allows us to combine effective material properties on the macro (sample) scale, such as elastic moduli or strength, with the morphology on the microscale. Commonly, such investigations are denoted as "in situ µXRCT" whereby the sample is tested inside the µXRCT system.[6,14,15] Based on the characterization results of *in situ* µXRCT investigations, the improvement

validation of (macroscale) physical models can be performed. Especially in the field of experimental mechanics of materials with inherent microstructure (such as foams) and porous media research, this is of unprecedented interest.

Compared to mechanical *in situ* investigations using two-dimensional (2D) imaging methods (e.g., optical microscopy), one of the challenges faced by 3D imaging methods [e.g., µXRCT or 3D X-Ray Diffraction (3DXRD)] is that the investigated sample must be precisely rotated around a fixed rotational axis under the applied mechanical boundary conditions. Consequently, over the past one to two decades, numerous *in situ* setups have been developed to address this challenge.[2,16]

A commonly employed approach for mechanical µXRCT investigations is the usage of setups consisting of short-circuited tubular load frames, e.g., Refs. 16–18. This concept is illustrated in Fig. 1(a). In such test rigs, the loading force is applied to the sample via an integrated actuator. The reaction force is carried by an almost X-ray transparent outer tube often made out of poly(methyl methacrylate) (PMMA). Test rigs based on this
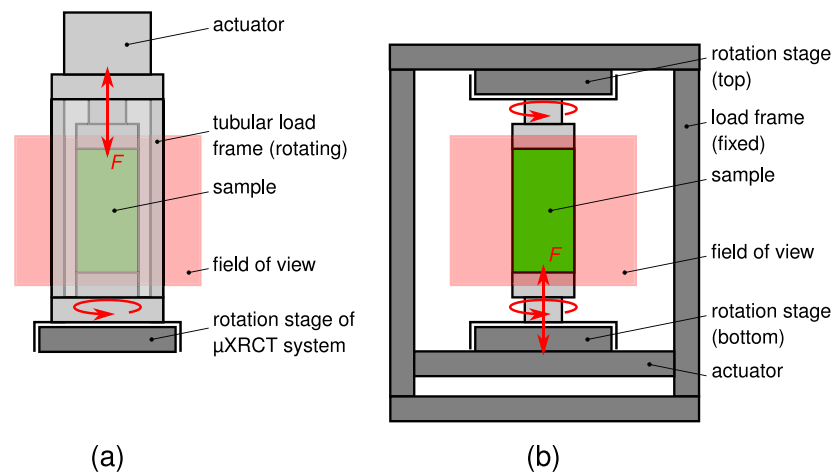
FIG. 1. Concepts to perform mechanical (tension/compression) *in situ* μXRCT experiments. (a) Tubular load frame concept positioned on the system's rotation stage and (b) fixed load frame with two rotation stages. Bright gray parts rotate during image acquisition, and dark gray parts are fixed.

concept are commercially available. For instance, Deben UK Ltd., UK, offers several systems that vary in terms of their maximum possible tensile/compressive force (from 500 N *CT500* to 5 kN *CT5000*) with max. 10 mm travel range. Similarly, Bruker Corp., USA, offers a system for tensile and compressive testing up to 440 N in combination with max. 11 mm travel range and a system for pure compressive testing up to 4.4 kN and max. 5.5 mm travel range. Other options like integrated temperature control are also possible depending on the addressed research question, e.g., Refs. 2, 16, and 19 and therein cited literature. Such test rigs are based on lightweight designs (Deben's *CT500* ≈ 1 kg and *CT5000* ≈ 5.5 kg) and are directly mounted on the available positioning system of the μXRCT system. Thus, they take advantage of the high precision rotational stages of the μXRCT systems. Due to the simple handling and high portability of these test rigs, they can be considered as the quasi standard for *in situ* μXRCT investigations, in particular, in beamlines of synchrotron facilities. These test rigs are often designed for very specific investigation requirements. This means that different adaptions of test rigs are necessary to accommodate various factors, such as sample size, sample geometry, load case (tension/compression and torsion), and maximum loading. For laboratory systems with a conical x-ray beam using the concept of geometric magnification,[20,21] the size of tubular rigs can be problematic. High magnifications (small voxel sizes) are requiring sample locations close to the x-ray source. Since the diameter of the tubular rigs limits the closest possible distance to the x-ray source, there is a technical magnification limit. Furthermore, the presence of the surrounding tubular frame (e.g., made of PMMA) can result in an undesired x-ray beam attenuation. In particular, the realization of combined loading (sequential or superimposed tension/compression and torque load) is a challenging task since all acting elements and measurement techniques must be integrated into the test rig, leading to a complex and expensive design. While some of these points have only limited relevance for *in situ* investigations at synchrotron beamlines, they impose significant limitations on lab-based *in situ* studies.

An alternative and more versatile approach is the use of a non-rotating test rig (not covering the field of view) with two aligned, synchronized rotation stages, shown in Fig. 1(b). The two synchronized rotation stages allow for the rotation of the pre-loaded sample during the image acquisition process. Via an integrated actuator in the load frame, tensile and compressive forces are applied to the sample, comparable to an universal testing machine. Besides the "stress-free rigid body" co-rotation of the pre-loaded sample for the image acquisition process, the two rotational stages also enable pre-loading counter-rotation. Thus, a torsional moment could be superimposed to the axial force. The implementation of this very general concept has been reported by a limited number of authors. To mention is the test rig by Refs. 22 and 23 designed for transmission imaging and tomography, the apparatus designed for the research reactor FRMII (Garching near Munich) for neutron diffraction measurements,[24] and the load frame insert (RAMS) presented by Ref. 25, designed for concurrent applications, such as 3DXRD and μXRCT. To the best of the authors' knowledge, there are currently only two commercial vendors offering comparable setups: on the one hand, the *Deben CT20*kN from Deben UK Ltd., UK, providing up to ±20 kN axial loading and 50 mm travel range, and, on the other hand, the *Psylotech xTS* in different versions from Psylotech Inc., USA, providing ±(1.6, 4.5, 10, 25, and 45) kN axial loading and (40, 24, 25, 25, and 100) mm travel ranges. Compared to the short-circuited tubular rig design, axial forces and travel ranges can be significantly higher. The challenges that are intrinsically associated with this design are the alignment and synchronization of the two required rotation stages.

In our previous work,[26] we presented an open, modular, and highly flexible μXRCT system, built up and operated at the Porous Media Lab (PML) of the Institute of Applied Mechanics (CE) of the University of Stuttgart, mainly used for porous media research. Building upon the existing system, our aim was to develop a versatile and universal test rig to perform mechanical *in situ* experiments for a wide range of mechanical load cases (tension, compression, and torsion) or combinations of them. At the PML, we have a

wide range of possible sample sizes (diameter 5–100 mm) and related sample stiffnesses [from stiff crystalline rocks to soft polymer foams (Young's modulus from 100 GPa to 10 kPa)]. Furthermore, for hydro-mechanically coupled characterization of fluid-saturated porous materials, such as soils or rocks, frequently oedometer and triaxial cells are required to control the inherent pore fluid pressure and the 3D total stress state through an applied axial force and a controlled pressure of the confining medium. To ensure a simple and reliable cell design, we aimed for a solution where the axial load is applied externally through a non-rotating test rig in comparison to designs proposed by Refs. 27 and 28. Such an experimental setup can only be realized by a test rig with two integrated rotational stages as described above.

Within this contribution, a modular experimental setup and test rig design is introduced. It is based on the fundamental idea of using a standard uniaxial universal testing device including its flexible and modular control unit with all its advantages instead of an individually designed and highly specialized test rig. With the exception of some adapter plates, all remaining components of the test rig are commercially available standard components that fit with the open, modular, and flexible basic concept of the underlying μXRCT system.

In the following, a detailed description of the developed *in situ* setup for mechanical testing as well as the integration in the existing μXRCT system is given. To demonstrate the versatile applicability of the setup, we show three different application examples related to different research questions. The acquired datasets (projection images and reconstructed images, including meta and logging/measurement data) of the presented examples are published open access. The examples are chosen carefully and will point out the versatile design and the possibility of the modular integration of special cell types. Here, we focus on an oedometer cell and a triaxial (flow) cell. A subsequent discussion about this development and related possible improvement suggestions concludes this contribution.

II. DESIGN CHARACTERISTICS

A. Requirements

(i) The fundamental requirement was the integration into the existing μXRCT system[26] as well as the preservation of the functionality of the old system state. Thus, two complementary and partly redundant (with regard to imaging) setups are available after the extension. (ii) On the assumption of a cylindrical sample geometry, the expected sample diameter will be in the range of 5–100 mm, dependent on the stiffness of the investigated sample (stiff to soft). (iii) A maximum uniaxial stress of about 100 MPa should be possible when cylindrical core samples in the range of 5–6 mm diameter are examined, resulting in a required force F_z of about 2.9 kN. (iv) A maximum shear stress from torsional loading of about 100 MPa should be possible when cylindrical core samples in the range of 5–6 mm diameter are examined, resulting in a required torque M_z of 4.3 N m. (v) The sample size is therefore determined, on the one hand, by the smallest detail of the microstructure to be resolved and, on the other hand, by the stress state to be applied. Hence, the possible adjustable geometric magnification $M = SDD/SOD$ should be between ≈1 and 25 for a given source–detector-distance SDD of 1000 mm and a variable source–object-distance SOD. (vi) Load com-
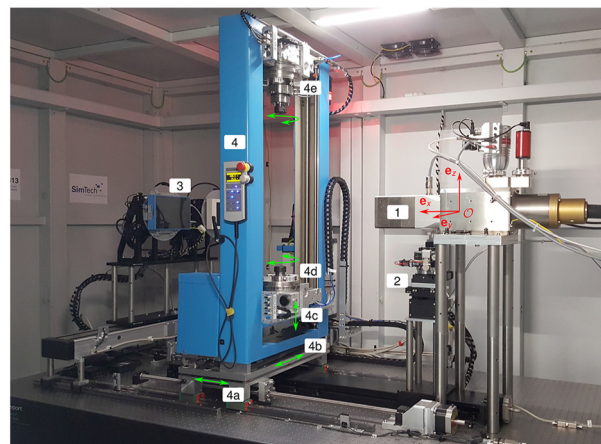
FIG. 2. Integration of the test rig based on a UTM in the open, modular, and flexible μXRCT system presented in Ref. 26. The classical setup could be completely preserved. The whole setup is located in a lead-shielded accessible cabin. Possible moving directions of the motorized linear and rotational stages for positioning/loading are illustrated by green arrows. They are related to the defined $\mathbf{e}_x$, $\mathbf{e}_y$, and $\mathbf{e}_z$ coordinate system. The traverse "4c" applies the axial force F_z. Rotation stages "4d" and "4e" allow rotation of the pre-loaded sample for the image acquisition and can be additionally used to superimpose a torsional moment M_z by counter-rotation.

binations of tension, compression, and torsion (superimposed or sequential) shall be possible. (vii) Additionally, integration of cells with a maximum possible height of 500 mm shall be possible.

B. Load frame

To achieve the requirements, as the load frame, a refurbished *Zwick 1445* 10 kN Universal Testing Machine (UTM) with a maximum load capacity of 10 kN is used, cf. Fig. 2 ("4"). The UTM was refurbished from DOLI Elektronik GmbH, Germany, and equipped with a modern *EDC 222V* controlling system. The maximum possible axial loading (compressive/tensile force) and torque are currently limited by the used rotation stages. The Zwick 1445 UTM has one
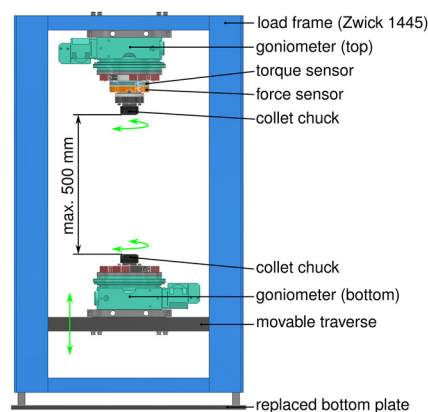

FIG. 3. Design of the modular test rig.

movable traverse, which positions the bottom rotation stage vertically and imposes the uniaxial force/displacement to the sample, cf. Fig. 2 ("4c" and "4d") and Fig. 3. The second required rotation stage is positioned on the fixed upper traverse of the load frame, cf. Fig. 2 ("4e"). Consequently, the upper test chamber of the UTM is used for experiments. The arrangement of the rotation stages is motivated by the following thoughts. The setup can also be used for conventional scans without mechanical loading of the sample. In this case, just the bottom rotation stage is employed, and the movable traverse serves as a vertical positioning system. Latter also opens up the possibility of imaging long samples by helical cone beam scanning. The relatively large distance between the two rotation stages enables the integration of long-building cells and other long-building experimental setups. By using a UTM instead of a customized load frame solution, automatically, all benefits of a conventional UTM are intrinsically given, e.g., high stiffness and no backlash as well as the integrated measurement and controlling system, including the required software.

C. Rotation stages

Two goniometers *411-X3 W2* from XHuber, Germany, are employed as rotation stages. These meet the requirements regarding the maximum axial load (±3.1 kN), the maximum possible torque (±15 N m), the required accuracy, and a compact design. The goniometers have an integrated gear ratio of $i_1 = 360 : 1$. Since we are not aiming for fast rotations, standard stepper motors with an additional gear of $i_2 = 10 : 1$ are used, resulting in a total gear ratio of $i = i_1 i_2 = 3600 : 1$. Hereby, sufficiently high torque moments with ordinary stepper motors can be achieved, which can be controlled by the same controller as all other motion stages in the µXRCT system. The goniometers are specified with an accuracy $\leq 15''$, an unidirectional repeatability $\leq 2''$, an eccentricity $\leq 2\,\mu$m, and a wobble $\leq 3''$. When combined with a stepwise rotation scanning protocol for the image acquisition, the maximum synchronization error between both rotation stages is consequently $\leq 30''$ at the respective discrete angular position. One full step of the used stepper motors corresponds to $1.8''$ rotation of the goniometers. Both goniometers are additionally equipped with an optical encoder system from Renishaw to have the possibility to operate them also in closed-loop mode. In the used stepwise rotation scanning protocol, the angle repeatability is sufficiently high in open-loop mode, and the optical encoder system is not absolutely required. The closed-loop mode offers the possibility to synchronize the rotation of both goniometers using additional equipment as it is of interest in a continuous rotation scanning protocol. A drawback of the high gear ratio is that a full revolution takes ~720 s. Even when acquiring only a limited number of projections from a few angular positions for 3D reconstruction, this imposes a limit on the minimum required scan time for a single 3D image ("time step"). Compared to the standard design of the goniometers, a modified version with a central aperture of 100 mm is used to have a penetration possibility for sensor cables (transmission of power and electrical signals). Slip rings with 36 (24) poles in the bottom (top) goniometer are installed to make infinity rotations possible.

D. Assembly and additional equipment

To measure the applied force and torque, a solution from ME-Meßsysteme GmbH, Germany, is employed. The solution consists of two separate sensors, which can be combined into a compact unit. As the axial load cell the ring force sensor *KR110a* in the ±5 kN version and as the torque sensor the *TD100a* in the ±20 N m variant are installed. The sensor unit is positioned between the top goniometer and the collet chuck, which is used to fix the sample holder, cf. Fig. 3. The sensors are connected to the controlling unit of the UTM via the slip ring of the top goniometer mentioned above.

To make the installation of additional sensor equipment simple, the 36 (bottom) and 24 (top) possible signal wire connections are subdivided and contacted to suitable connectors (9-pin D-subminiature connectors). These are located on one side next to the collet chucks close to the sample and on the other side next to the left UTM post, cf. Fig. 2 ("4e" and "4c"). Collet chucks in combination with precision-ground collets of different inner diameters (up to 20 mm) are employed as the basic interface between the rotation stages and all kinds of different sample holders and adapters. This connection ensures a reliable force and torque transfer. Depending on the experiment, customized adapters are used to mount the sample or the experimental setup.

Each rotation stage, including all other described equipment, is mounted on an adapter plate and forms a sub-assembly unit. With just four screws, each unit can be installed and removed from the load frame, cf. Fig. 3. That makes the maintenance or modification of the setup simple.

The measured total compliance of the test rig in the shown design (load frame, rotation stages, collet chucks, etc.) with a typical distance of 400 mm between the two rotation stages is about 0.0942 mm kN^{-1} under tension and -0.0836 mm kN^{-1} under compression load.

E. Control and data acquisition

We distinguish primarily between the control of the UTM and the control of the µXRCT scanner to which the two goniometers are assigned.

To control the two rotation stages, we use two available channels of the already employed multi-axis motion controllers used for the other motion stages of the µXRCT system [*Standa 8SMC4/5-Ethernet/RS232-B19x3-8/12* controllers with total 20 channels from Standa Ltd., Lithuania, with the software package *XILab* (*Version 1.14.12*)]. The control of the two rotational stages is integrated into the overall scan loop controlled via the scripting language *MATLAB* from The MathWorks, Inc. The implementation was designed with the lower rotation stage as the master and the upper rotation stage as the slave. The application of a torque/twisting-angle to the sample can be performed either by rotating both goniometers against each other or by rotating only one relative to the other. Given that the uniaxial load/displacement is applied from the lower goniometer and the top of the sample can be considered stationary, the twist is typically imposed using only the lower goniometer, as performed in the application example in Sec. III A; see Fig. 4.

Control of the UTM can be achieved through two ways. On the one hand, the UTM can be controlled using the graphical user interface *Test&Motion* (*Version 4.6.0.52*) provided by DOLI Elektronik with all functionality, or on the other hand, script-based control is also available. To achieve this, the provided *32-bit DoPE Dynamic Link Library* (*DLL*) from DOLI Elektronik, which serves as the interface to access all EDC functions and finally controls the UTM, was embedded in MATLAB (64-bit). To overcome the challenge of uti-
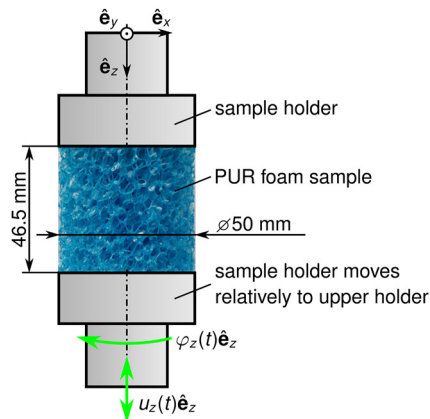
FIG. 4. PUR foam sample with sample holders.

lizing a 32-bit DLL in a 64-bit application, the COM (Component Object Model) method was used, e.g., Refs. 29 and 30. With this on hand, the UTM could be integrated into the MATLAB control loop.[26] Consequently, the used software concept works entirely without trigger signals. In the current configuration, the force as well as the torque is measured by the controlling system of the UTM. Latter enables a force-controlled regulation of the testing machine. An additional remote control unit (*RMC7* from DOLI Elektronik) positioned at the UTM inside the lead-shielded cabin facilitates the installation of samples and experimental setups, cf. Fig. 2 ("4").

F. Integration into the µXRCT system

To install the whole setup into the scanner, we aimed to preserve the old system state to establish two complementary working setups. This approach prevented a long downtime of the µXRCT system for the upgrade and will help reduce system downtime in the future in case of modifications. Additionally, the well-calibrated conventional system simplifies the calibration process of the mechanical *in situ* test rig presented in this study. For this, the old system had to be slightly mechanically modified (lifted). After the modifications, it is possible to bring the conventional positioning stack to a parking position below the front of the x-ray source, cf. Fig. 2 ("2").

The UTM along with the implemented goniometers shown in Fig. 3 is placed on two self-built translational stages. With the adjustment option in the $\mathbf{e}_x$-direction, the geometric magnification M of the sample can be set, and with the second one ($\mathbf{e}_y$-direction), the center of rotation can be set, cf. Fig. 2 ("4a" and "4b"). For this, linear rails and guideways from HIWIN Technologies Corporation, Taiwan, in combination with direct-driven ball screw systems are employed. For the stage used for the positioning in $\mathbf{e}_x$-direction, a ground ball screw with a diameter of 20 mm, a length of 1200 mm, and a spindle pitch of 2 mm is employed. The possible travel range covers the complete *SDD* of 1000 mm. The positioning of the test rig in the lateral direction is realized by a ground ball screw with a spindle pitch of 2 mm due to the significantly shorter travel range of about ±30 mm in a 10 mm diameter version. Due to height limitations caused by the existing lead-shielded cabin, the original

bottom plate of the UTM was replaced by an integrated solution to reduce the overall setup height. As for almost all other motorized stages in the µXRCT system, we use direct-driven stepper motors, *Vexta PK296M-E4.5B* from Oriental Motor Europa GmbH, Germany. They are controlled with the same controllers as all other motorized stages.

III. APPLICATION EXAMPLES

Three different examples of mechanical and hydro-mechanical *in situ* investigations related to different research questions are shown in this section. The selection is intended to demonstrate the versatility of the setup and the broad range of potential applications. The investigated materials range from man-made polyurethane foam and granular mixtures to marine limestone with sample sizes ranging from 80 to 6.3 mm in diameter. We start with an example where no additional apparatus is required, Sec. III A. Typical for mechanical and hydro-mechanical porous media investigations is the use of oedometer and triaxial (flow) cells to impose three-dimensional stress states. Within examples two and three, Secs. III B and III C, we show the design of the corresponding cells and their integration in the testing rig. All experiments were subjected to 3D imaging in interrupted time-lapse mode.[31,32] The 3D reconstruction of all scans was performed with the software *Octopus Reconstruction* (*Version 8.9.4-64 bit*)[33] using the FDK reconstruction algorithm.[34]

A. Combined loading and large deformation of an open-cell polyurethane foam sample

Over the past two decades, numerous studies of deformation experiments combined with *in situ* XRCT imaging on different foam materials have been carried out, e.g., Refs. 35–37. Most of these studies were limited to uniaxial loads (compression or tension). Due to their microstructure, the uniaxial compression of so-called open-cell foam structures typically results in a stress–strain curve, which can be separated into three regimes: (i) linear-elastic regime, (ii) collapse regime, and (iii) densification regime.[13,37] Due to the highly non-linear material behavior in the collapse regime, the loading sequence for combined compression–torsion loading influences the effective material response. In order to model such a sequence depending material response, the foam microstructure has to be considered and evaluated at different combined load states.

The first example demonstrates the possibility of investigating such phenomena in more detail, requiring combined loading under large deformations. For this purpose, an open-cell reticulated polyurethane (PUR) foam sample with ten pores per inch is considered. For detailed information about foam materials, in general, and, in particular, for polymer foams, it is referred to Refs. 13 and 38. To be able to impose compression, tension, and torsion on the sample, a cylindrical sample geometry is chosen. The parallel ends of a 50 mm thick piece of an open-cell reticulated polyurethane sheet were bonded using a two-component adhesive onto coaxially aligned polyvinyl chloride (PVC) sample holders. Afterward, the circular contour of the sample holders was used to bring the sample to the final cylindrical shape with a final diameter of 50 mm and length of 46.5 mm due to shrinkage caused by the adhesive. Figure 4 shows a sketch of the prepared sample.

The same sample was subjected to two different displacement- and twist-angle-controlled loading protocols, A and B. Both include

TABLE I. Load protocols A and B. For all load steps, a strain rate $|\dot{\varepsilon}_z| = 0.01$ min^{-1} and a twist angle rate $|\dot{\varphi}_z| = 1$ deg min^{-1} were used.

| Load step | Protocol A | | Protocol B | | |
	ε_z [−]	φ_z (deg)	ε_z [−]	φ_z (deg)	µXRCT scan[a]
0	0	0	0	0	A_I and B_I
1	0	20	−0.2	0	⋯
2	−0.2	20	−0.2	20	A_{II} and B_{II}
3	−0.2	0	0.1	20	⋯
4	0.1	0	0.1	0	A_{III} and B_{III}
5	0	0	0	0	A_{IV} and B_{IV}

[a]The corresponding scan was performed after applying the load step.

compression, torsion, and tension. The applied load steps are summarized in Table I.

Here, $\varepsilon_z(t) = u_z(t)/l_0$ is the axial strain given by the sample virgin length l_0 and the applied displacement $u_z(t)$ and $\varphi_z(t)$ is the angle of twist. Both depend on the time t. As it is evident, the only difference between the two protocols lies in the sequence of imposing compression and torsion as well as the sequence of torsion unloading in combination with tension. Since the warping of the end cross sections is restrained by the fixed connection to the sample holders, we are aware that axial stresses are induced under the torsion load (warping torsion). Furthermore, the compression test is influenced by the rigid fixing of the rigid connection of the foam struts to the PVC sample holders. Scans were performed from the initial state (A_I and B_I) after the combined torsion/compression loading (A_{II} and B_{II}) followed by a tensile loading (A_{III} and B_{III}) and at the end state (A_{IV} and B_{IV}). To account for viscoelastic material behavior and thus avoid motion artifacts during the scan, a relaxation time of 20 min was considered before each scan. The time interval between experiments A and B was ~12 hours.

In Figs. 5(a) and 5(b), the acquired data over time by the UTM for both loading protocols are given. The relaxation periods

are marked in gray, and the µXRCT scan periods are marked in orange. All scans were performed with identical settings. The geometric magnification was set to $M = 2.2$, resulting in a voxel size of 68 µm using the 2×2 binning mode of the Dexela 1512 detector. With this, the whole foam sample was imaged. The tube voltage and current were set to 80 kV and 135 µA. In total, 1440 projection angles and two in-plane detector positions for bad pixel compensation were employed.[26] For each projection, an exposure time of 500 ms was used.

Image processing was carried out with the academic version of Dragonfly (Version 2020.2.0.941).[39] The segmentation of the foam structure was performed by applying thresholding using Otsu's algorithm[40] to each 2D xy-slice. A morphological closing procedure followed this step in 3D with a cubic kernel of five voxels. The remaining voxel islands (26 connected) below a voxel count of nine voxels were removed afterward. In Fig. 6, a comparison of the microstructure for both loading protocols for the first three imaged time steps is given. To facilitate this comparison, a cuboid subvolume with a thickness of 6 mm covering the whole sample height and diameter was extracted from the center region and overlaid for each time step. As can be seen, the foam structure for the torsion/compression load differs depending on the loading sequence (A_{II} vs B_{II}). Comparing A_I and B_I ensures that almost the same foam structure is initially given. To further quantify this, we determine the intersection set of $A_i \cap B_i$ under the scanned conditions $i = \{I, II, III, IV\}$ and relate the resulting volume to the volume of A_i. For $i = I$, $i = III$, and $i = IV$, the relative intersection volume is 86.55%, 90.57 %, and 92.40%, whereas for $i = II$, the relative intersection volume is only 43.54%, confirming the dependence of the foam structure on the loading sequence.

Sparse graphs based on the segmented foam volumes (complete sample) might be deduced to quantify the evolving microstructure in more detail. For illustrative purposes, in Fig. 6(b), the sparse graph of the foam initial state before loading with protocol A shown in Fig. 6(a) is given together with possible geometrical definitions of the sparse graph edges. Characteristic values of the sparse graph, which potentially can describe the deformation state, are
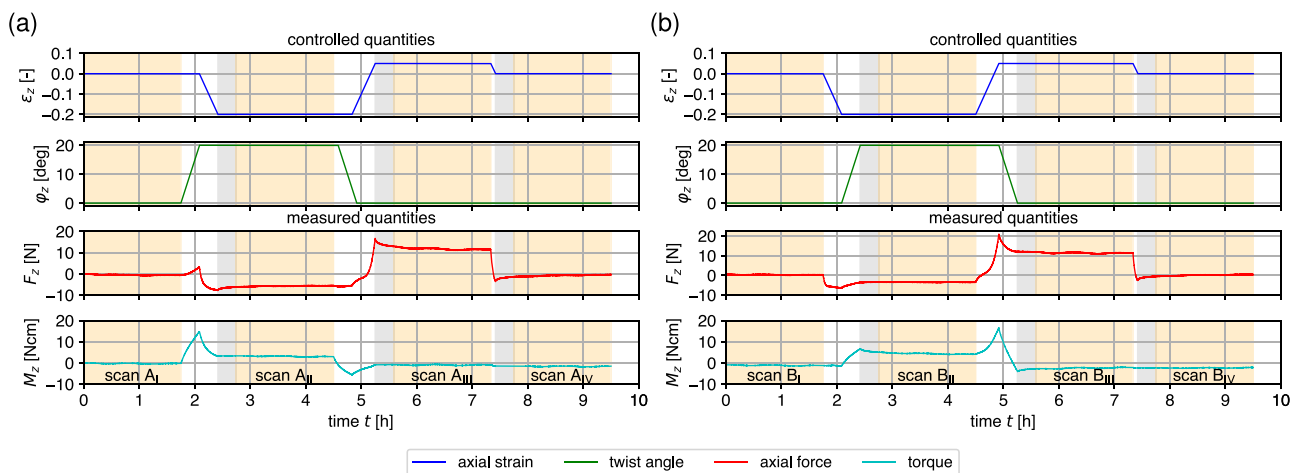
FIG. 5. Controlled and measured effective quantities during the test of the same cylindrical PUR foam sample. (a) Load protocol A. (b) Load protocol B.
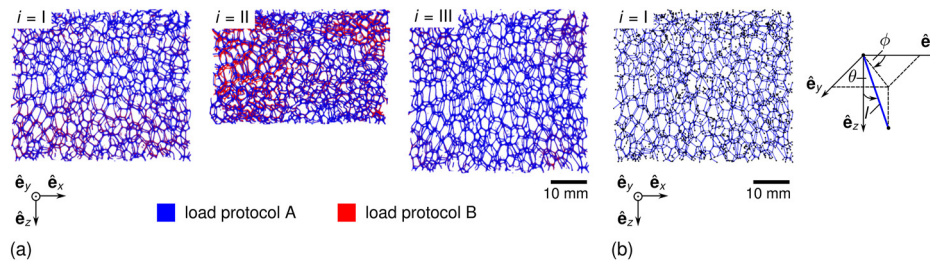
FIG. 6. (a) Comparison of the segmented PUR foam structure for both loading protocols based on a 6 mm thick rectangular cuboid subvolume in the sample's center. (b) Left: sparse graph of the subvolume of A_I. Right: geometric definitions of the sparse graph edges.

the length l_k of each edge element $k \in \{1, \ldots, K\}$ and its orientation given by the polar angle $\theta_k \in [0,90]$ deg and the azimuth angle $\phi_k \in [-90, 90)$ deg of all K edges. The undeformed sparse graph could be used to derive a micromechanical Finite Element (FE) model using beam elements for the struts, e.g., Refs. 41 and 42 and therein cited literature. Besides the effective material response, the microstructure can be characterized based on the sparse graphs for the different load steps. This modeling approach should preserve the sequence-dependent material behavior given in Fig. 5. However, it is computationally expensive. To account for this, a data-driven surrogate model could be derived and trained from the FE-model, e.g., Ref. 43 and therein cited literature, that might preserve the loading sequence behavior on the effective level. The underlying datasets of this example can be found at https://doi.org/10.18419/darus-2834.[44]

B. Study of granular media into an oedometer cell

The second example addresses the relatively straightforward implementation and integration of customized cells. The mechanical investigation of granular materials in the solid state is frequently performed in triaxial or oedometer cells to control the 3D stress/strain state. In order to obtain information about the effective structure, e.g., the small-strain stiffness, granular media are frequently characterized, employing ultrasonic wave propagation measurements.[46–48] If the bulk density ρ of the sample is known, the small-strain stiffness can be derived from the determined wave propagation velocity. For instance, the longitudinal P-wave modulus $\widetilde{M}$ is given by $\widetilde{M} = \rho v_P^2$ with the P-wave velocity v_P.

It has been shown that the effective stiffness of biphasic monodisperse particle mixtures of stiff and soft particles does not follow classical mixture rules and effective medium theories.[49] In order to investigate this kind of phenomenon further, microstructural information is necessary. Therefore, an oedometer cell with integrated P-wave ultrasonic through transmission measurement technique was designed and implemented to investigate different kinds of mixture ratios of stiff (glass) and soft (rubber) spherical particles of the same diameter (4 mm) *in situ*. In Fig. 7, the system integration as well as the design of the cell including a schematic view
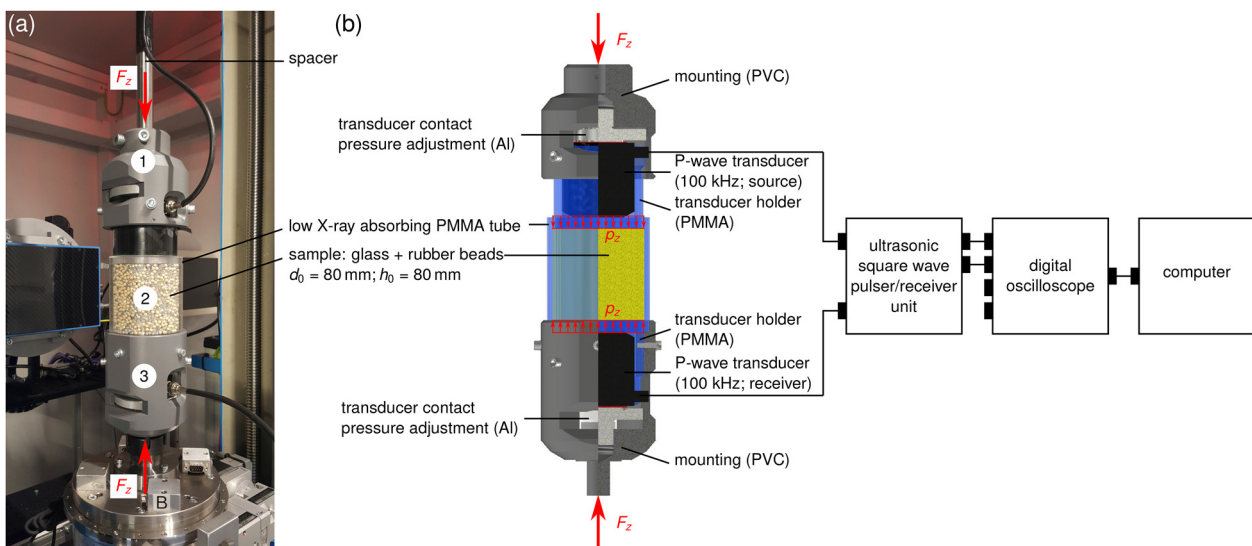
FIG. 7. Customized oedometer cell filled with a monodisperse glass–rubber particle mixture (2). To measure the sample stiffness *in situ*, ultrasonic P-wave transducers are integrated into the top part (1) and the bottom part (3) of the cell. (a) Photograph of the implemented cell into the μXRCT device. (b) Three-quarter section view of the oedometer cell in combination with the acoustic wave propagation setup.
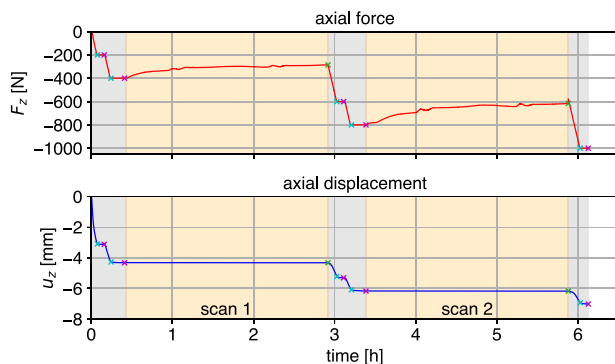
FIG. 8. *In situ* measured data for 30 volume-percent rubber particles. Controlled/measured force and displacement. Force-controlled periods are highlighted in gray, and displacement-controlled periods are highlighted in orange.

of the wave propagation measurement setup is shown. For a detailed description of the oedometer cell, the experimental setup, and the investigation, it is referred to Refs. 50 and 51.

In Fig. 8, the measured/controlled quantities by the UTM, and, in Fig. 9, the signals over time from the ultrasonic measurements are exemplarily shown for a mixture consisting of 30 volume-percent rubber particles. Stiffness measurement using the ultrasonic wave propagation technique was performed at different preload levels, $|F_z| = \{200, 400, 600, 800, 1000\}$ N, since the mixture stiffness is not only governed by the mixture ratio but also by the applied static preload F_z influencing the Hertzian contact pressure between particles.[52] As the preload increases, the travel time Δt of the P-wave decreases as obvious from Fig. 9. Consequently, the P-wave velocity $v_P = h/\Delta t$ and the P-wave modulus increase where h denotes the current sample height. In this case, the travel times Δt are determined using a peak-to-peak approach[49,52] adopted from Ref. 53. Scanning was performed *in situ* under $|F_z| = \{400, 800\}$ N with identical scan settings. For this, the geometric magnification was set to $M = 1.36$ to have the entire mixture sample into the field of view using the Dexela 1512 detector in 2×2 binning mode. This results in a voxel size of 110 μm, sufficiently high to resolve the particles accurately having a diameter of 4 mm. The tube acceleration voltage was set to 110 kV, and the tube acceleration flux was set to 110 μA in combination with a detector exposure time of 1000 ms. All remaining scan settings were chosen identically to the first application example; see Sec. III A. At each load level, the load was held (force-controlled) before measuring the mixture stiffness to account for creeping. For the μXRCT scans, it was switched to displacement-control to avoid particle movements. As can be observed in Fig. 8, some relaxation took place during the imaging. Since the particles are not bonded together, it is assumed that they may have experienced minimal vibrations and slight movement due to the error of coaxiality between the two rotation stages, causing them to settle. In the reconstructed images, no movement errors could be detected. However, the influence of the relaxation can be clearly seen in the acoustic wave propagation signals measured before and after the μXRCT scanning, cf. Fig. 9.

Besides the microstructural characterization of different mixture ratios, the non-homogeneous compaction behavior under different compression loads is crucial. For demonstrative purposes,
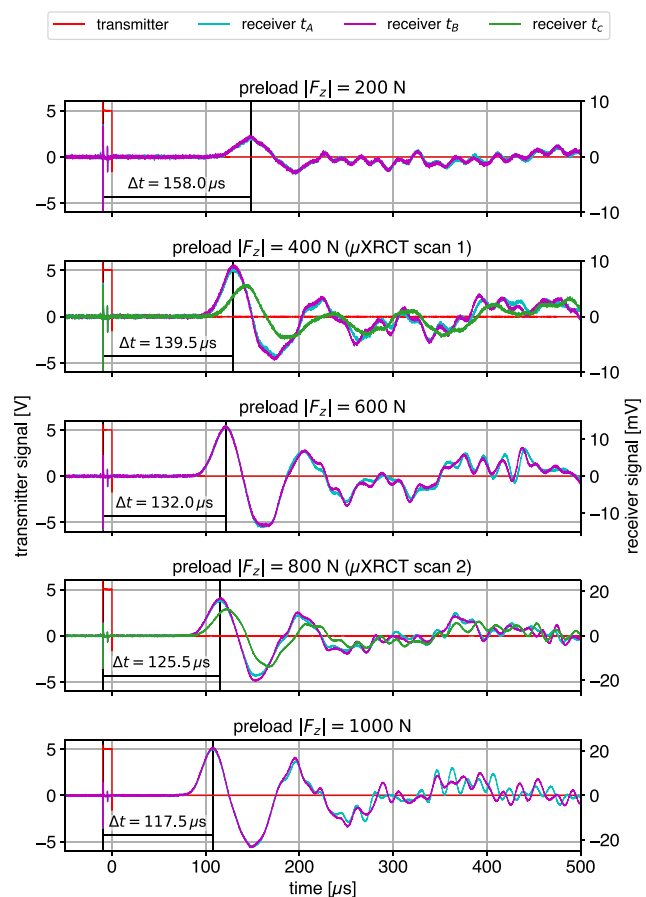
FIG. 9. *In situ* measured data for 30 volume-percent rubber particles. Recorded ultrasonic transducer signals (transmitter and receiver) for all five load steps. Receiver signals correspond with measurement time points according to Fig. 8.

in Figs. 10(a) and 10(b), the same intersection views (zx-plane, $y = 486$) under the two different preloads ($|F_z| = \{400, 800\}$ N) are shown as well as in (c) their overlay. In the latter, the movement of the particles is visible. In order to study the change in the particle network under a compression load in 3D further, particle tracking might be performed by digital volume correlation methods[54–56] implemented, e.g., in the spam library.[57] This makes it possible to quantify local deformations and to understand the particulate structure in more detail. The underlying datasets for the shown example can be found at https://doi.org/10.18419/darus-2833.[45]

C. Rock fracturing experiments in a triaxial cell

In the last example, we address high-resolution *in situ* scanning and accurate load controlling possibilities (force-/displacement-controlled) to emphasize the benefits of the integrated UTM. Additionally, the ease of design and integration of triaxial (flow) cells that benefit from the selected load frame approach is demonstrated. Such kinds of cells are required to study materials *in situ* under geological reservoir conditions (high confining and pore fluid pressure and high temperature). After presenting the design of the in-house devel-
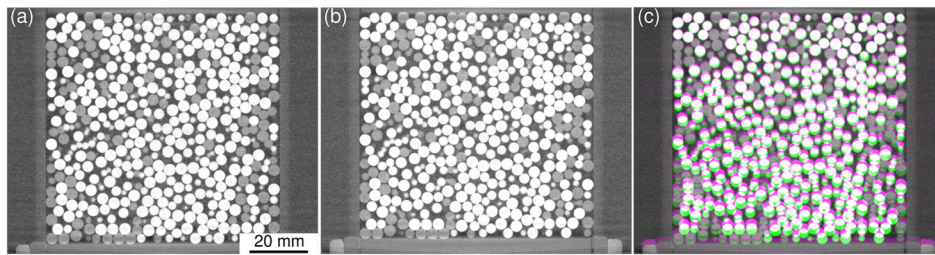
FIG. 10. μXRCT images for 30 volume-percent rubber particles (zx-slice, $y = 486$ corresponding to dataset[45] voxel coordinates). (a) Preload $|F_z| = 400$ N. (b) Preload $|F_z| = 800$ N. (c) Overlay of (a) and (b); gray regions show where the two images have the same intensities; magenta and green regions show where the intensities are different.

oped and built cell, we show first results of the implementation of a workflow to perform so-called Natural Hydraulic Fracturing (NHF) of a marine limestone core sample with a length of $l_0 = 15$ mm and a diameter $d_0 = 6.37$ mm. Since the fracturing has not yet been successful, the same sample is subsequently subjected to a Confined Compressive Strength (CCS) test.

1. Triaxial flow cell design and image acquisition settings

The developed and built low x-ray absorbing triaxial flow cell for confining pressures σ_r up to 42.5 MPa is based on the conceptual design of the flow cell presented in Ref. 59 for 1/8-in. diameter cylindrical core samples. The design was modified to control also the
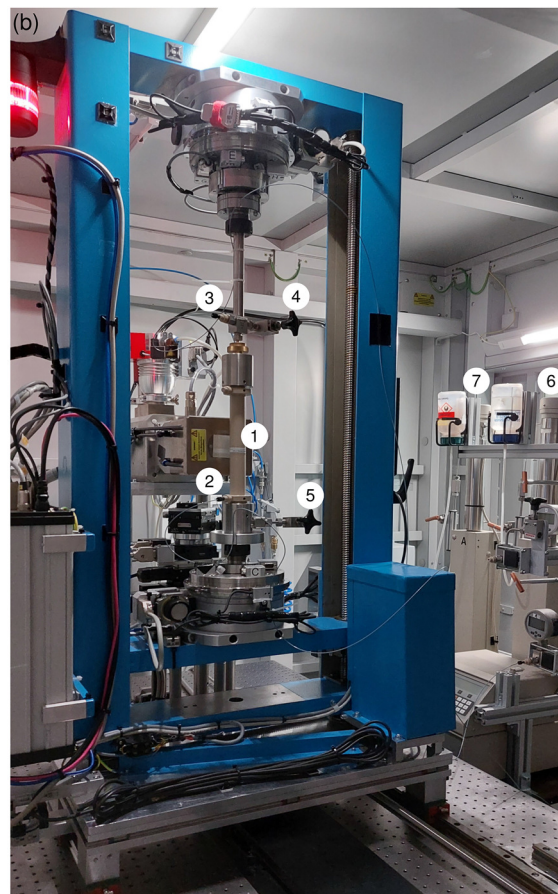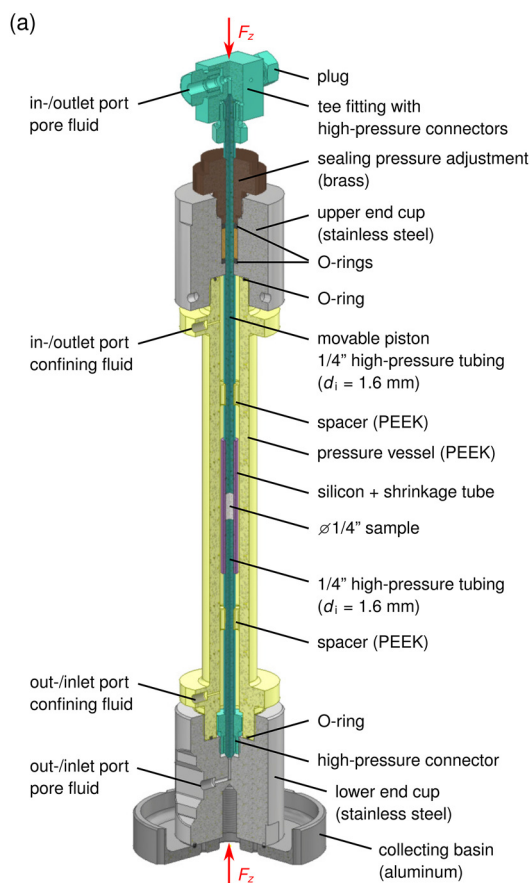
FIG. 11. (a) Low x-ray absorbing triaxial flow cell for cylindrical core samples with 1/4-in. diameter. Maximum possible confining pressure $\sigma_r = 42.5$ MPa (on the curved sample surface) and axial loading $\sigma_a = 100$ MPa. (b) *In situ* setup with the installed and connected triaxial flow cell. (1) triaxial flow cell, (2) confining fluid connection, (3) pore fluid connection, (4) pore fluid inlet valve, (5) pore fluid outlet valve, (6) syringe pump confining fluid, and (7) syringe pump pore fluid.

axial sample load σ_a in addition to the confining pressure σ_r acting on the curved sample surface and the pore fluid pressure p. For this, the design was extended by a movable upper piston loaded externally by the installed UTM, cf. Fig. 11(a). The axial loading of the sample is determined by $\sigma_a = F_z/A_0$ with the applied force F_z on the piston and the sample's cross section area $A_0 = \pi d_0^2/4$. The cell is designed for 1/4-in. cylindrical core samples to take advantage of the entire horizontal field of view of about 6 mm at the highest possible spatial resolution of the used system.[26] Furthermore, transitioning from 1/8-in. to 1/4-in. core samples simplifies and significantly improves the sample preparation and installation process with regard to accuracy and handling. The complete prepared setup with the tube connections to the two employed high-pressure syringe pumps *100DX* from Teledyne Isco, Inc., Lincoln, USA, is depicted in Fig. 11(b).

Concerning imaging, we distinguish between overview scans and detail scans in the following. Overview scans show the complete sample, and detail scans show the middle section of the sample with a higher spatial resolution. For the overview (detailed) scans, we used a geometric magnification of $M = 6.6$ ($M = 16.5$), resulting in a voxel size of 7.5 μm (3.0 μm). All other settings remained unchanged. The tube voltage and current were set to 110 kV and 110 μA, respectively. A 0.5 mm thick Al-prefilter was used to harden the x-ray spectrum.

1800 projection angles and three in-plane detector positions for bad pixel compensation were employed[26] using the Shad-o-Box 6K HS detector. For each projection, an exposure time of 2000 ms was used.

2. Natural hydraulic fracturing

Natural hydraulic fractures are inferred to form where pore pressure exceeds the least compressive stress by an amount equal to the tensile strength of the rock. An experimental protocol to produce such kinds of tensile fractures was proposed and successfully demonstrated by Ref. 60 for different rock core samples having a diameter of 50 mm and a length of 125 mm using a conventional triaxial cell. The procedure has also been successfully applied to samples with a diameter of 30 mm and a length of 75 mm. Performing the procedure *in situ* would provide, for instance, the possibility to directly characterize the fracture surface's roughness and investigate other mechanisms, e.g., leakage mitigation methods and fracture stiffness, e.g., Refs. 61–63.

The basic experimental protocol for the NHF procedure is adopted from Ref. 60. The initial boundary conditions before the NHF is performed are given by the initial axial load $\sigma_a^i = 36$ MPa, the initial confining pressure $\sigma_r^i = 38$ MPa, and an initial pore pressure $p^i = 35$ MPa. The NHF procedure is based on the fact that mechanical equilibrium is reached before hydrologic equilibrium if the pore
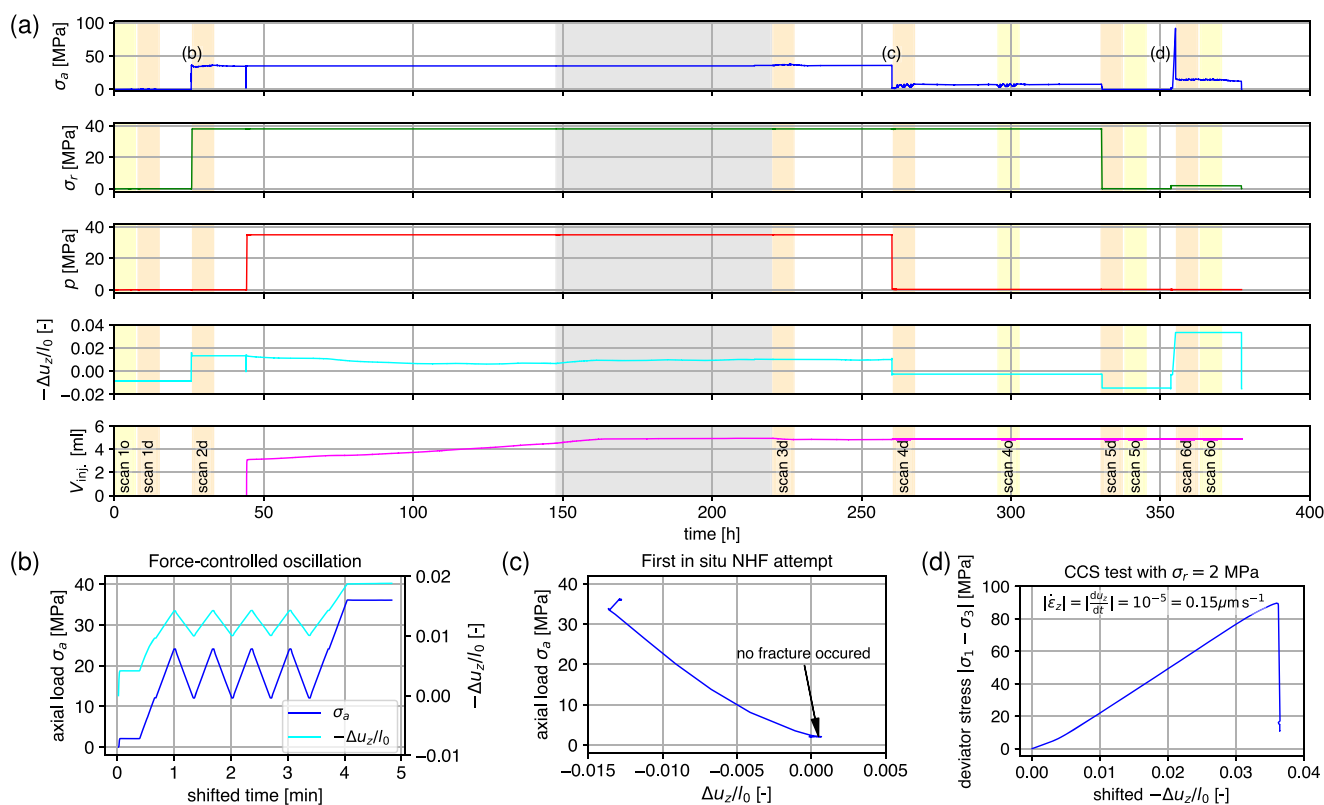
FIG. 12. (a) *In situ* controlled/measured boundary conditions of the fracturing experiment on a limestone sample. Yellow indicates acquired overview scans, and orange indicates detailed scans. (b) Force-controlled oscillating to evaluate the behavior of the piston sealing and to ensure proper contact with the sample. (c) Unsuccessful NHF attempt. (d) Successful performed CCS test until failure.

pressure at the core ends and the axial load is decreased simultaneously to $p^f = 0$ MPa and $\sigma_a^f = 2$ MPa. This results in $p > \sigma_a^f$ within the sample except close to the sample core ends for a specific time depending on the diffusivity. On the one hand, this results in a pore pressure gradient and, on the other hand, in tensile stresses in axial direction. To maintain pore pressure for some time in the sample center, we use a 73% glycerin solution as pore fluid having a viscosity of $\eta = 0.03$ Pa s[64] and consequently reduces the diffusivity. It is referred to Ref. 60 for further details about the procedure.

For the performance demonstration of the setup, scans were acquired under different sample conditions before the initial conditions for the NHF protocol were reached and after the NHF protocol was applied. The logged data of the first *in situ* attempt are given in Fig. 12(a). In addition to the axial load σ_a, the confining pressure σ_r, and the pore pressure p, the displacement Δu_z of the traverse to apply σ_a related to l_0 and the injected pore fluid volume $V_{inj.}$ are shown.

The first overview and detail scan (scan 1o and scan 1d) show the installed dry sample without loading. Before imposing the axial load σ_a^i, a contact load of $\sigma_a = 2$ MPa was established and afterward five oscillation cycles with $\sigma_a = 16 \pm 6$ MPa were run (force-controlled), Fig. 12(b). In the next step, the confining pressure $\sigma_r^i = 38$ MPa was applied. A second detail scan was performed from the dry, loaded sample (scan 2d). Subsequently, the sample was saturated pressure-controlled ($p^i = 35$ MPa) with glycerin solution. After reaching constant flow, the outlet valve was closed to achieve a uniform pressure distribution of $p^i = 35$ MPa in the sample. Both took several days due to the sample's low permeability and the high viscosity of the pore fluid. The intrinsic sample permeability under the defined loading state is given by $k = Q\eta l_0 (A_0 \Delta p)^{-1} = 1.9073 \times 10^{-18}$ m^2 based on the average volume flow rate $Q = 281.9978$ nl/min of the last 24 h before closing the outlet valve. The volume flow rate is determined based on the injected pore fluid volume $V_{inj.}$, cf. Fig. 12(a). Δp denotes the pressure difference between in- and outlet. In this state, a further detailed scan was performed (scan 3d). The NHF procedure was performed in the next step, Fig. 12(c). At the final state, $\sigma_a^f = 2$ MPa, $\sigma_r^i = 380$ MPa, and $p^f = 0$ MPa, a detail and overview scan (scan 4d and scan 4o) were acquired. A further detail and overview scan (scan 5d and scan 5o) of the completely unloaded sample were acquired to open the potentially generated fracture. Unfortunately, also in this state, no fracture could be detected. Figure 13 shows a registered representative vertical cross section of the sample during states 1, 2, 3, and 5 and the image quality. The registration was carried out with the help of the spam library.[57]

3. Confined compressive strength test

Following the unsuccessful NHF attempt in the partially saturated state, a CCS test was carried out under drained conditions, e.g., Ref. 65. Starting from a hydrostatic stress state with $\sigma_r = \sigma_a = 2$ MPa, which was held for 30 min, the axial compressive load σ_a was displacement-controlled increased
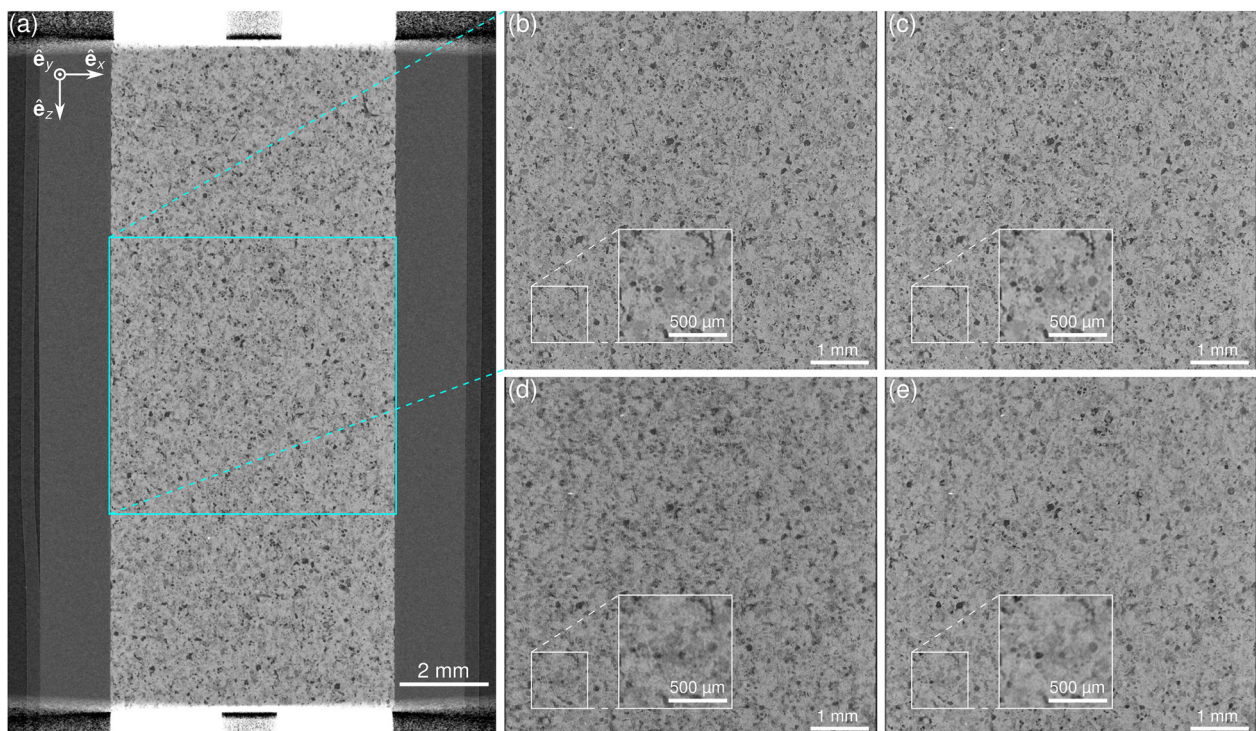
FIG. 13. (a) Overview scan ($M = 6.6$) of the initial unloaded, dry state (scan 1o). (b)-(e) Registered detailed scans ($M = 16.5$) of (b) unloaded, dry state (scan 1d), (c) loaded, dry state (scan 2d), (d) loaded, saturated state (scan 3d), and (e) unloaded, partially saturated state after NHF attempt (scan 5d).
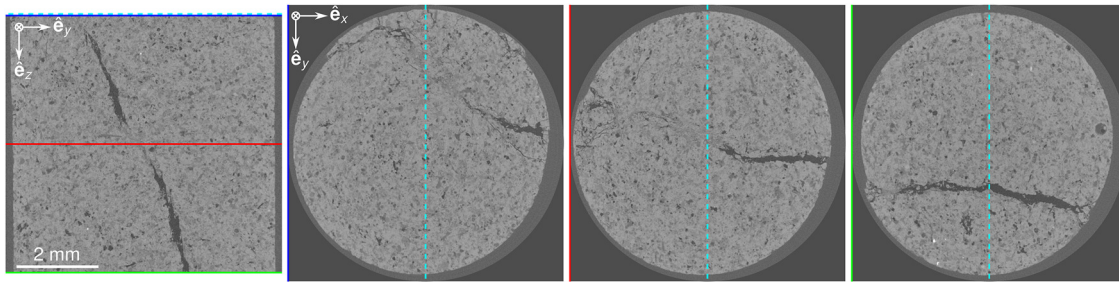
FIG. 14. Representative section planes of the detail scan (scan 6d) after CCS test. (yz-slice, $x = 1450$; xy-slices, $z = 84$, $z = 1154$, and $z = 2224$ corresponding to dataset[58] voxel coordinates.)

until failure of the sample occurred under unchanged confining stress σ_r. In Fig. 12(d), the deviatoric stress over the measured axial displacement is shown. The typical regimes compaction, linear-elastic deformation, crack-generation and stable-propagation, unstable cracks grow until failure, as well as post-failure can be identified.[66] In the post-failure regime, the experiment was stopped. Detail and overview scans (scans 6d and 6o) under the remaining strength were performed in displacement-controlled mode to visualize and investigate the generated fracture pattern. As can be seen from Fig. 14, a simple shear failure happened under a shear fracture plane angle of about 66 deg, e.g., Ref. 67. For further quantification, fracture segmentation has to be carried out, e.g., with the approach proposed by Ref. 68.

Although the NHF protocol has not yet been successful, this example demonstrates the general possibilities and the excellent quality of the recorded datasets and, consequently, the setup's potential. No restrictions concerning the controlling possibilities exist as frequently given by commercial standard compression cells, e.g., Ref. 69. The underlying datasets for the shown example can be found at https://doi.org/10.18419/darus-3106.[58]

IV. DISCUSSION AND CONCLUSION

The implementation of mechanical *in situ* investigations can be performed in different manners. The added value of data generated by *in situ* measurements is beyond question. The implementation of corresponding experiments should be as simple as possible especially in lab-based systems. Different realization possibilities were mentioned in Sec. I for the classical configuration of a stationary x-ray source. The setup presented in this contribution aims to have a modular concept based on the approach of a UTM as load frame with two integrated rotation stages. This approach leads to a versatile and extendable setup that eliminates the need for multiple individual solutions.

Three examples were given to demonstrate the broad scope of applications of the setup presented. The focus of the first example was to show the possibility of combined compression/tension and torsion loading under large deformations. Examples two and three demonstrated the integration and design of special cells typically required for porous media investigations. Since the axial load is applied externally by the UTM, the cell designs and the control

and force measurement are conceivably straightforward, which is a general advantage of the conceptual design.

The most critical part of the design is the coaxial arrangement of the upper and lower rotation stages. If this is not fulfilled, bending stresses and others are induced during the rotation for imaging, which leads to motion artifacts in the reconstructed images and unintentional stress/strain states within the sample. Since the set geometric magnification amplifies coaxial errors, even minor errors in the micrometer range can influence the results badly. While motion artifacts can be corrected within certain limits by software algorithms during reconstruction (e.g., an adjusted center of rotation in rotation axis direction), the potential additional superimposed unknown stresses/strains are more critical. Software algorithms cannot compensate for them. The high versatility of the here shown system, which offers endless possibilities, is simultaneously the most significant disadvantage in handling the error of coaxiality of the two rotation stages, mainly observable in the logging data of the UTM rather than in the image quality. The relatively large distance between the two rotational stages allows for the integration of high experimental setups (e.g., oedometer cells, triaxial cells, or oscillating setups for fatigue investigations). Therefore, using appropriate spacers is unavoidable when much shorter standard samples or shorter setups are installed. Thus, we want to address some suggestions for improvement.

The wobbling error of the upper rotational stage due to the required long spacers might be reduced by a second movable and controlled traverse. None of the implementations mentioned in the introduction, nor the few commercial systems available, have this feature, but it is considered highly useful. In addition, placing the entire setup on a vertical stage could be extremely helpful, making positioning the field of view for a loaded sample significantly more straightforward.

Due to the variable distance of the two collet chucks of the two rotation stages, a readjustment of the rotation centers to each other is nearly inevitable when changing the position. Otherwise, eccentricity problems with all consequences are the result. Therefore, integration of adjustment possibilities in the form of XY flexure elements, e.g., Refs. 70 and 71, for one of the two rotation stages could improve this problem (e.g., between the movable traverse and lower rotation stage). Integration of XY flexure elements between the collet chucks and the rotation stages to enable a more precise alignment of the sample holder interface is also recommended, com-

parable to Ref. 25. Due to the modular design of the presented setup, subsequent integration of appropriately designed flexure elements is possible without significant modifications and is planned for the near future. Appropriate calibration is envisaged, for instance, by exploiting the x-ray beam using a specially designed phantom. Even though the relatively slow rotation stages are currently not limiting with regard to planned *in situ* investigations, correspondingly faster rotation stages would simplify handling (e.g., by using a different drive concept such as DC motors).

The inherent issue of coaxiality resulting from the use of two required rotation stages within the load frame can be completely avoided by employing load cells with a low x-ray absorbing tubular load frame, directly mounted on the system's rotation stage as described in the introduction, cf. Fig. 1. In particular, this kind of implementation seems more recommendable for high-resolution scans in the single micrometer resolution range or even sub-micrometer range (e.g., using a nano-focus x-ray source) since the manufacturing accuracy is always a limiting factor of the concept using two rotation stages combined with a wide possible force range. The made error of coaxiality always has to be considered relative to the aimed spatial resolution and evaluated. To what extent the unintended superimposed stress/strain states affect the goal of the investigation is a case-by-case decision. For systems with micro-focus x-ray sources and overall system spatial resolution in the two-digit micrometer range or even higher and if a highly versatile setup is required, the presented approach is capable and recommendable especially if the suggested improvements are considered. Since the proposed approach is modular, the investment risk is comparatively low compared to highly integrated solutions. Based on the presented examples, the high potential of this approach is obvious.

A significant advantage of using a proven UTM, including its controlling system, compared to entirely developing a load frame, drive concept, and controlling system in-house is that the entire wealth of experience from these areas can be drawn upon. A middle course was taken for the apparatus designed for the research reactor FRMII (Garching near Munich).[24] Here, the mechanical parts of the apparatus are entirely customized, but for the controlling system, electronics and software from DOLI Elektronik GmbH Germany are used. Out of the box, the presented setup can be used for time-resolved mechanical testing in combination with 2D x-ray imaging. In this case, no rotation of the sample is needed, and the temporal resolution is only limited by the time needed for a single projection image (given by the detector's frame rate in combination with the x-ray power). With particular assumptions, e.g., axial symmetry of the sample state, it is possible to investigate interesting effects time-resolved in 3D, as recently proposed by Ref. 72.

ACKNOWLEDGMENTS

AUTHOR DECLARATIONS

Conflict of Interest

The authors have no conflicts to disclose.

Author Contributions

Matthias Ruf: Conceptualization (equal); Data curation (lead); Formal analysis (lead); Investigation (lead); Methodology (equal); Software (equal); Visualization (lead); Writing – original draft (lead); Writing – review & editing (lead). **Dongwon Lee**: Investigation (supporting); Software (equal); Writing – original draft (supporting); Writing – review & editing (supporting). **Holger Steeb**: Conceptualization (equal); Data curation (supporting); Formal analysis (supporting); Funding acquisition (lead); Methodology (equal); Writing – original draft (supporting); Writing – review & editing (supporting).

DATA AVAILABILITY

The image data (reconstructed datasets, projection datasets, and metadata) and measurement data of the UTM and other employed devices of all application examples that support the findings of this study are openly available in the Data Repository of the University of Stuttgart (DaRUS) at http://doi.org/10.18419/darus-2834,[44] http://doi.org/10.18419/darus-2833,[45] and http://doi.org/10.18419/darus-3106.[58]

REFERENCES

[1] P. J. Withers, C. Bouman, S. Carmignato, V. Cnudde, D. Grimaldi, C. K. Hagen, E. Maire, M. Manley, A. Du Plessis, and S. R. Stock, "X-ray computed tomography," Nat. Rev. Methods Primers **1**, 18 (2021).

[2] Y. Gao, W. Hu, S. Xin, and L. Sun, "A review of applications of CT imaging on fiber reinforced composites," J. Compos. Mater. **56**, 133–164 (2021).

[3] L. Vásárhelyi, Z. Kónya, Á. Kukovecz, and R. Vajtai, "Microcomputed tomography–based characterization of advanced materials: A review," Mater. Today Adv. **8**, 100084 (2020).

[4] E. Maire and P. Withers, "Quantitative X-ray tomography," Int. Mater. Rev. **59**, 1–43 (2013).

[5] E. N. Landis and D. T. Keane, "X-ray microtomography," Mater. Charact. **61**, 1305–1316 (2010).

[6] S. R. Stock, "Recent advances in X-ray microtomography applied to materials," Int. Mater. Rev. **53**, 129–181 (2008).

[7] G. Viggiani, E. Andò, D. Takano, and J. C. Santamarina, "Laboratory x-ray tomography: A valuable experimental tool for revealing processes in soils," Geotech. Test. J. **38**, 20140060 (2014).

[8] V. Cnudde and M. Boone, "High-resolution X-ray computed tomography in geosciences: A review of the current technology and applications," Earth-Sci. Rev. **123**, 1–17 (2013).

[9] D. Wildenschild and A. P. Sheppard, "X-ray imaging and analysis techniques for quantifying pore-scale structure and processes in subsurface porous medium systems," Adv. Water Resour. **51**, 217–246 (2013).

[10] R. Mizutani and Y. Suzuki, "X-ray microtomography in biology," Micron **43**, 104–115 (2012).

[11] L. Schoeman, P. Williams, A. du Plessis, and M. Manley, "X-ray micro-computed tomography (μCT) for non-destructive characterisation of food microstructure," Trends Food Sci. Technol. **47**, 10–24 (2016).

[12]N. Kotwaliwale, K. Singh, A. Kalne, S. N. Jha, N. Seth, and A. Kar, "X-ray imaging methods for internal quality evaluation of agricultural produce," J. Food Sci. Technol. **51**, 1–15 (2011).

[13]L. Gibson and M. Ashby, *Cellular Solids* (Cambridge University Press, 1999).

[14]*In-Situ X-Ray Tomographic Study of Materials*, edited by E. Maire, J. Adrien, and P. J. Withers (MDPI, 2020).

[15]L. Salvo, M. Suéry, A. Marmottant, N. Limodin, and D. Bernard, "3D imaging in material science: Application of X-ray tomography," C. R. Phys. **11**, 641–649 (2010).

[16]J.-Y. Buffiere, E. Maire, J. Adrien, J.-P. Masse, and E. Boller, "*In situ* experiments with X ray tomography: An attractive tool for experimental mechanics," Exp. Mech. **50**, 289–305 (2010).

[17]S. S. Singh, J. J. Williams, P. Hruby, X. Xiao, F. De Carlo, and N. Chawla, "*In situ* experimental techniques to study the mechanical behavior of materials using X-ray synchrotron tomography," Integr. Mater. Manuf. Innovation **3**, 109–122 (2014).

[18]E. Maire, C. Le Bourlot, J. Adrien, A. Mortensen, and R. Mokso, "20 Hz X-ray tomography during an *in situ* tensile test," Int. J. Fract. **200**, 3–12 (2016).

[19]A. Haboub, H. A. Bale, J. R. Nasiatka, B. N. Cox, D. B. Marshall, R. O. Ritchie, and A. A. MacDowell, "Tensile testing of materials at high temperatures above 1700 °C with *in situ* synchrotron X-ray micro-tomography," Rev. Sci. Instrum. **85**, 083702 (2014).

[20]*Industrial X-Ray Computed Tomography*, edited by S. Carmignato, W. Dewulf, and R. Leach (Springer International Publishing, 2018).

[21]S. R. Stock, *MicroComputed Tomography: Methodology and Applications*, 2nd ed. (CRC Press, Boca Raton, FL, 2019).

[22]R. Woracek, D. Penumadu, N. Kardjilov, A. Hilger, M. Strobl, R. C. Wimpory, I. Manke, and J. Banhart, "Neutron Bragg-edge-imaging for strain mapping under *in situ* tensile loading," J. Appl. Phys. **109**, 093506 (2011).

[23]R. Woracek, "Energy selective neutron imaging for the characterization of polycrystalline materialspolycrystalline material," Ph.D. thesis, University of Tennessee, 2015.

[24]M. Hoelzel, W. Gan, M. Hofmann, C. Randau, G. Seidl, P. Jüttner, and W. Schmahl, "Rotatable multifunctional load frames for neutron diffractometers at FRM II—Design, specifications and applications," Nucl. Instrum. Methods Phys. Res., Sect. A **711**, 101–105 (2013).

[25]P. A. Shade, B. Blank, J. C. Schuren, T. J. Turner, P. Kenesei, K. Goetze, R. M. Suter, J. V. Bernier, S. F. Li, J. Lind, U. Lienert, and J. Almer, "A rotational and axial motion system load frame insert for *in situ* high energy x-ray studies," Rev. Sci. Instrum. **86**, 093902 (2015).

[26]M. Ruf and H. Steeb, "An open, modular, and flexible micro X-ray computed tomography system for research," Rev. Sci. Instrum. **91**, 113102 (2020).

[27]N. Francois, R. Cruikshank, A. Herring, A. Kingston, S. Webster, M. Knackstedt, and M. Saadatfar, "A versatile microtomography system to study *in situ* the failure and fragmentation in geomaterials," Rev. Sci. Instrum. **93**, 083704 (2022).

[28]G. Shahin and R. C. Hurley, "HP-TACO: A high-pressure triaxial compression apparatus for *in situ* x-ray measurements in geomaterials," Rev. Sci. Instrum. **93**, 113907 (2022).

[29]M. Becker, "Accessing 32-bit DLLs from 64-bit code," 2007 https://blog.mattmags.com/2007/06/30/accessing-32-bit-dlls-from-64-bit-code/ (accessed May 27, 2022).

[30]M. Dunn, "Introduction to COM - what it is and how to use it," 2000 https://www.codeproject.com/Articles/633/Introduction-to-COM-What-It-Is-and-How-to-Use-It (accessed May 27, 2022).

[31]S. Garcea, Y. Wang, and P. Withers, "X-ray computed tomography of polymer composites," Compos. Sci. Technol. **156**, 305–319 (2018).

[32]P. Gajjar, J. S. Jørgensen, J. R. A. Godinho, C. G. Johnson, A. Ramsey, and P. J. Withers, "New software protocols for enabling laboratory based temporal CT," Rev. Sci. Instrum. **89**, 093702 (2018).

[33]J. Vlassenbroeck, M. Dierick, B. Masschaele, V. Cnudde, L. Van Hoorebeke, and P. Jacobs, "Software tools for quantification of X-ray microtomography at the UGCT," Nucl. Instrum. Methods Phys. Res., Sect. A **580**, 442–445 (2007).

[34]L. A. Feldkamp, L. C. Davis, and J. W. Kress, "Practical cone-beam algorithm," J. Opt. Soc. Am. A **1**, 612 (1984).

[35]B. M. Patterson, K. Henderson, R. D. Gilbertson, S. Tornga, N. L. Cordes, M. E. Chavez, and Z. Smith, "Morphological and performance measures of polyurethane foams using X-ray CT and mechanical testing," Microsc. Microanal. **20**, 1284–1293 (2014).

[36]J. Adrien, E. Maire, N. Gimenez, and V. Sauvantmoynot, "Experimental study of the compression behaviour of syntactic foams by *in situ* X-ray tomography," Acta Mater. **55**, 1667–1679 (2007).

[37]J. A. Elliott, A. H. Windle, J. R. Hobdell, G. Eeckhaut, R. J. Oldman, W. Ludwig, E. Boller, P. Cloetens, and J. Baruchel, "In-situ deformation of an open-cell flexible polyurethane foam characterised by 3D computed microtomography," J. Mater. Sci. **37**, 1547–1555 (2002).

[38]N. Mills, *Polymer Foams Handbook* (Elsevier, 2007).

[39]Object Research Systems (ORS) Inc., Montreal, Canada, "Dragonfly 2020.2.0.941 (computer software)," 2020, available online: http://www.theobjects.com/dragonfly.

[40]N. Otsu, "A threshold selection method from gray-level histograms," IEEE Trans. Syst. Man Cybern. **9**, 62–66 (1979).

[41]S. Diebels and H. Steeb, "The size effect in foams and its theoretical and numerical investigation," Proc. R. Soc. London, Ser. A **458**, 2869–2883 (2002).

[42]S. Diebels and H. Steeb, "Stress and couple stress in foams," Comput. Mater. Sci. **28**, 714–722 (2003).

[43]B. M. de Gooijer, J. Havinga, H. J. M. Geijselaers, and A. H. van den Boogaard, "Evaluation of POD based surrogate models of fields resulting from nonlinear FEM simulations," Adv. Model. Simul. Eng. Sci. **8**, 25 (2021).

[44]M. Ruf and H. Steeb, "*In situ* micro-XRCT data sets of an open-cell polyurethane foam sample under combined loading conditions (compression + torsion, tension)," DaRUS (2023).

[45]M. Ruf, K. Taghizadeh, and H. Steeb, "micro-XRCT data sets and *in situ* measured ultrasonic wave propagation of a pre-stressed monodisperse rubber and glass particle mixture with 30% volume rubber content," DaRUS (2022).

[46]X. Jia, C. Caroli, and B. Velicky, "Ultrasound propagation in externally stressed granular media," Phys. Rev. Lett. **82**, 1863 (1999).

[47]X. Jia and P. Mills, "Sound propagation in dense granular materials," in *Powders and Grains 2001* (Balkema, 2001), pp. 105–112.

[48]E. Somfai, J.-N. Roux, J. H. Snoeijer, M. Van Hecke, and W. Van Saarloos, "Elastic wave propagation in confined granular systems," Phys. Rev. E **72**, 021301 (2005).

[49]K. Taghizadeh, H. Steeb, S. Luding, and V. Magnanimo, "Elastic waves in particulate glass-rubber mixtures," Proc. R. Soc. A **477**, 20200834 (2021).

[50]M. Ruf, K. Taghizadeh, and H. Steeb, "Multi-scale characterization of granular media by *in situ* laboratory X-ray computed tomography," GAMM-Mitt. **45**, e20220001 (2022).

[51]K. Taghizadeh, M. Ruf, S. Luding, and H. Steeb, "X-ray 3D imaging–based microunderstanding of granular mixtures: Stiffness enhancement by adding small fractions of soft particles," Proc. Natl. Acad. Sci. U. S. A. **120**, e2219999120 (2023).

[52]K. Taghizadeh, H. Steeb, V. Magnanimo, and S. Luding, "Elastic waves in particulate glass-rubber mixture: Experimental and numerical investigations/studies," EPJ Web Conf. **140**, 12019 (2017).

[53]J. O'Donovan, C. O'Sullivan, G. Marketos, and D. Muir Wood, "Analysis of bender element test interpretation using the discrete element method," Granular Matter **17**, 197–216 (2015).

[54]B. K. Bay, T. S. Smith, D. P. Fyhrie, and M. Saad, "Digital volume correlation: Three-dimensional strain mapping using X-ray tomography," Exp. Mech. **39**, 217–226 (1999).

[55]T. S. Smith, B. K. Bay, and M. M. Rashid, "Digital volume correlation including rotational degrees of freedom during minimization," Exp. Mech. **42**, 272–278 (2002).

[56]S. Roux, F. Hild, P. Viot, and D. Bernard, "Three-dimensional image correlation from X-ray computed tomography of solid foam," Composites, Part A **39**, 1253–1265 (2008).

[57]O. Stamati, E. Andò, E. Roubin, R. Cailletaud, M. Wiebicke, G. Pinzon, C. Couture, R. Hurley, R. Caulk, D. Caillerie, T. Matsushima, P. Bésuelle, F. Bertoni, T. Arnaud, A. Laborin, R. Rorato, Y. Sun, A. Tengattini, O. Okubadejo, J.-B. Colliat, M. Saadatfar, F. Garcia, C. Papazoglou, I. Vego, S. Brisard,

J. Dijkstra, and G. Birmpilis, "spam: Software for practical analysis of materials," J. Open Source Softw. **5**, 2286 (2020).

[58]M. Ruf and H. Steeb, "*In situ* performed fracturing experiment of a limestone sample using an X-ray transparent triaxial cell: Micro-XRCT data sets and measurement data," DaRUS (2023).

[59]F. Fusseis, H. Steeb, X. Xiao, W. l. Zhu, I. B. Butler, S. Elphick, and U. Mäder, "A low-cost X-ray-transparent experimental cell for synchrotron-based X-ray microtomography studies under geological reservoir conditions," J. Synchrotron Radiat. **21**, 251–253 (2014).

[60]M. E. French, D. F. Boutt, and L. B. Goodwin, "Sample dilation and fracture in response to high pore fluid pressure and strain rate in quartz-rich sandstone and siltstone," J. Geophys. Res.: Solid Earth **117**, B03215 (2012).

[61]M. Umar, K. A. Kassim, and K. T. Ping Chiet, "Biological process of soil improvement in civil engineering: A review," J. Rock Mech. Geotech. Eng. **8**, 767–774 (2016).

[62]C. Kluge, G. Blöcher, H. Hofmann, A. Barnhoorn, J. Schmittbuhl, and D. Bruhn, "The stress-memory effect of fracture stiffness during cyclic loading in low-permeability sandstone," J. Geophys. Res.: Solid Earth **126**, e2020JB021469, https://doi.org/10.1029/2020jb021469 (2021).

[63]B. Li, X. Cui, L. Zou, and V. Cvetkovic, "On the relationship between normal stiffness and permeability of rock fractures," Geophys. Res. Lett. **48**, e2021GL095593, https://doi.org/10.1029/2021gl095593 (2021).

[64]N.-S. Cheng, "Formula for the viscosity of a glycerol-water mixture," Ind. Eng. Chem. Res. **47**, 3285–3288 (2008).

[65]C. McPhee, J. Reed, and I. Zubizarreta, "Geomechanics tests," in *Developments in Petroleum Science* (Elsevier, 2015), pp. 671–779.

[66]W. Li, X. An, and H. Li, "Limestone mechanical deformation behavior and failure mechanisms: A review," Acta Geochim. **37**, 153–170 (2018).

[67]B. M. Das, *Principles of Geotechnical Engineering*, 7th ed. (Wadsworth Publishing, Belmont, CA, 2009).

[68]H. Deng, J. P. Fitts, and C. A. Peters, "Quantifying fracture geometry with X-ray tomography: Technique of Iterative Local Thresholding (TILT) for 3D image segmentation," Comput. Geosci. **20**, 231–244 (2016).

[69]J. F. Van Stappen, T. De Kock, G. De Schutter, and V. Cnudde, "Uniaxial compressive strength measurements of limestone plugs and cores: A size comparison and X-ray CT study," Bull. Eng. Geol. Environ. **78**, 5301–5310 (2019).

[70]S. T. Smith, *Flexures* (CRC Press, 2000).

[71]C. Jiao, Z. Wang, B. Lv, G. Wang, and W. Yue, "Design and analysis of a novel flexure-based xy micropositioning stage," Appl. Sci. **10**, 8336 (2020).

[72]S. N. Olufsen, K. R. Tekseth, D. W. Breiby, A. H. Clausen, and O. S. Hopperstad, "A technique for *in situ* X-ray computed tomography of deformation-induced cavitation in thermoplastics," Polym. Test. **91**, 106834 (2020).

Chapter IV:
Multi-Scale Characterization of Granular Media by In Situ Laboratory X-Ray Computed Tomography

ORIGINAL PAPER

Multi-scale characterization of granular media by in situ laboratory X-ray computed tomography

Matthias Ruf[1] | **Kianoosh Taghizadeh**[1,2] | **Holger Steeb**[1,3]

[1]Institute of Applied Mechanics (CE), University of Stuttgart, Stuttgart, Germany

[2]Multiscale Mechanics (MSM), University of Twente, Enschede, The Netherlands

[3]SC SimTech, University of Stuttgart, Stuttgart, Germany

Correspondence
Matthias Ruf, Institute of Applied Mechanics (CE), University of Stuttgart, Pfaffenwaldring 7, D-70569 Stuttgart, Germany.
Email: matthias.ruf@mechbau.uni-stuttgart.de

Funding information
German Research Foundation (DFG), Grant/Award Numbers: STE 969/13-1, STE-969/16-1, 327154368

Abstract

Investigations of biphasic monodisperse soft (rubber) and stiff (glass) particle mixtures under hydrostatic conditions show an interesting behavior with regard to the effective stiffness. P-wave modulus measured by acoustic wave propagation at ultrasonic frequencies showed a significant decline while more soft particles are added, that is, higher rubber volume fractions, due to a change in the microstructure of the granular medium. However, for small volume fractions of soft particles, it could be observed that the P-wave modulus is increasing. This result cannot be explained by classical mixture rules or effective medium theories. For the understanding of those effects, a detailed insight into the microstructure of the granular medium is necessary. To gain this information and link it later back to the measured effective mechanical properties, high-resolution micro X-ray computed tomography (µXRCT) imaging is a well-established tool. With µXRCT imaging, the granular microstructure can be visualized in 3D and characterized subsequently. Combining classical effective characterization methods with µXRCT imaging can help to solve a variety of multi-scale problems. Performing the characterization step in situ, meaning inside the laboratory-based µXRCT scanner, has the advantage that exactly the same samples are mechanically characterized and visualized. To address the mentioned observation above, we designed a low X-ray absorbing oedometer cell with integrated broadband piezoelectric P-wave transducers which enables this kind of investigation inside a laboratory-based µXRCT scanner. The focus of this contribution is on the general experimental methodology which can be transferred to other multi-scale problems. It starts with a description of the image acquisition and ends with the post-processing of the in situ acquired image data. To demonstrate this, cylindrical samples consisting of the same monodisperse rubber and glass particle mixtures that were studied before under hydrostatic stress conditions are considered. Selected results are presented to explain the single steps.

KEYWORDS

granular media, wave propagation, X-ray computed tomography

1 | INTRODUCTION

Granular mixtures are of interest for a large number of fields, materials, and applications, including mineral processing, environmental engineering, geomechanics, and geophysics, and have received a lot of attention in the last decades. A specific example in geotechnical engineering is the increasing incorporation of recycled materials (e.g., shredded or granulated rubber, crushed glass) often used into conventional designs and soil improvement projects [4,12,25]. Moreover, sophisticated mixtures of asphalt and concrete are widely used to construct roads [14,15,48,61,63].

Probing a granular media with (ultra) sound waves gives useful information on the state, the structure and the mechanical properties of the bulk media as there is a one-to-one relation between a wave speed and small-strain stiffness of packings. Estimation of stiffness has traditionally been made in a triaxial apparatus using precise displacement transducers or resonant column devices [1,42]. However, these methods have a disadvantage of destructing samples, whereas ultrasonic measurements (by propagation of an elastic wave) are widely accepted for their rapid, nondestructive, and low-cost evaluation methods. Earlier studies using a wave propagation technique have shown that the dissipative, elastic and lightweight properties of materials (like soils, asphalt, etc.) can be enhanced by deliberately adding dissipative, soft, light inclusions of various types and compositions. Therefore, such a tailored system with improved material properties leads to new application designs.

To study this systematically, the simplest synthetic granular medium is a biphasic mixture of monodisperse soft and stiff particles. In [55], such mixtures under different hydrostatic stresses as well as for different volume fractions were investigated. Measured P-wave moduli showed a significant decline while more soft particles are added, that is, higher rubber volume fractions, due to a change in the microstructure of the granular medium. However, for small volume fractions of soft particles, it could be observed that the P-wave modulus is increasing which is unexpected and not covered by conventional mixture rules. Based on classical mechanical characterization methods such phenomena can be well observed and allow speculations about the physical explanation. However, these remain pure hypotheses. To understand such effects, it is required to have an insight into the microstructure on the particle scale.

There is a diverse array of experimental imaging techniques which can be exploited in order to investigate particulate systems. One of them is attenuation-based micro X-ray Computed Tomography (μXRCT) [6,7,19,41,51]. μXRCT imaging is in general a nondestructive imaging technique that offers the possibility to visualize the internal structure of objects. In contrast to other microscopy imaging methods like optical microscopy, it provides a 3-dimensional (3D) representation of the investigated sample. The method is based on the physical effect of X-ray attenuation which depends among other things on the atomic number and consequently on the chemical composition in each material point. The final, so called reconstructed 3D volume resulting from an μXRCT scan is typically represented as a stack of 2-dimensional (2D) gray value images. Through subsequent post-processing of the 3D raw image data, different material phases can be identified and subsequently segmented [16,40,44,57]. Based on the segmented 3D volume, quantifications on different length scales can be performed. One example to be mentioned on the macroscopic level is the determination of the volume fractions of the individual phases as well as their distribution. But it is also possible to obtain detailed quantities such as the coordination number of individual particles in the case of granular materials. Consequently, experimental results and observed phenomena obtained by classical characterization methods can be better and more comprehensively understood by help of μXRCT.

If μXRCT imaging is combined with classical mechanical characterization methods and performed at the same location we talk about in situ μXRCT imaging [5]. In situ imaging in contrast to running the experiments ex situ in sequential order allows that exactly the same sample is mechanically characterized and visualized. In particular, for granular media, this makes sense since each packing is more or less unique. Motivated by the example mentioned above, within this contribution the general methodology is described how such experiments can be performed in a laboratory μXRCT system. A comparable experiment was recently performed by [62]. However, the focus was on a mixture consisting of monodisperse sapphire spheres with radii between 94 and 103 μm subjected to uniaxial compression, and the experiment was performed in a synchrotron radiation facility instead of a laboratory-based setup used in the present investigation.

In the following, we start with a short overview of image-based characterization using XRCT. The combination (in situ) of this method with the traditional ultrasonic through-transmission measurement technique is the focus of Section 3. We apply this to investigate the identical monodisperse particulate systems as in [56] consisting of weak (rubber) and stiff (glass) particles of different volume fractions. We show a possible realization including the required hardware as well as the overall workflow. Based on this, some selected results of the investigation are provided in Section 4 to give a motivation of what is in general possible. The acquired experimental data for one selected mixture is open access published for

demonstrative purposes. The proposed in situ workflow is discussed in Section 5. A summary of the presented work is given in Section 6.

2 | IMAGE-BASED CHARACTERIZATION USING XRCT

The capability which µXRCT as a nondestructive imaging technique offers are meanwhile well known in many research domains and it is becoming more and more a routine microscopy technique [8,11,23,24,29,31,45,51,52]. The method is based on the revolutionary discovery of X-ray radiation by Wilhelm Röntgen in 1895 [41]. X-rays are high-energy electro-magnetic waves with a wavelength in the range of 0.01–10 nm. They have a long absorption length and interact with matter through different mechanisms (photoelectric effect, Compton scattering, Rayleigh/Thomson scattering, and pair produc-tion) [7]. Depending on the material penetrated, X-rays are attenuated to different degrees. Assuming a monochromatic X-ray beam, the Beer–Lambert law formulates mathematically the transmitted intensity I of an X-ray beam penetrating an object along the straight ray path from 0 to $\tilde{s}$ by

$$I(\tilde{s}) = I_0 e^{-\int_0^{\tilde{s}} \mu(s) ds}, \tag{1}$$

where I_0 is the initial intensity of the X-ray beam and $\mu(s)$ are the unknown local linear attenuation coefficients along the ray path [6,7,51]. If an object is irradiated from one side and the attenuated X-ray beam is measured on the opposite side by an X-ray detector, a so-called radiogram or projection image results. The distribution of the X-ray intensity I is typically represented as a gray value image as displayed in Figure 1A showing one projection image of a cylindrical sample containing monodisperse soft (rubber) and stiff (glass) particles. According to Equation (1), each pixel of such an image represents the intensity I of all attenuated X-ray photons which are captured by the specific sensor pixel during the adjusted exposure time. The darker the gray value the less the intensity I and vice versa in the radiogram. Since each pixel contains just the integral information for one specific X-ray path, it is not possible to back-calculate the unknown linear attenuation values in the material points from one radiogram. However, if a sufficiently large set of projections is taken from different directions, compare Figure 1B, enough information is available to calculate the attenuation coefficient for each material point, compare Figure 1C. The 3D distribution of the calculated attenuation coefficient then represents the inner structure of the investigated object. It is to mention, due to different reasons, that the absolute values of the 3D images are mostly only correlating with the theoretical attenuation coefficients and are not identical.

The general method for the determination of the 3D structure based on numerous projection images is called recon-struction [6,19]. To capture projections from different directions, in µXRCT imaging typically the sample is rotated, compare Figure 1A,B. The number n of required equidistant projection angles φ_i over one turn of the sample correlates with the number of detector pixel columns. The size/discretization of the 3D volume is given by the resolution of the detector. The base area (x- and y-direction) corresponds with the number of detector pixels in the horizontal direction and the maximum height (z-direction) with the number of vertical detector pixels, compare Figure 1C. Corresponding to the term pixel in 2D, in 3D the term voxel is used [40]. Assuming an identical voxel edge length, the edge length of one voxel is given by the ratio of the detector pixel size and the applied geometric magnification $M_{geo.}$. The adjustment of the magnification in a cone beam system is performed by geometric magnification. If we assume the source-detector-distance (SDD) is fixed, the geometric magnification $M_{geo.}$ is adjusted by varying the source-object-distance (SOD) and is given by the ratio $M_{geo.} = $ SDD/SOD. The maximum theoretically achievable spatial resolution correlates with the underlying focal spot size of the used X-ray source for the adjusted power setting [51]. A micro-focus X-ray source typically has a focal spot size in the micrometer range and results in a theoretical system resolution which is also in the micrometer range.

For the reconstruction itself, it is distinguished between two groups of reconstruction techniques. On the one side, there are analytical reconstruction techniques and on the other side algebraic ones, for example, [6,19]. While the first group of methods tries to solve the inverse problem analytically, the second group treats it as an optimization problem. Both have their respective advantages and disadvantages. The shape of the X-ray beam has a significant influence on the reconstruction, in particular for the analytical techniques. The ideal case of a parallel X-ray beam is only present in beamlines of synchrotron radiation facilities [37] and not given in laboratory µXRCT systems. To account for the con-ical beam shape in laboratory µXRCT systems, the so-called FDK algorithm is mostly applied. The FDK approach is a practical analytical cone-beam algorithm which goes back to Feldkamp, Davis, and Kress [10]. Independent of the used reconstruction techniques, the final raw data set consists of a stack of slices called tomograms, compare Figure 1C. The
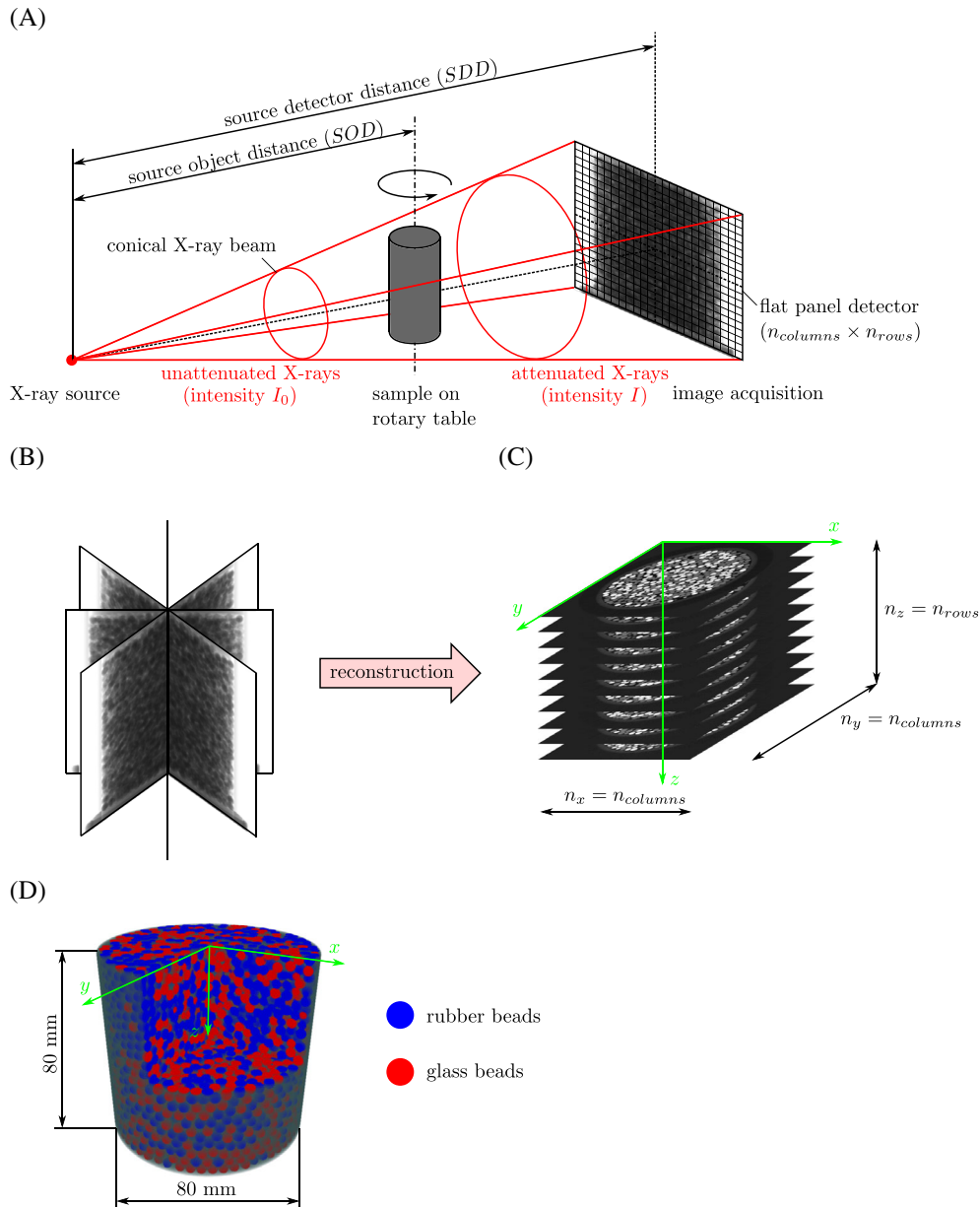
(A)

(B)

(C)

(D)

FIGURE 1   Illustration of the principle of attenuation-based X-ray computed tomography (XRCT) imaging based on the scan of a cylindrical sample of monodisperse stiff (glass) and soft (rubber) particles. (A) Cone beam μXRCT, (B) 2D projection images from n equidisant angles φ_i, (C) 3D raw volume, and (D) 3D segmented volume after post-processing

voxel values, typically represented as gray values, represent their influence on X-ray attenuation. The brighter they are the higher their influence on the X-ray attenuation corresponding with the material density. The bright gray voxels in Figure 1C correspond to the stiff (glass) particles and the dark gray ones to the (soft) rubber particles and the nearly black voxels reproduce the air phase. The reconstructed data set contains a certain amount of noise due to the procedure as well as potentially other hardly avoidable artifacts [7,41,51].

By subsequent image processing, based on the 3D raw volume, different kinds of information can be extracted from the data set. For this purpose, a so-called segmentation of the different phases is usually carried out. Segmentation is the partitioning of a gray-scale image into disjoint regions that are homogeneous with respect to some characteristics [16,41,44,57].

In the simplest case, this can be achieved by defining a threshold value, since the individual phases differ in terms of the average gray value. To determine the related threshold values, a histogram of the underlying gray value distribution of the raw data set is usually employed. The most well-known approach based on this scheme is the "Otsu

method" [36]. However, due to the intrinsic present noise in the raw data set, incorrect assignment of different individual voxels occurs. To account for this, various filtering techniques are used [16,44,57]. It is worth mentioning that in recent years, more and more image segmentation techniques using machine learning have been proposed as new approaches due to their well-known benefits [20,22]. Which phases have to be separated depends on the scientific question. Exemplary, in Figure 1D, the separation of the soft (rubber) and stiff (glass) particles, as well as the pore space (transparent), is shown.

By repeating the scanning process as well as the image processing, the evolution of physical processes (e.g., deformation, crack initiation, and growth) over time can be observed. The final result is one stack of tomograms (3D image) for each time step. What kind of processes can be observed depends on the required acquisition time for one complete scan. While acquisition times of less than one second for one complete scan are achievable in beamlines of synchrotron radiation facilities [5,13,28,37], the acquisition time in a standard lab-based μXRCT system is between some minutes up to several hours, correlating with the required scan quality. This is one limitation of physical processes which can be studied. However, processes which can be stopped in an equilibrium state are also open for investigation in a laboratory system. For time-resolved scans, the term 4-dimensional (4D) scanning (space + time) is frequently used.

3 | IN SITU EXPERIMENTAL TESTING

The combination of μXRCT imaging with classical mechanical characterization methods is an excellent technique to better understand the behavior of materials as well as physical processes in general, compare [5,49]. In this context often the term "in situ X-ray computed tomography" is used. "In situ" is a Latin phrase and translates literally to "on-site" or "on place" and is the antonym of "ex situ." In the experimental mechanics' context, it describes the way the measurement is taken, highlighting that the measurements are acquired in the same place the phenomenon is occurring without removing/installing the sample each time. Thus, in situ μXRCT means that the mechanical characterization is performed inside the scanner. It offers the possibility to enrich the information on the macroscopic level, for example, resulting from acoustic measurements as demonstrated within this contribution, with information on the microscopic level resulting from 3D imaging. In the following, we provide an overview of the applied workflow and used hardware to investigate particulate systems with acoustic wave measurements combined with in situ μXRCT imaging.

3.1 | Stiffness determination based on wave propagation measurement

Mechanical (sound) waves are disturbances that propagate through space and time in a medium in which deformation leads to elastic restoring forces. This produces a transfer of momentum and energy from one material point to another, usually involving little or no associated mass transport if the amplitude is small enough. The P-wave, or primary wave, is the fastest and the first wave detected by seismographs. They are able to move through both, solid rock as well as through liquids. P-waves are compressional or longitudinal waves that oscillate the ground back and forth along the direction of wave travel, in much the same way that sound waves (which are also compressional) move air back and forth as the waves travel from the sound source to a sound receiver. In a longitudinal wave, the particle displacement is parallel to the direction of wave propagation [30,32,33,47,53].

Quantitative ultrasonic measurement has been widely-used by different disciplines ((geo-)physics, soil and geomechanics, materials sciences, mechanical and civil engineering) to describe the small strain stiffness behavior of a particulate system, as can be found in literature [17,18,50,58]. Velocity testing by through transmission ultrasound methods has gained popularity due to its relative ease of obtaining the modulus of a sample. Figure 2 shows a schematic view of the used low-frequency ultrasound setup integrated into an oedometer cell including its electrical pieces, compare Figures 3 and 4. For our highly attenuating particulate system, it consists of a pair of 100 kHz P-wave broadband piezoelectric transducers (Olympus-Panametrics Videoscan V1011), an ultrasonic square wave pulser/receiver unit (Olympus-Panametrics 5077PR), and a digital oscilloscope (PicoScope 5444B). Piezoelectric transducers are used to determine the small-strain compression stiffness, M, of the granular system by determining the velocity of mechanical waves ("speed of sound") through the tested samples. The transducers are generally used in pairs when one transducer operates as a transmitter and the other as a receiver. The transmitting transducer is generally embedded at one end of the particulate sample and the receiving is, aligned with the transmitter, embedded at the other end. This allows to probe the stiffness of the soil or particulate sample along a given stress path. The transmitting transducer transforms the input
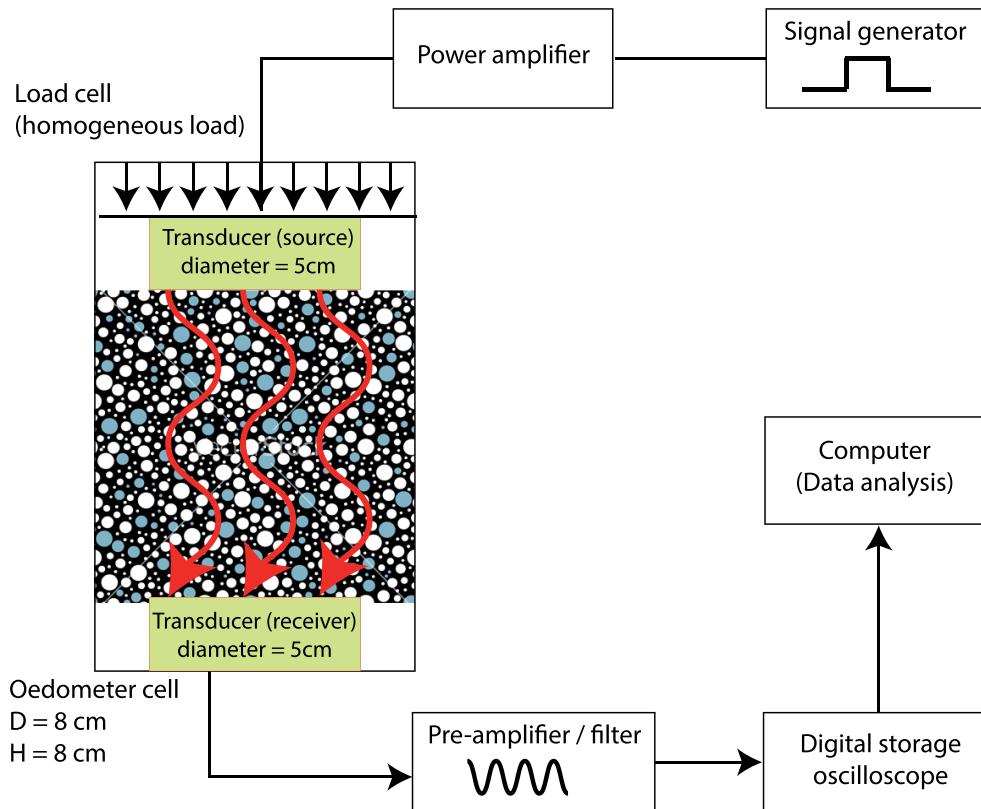
FIGURE 2 Schematic view of wave propagation measurement setup [55]

electric signal to an acoustic wave and sends it through the medium. The receiving transducer receives the propagated mechanical sound wave and transforms it back to an electronical signal which can be acquired by the digitizer, compare [27,43] for technical details on the transducers. Transducers are often incorporated in geomechanical and geophysical laboratory testing equipment such as in triaxial or oedometers cells.

The P-wave velocity (V_P) can be calculated from the travel time (t_P), given the height (H) of the sample in the actual configuration, $V_P = H/t_P$. Knowing the elastic wave velocity (V_P) and knowing the total bulk density (ρ_B) of the particulate system, the longitudinal P-wave stiffness of the sample (M) is determined, $M = \rho_B V_P^2$. In our investigations, the sample consists of monodisperse rubber and glass particles leading to a bulk density $\rho_B = \nu \rho_r + (1 - \nu)\rho_g$, where ρ_r and ρ_g are the bulk densities for 100% of rubber and glass particles, respectively. The volume fraction of the rubber particles is denoted with ν.

3.2 | μXRCT system and oedometer cell

The experimental study was performed in an open, modular, and flexible lab-based μXRCT system with an intrinsic large space allowing for the installation of a mechanical testing device required for in situ investigations. A detailed description of the system can be found in [38]. The system presented in [38] was extended by the integration of a load frame for mechanical in situ μXRCT investigations, compare Figure 3A. For this, a Zwick 1445 10 kN Universal Testing Machine (UTM), refurbished from Doli Elektronik GmbH, Germany, and equipped with a modern EDC 222V controlling system, is employed. In the UTM, two rotary tables with high loading capacities (XHuber 1-Circle Goniometer 411-X3W2) are integrated. The rotary tables are prestressed with the controlled force $F_{\text{stat.}}$ applied to the sample during the image acquisition process. The X-ray source of the system is an open micro-focus tube with tungsten transmission target (FineTec FORE 180.01C TT) from FineTec FineFocus Technology GmbH, Germany. For the image acquisition, a Dexela detector 1512NDT with GOS-based DRZ Standard scintillator option from PerkinElmer, Inc., Waltham, MA, USA is applied. To perform ultrasonic through transmission measurements in situ, a low X-ray absorbing oedometer cell was designed and manufactured in-house. Compared to a triaxial cell, only the vertical stress in the axial direction is controlled. In Figure 3,
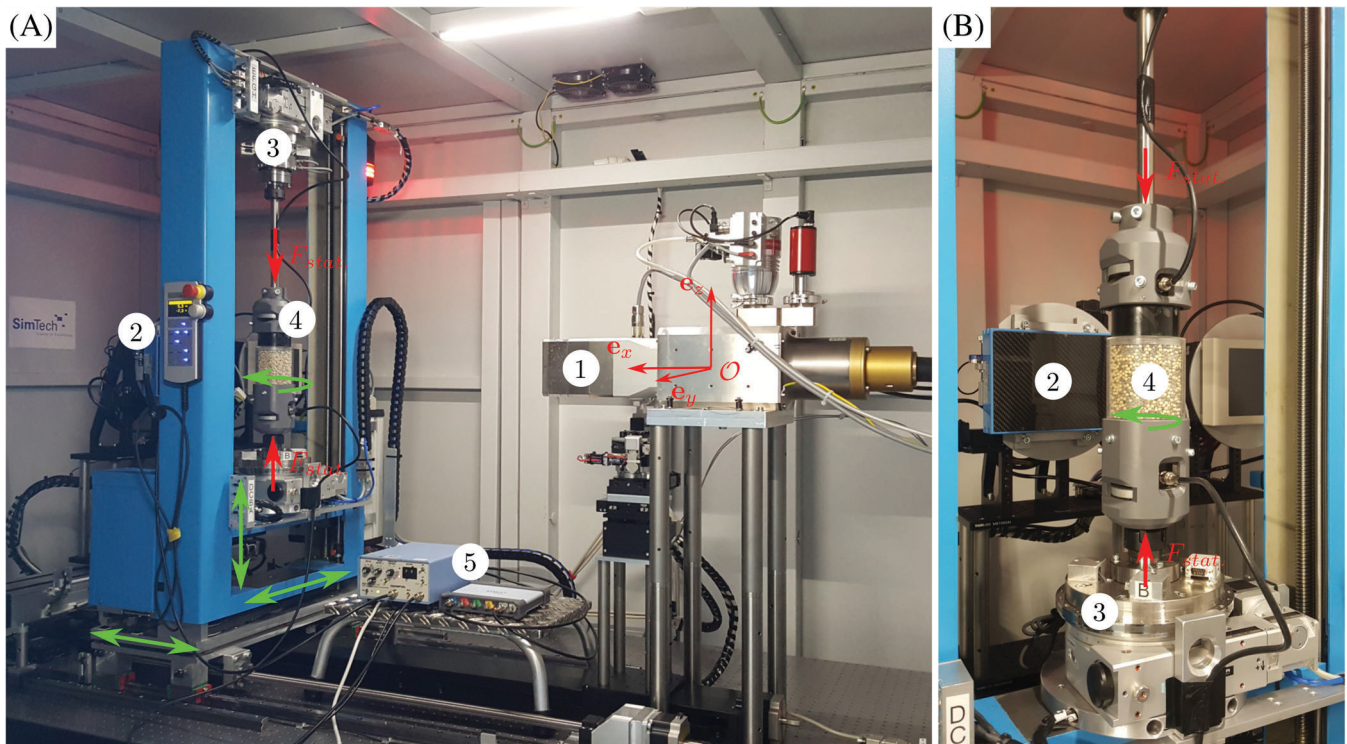
FIGURE 3 Experimental in situ setup: (1) X-ray source, (2) X-ray flat panel detector, (3) universal testing machine with synchronized rotary tables, (4) oedometer cell with integrated P-wave transducers containing monodisperse glass and rubber particles, and (5) square wave/pulser receiver unit and PC oscilloscope for ultrasonic measurements

the oedometer cell installed in the μXRCT-system and loaded by the employed universal testing device is presented. Further, the electrical devices for the ultrasonic testing corresponding to the schematic Figure 2 can be seen. A detailed view of the oedometer cell design is provided in Figure 4. The oedometer cell consists of three components. The top (1) and bottom (3) parts, both with integrated P-wave transducers, transfer the applied axial compression force $F_{stat.}$ to the sample and results in the axial stresses denoted as pressure $p_{stat.}$. As transducers, a pair of 100 kHz P-wave broadband piezoelectric transducers (Olympus-Panametrics Videoscan V1011) is employed, compare Section 3.1. For the coupling of the transducers to the poly(methyl methacrylate) (PMMA) holders of the oedometer cell, an adequate couplant fluid is used. On both sides, the wave travels through a 10 mm long PMMA distance, before and after the wave enters and leaves the sample. The contact pressure $p_{cont.}$ in between the transducers and the PMMA holders can be adjusted by an adjusting wheel. The sample is held in a rigid confining ring (2) made out of PMMA which prevents lateral displacement of the investigated mixture. Between the PMMA ring and the top and bottom part is a small gap in the radial direction to ensure that the emitted waves propagate through the sample. PMMA is used for the confining ring, as it has a very low attenuation coefficient. The inner diameter D of the PMMA ring is 80 mm. The sample height H can be varied from 70 to 80 mm.

To capture the whole cell content (diameter 80 mm; height 80 mm), a geometric magnification $M_{geo.} = 1.36$ was set for all particulate systems. This leads to a field of view of 106.92 mm × 84.48 mm. Since we are not interested in small features (bead diameter 4 mm) all projection images were acquired in 2 × 2 detector binning mode. This means, that the detector's full resolution of 1944 × 1536 pixels with 74.8 μm pixel pitch and 14-bit pixel depth is reduced to 972 × 768 pixels with a pixel size of 149.6 μm. On one side, this significantly improves the signal-to-noise ratio (SNR), and on the other side, the final tomogram data set size is reduced by factor 8. Both simplify the subsequent image processing significantly without the loss of information required for the presented study. For all scans, an acceleration voltage of 110 kV with an acceleration flux of 110 μA for the X-ray source were set. For all scans, 1440 equidistant projection angles were used in combination with a detector exposure time of 1000 ms. Further, a detector bad pixel compensation as described in [38] was employed using two different projection positions for each projection angle. The final tomogram stacks have a size of 972 × 972 × 768 voxels with the uniform voxel edge length of 110 μm. The 3D reconstruction of all scans was performed with the software Octopus Reconstruction (Version 8.9.4-64 bit) [60] using the filtered back projection (FBP) method [19]
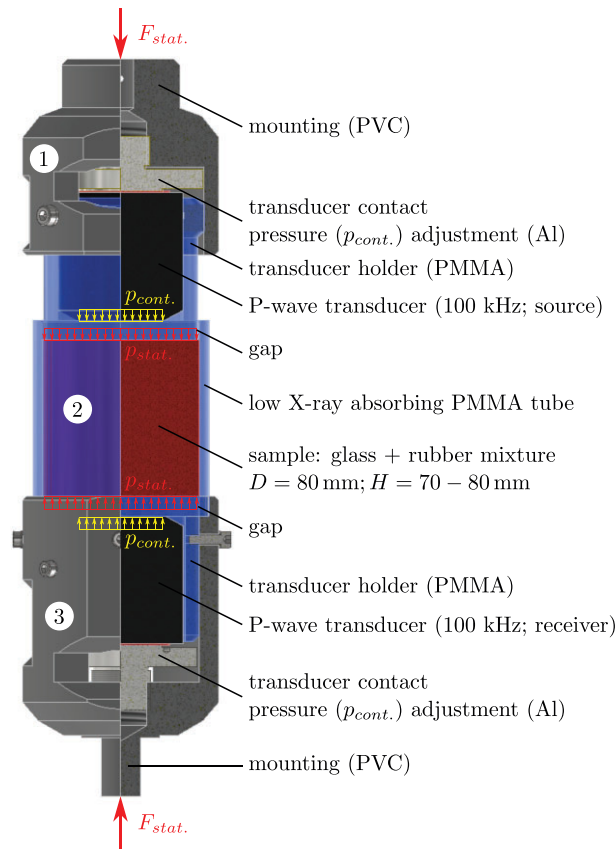
FIGURE 4 Three-quarter section view of the low X-ray absorbing oedometer cell with integrated ultrasonic transducers for in situ measurements

in combination with the FDK reconstruction algorithm [10]. To account for common artifacts in μXRCT imaging (ring artifacts and beam hardening), different types of filters were used. Based on the tomograms, segmentation is performed to distinguish between the rubber and glass beads and the remaining pore space. The segmentation workflow is described in detail in Section 3.3.

3.3 | Image analysis

Here, we present steps taken using the Dragonfly software version 2020.2 for Windows from Object Research Systems (ORS, Montreal, QC, Canada) [34], for the segmentation and the subsequent quantification of mixture samples. An important step before interpreting the data is to identify individual particles. To increase the quality of images and reduce unwanted noise, one can apply different image filtering techniques before segmenting the phases, that is, separating different objects in an image. Here, a 3D-median smoothing function with a kernel size of seven was applied on image stacks. Next, voxels of images were manually divided into three different regions of interest (air, rubber, and glass) which are used as boundaries of objects. After segmenting samples into three separate regions (air, rubber, and glass), watershed transform technique is employed on defined markers of individual particles to label every particle in the separated regimes of rubber and glass. The watershed is a classical region-based algorithm that has its origins in mathematical morphology [3,9,46,59] used for segmentation. Starting from user-defined markers, the watershed algorithm treats pixels values as a local topography (elevation). The algorithm floods basins from the markers until basins attributed to different markers meet on watershed lines. In many cases, markers are chosen as local minima of the image, from which basins are flooded.

Figure 5 shows a z-direction view of a layer of particles prepared at two rubber fractions, $\nu = 0.1$ (left) and 0.5 (right), under 800 N load in the oedometer cell. Light and dark gray pixels represent glass and rubber particles respectively in

the first row. Second row shows the segmented pixels in the regions of interests (rubber (blue) and glass (red)) for which deep learning was employed. Thanks to the watershed transform technique, particles of segmented regions are labeled individually (third row).

3.4 | Investigated particulate samples and measurement workflow

All investigated samples are made of monodisperse glass and rubber beads with 4 mm diameter. Further information on the material characteristics for both, glass and rubber beads, can be found in [55]. Particles are poured carefully into the oedometer cell described in Section 3.2. Samples are prepared at different rubber volume fractions, $v = v_r/v_c$, from $v = 0$ to 1 in 0.1 increments, where v_r is the volume possessed by the rubber particles and v_c is the total volume of particles in the oedometer cell. All mixtures are tested in the custom-made oedometer cell with the sample height (unloaded) and diameter equal to 80 mm, compare Figures 3 and 4 ex situ without imaging. The prepared samples are uniaxially compressed in the axial direction via the top piston of the oedometer cell in subsequent force increments from $F = 200$ to 1000 N. At each instant step, the system was relaxed for some time at the defined force to overcome the creep behavior of soft particles. Then, at each intermediate load step, a high voltage burst signal (P-wave) is excited from the top cap (the sound source)
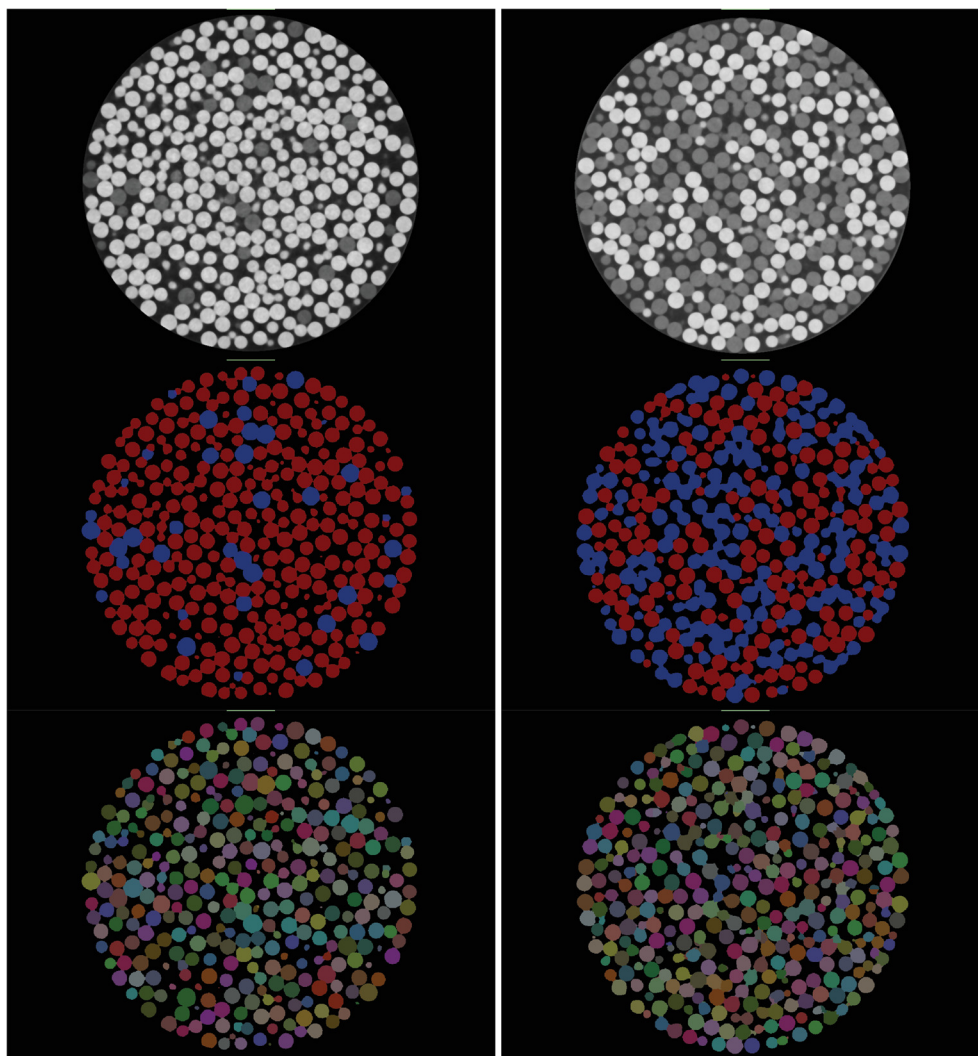
FIGURE 5 A top view of a xy-layer of particles for samples prepared with $v = 0.1$ (left column) and 0.5 (right column). Top to bottom shows the steps taken from a reconstructed raw image (first row) to segmented (second row), and labeled (third row). The 3D raw dataset for $v = 0.5$, here presented with a single slice ("slice_xy_0322.tif"), can be found in [39]

I. In situ data acquisition

1. Static preloading of granular mixture with $F_{stat.}$
2. Determination of mixture stiffness by acoustic wave propagation measurement
   - Traveling time t_P with mixture height $H \Rightarrow$ wave velocity $V_P = H/t_P$
   - Wave velocity V_P with mixture density $\rho_B \Rightarrow$ P-wave modulus $M = \rho_B V_P{}^2$
3. micro X-Ray Computed Tomography (µXRCT) scan of the preloaded mixture
   (acquisition of projections + 3D volume reconstruction with Filtered Back Projection (FBP))

II. Image data processing

4. Segmentation of soft and stiff particle phase via thresholding (different X-ray attenuation coefficients)
5. Separating of single particles by watershed algorithm $\Rightarrow$ labeling of each particle
6. Extracting information about particle contacts, networks etc.

FIGURE 6 In situ workflow summary

transducer and the bottom transducer collects the signal. To remove the influence of network configurations and user errors on outputs, each experiment was repeated at least 3 times by mounting and dismounting particles into the cell. For the calculation of the system stiffness besides the wave propagation time t_P, the exact height H of the compressed packing is required. This is determined based on the loading protocol of the UTM. Since about 2 h are needed for one µXRCT scan, only a subset of the possible combinations of the parameter space (rubber volume fraction v and preload $F_{stat.}$) were scanned in situ. µXRCT imaging was performed for a preload $F_{stat.} = 400$ N and $F_{stat.} = 800$ N in combination with rubber volume fractions $v = \{0.1, 0.2, 0.3, 0.4, 0.5, 0.6\}$. Otherwise, the procedure is identical to the previously performed ex situ measurements. During the image acquisition, it is switched from force-control to displacement-control to avoid slight movements of the particles due to relaxation processes. The selection is based on previous knowledge from comparable experiments in a triaxial cell without µXRCT imaging [55] as well as the before performed ex situ measurements in the oedometer cell. A summary of the applied in situ workflow is given in Figure 6.

4 | RESULTS—INSIGHT INTO GRANULAR MEDIA

Measurement of ultrasound velocity V_P provides complementary information about material properties, and combined use of velocity and topological structure in seismic analysis provides greater insight into the granular packings. Here, we first report the results on the bulk stiffness of granular mixtures with diverse rubber content obtained by the experimental tests. Particular attention is devoted to the dependence of sound velocity on the applied load and soft-stiff composition of samples, since this is an important controllable experimental parameter [21,26,55]. After that, X-ray images taken during wave propagation are analysed to obtain micro-insights of packings.

4.1 | Material characterization by ultrasonic measurements

Figure 7 shows the compressional modulus M determined for samples prepared with rubber fractions from $v = 0.1$ to 0.6 at five different load steps acquired in situ. The underlying data of the mixture with $v = 0.5$ (ultrasonic measurement data as well as measured force and displacement data of the UTM) together with the recorded µXRCT dataset (reconstructed data set, projection data set, and metadata) is for illustrative purposes available in [39]. M modulus shows high stiffness for rubber content up to $v = 0.3$ where the bulk behavior of samples is highly controlled by the stiff phase. Previous experimental studies under triaxial stress conditions showed already that a small amount of soft particles enhances the effective stiffness of the medium [55]. Thus, the effective stiffness of biphasic monodisperse granular mixtures consisting of stiff and soft particles does not follow a simple mixture rule. The highest modulus is observed at $v \approx 0.2$. Thus, granular

(A)

(B)
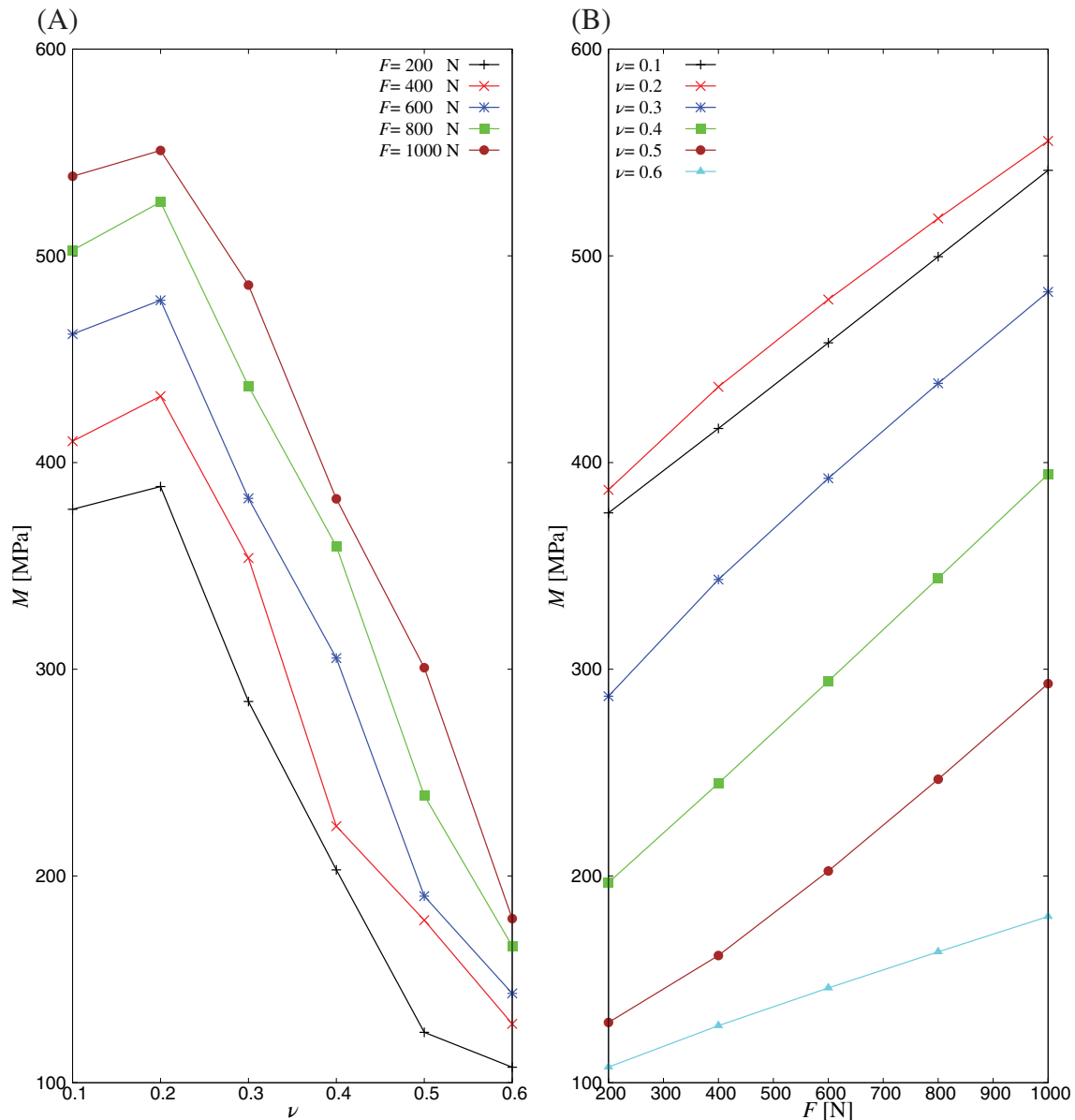
FIGURE 7 (A) In situ measured P-wave modulus M against rubber fraction ν. (B) P-wave modulus against uniaxial applied load from $F = 200$ to $1000 \, \text{N}$. The underlying measurement data for $\nu = 0.5$ is provided in [39]. For the full range of mixtures (measurements performed without imaging in a triaxial cell), see [56]

mixtures can be manipulated to obtain aggregates with even higher stiffness, but lighter and more dissipative thanks to rubber, when appropriate external conditions are matched (in this case the pressure) [21]. Increasing the amount of rubber particles, here $0.3 < \nu < 0.6$, reduces the effective stiffness where a phase transition from stiff to soft phase occurs.

4.2 | Image characterization

Progress in the application of μXRCT imaging in the field of geomechanics allows all the individual particles of packings in a test sample to be seen and identified uniquely in 3D. Combining such imaging capabilities with experiments carried out "in situ" within an imaging setup (shown in Figure 3) has led to the possibility of directly observing the topology of packings.

Granular matter has a heterogeneous nature, this is expressed as force chains through the medium. These force chains spread the forces through the contact with another particle [53,54]. This causes that neighboring particles could have forces of different magnitudes and nonisotropic distributions of stress throughout the medium [2]. This heterogeneity is manifest of the fact that granular matter exhibits a strong configuration and history dependence. One of the interesting outcomes of µXRCT imaging of particulate systems is its potential to depict contact networks which provide micro-structural information.

A 3D view of labeled particles is shown in Figure 8A for a sample prepared with $\nu = 0.5$; and the contact network of the sample is illustrated in Figure 8B. Center of particles, marked with different colors, are connected with black lines. The color code of the number of contacts follows as black (zero), magenta (one), blue (two), red (three), green (four), yellow (five), orange (six), and white (above six). Next, to enhance micro-structural investigation, glass and rubber particles are separated as a result of labelling every particles for samples with volume fraction of $\nu = 0.1$ (Figure 9) and 0.5 (Figure 10). Looking at glass (Figure 9A) and rubber (Figure 9B) networks of $\nu = 0.1$, it is not surprising to see the scatter
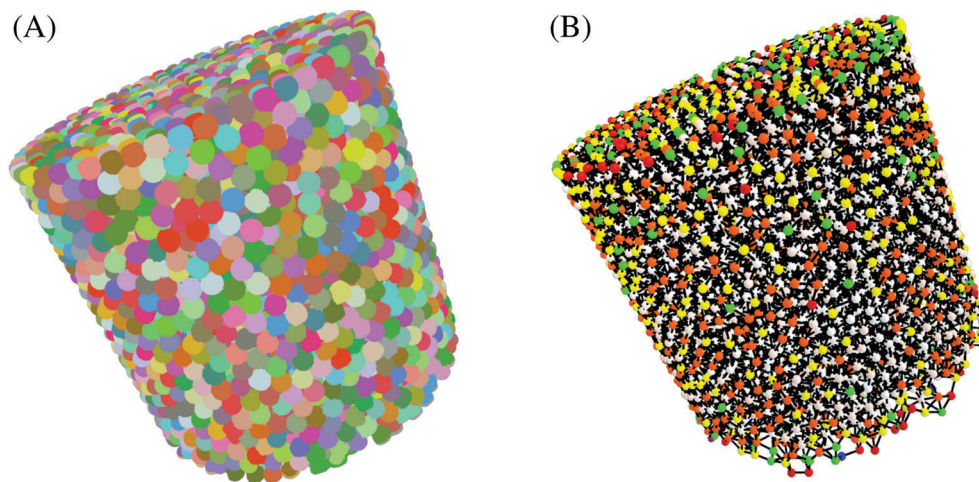
FIGURE 8 (A) 3D view of labeled particles for a sample prepared with $\nu = 0.5$. (B) The network of contacts of the sample in which different particles colors represent a number of contact each particle carries. Particles carrying zero, one, two, three, four, five, six, and above six number of contacts are colored by black, magenta, blue, red, green, yellow, orange, and white, respectively.
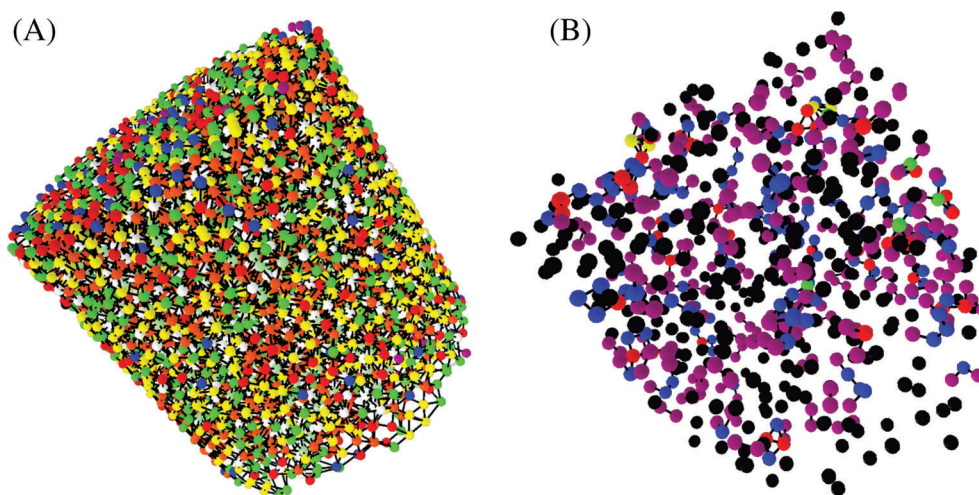
FIGURE 9 3D view of (A) glass and (B) rubber particles network for a sample prepared with rubber fraction $\nu = 0.1$, respectively. Particles center are marked with different colors based on their number of contacts and connected with black lines. Particles carrying zero, one, two, three, four, five, six, and above six number of contacts to the same particle phase are colored by black, magenta, blue, red, green, yellow, orange, and white, respectively.
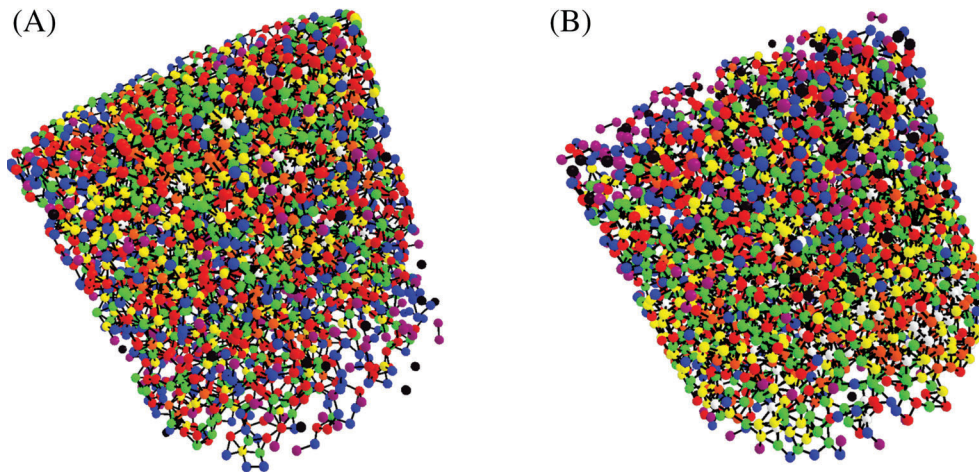
FIGURE 10 3D view of (A) glass and (B) rubber particles network for a sample prepared with rubber fraction $v = 0.5$, respectively. Particles center are marked with different colors based on their number of contacts and connected with black lines. Particles carrying zero, one, two, three, four, five, six, and above six number of contacts to the same particle phase are colored by black, magenta, blue, red, green, yellow, orange, and white, respectively.

of rubbers among glass beads. These rubbers which do not carry number of contacts above three are called rattlers. Rattlers do not transfer force between each other as their number of contact are not sufficient to form a chain of particles; whereas, moving to a sample with higher rubber fraction $v = 0.5$ (Figure 10), we do not see rattles neither in the glass and nor in the rubber networks. This observation explains why M modulus remains fairly constant for samples with low rubber volume fraction ($v \leq 0.3$) in Figure 7 since their bulk behavior is controlled by stiff particles. But in case of intermediate regime, v between 0.4 and 0.6, forces are distributed among glass and rubber chains which leads to a smaller M modulus.

5 | DISCUSSION

As is almost always the case, no experimental investigation is perfect. The problems that arise must be critically questioned with regard to their influence on the scientific question. The motivation for the presented study was given by investigations of the same kinds of mixtures in a conventional triaxial cell with well-defined boundary conditions [55]. Since it is quite more complicated to design and build such a cell that can be used in an μXRCT device, we went for an oedometer cell. As the results in Figure 7 show, we can observe the same phenomenon. As a consequence, it is an admissible simplification for the problem under investigation.

One common significant uncertainty and difficulty is associated with determining the exact wave propagation time by ultrasonic measurements required to calculate the sample stiffness. Suggested criteria and recommendations vary depending on the installation, application, and input signal. The most common methodology is to interpret the received signal in the time domain. It is typical to consider the first peak at the receiver transducer as arrival time and the required time difference minus the needed time in the other parts as the travel time of the signal within the packings [35] which was consistently done within this study. However, in particular, for high rubber packings, choosing a peak is not easy since the wave contains high-frequency tones raised from the cluster of rubber particles. Thus, a low-pass filter was applied to remove unwanted noises. For high rubber volume fractions, this is nevertheless a difficult undertaking and not completely objective. Although the same experimental protocol and measurement were applied, a user error is inevitable. To account for this, ex situ measurements were repeated three times in the past and are consistent with the in situ acquired data shown in Figure 7.

During the image acquisition period which takes up to 2 h, the piston control of the uniaxial machine was switched from force-control to displacement-control. This was done to avoid slight movements of the particles due to creeping processes caused by the (viscoelastic) rubber particles. As a result, a corresponding relaxation can be observed in the measured force. For instance, for a mixture ratio of $v = 0.5$, the measured force (stress) decreased from 400 to 340 N (80 to 68 kPa) and from 800 to 696 N (159 to 138 kPa) which means a reduction of about 15% and 13%. However, this is only slightly

critical with respect to particle movements at least in the range of resolution used. This can be confirmed by the final quality of the 3D images as well as by comparing the in situ ultrasonic measurement results with the before performed ex situ measurements. Consequently, the relatively long μXRCT scan time has no significant influence on the imaging. In the shown concept, the static preload $F_{stat.}$ is applied using a load frame, here a modified traditional universal testing machine. Consequently, two rotary tables must be used to rotate the prestressed sample. While this concept generally offers extremely great flexibility (uniaxial tension/compression and torsion) compared to specially designed load cells with integrated actuators, compare [5,49] and the literature cited therein, it also presents some difficulties. The major problem is the accurate alignment of the two rotatory tables in the micrometer range. Each eccentricity error leads either to an undefined stress state and/or to bad image quality due to potential movement errors in soft samples since the error is multiplied with the set geometric magnification ($M_{geo.}$). However, because an extremely low geometric magnification is applied here ($M_{geo.} = 1.36$) and, in addition, the individual particles are comparatively large with a diameter of 4 mm, this influence is to be classified as minor on the underlying scientific question. Although it is slightly present in the samples with a very low rubber fraction. To get completely rid of this error source the alignment of the rotary tables should be further improved which is technically challenging or alternatively, a load cell with integrated actuator could be employed. However, the latter leads to a significantly more complicated and expensive cell design. Therefore, this approach was intentionally not chosen. Common artifacts in μXRCT imaging (e.g., noise, ring artifacts, system alignment errors, and beam hardening) could be reduced to a minimum by the combined usage of hardware precautions and software-based corrections. In general, it is advantageous to use relatively large particles as in our approach, as this significantly reduces many potential sources of error.

Segmentation of μXRCT data is certainly the most critical step before quantitative analyses. Due to the good quality of the raw datasets (justifying the scanning time of 2 h), and the fact that only three high-contrast phases (air, glass, and rubber) had to be segmented, this could be accomplished with a straight forward traditional workflow. Since the exact composition of each mixture is known (total particle volume and number of particles), the segmentation and subsequent separation of the single particles could be validated quite easily on a global level. The exact deformation of the individual particles is not of interest for the presented study. Consequently, the image processing and the quantification can be judged as very reliable.

In the result part, just some selected 3D visualization of two datasets were shown. Further analysis of the 3D data has to be performed to get more information out of it and to finally link back to the observable effects on the macroscale. Since the general methodology of the experiments was the focus of this work, this was deliberately not presented here.

It can be concluded that the presented in situ setup in combination with the applied workflow is adequate to get a more comprehensive understanding of particulate systems as presented in this contribution. Further, it demonstrates that an investigation of such kinds of questions are accessible with a laboratory-based μXRCT system if some boundary conditions are fulfilled, for example, an intrinsic large space within the system.

6 | SUMMARY

Understanding the response of granular-based systems in applications requires a detailed grasp of the connection between the basic ingredients (particles) and the macroscale properties of the systems considered. These are complex systems and an understanding of the overall behavior cannot be gained by studying individual particles. While significant progress has been made during the last decades on understanding relevant physical mechanisms, there are still many open questions, starting from the physics of particle interactions to general features of multiscale models that will bridge the different spatial and temporal scales of interest. The purpose of this contribution was to describe an in situ characterization approach for the combination of traditional experimental techniques with 3D imaging in order to explore a micro-macro relation of granular assemblies.

The given work started initially with a short overview about attenuation-based μXRCT imaging in Section 2. Based on this, a detailed explanation of how μXRCT and wave propagation measuring technique are combined was demonstrated in Section 3. For this, a low X-ray absorbing oedometer cell with integrated P-wave transducers was designed and built. The cell was integrated into a modular μXRCT-system which was extended by a load frame using a refurbished universal testing machine. This approach enables applying in a flexible manner different kinds of load cases needed for advanced mechanical in situ investigations. A typical approach to segment different material phases of the 3D tomograms was explained step-by-step. The sample material chosen for the study is a composition of monodisperse granular particles,

glass, and rubber beads; not only because of the ubiquity of granular materials but also because it is a paradigm for complex disordered media and the unique characteristics exhibited by various physical phenomena associated with mechanical waves in it (dispersion, scattering attenuation, intrinsic attenuation, diffusion, weak localization, energy transfer across different frequencies, etc.).

In Section 4, the effect of rubber volume content variation of the studied glass-rubber mixtures on the compressive elastic modulus (P-wave modulus) by means of wave propagation at different uniaxial preload levels was shown. It was demonstrated that the modulus of the mixtures can be increased by adding low portions of soft particles since it is dominated by stiff particles. Adding more soft particles into assemblies led to a transition from stiff to soft dominated regime where bulk behavior of samples is mainly controlled by soft phase. The macro behavior of such granular samples can hardly be described without micro information. To gain more insights, µXRCT imaging was performed in situ for two of the five examined preloads. Analyzing images helped to understand the transition mechanism from stiff to soft controlled regime by separating glass and rubber networks. It was found that due to the isolation of rubber particles, rattlers, the samples were dominated by glass grains. Whereas, a sample with 50 % of rubber and glass has distributed number of contacts, fairly, among themselves.

The combination of experimental material characterization and image characterization techniques is a complex procedure that was explained carefully in this article. However, it could be demonstrated what incredible potential it has. In particular, since many problems from the field of mechanics are accessible in laboratory-based µXRCT systems.

CONFLICT OF INTEREST
The authors declare no potential conflict of interests.

ORCID
Matthias Ruf https://orcid.org/0000-0003-0299-5921
Kianoosh Taghizadeh https://orcid.org/0000-0003-3394-3251
Holger Steeb https://orcid.org/0000-0001-7602-4920

REFERENCES
[1] J. H. Atkinson and G. Sallfors, *Experimental determination of soil properties. General report to session 1*, Proc. 10th ECSMFE, Florence, Vol. 3, 1991, pp. 915–956.
[2] D. S. Bassett, E. T. Owens, K. E. Daniels, and M. A. Porter, Influence of network topology on sound propagation in granular materials, Phys. Rev. E **86** (2012), 041306.
[3] S. Beucher, The watershed transformation applied to image segmentation, Scanning Microsc. **1992** (1992), 28.
[4] P. J. Bosscher, T. B. Edil, and S. Kuraoka, Design of highway embankments using tire chips, J. Geotech. Geoenviron. Eng. **123** (1997), 295–304.
[5] J. Y. Buffiere, E. Maire, J. Adrien, J. P. Masse, and E. Boller, In situ experiments with X ray tomography: An attractive tool for experimental mechanics, Exp. Mech. **50** (2010), 289–305.
[6] T. M. Buzug, *Computed tomography*, Springer, Berlin Heidelberg, 2008.
[7] S. Carmignato, W. Dewulf, and R. Leach, Eds., *Industrial X-ray computed tomography*, Springer International Publishing, Berlin, Germany, 2018.
[8] V. Cnudde and M. Boone, High-resolution X-ray computed tomography in geosciences: A review of the current technology and applications, Earth Sci. Rev. **123** (2013), 1–17.
[9] H. Digabel and C. Lantuéjoul, *Iterative algorithms*, Proc. 2nd Eur. Symp. Quant. Anal. Microstruct. Mater. Sci. Biol. Med., Vol. **19**, 1978, pp. 8.
[10] L. A. Feldkamp, L. C. Davis, and J. W. Kress, Practical cone-beam algorithm, J. Opt. Soc. Am. A **1** (1984), 612.
[11] Y. Gao, W. Hu, S. Xin, and L. Sun, A review of applications of CT imaging on fiber reinforced composites, J. Compos. Mater. **56** (2021), 133–164.
[12] V. K. Garga and V. O'Shaughnessy, Tire-reinforced earthfill. Part 1: Construction of a test fill, performance, and retaining wall design, Can. Geotechn. J. **37** (2000), 75–96.

[13] S. Hasan, V. Niasar, N. Karadimitriou, J. Godinho, N. Vo, S. An, A. Rabbani, and H. Steeb, Direct characterization of solute transport in unsaturated porous media using fast X-ray synchrotron microtomography, Proc. Natl. Acad. Sci. **117** (2020), 23443–23449.

[14] T. C. Heimdahl and A. Drescher, Elastic anisotropy of tire shreds, J. Geotechnical Geoenviron. Eng. **125** (1999), 383–389.

[15] S. Hınıslıoğlu and E. Ağar, Use of waste high density polyethylene as bitumen modifier in asphalt concrete mix, Mater. Lett. **58** (2004), 267–271.

[16] P. Iassonov, T. Gebrenegus, and M. Tuller, Segmentation of X-ray computed tomography images of porous materials: A crucial step for characterization and quantitative analysis of pore structures, Water Resources Res. **45** (2009), 1–12.

[17] X. Jia, C. Caroli, and B. Velicky, Ultrasound propagation in externally stressed granular media, Phys. Rev. Lett. **82** (1999), 1863–1866.

[18] X. Jia and P. Mills, Sound propagation in dense granular materials, Powders Grains **2001** (2001), 105–112.

[19] A. C. Kak and M. Slaney, Principles of computerized tomographic imaging (classics in applied mathematics), Society of Industrial and Applied Mathematics (1987).

[20] S. Karimpouli, P. Tahmasebi, H. L. Ramandi, P. Mostaghimi, and M. Saadatfar, Stochastic modeling of coal fracture network by direct use of micro-computed tomography images, Int. J. Coal Geol. **179** (2017), 153–163.

[21] H. K. Kim and J. C. Santamarina, Sand-rubber mixtures (large rubber chips), Can. Geotechn. J. **45** (2008), 1457–1466.

[22] O. Kodym and M. Španěl, *Semi-automatic CT image segmentation using random forests learned from partial annotations*, Proc. 11th Int. Joint Conf. Biomed. Eng. Syst. Technol. BIOIMAGING, 2018:124-131; SciTePress.

[23] N. Kotwaliwale, K. Singh, A. Kalne, S. N. Jha, N. Seth, and A. Kar, X-ray imaging methods for internal quality evaluation of agricultural produce, J. Food Sci. Technol. **51** (2011), 1–15.

[24] E. N. Landis and D. T. Keane, X-ray microtomography, Mater. Charact. **61** (2010), 1305–1316.

[25] J. H. Lee, R. Salgado, A. Bernal, and C. W. Lovell, Shredded tires and rubber-sand as lightweight backfill, J. Geotechn. Geoenviron. Eng. **125** (1999), 132–141.

[26] J. S. Lee, J. Dodds, and J. C. Santamarina, Behavior of rigid-soft particle mixtures, J. Mater. Civil Eng. **19** (2007), 179–184.

[27] J. S. Lee and J. C. Santamarina, Bender elements: Performance and signal interpretation, J. Geotechn. Geoenviron. Eng. **131** (2005), 1063–1070.

[28] E. Maire, C. L. Bourlot, J. Adrien, A. Mortensen, and R. Mokso, 20 Hz X-ray tomography during an in situ tensile test, Int. J. Fract. **200** (2016), 3–12.

[29] E. Maire and P. J. Withers, Quantitative X-ray tomography, Int. Mater Rev **59** (2013), 1–43.

[30] A. Misra and N. Nejadsadeghi, Longitudinal and transverse elastic waves in 1D granular materials modeled as micromorphic continua, Wave Motion **90** (2019), 175–195.

[31] R. Mizutani and Y. Suzuki, X-ray microtomography in biology, Micron **43** (2012), 104–115.

[32] O. Mouraille and S. Luding, Sound wave propagation in weakly polydisperse granular materials, Ultrasonics **48** (2008), 498–505.

[33] V. F. Nesterenko, Propagation of nonlinear compression pulses in granular media, J. Appl. Mech Tech. Phys. **24** (1984), 733–743.

[34] Object Research Systems (ORS) Inc, Dragonfly 3.1 (computer software)., Montreal, Canada. http://www.theobjects.com/dragonfly.

[35] J. O'Donovan, C. O'sullivan, G. Marketos, and D. M. Wood, Analysis of bender element test interpretation using the discrete element method, Granul. Matter **17** (2015), 197–216.

[36] N. Otsu, A threshold selection method from gray-level histograms, IEEE Trans. Syst. Man Cybern. **9** (1979), 62–66.

[37] P. S. Rahimabadi, M. Khodaei, and K. R. Koswattage, Review on applications of synchrotron-based X-ray techniques in materials characterization, X-Ray Spectrom **49** (2020), 348–373.

[38] M. Ruf and H. Steeb, An open, modular, and flexible micro X-ray computed tomography system for research, Rev. Sci. Instr. **91** (2020), 113102.

[39] M. Ruf, K. Taghizadeh, and H. Steeb, 2021. Micro-XRCT data sets and in situ measured ultrasonic wave propagation of a pre-stressed monodisperse rubber and glass particle mixture with 50% volume rubber content. DaRUS. https://doi.org/10.18419/darus-2208.

[40] J. C. Russ and F. B. Neal, *The image processing handbook*, 7th ed., CRC Press, Boca Raton, FL, 2016.

[41] P. Russo, Ed., *Handbook of X-ray imaging: Physics and technology*, CRC Press, Boca Raton, FL, 2018.

[42] J. Santamarina and M. Aloufi, Small strain stiffness: A micromechanical experimental study, Proc. Pre-Failure Deform. Char. Geomater. **1** (1999), 451–458.

[43] A. Sawangsuriya, "*Wave propagation methods for determining stiffness of geomaterials,*" *Wave processes in classical and new solids*, edited by London, IntechOpen, London, UK, 2012, pp. 157–200.

[44] S. Schlüter, A. Sheppard, K. Brown, and D. Wildenschild, Image processing of multiphase images obtained via X-ray microtomography: A review, Water Resources Res. **50** (2014), 3615–3639.

[45] L. Schoeman, P. Williams, A. du Plessis, and M. Manley, X-ray micro-computed tomography (μCT) for non-destructive characterisation of food microstructure, Trends Food Sci. Technol. **47** (2016), 10–24.

[46] J. Serra, Introduction to mathematical morphology, Comput. Vision, Graph. Image Process. **35** (1986), 283–305.

[47] R. K. Shrivastava and S. Luding, Effect of disorder on bulk sound wave speed: A multiscale spectral analysis, Nonlinear Processes Geophys. **24** (2017), 435–454.

[48] R. Siddique and T. R. Naik, Properties of concrete containing scrap-tire rubber–An overview, Waste Manag. **24** (2004), 563–569.

[49] S. S. Singh, J. J. Williams, P. Hruby, X. Xiao, F. D. Carlo, and N. Chawla, In situ experimental techniques to study the mechanical behavior of materials using X-ray synchrotron tomography, Integr. Mater. Manuf. Innovat. **3** (2014), 109–122.

[50] E. Somfai, J. N. Roux, J. H. Snoeijer, M. Van Hecke, and W. Van Saarloos, Elastic wave propagation in confined granular systems, Phys. Rev. E **72** (2005), 021301.

[51] S. R. Stock, *MicroComputed tomography: Methodology and applications*, CRC Press, Boca Raton, FL, 2008.

[52] S. R. Stock, Recent advances in X-ray microtomography applied to materials, Int. Mater. Rev. **53** (2008), 129–181.

[53] K. Taghizadeh, R. K. Shrivastava, and S. Luding, Stochastic model for energy propagation in disordered granular chains, Materials **14** (2021), 1815.

[54] K. Taghizadeh, H. Steeb, and S. Luding, Energy propagation in 1D granular soft-stiff chain, EPJ Web Conf. **249** (2021), 02002.

[55] K. Taghizadeh, H. Steeb, S. Luding, and V. Magnanimo, Elastic waves in particulate glass-rubber mixtures, Proc. Royal Soc. A **477** (2021), 20200834.

[56] K. Taghizadeh, H. Steeb, V. Magnanimo, and S. Luding, Elastic waves in particulate glass-rubber mixture: Experimental and numerical investigations/studies, EPJ Web Conf. **140** (2017), 12019.

[57] M. Tuller, R. Kulkarni, and W. Fink, "*Segmentation of X-ray CT data of porous materials: A review of global and locally adaptive algorithms,*" *Soil–water–root processes: Advances in tomography and imaging*, John Wiley & Sons, Hoboken, NJ, 2013, pp. 157–182.

[58] S. Van den Wildenberg, A. Tourin, and X. Jia, Sound velocity fluctuations in confined granular materials: Coarse-graining lengths and elastic heterogeneities, EPL (Europhys. Lett.) **115** (2016), 34005.

[59] L. Vincent and P. Soille, Watersheds in digital spaces: An efficient algorithm based on immersion simulations, IEEE Trans. Pattern Anal. Mach. Intell. **13** (1991), 583–598.

[60] J. Vlassenbroeck, M. Dierick, B. Masschaele, V. Cnudde, L. Van Hoorebeke, and P. Jacobs, Software tools for quantification of X-ray microtomography at the UGCT, Nucl. Instr. Methods Phys. Res. Sect. A Acceler. Spectrom. Detect. Assoc. Equip. **580** (2007), 442–445.

[61] F. Xiao, S. Amirkhanian, and C. H. Juang, Rutting resistance of rubberized asphalt concrete pavements containing reclaimed asphalt pavement mixtures, J. Mater. Civil Eng. **19** (2007), 475–483.

[62] C. Zhai, E. B. Herbold, and R. C. Hurley, The influence of packing structure and interparticle forces on ultrasound transmission in granular media, Proc. Natl. Acad. Sci. **117** (2020), 16234–16242.

[63] J. G. Zornberg, A. R. Cabral, and C. Viratjandr, Behaviour of tire shred sand mixtures, Can. Geotechn. J. **41** (2004), 227–241.

Appendix

Appendix A:
Digital Rock Physics Applied to Squirt Flow

Check for updates

Digital rock physics applied to squirt flow

Simón Lissa[1], Matthias Ruf[2], Holger Steeb[3], and Beatriz Quintal[1]

ABSTRACT

We have developed a workflow for computing the seis mic wave moduli dispersion and attenuation due to squirt flow in a numerical model derived from a micro X ray com puted tomography image of cracked (through thermal treat ment) Carrara marble sample. To generate the numerical model, the image is processed, segmented, and meshed. The finite element method is adopted to solve the linearized, quasistatic Navier Stokes equations describing laminar flow of a compressible viscous fluid inside the cracks coupled with the quasistatic Lamé Navier equations for the solid phase. We compute the effective P and S wave moduli in the three Cartesian directions for a model in dry condi tions (saturated with air) and for a smaller model fully sa turated with glycerin and having either drained or undrained boundary conditions. For the model saturated with glycerin, the results indicate significant and frequency dependent P and S wave attenuation and the corresponding dispersion caused by squirt flow. Squirt flow occurs in response to fluid pressure gradients induced in the cracks by the imposed de formations. Our digital rock physics workflow can be used to interpret laboratory measurements of attenuation using images of the rock sample.

INTRODUCTION

The characterization of fluid saturated rocks plays a fundamental role in several activities such as monitoring of CO_2 geologic seques tration, geothermal energy production, exploration, and production of oil and gas (Klimentos, 1995; Metz et al., 2005; Tester et al., 2007). Seismic waves are known to be affected by rock hetero geneities as well as by the fluid in the pore space; therefore, seismic

methods are important tools for inferring rock and fluid properties. At the microscale, pores and cracks are examples of rock hetero geneities. In fluid saturated rocks, and considering seismic wave lengths much bigger than the pore sizes, a physical phenomenon known as squirt flow results in seismic attenuation and velocity dispersion (O'Connell and Budiansky, 1977; Murphy et al., 1986). In this process, the deformation of compliant flat pores (pores having a low aspect ratio, such as cracks and grain contacts) produced by a passing seismic wave, creates a fluid pressure gra dient between the deformed pore and another stiffer pore if they are hydraulically connected. Then, during fluid pressure diffusion, friction within the viscous fluid dissipates energy. The frequency dependent seismic response of squirt flow has been studied analyti cally (O'Connell and Budiansky, 1977; Mavko and Jizba, 1991; Dvorkin et al., 1995; Gurevich et al., 2010), numerically (Quintal et al., 2016, 2019; Das et al., 2019; Alkhimenkov et al., 2020a, 2020b; Lissa et al., 2020), and experimentally (Pimienta et al., 2015a, 2015b; Subramaniyan et al., 2015; Borgomano et al., 2019; Chapman et al., 2019).

Digital rock physics (DRP) studies aim to numerically reproduce laboratory measurements of rock properties based on high resolu tion rock images. Examples of rock properties obtained through DRP are pore space geometry (Arns et al., 2005; Golab et al., 2010), hydraulic permeability (Fredrich et al., 1993; Sain et al., 2014), electrical conductivity (Arns et al., 2001), and elastic rock moduli (Arns et al., 2002; Saenger et al., 2011; Madonna et al., 2012; Saxena and Mavko, 2016), among others (e.g., Sommacal et al., 2016). Considering that those properties can be obtained on the same sample, one of the most important advantages of DRP is its potential for finding relations between the obtained prop erties. DRP also provides a detailed insight into the studied physics at the pore scale and can be used as a feasibility analysis for plan ning laboratory experiments. However, the method has limitations, such as the lack of software and hardware capabilities for consid ering big enough models, the limited resolution in imaging, and

errors in the segmentation processes. These constraints commonly result in differences between laboratory measurements and numeri cal estimations (Dvorkin et al., 2011; Andrä et al., 2013a, 2013b). As an example, Sarout et al. (2017) invert the geometric crack prop erties (crack density, aspect ratio, and aperture) of a thermally treated Carrara marble sample from the elastic moduli measured in the laboratory. The inferred crack parameters were significantly lower (one order of magnitude for crack aperture and aspect ratio) than those obtained from segmented 2D microscope images or 3D micro X ray computed tomography (μXRCT) images of the same rock sample by Delle Piane et al. (2015). The cause of this differ ence was attributed to the imaging technique, which is not capable of resolving the smallest heterogeneities of the rock, such as the roughness of crack walls. These limitations represent a fundamental challenge for obtaining accurate DRP results.

A well known representation of a pore geometry in which squirt flow takes place is a compliant, or low aspect ratio, pore that is hy draulically connected to an isometric pore (Murphy et al., 1986; Gurevich et al., 2010). Another classic pore geometry in which squirt flow takes place is interconnected cracks (e.g., O'Connell and Budiansky, 1977). In this scenario, given the orientation of two interconnected cracks, one of them will be more deformed by the passing wave due to its orientation and this will induce a fluid pressure gradient between cracks and thus dissipation.

Recently, Das et al. (2019) present a DRP analysis of a squirt flow scenario. They use the finite element method to study the fluid dynamics at the pore scale accounting for inertial effects and fluid pressure diffusion. They apply their workflow to a 3D model de rived from a μXRCT image of Berea sandstone and show fluid pres sure gradients in the pore space. However, all of the pores present in their model have relatively large aspect ratios; consequently, they observe negligible P wave modulus dispersion and attenuation due to squirt flow. Quantitative DRP analysis of energy dissipation due to squirt flow remains elusive and in need of further devel opment.

In this work, we present a novel and detailed workflow for nu merically obtaining seismic wave moduli dispersion and attenuation caused by squirt flow on models derived from a μXRCT image of a rock sample having interconnected cracks. For this, a sample of Carrara marble is thermally treated, which initiates cracks at the grain boundaries as a consequence of the anisotropic thermal expan sion of the grains; subsequently, a μXRCT image of the sample is obtained (Ruf and Steeb, 2020a). Filtering, segmentation, and meshing procedures are applied on a subvolume of the rock image to create the 3D numerical model. We provide a detailed description of the model generation workflow. We then solve the coupled Lamé Navier and Navier Stokes equations in the solid and the fluid domains, in the frequency domain, neglecting inertia terms and us ing the finite element method (Quintal et al., 2019). This numerical solution is based on an upscaling procedure in which the hetero geneous medium behaves as an effective homogeneous viscoelastic medium (Jänicke et al., 2015), which allows us to obtain the P and S wave moduli dispersion and attenuation. First, we consider the model in dry conditions to analyze the model size effects on the P and S wave velocities by comparing results from the full model with results obtained from a subvolume. The same subvolume is then analyzed under full saturation with glycerin to compute attenu ation and dispersion considering drained and undrained boundary conditions. A visualization of the fluid pressure and energy dissi

pation rate in the cracks allow for a better understanding of the squirt flow process.

WORKFLOW

Sample preparation and imaging

In this study, we focus on the attenuation and dispersion of seis mic wave moduli due to squirt flow occurring between hydrauli cally connected cracks. The first step of the work consists of creating a homogeneous, hydraulically connected crack network in an almost nonporous Carrara marble sample. Carrara marble is composed almost entirely of calcite and was proven to be a very suitable material for this purpose; see, for example, Peacock et al. (1994), Delle Piane et al. (2015), and Sarout et al. (2017) because it combines several positive aspects such as a high mineral purity, very low porosity, and permeability.

From a Carrara marble block with thickness of 80 mm, a cylin drical core with a diameter of 30 mm and a length of 80 mm is extracted by using a water cooled diamond drill. Afterward, we ap ply a thermal treatment to artificially create the required crack net work, which is an often applied method in experimental rock physics (Brotons et al., 2014; Delle Piane et al., 2015; Sarout et al., 2017; Pimienta et al., 2019). For this, the sample is heated up with a heating rate of 3 K/min from room temperature (20°C) to 600°C. We use 600°C as maximum temperature to achieve a maximum effect regarding the initiated crack network volume, but avoiding the cal cite decomposition, which significantly starts above 600°C (Rodri guez Navarro et al., 2009). The heating rate is a compromise between the needed time for the heating up period and preventing high temperature gradients inside the sample. To ensure a uniform temperature distribution within the sample, the maximum temper ature is held for 2 h as shown in Sarout et al. (2017). Then, the sample is slowly cooled down to room temperature, which is per formed inside the turned off but still closed furnace, which does not allow a direct control of the cooling rate. The resulting maximum cooling rate is approximately 6.1 K/min and directly occurs after the switching off. With the help of this treatment, cracks are formed at the grain boundaries as a consequence of the anisotropic thermal expansion of the calcite grains during the heating up phase (Clarke, 1980; Evans and Clarke, 1980; Fredrich and Fong Wong, 1986), which is in general also responsible for the physical weathering of marbles (Siegesmund et al., 2000). Because the thermal aniso tropic expansion of the grains depends on the temperature, the ap plied maximum temperature can be used to influence the initiated crack network volume as experimentally shown, for instance, by Pimienta et al. (2019).

For measuring the bulk volume change, a perfect cylindrical shape of the sample was assumed and the sample's length and diam eter were measured before and after the thermal treatment with a micrometer caliper with precision of 0.001 mm. The applied ther mal treatment leads to a bulk volume increase of approximately 2.05% under ambient conditions as a consequence of the created crack network volume.

Because we are interested in very small features, it is essential to extract a small sample for the μXRCT imaging from the thermally treated sample. In our case, a cylindrical core with a diameter of 5 mm and a length of approximately 10 mm is extracted by again susing a water cooled diamond drill. An illustration of the μXRCT data set is shown in Figure 1. To better show the homogeneous dis

tribution of cracks, a partial volume is removed. It is possible to observe the initiated crack network (pore space), mainly located at the grain contacts, in dark gray, and the calcite grains in lighter gray. The imaging process results in a voxel size of 2 μm. Further details regarding this process can be found in Appendix A.

Image denoising and segmentation

Considering that applying our workflow to the whole image volume depicted in Figure 1 is computationally very costly, we only analyze two subvolumes. Figure 2 shows a quarter of one slice of the raw μXRCT data set. The orange box pictures the location of the big volume considered in our analysis, which is defined by $x = [1858, 2158]$, $y = [1620, 1920]$, and $z = [135, 435]$ of the open access images provided by Ruf and Steeb (2020a). The location of the small model is shown by the green box defined by $x = [1858, 2008]$, $y = [1620, 1770]$, and $z = [135, 285]$. The cubes have 150^3 and 300^3 voxels (or 300 and 600 μm side), respectively. For image processing, segmentation, and surface meshing, we use AVIZO 2019.1.

Image denoising

A subvolume of the raw μXRCT image is imported. The *nonlocal means* filter (Buades et al., 2005; Gastal and Oliveira, 2012), which is included in the *sandbox filter*, is used for denoising. The filter works assigning a weight to each voxel based on the similarity of its gray value and the neighborhood voxels inside certain window. A voxel having neighbor voxels with gray values similar to its own gray value receives a high weight. Then, a weighted average is computed for assigning a new gray intensity value to each voxel. The application of this filter increases the contrast between the grain and the cracks, simplifying the subsequent image segmentation. The filter parameters used are a 10 pixel disk shape search windows in the xy plane with a local neighborhood of 1.0, and a similarity value of 0.8. The result of its implementation can be observed in Figure 3 in comparison with the raw image for one slice of the cube. Most of the dark gray values located on the grains have been assigned with lighter gray values, whereas the dark gray values located on the cracks remain intact. Figure 4 shows the normalized histograms of the raw and filtered images. It is possible to observe an increase in the number of voxels having light gray values corresponding to the grains (i.e., the histogram peak), as well as a decrease in the number of voxels having dark gray values.
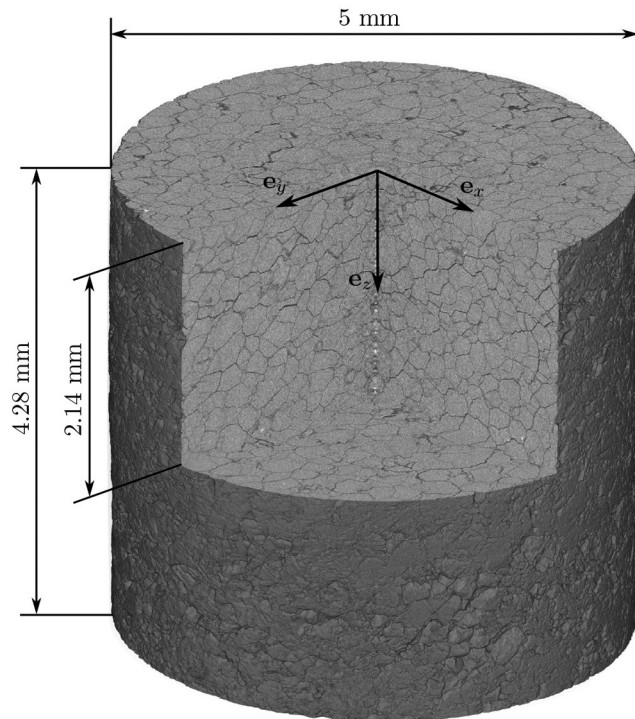
Segmentation

Using the histograms of the images, an initial selection of the grain phase is manually made. That is the gray intensity values in the range of [0.4 1.0] in Figure 4, which includes the histogram peak. As a result, almost all grains and a significant part of the cracks are selected. Then, to identify the cracks by separating the grains, the *separate objects* module is used. This module creates a map of distances from the inner part of each grain as input to a watershed algorithm (e.g., Beucher and Meyer, 1993; Ohser and Schladitz, 2009). The voxels located at the maximum distances from the inner part of the grains are removed from the grain phase and assigned with a new phase constituting the cracks. The outcome is a suspension, given that there are no contact areas between grains anymore. For fixing this, we delete from the crack phase (and assign to the grain phase) the parts of the cracks having the lightest gray values of the image histogram. Those parts are all the voxels with a gray intensity value located on the right of the red dotted line shown in Figure 4. After this, we obtain a segmentation of two phases

Figure 1. Illustration of the resulting μXRCT data set of the thermally treated Carrara marble core sample with microcracks along the grain boundaries (Ruf and Steeb, 2020a) and definition of the underlying voxel coordinate system used here.
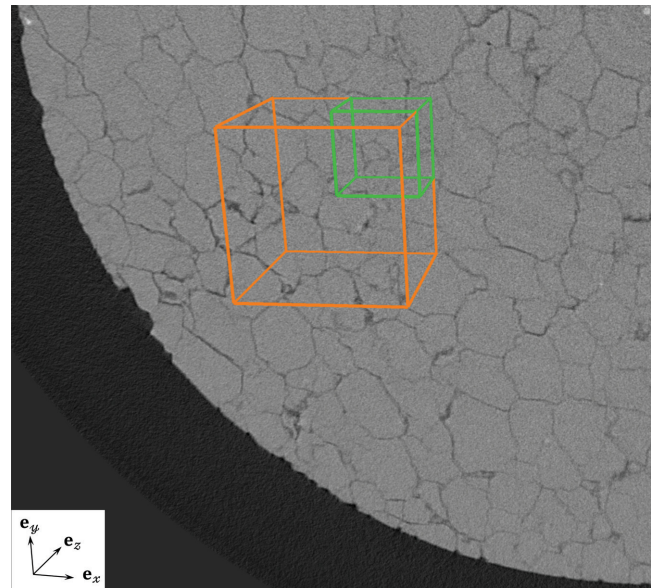
Figure 2. A quarter of the slice 135.tif of the thermally treated Carrara marble μXRCT data set (Ruf and Steeb, 2020a). The cubes show locations of the subvolumes considered in our analysis having 300 μm side (the green cube) and 600 μm side (the orange cube).
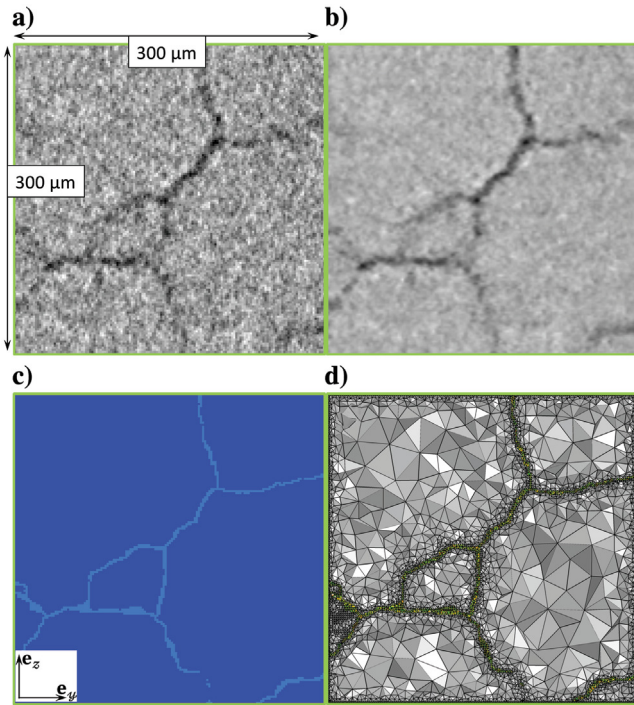
a)   b)

c)   d)

Figure 3. Cross section (*yz* plane) for *x* = 1974 of the small sub volume used in our analysis showing the image processing steps. (a) Raw, (b) filtered, (c) segmented, and (d) meshed.
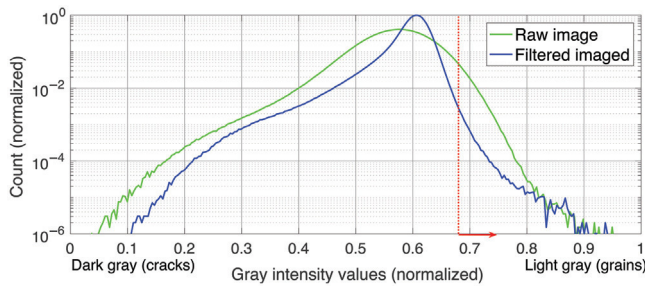

Figure 4. Histograms of the gray intensity values of the raw (green) and filtered (blue) images. The dotted red line corresponds to the selected cutoff (selecting the voxels having gray intensity values in the red arrow direction) to create contact areas between grains during the segmentation process.

(cracks and grains) having thin cracks and contact areas between grains. At this stage, it is possible to find a small number of voxels corresponding to one phase completely surrounded by voxels cor responding to the other phase. These isolated small number of vox els, or islands, would have negligible effects on the analyzed physics and would still require an important number of mesh ele ments. For reducing the required mesh elements of the numerical models, we segment as grains all the isolated pore space and as pores all the isolated grains whose volume is lower than 50 voxels (or 400 μm^3 approximately) by using the module *remove islands*. Figure 3 shows one slice of the segmented cube. Figure 5 shows the segmented cubes that are formed only by the elastic solid grains (transparent gray) and the pore space (blue). The latest corresponds to the cracks initiated along the grain boundaries.

Meshing the numerical models

After the segmentation process, each segmented cube is con verted into a surface format in AVIZO using the *generate surface* module. This module creates triangular elements on every surface between the two segmented phases and on the boundaries of the cubes. The total number of triangular elements constituting the sur faces is 0.9 million for the small model. In the case of the big model, we implement the *remesh surface* module for reducing the number of triangles (by increasing their sizes) from 6 to 1.8 million. The model surfaces are exported as **.stl* files. Note that, at this stage, we have only the grain phase and cube boundaries meshed with triangular elements.

We import the **.stl* files in COMSOL Multiphysics version 5.5 directly into the *mesh* tab. The *detect boundaries* option is used, using a minimum angle of 30° and keeping the default option for the remaining parameters. This criterium properly imports the smallest element of the surface mesh and avoids the intersection between elements that can be created using the minimal elements importing option. Then, the *create domains* module is applied be fore to create a free tetrahedral volumetric mesh. It assigns a domain number to each closed surface. Given that for our model the grains are fully connected, as well as the cracks, the number of domains is two. The big model cannot be analyzed under glycerin saturation conditions due to computational limitations and the *extremely coarse* size for the tetrahedral elements is selected for the crack and grain domains. Considering the attenuation mechanism intended to be studied in our work, the energy dissipation takes place inside the cracks. Therefore, the *extremely fine* size for the mesh is selected

a)   b)
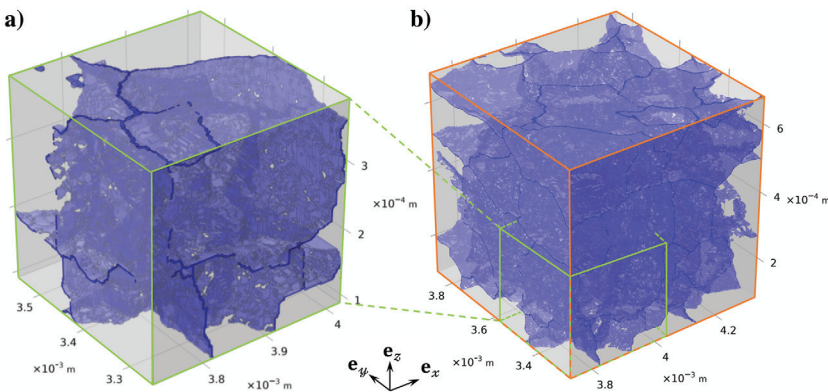
Figure 5. Cubes derived from the μXRCT images with dimensions of (a) 300 μm side and (b) 600 μm side showing the two segmented phases: the pore space (blue) and the solid grain (transparent gray).

inside the cracks for the small model, which will be analyzed under glycerin saturation. For reducing the number of elements of the mesh, the *extremely coarse* size of the tetrahedral elements is selected for the grains. Figure 6 shows the mesh for the small model colored by the skewness quality property, which is a measure of the skew of the mesh element angles with respect to the ones of an ideal element. The total number of elements is approximately 4.5 million for the small model and 6.3 million for the big model. Quadratic shape functions are used, and approximately 18 and 26 million degrees of freedom are solved for the small and big models, respectively.

Numerical solution

We use the linearized, quasistatic Navier Stokes equations to describe the laminar flow of a compressible viscous fluid inside the cracks and pores, coupled with the quasistatic Lamé Navier equations, for a linear elastic solid (Quintal et al., 2016, 2019). The equations are solved in the frequency domain, and the mathematical formulation is described in Appendix B.

To emulate the deformation caused by either a P or S wave in any direction, we apply an harmonic displacement perpendicular (for a P wave) or parallel (for a S wave) to one boundary of the model. In addition, we consider either drained or undrained boundary conditions, as the pore space is completely filled with a fluid (air or glycerin). For instance, for the P wave in the z direction under drained conditions, no displacements in the x and y direction are allowed on the grains at the lateral boundaries (i.e., no constrains on the cracks allowing fluid flow at the boundaries) and no displacements in any direction are allowed at the bottom boundary (i.e., the boundary opposite to that where a perpendicular displacement is applied). To obtain the undrained response we apply the same conditions, but to both grains and cracks on the lateral boundaries. In the case of the S wave shearing the plane xz under drained conditions, the displacements in the y direction are set to zero on the grains at the lateral boundaries and the displacements in all directions are set to zero at the bottom (opposite side). To obtain the undrained response on the lateral boundaries too, we wrap the model with a thin layer (2 μm) of a solid elastic material with properties K = 10 GPa and μ = 10 GPa.

After the numerical simulations, we can calculate the effective complex P wave (H) and S wave (μ) moduli and the corresponding seismic attenuation (Q^{-1}) as (Lakes, 2009; Jänicke et al., 2015)

$$H_i(\omega) = \frac{\langle \sigma_{ii}(\omega) \rangle}{\langle \epsilon_{ii}(\omega) \rangle}, \tag{1}$$

$$\mu_{ij}(\omega) = \frac{1}{2} \frac{\langle \sigma_{ij}(\omega) \rangle}{\langle \epsilon_{ij}(\omega) \rangle}, \tag{2}$$

$$Q_H^{-1}(\omega) = \frac{\langle \mathrm{Im}[H(\omega)] \rangle}{\langle \mathrm{Re}[H(\omega)] \rangle}, \tag{3}$$

$$Q_\mu^{-1}(\omega) = \frac{\langle \mathrm{Im}[\mu(\omega)] \rangle}{\langle \mathrm{Re}[\mu(\omega)] \rangle}, \tag{4}$$

Table 1. Material properties of the models (Mavko et al., 2009; Pimienta et al., 2016).

Grains (calcite)	Fluid (air)	Fluid (glycerin)
$K^S = 70$ GPa	$K^F = 1 \times 10^{-4}$ GPa	$K^F = 4.35$ GPa
$\mu = 30$ GPa	$\eta = 2 \times 10^{-5}$ Pa $\cdot$ s	$\eta = 1$ Pa $\cdot$ s

Table 2. Velocities of the models in dry conditions.

Velocity	Small model	Big model	Laboratory
V_P^x	4175 m/s	3830 m/s	
V_P^y	4310 m/s	4170 m/s	
V_P^z	3700 m/s	2675 m/s	1825 m/s
V_S^{xy}	2420 m/s	2430 m/s	
V_S^{xz}	2205 m/s	1970 m/s	
V_S^{yz}	2230 m/s	2005 m/s	1283 m/s
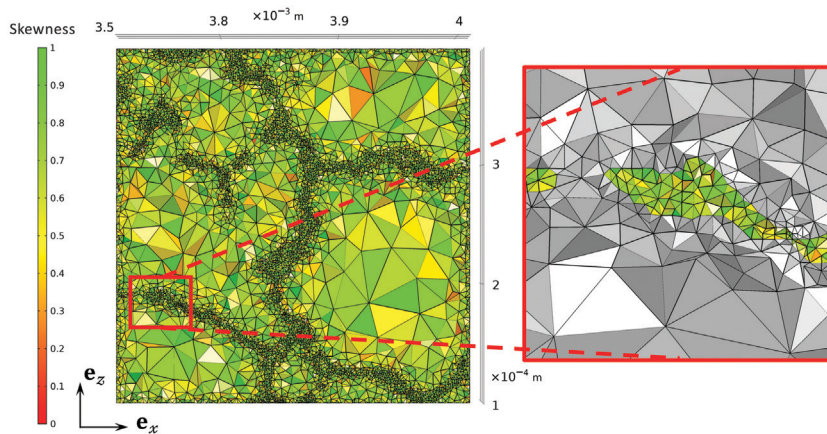
Figure 6. Slice of the small numerical model showing the mesh colored by the quality attribute *skewness*. The inset shows the mesh inside the cracks in colors and the one inside the grains in gray.
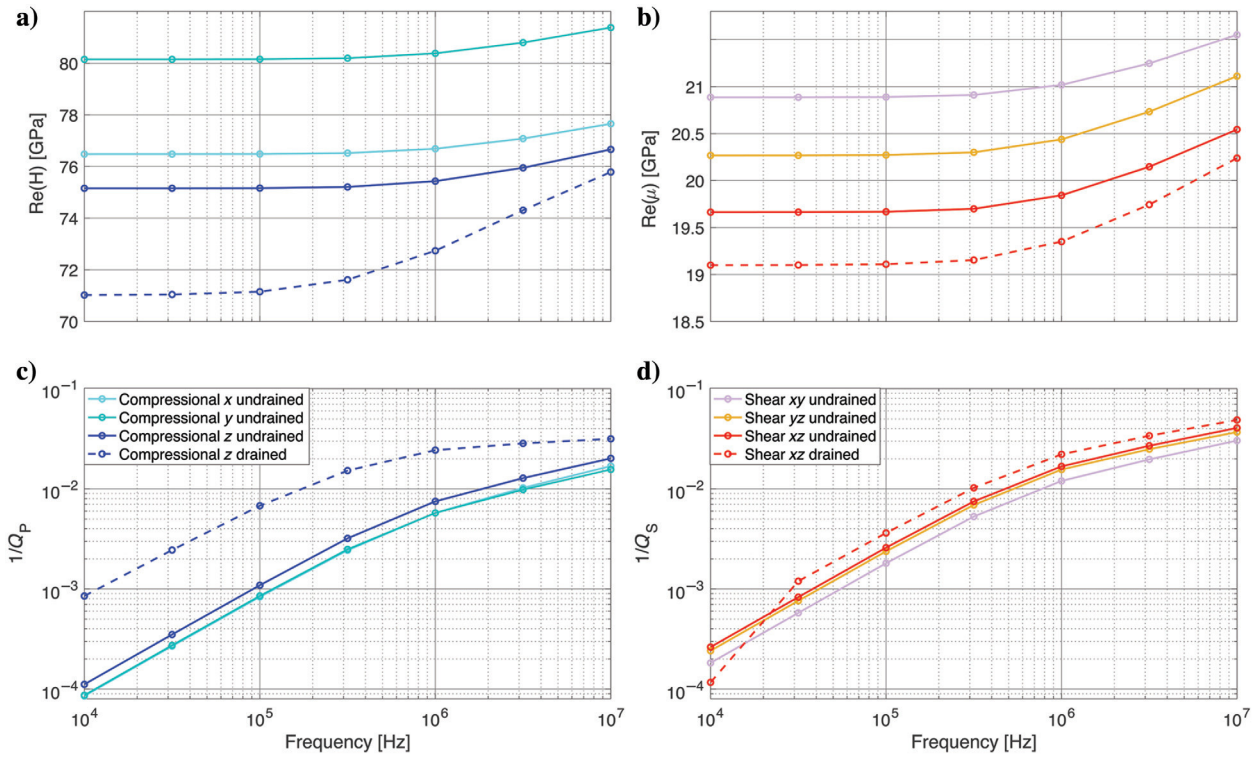
Figure 7. Real part of the (a and b) P and S wave moduli, and (c and d) attenuation $1/Q$, in the x , y , and z directions for the small model.

Figure 8. Fluid pressure in the pore space for the whole small model (Figure 5) with (a and c) drained and (b and d) undrained boundary conditions as a response to compressional harmonic tests in the vertical direction with a displacement amplitude of 10^{-3} μm at (a and b) 10^4 Hz and (c and d) 10^7 Hz.
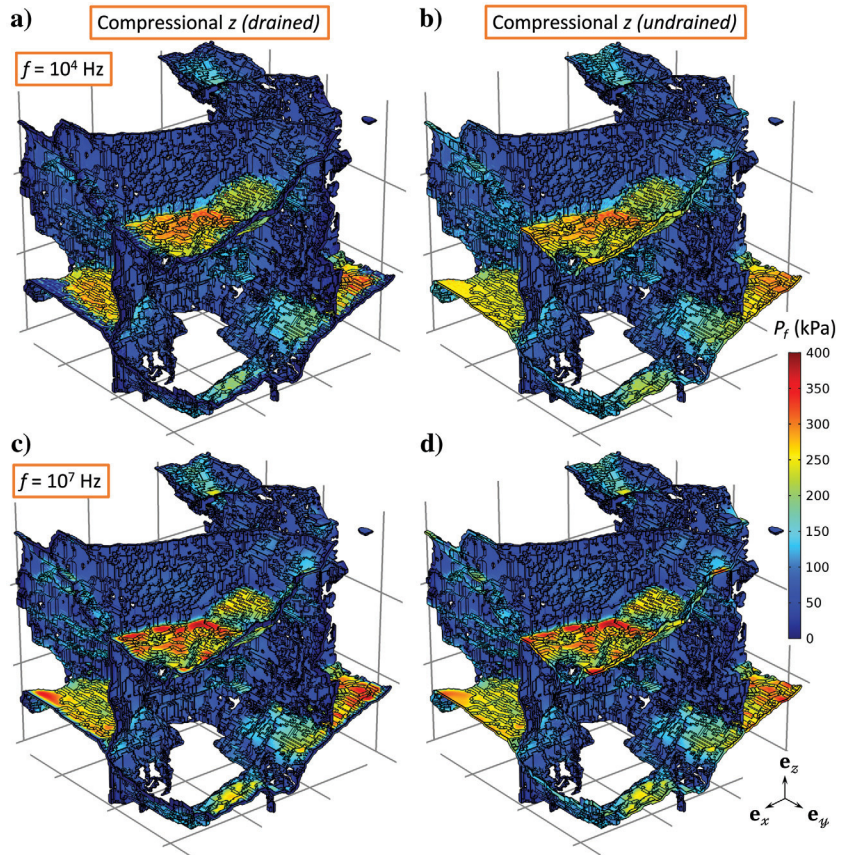
where $\langle \sigma_{ij}(\omega) \rangle$ and $\langle \epsilon_{ij}(\omega) \rangle$ represent the volumetric averages of the stress and strain matrix components σ_{ij} and ϵ_{ij}, respectively, for each angular frequency ω and the Re and Im operators extract the real and imaginary parts of a complex number.

The sizes of the studied numerical models are limited by the hardware used to solve the equations. The simulations are performed for seven frequencies from 10^4 to 10^7 Hz using the direct solver PARDISO (Schenk and Gärtner, 2004). For the biggest model considered in this analysis, 800 GB of RAM are used taking 2 h to solve the equations at each frequency.

RESULTS

To analyze the model size effects on the P and S wave velocities, we compare the results from the full model (the big model) with those obtained from a subvolume of it (the small model). The velocities are computed in the three Cartesian directions to analyze potential anisotropic effects and also compared with those obtained from ultrasonic measurements in the laboratory. Then, we analyze the P and S wave moduli dispersion and attenuation due to squirt flow for the small model fully saturated with glycerin having either drained or undrained boundary conditions.

Dry conditions

The harmonic numerical test is applied in shear and compressional modes in all three Cartesian directions considering the big and small models presented in Figure 5. We use air properties for the material filling the cracks (Table 1) and a frequency of 10^6 Hz, to be consistent with existing ultrasonic measurements performed on a sibling sample. Considering a grain density of calcite, $\rho_g = 2700$ kg/m^3, and a porosity of 4% obtained as the ratio between the volume occupied by the cracks and the volume of the model, we calculate as the weighted average a bulk density for the air saturated models of $\rho_{bulk} = 2590$ kg/m^3. We compare the numerical results with the ultrasonic P and S wave velocities measured on the whole cracked sample (with a diameter of 29 mm and a length 72.5 mm) in dry and unconfined conditions. Table 2 shows these velocities. In general, the numerically obtained velocities exhibit a clear tendency toward lower magnitudes when increasing the model size. Much lower magnitudes can be observed for the velocities measured at the laboratory on the whole sample.

Saturated conditions

To quantify the dissipation taking place in the fluid filling the cracks of the small model, we follow the numerical methodology previously described. Table 1 shows the material properties used for the grain material (calcite) and fluid in the cracks (glycerin), which are assigned to the two phases. The compressibility contrast between the cracks having different orientations and aspect ratios, provided that they are hydraulically connected, induces fluid pressure gradients between them. During the consequent fluid pressure diffusion, friction in the viscous fluid dissipates energy. The real part of the P and S wave moduli and the corresponding attenuation in the three Cartesian directions for the small model are presented in Figure 7. At frequencies higher than 10^5 Hz, significant P and S wave moduli dispersion and attenuation can be observed. It can also be observed that the maximum attenuation is slightly higher for the S wave than for the P wave. This is due to the fact that, such as

during the hemicycle of a wave, the shear test produces a maximum compression on the cracks oriented at 45° from the incidence direction and those oriented at −45° suffer a maximum dilatation. As a result, a higher fluid pressure gradient is generated compared to that generated by the compressional test that only compresses the cracks. In addition, drained boundary conditions increase the P wave modulus dispersion and attenuation in the vertical direction for the considered frequency range. In the case of the shear test, drained boundary conditions show results that are more similar to those for undrained boundary conditions.

To better illustrate the squirt flow process, Figure 8 shows the fluid pressure in the pore space with drained and undrained boundary conditions, as a result of the applied compressional harmonic test in the vertical direction with a displacement amplitude of 10^{-3} μm at 10^4 and 10^7 Hz. In addition, in Figure 9, a slice of the model shows the fluid pressure in the cracks and the energy dissipation rate (Winter, 1987) at 10^7 Hz calculated as

$$
D(\omega) = 2\eta(\dot{\epsilon}_{xx}^2 + \dot{\epsilon}_{yy}^2 + \dot{\epsilon}_{zz}^2 + 2\dot{\epsilon}_{xy}^2 + 2\dot{\epsilon}_{xz}^2 + 2\dot{\epsilon}_{yz}^2)
$$
$$
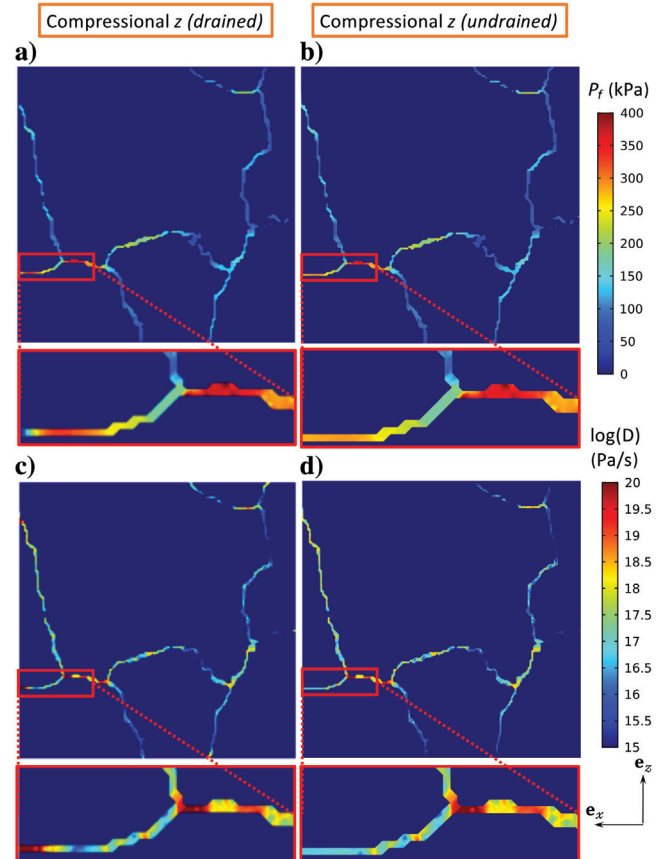- \frac{2}{3}\eta(\dot{\epsilon}_{xx} + \dot{\epsilon}_{yy} + \dot{\epsilon}_{zz})^2, \tag{5}
$$

Figure 9. (a and b) Fluid pressure P_f and (c and d) energy dissipation rate D on the plane xz at $y = 3.28 \times 10^{-3}$ m for the considered model with (a and c) drained and (b and d) undrained boundary conditions as a response to a compressional harmonic tests in the vertical direction with a displacement amplitude of 10^{-3} μm at 10^7 Hz.

where a dot on top of a variable implies the multiplication of the variable by $i\omega$. The approximately horizontal cracks exhibit the highest fluid pressure values (the warm colors), whereas the more vertically oriented cracks are less affected by the deformation in the vertical direction, resulting in lower fluid pressure. The dissipation exhibits maximum magnitudes where the fluid pressure gradients are maximum. In general, the results are similar for both considered boundary conditions except for the cracks located close to the boundaries. When drained boundary conditions are considered, the high fluid pressure in those cracks can partially equilibrate toward the exterior of the model; consequently, stronger dissipation can be observed. Figures 10 and 11 show the fluid pressure in the pore space and the energy dissipation rate for the shear test. It is possible to observe (better in Figure 11) the maximum fluid pressure in the cracks with inclinations close to 45°, whereas cracks with orientations closer to −45° show negative fluid pressure. The fluid pressure diffusion working to equilibrate the pressure gradients between the cracks is responsible for the energy dissipation shown in Figure 7. The dissipation for both considered boundary conditions is similar, which is in agreement with the dispersion and attenuation curves in Figure 7. Overall, both illustrated frequencies in Figures 8 and 10 are lower than the one corresponding to the attenuation peak due to squirt flow; consequently, small differences for the fluid pressure gradients can be observed between them, with the highest pressures occurring at 10^7 Hz.

DISCUSSION

The numerically calculated velocities for dry conditions (Table 2) tend to be smaller for the big model. However, the velocities for big and small models are similar in comparison with the ones obtained from laboratory measurements, which are much smaller. This significant discrepancy to the laboratory measurements can be explained by the fact that even the big model cannot be considered as an representative element volume (REV), as well as, by the presence of small cracks in the rock that are not recovered by the imaging process. The first argument is also supported by the general reduction of the velocities from the small model to the big model. Moreover, the P wave velocity in the z direction (V_P^z) for the big model presents a substantial reduction with respect to the small model. This suggests the predominant presence of horizontal cracks when increasing the model size. In addition, from the volume change of the whole samples after thermal treatment, a 2.05% porosity increment was estimated. In the case of the numerical models, we obtain 3.98% and 4.06% of porosity for the small and big models, respectively. These differences are likely associated with an overestimation of the crack aperture in our segmentation procedure as well as with the fact that the models cannot be considered as an REV.

The results for the fluid saturated small model show higher attenuation magnitudes for the shear test than for the compressional ones. These observations are in agreement with those obtained by Rubino et al. (2017) for 2D models having orthogonal connected fractures and by Hunziker et al. (2018) for isotropic 2D models having stochastic distributions of fractures. Although they model mesoscopic scale fractures represented as poroelastic media, their results for fracture to fracture fluid pressure diffusion are analogous to squirt flow in interconnected cracks as shown by Quintal et al. (2016).

The compressional and shear tests on our model exhibit significant attenuation at frequencies higher than 10^6 Hz (Figure 7). From the tendency of the curves, the squirt flow characteristic frequency of the considered model and material properties is expected to occur at frequencies higher than 10^7 Hz at which other attenuation mechanisms could prevail (such as scattering and Biot's global flow). However, as predicted in analytical solutions (e.g., Mavko and Jizba, 1991; Dvorkin et al., 1995; Gurevich et al., 2010), the characteristic frequency is proportional to the cube of the aspect ratio of the compliant cracks. This means that, if the cracks are thinner than the ones segmented in this work, the characteristic frequency would be at lower frequencies. That would be expected for laboratory measurements on the saturated samples given that they must present smaller crack apertures than the ones of our model, which were limited by the underlying maximum spatial resolution of the used μXRCT system (i.e., the voxel size of 2 μm).

For fully saturated porous samples, an attenuation peak associated with the drained undrained
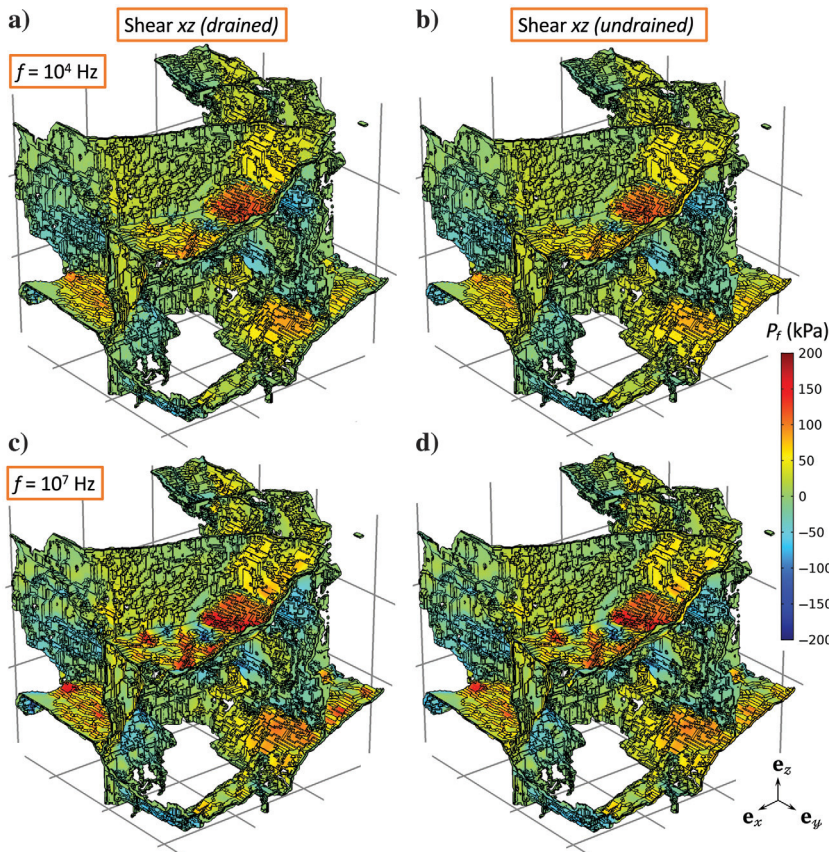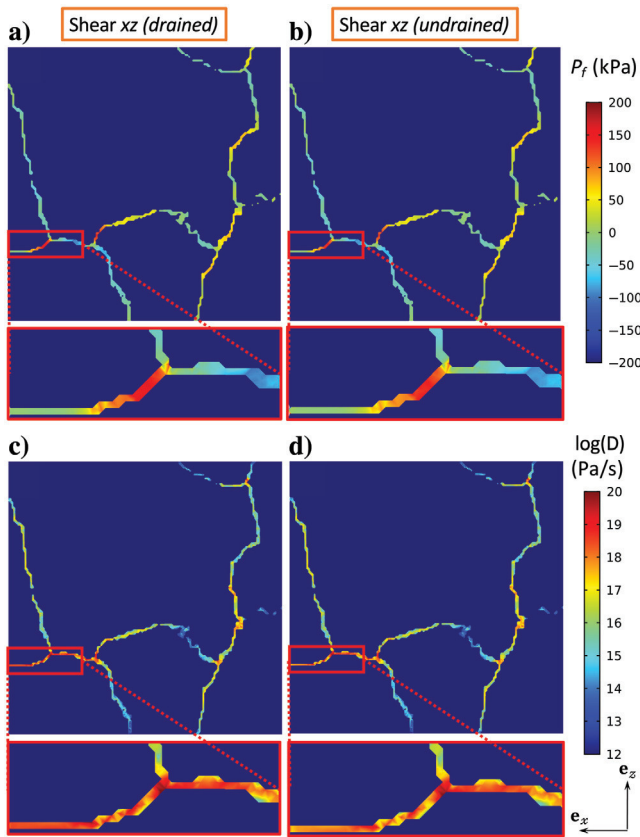

Figure 10. Fluid pressure in the pore space for the whole small model (Figure 5) with (a and c) drained and (b and d) undrained boundary conditions as a response to shear harmonic tests in the plane xz with a displacement amplitude of $10^{-3}\mu$m at (a and b) 10^4 Hz and (c and d) 10^7 Hz.

Figure 11. (a and b) Fluid pressure P_f and (c and d) energy dissipation rate D on the plane xz at $y = 3.28 \times 10^{-3}$ m for the considered model with (a and c) drained and (b and d) undrained boundary conditions as a response to a shear harmonic tests in the plane xz with a displacement amplitude of 10^{-3} μm at 10^7 Hz.

transition has been reported in laboratory measurements (e.g., Pimienta et al., 2015b; Chapman et al., 2019). The characteristic frequency associated with the drained undrained transition is commonly found at significantly lower frequencies than the one corresponding to squirt flow because it is mainly controlled by different properties, such as permeability and sample length, and it occurs at the mesoscopic (sample) scale (Pimienta et al., 2016). The seismic attenuation observed in our study for the models with drained boundary conditions occurs at a similar frequency range than that of the models with undrained boundary conditions because, in both cases, the characteristic frequency is controlled by the crack aspect ratio, leading to an increase in the (squirt) flow process. The attenuation observed for the compressional test was significantly higher for the model with drained boundary conditions due to local fluid pressure diffusion taking place in the cracks close to the model boundaries. In the case of the shear test, minor differences were found between the models with drained and undrained boundary conditions.

CONCLUSION

We presented a complete and detailed workflow for estimating frequency dependent seismic attenuation and velocity dispersion due to squirt flow based on μXRCT images of rock samples. For that, we first built numerical models by processing and segmenting a subvolume of μXRCT data set, here that of a cracked Carrara mar

ble sample. We then numerically computed, using the finite element method, the effective P and S wave velocities in all three Cartesian directions for two models of different sizes, the small model being a subvolume of the big one. The models were considered dry, or saturated with air, for these first measurements performed at 10^6 Hz. Although the P wave velocity in the z direction shows a considerable discrepancy, presumably due to the preferential presence of horizontal cracks, all the other velocities present a small reduction when increasing eight times the model size. Overall, the model velocities present an approximately isotropic behavior. In addition, the numerically estimated velocities are considerably higher than the ones estimated by laboratory measurements. This is because the numerical models are much smaller than the REV size and the presence of small cracks that are not recovered by the imaging and segmentation processes.

The small model was also analyzed fully saturated with glycerin, considering drained and undrained boundary conditions in a frequency range from 10^4 to 10^7 Hz. Significant P and S wave attenuation caused by squirt flow was observed at frequencies greater than 10^6 Hz. Moreover, the S wave attenuation was higher than the P wave attenuation. An increase in P wave attenuation, accompanied by a reduction in the P wave modulus, was observed when considering drained boundary conditions because these open boundaries also caused squirt flow in the cracks that are directly connected to the boundaries. We found minor differences in the S wave attenuation when comparing drained and undrained boundary conditions.

DATA AND MATERIALS AVAILABILITY

Data associated with this research are available and can be obtained by contacting the corresponding author. The numerical models (small and big cubes) used for the analysis can be found at: https://doi.org/10.5281/zenodo.4746139.

APPENDIX A

SAMPLE IMAGING

The scan of the sample is performed in a self built, modular μXRCT system using an open microfocus tube *FineTec FORE 180.01C TT* with a tungsten transmission target from Finetec Technologies GmbH, Germany, in combination with a *Shad o Box 6K HS* detector with a CsI scintillator option from Teledyne DALSA Inc., Waterloo, Ontario, Canada. The latter provides a resolution of 2940×2304 pixels by a pixel pitch of 49.5 μm. For more details about the system; see Ruf and Steeb (2020b). The geometric magnification is set to 24.78, which leads to the highest achievable spatial resolution of approximately 50 linepairs/mm of the system and results in a voxel size of 2 μm. With this setting, the corresponding field of view is 5.88 mm in the horizontal direction and 4.61 mm in the vertical direction. Consequently, the sample can be scanned over the entire diameter of 5 mm and basically allows the definition and

extraction of an appropriate REV. The XRCT data set and the re lated metadata (scan settings) are published (Ruf and Steeb, 2020a).

APPENDIX B

MATHEMATICAL FORMULATION

We use the linearized, quasistatic Navier Stokes equations, to de scribe the laminar flow of a compressible viscous fluid inside the cracks and pores, coupled with the quasistatic Lamé Navier equa tions, for the linear elastic solid grain (Quintal et al., 2016, 2019). The conservation of momentum is

$$\nabla \cdot \boldsymbol{\sigma} = \mathbf{0}, \tag{B-1}$$

where $\boldsymbol{\sigma}$ is the total stress tensor. In general, each material point can either be occupied by the fluid or the solid phase. Thus, the stress tensor can be written as the sum of the contributions of the solid and the fluid

$$\boldsymbol{\sigma} = \boldsymbol{\sigma}^S + \boldsymbol{\sigma}^F. \tag{B-2}$$

The generalized constitutive equation in the frequency domain is given by

$$\boldsymbol{\sigma} = K^S \text{tr}(\boldsymbol{\epsilon}_S)\mathbf{I} + 2\mu \text{dev}(\boldsymbol{\epsilon}_S) + K^F \text{tr}(\boldsymbol{\epsilon}_F)\mathbf{I} + 2i\omega\eta \text{dev}(\boldsymbol{\epsilon}_F), \tag{B-3}$$

where K^S and μ are the bulk and shear moduli of the solid phase, respectively, K^F and η are the bulk modulus and the shear viscosity of the fluid phase, respectively, $\boldsymbol{\epsilon}_S$ and $\boldsymbol{\epsilon}_F$ are the solid and fluid strain tensors, respectively, tr and dev are the trace and the devia toric operators, $\mathbf{I}$ is the identity tensor, ω is the angular frequency, and i is the imaginary unit. Acceleration terms are neglected, and squirt flow is the only possible cause for dissipation.

The generalized constitutive equation B 3 is valid for the solid and the fluid domain because it is reduced to Hooke's law in the elastic matrix,

$$\boldsymbol{\sigma}^S = K^S \text{tr}(\boldsymbol{\epsilon}_S)\mathbf{I} + 2\mu \text{dev}(\boldsymbol{\epsilon}_S), \tag{B-4}$$

and inside the cracks is reduced to

$$\boldsymbol{\sigma}^F = K^F \text{tr}(\boldsymbol{\epsilon}_F)\mathbf{I} + 2i\omega\eta \text{dev}(\boldsymbol{\epsilon}_F). \tag{B-5}$$

Combining equations B 1 and B 5 yields the quasistatic, linearized Navier Stokes equation.

REFERENCES

Alkhimenkov, Y., E. Caspari, B. Gurevich, N. D. Barbosa, S. Glubokov skikh, J. Hunziker, and B. Quintal, 2020a, Frequency dependent attenu ation and dispersion caused by squirt flow: Three dimensional numerical study: Geophysics, **85**, no. 3, MR129 MR145, doi: 10.1190/geo2019 0519.1.

Alkhimenkov, Y., E. Caspari, S. Lissa, and B. Quintal, 2020b, Azimuth , angle and frequency dependent seismic velocities of cracked rocks due to squirt flow: Solid Earth, **11**, 855 871, doi: 10.5194/se 11 855 2020.

Andrä, H., N. Combaret, J. Dvorkin, E. Glatt, J. Han, M. Kabel, Y. Keehm, F. Krzikalla, M. Lee, C. Madonna, M. Marsh, T. Mukerji, E. H. Saenger, R. Sain, N. Saxena, S. Ricker, A. Wiegmann, and X. Zhan, 2013a, Digital rock physics benchmarks Part 1: Imaging and segmentation: Com puters & Geosciences, **50**, 25 32, doi: 10.1016/j.cageo.2012.09.005.

Andrä, H., N. Combaret, J. Dvorkin, E. Glatt, J. Han, M. Kabel, Y. Keehm, F. Krzikalla, M. Lee, C. Madonna, M. Marsh, T. Mukerji, E. H. Saenger, R. Sain, N. Saxena, S. Ricker, A. Wiegmann, and X. Zhan, 2013b, Digital rock physics benchmarks Part 2: Computing effective properties: Com puters & Geosciences, **50**, 33 43, doi: 10.1016/j.cageo.2012.09.008.

Arns, C., F. Bauget, A. Limaye, A. Sakellariou, T. Senden, A. Sheppard, R. Sok, V. Pinczewski, S. Bakke, and L. I. Berge, 2005, Pore scale charac terization of carbonates using X ray microtomography: SPE Journal, **10**, 475 484, doi: 10.2118/90368 PA.

Arns, C. H., M. A. Knackstedt, W. V. Pinczewski, and E. J. Garboczi, 2002, Computation of linear elastic properties from microtomographic images: Methodology and agreement between theory and experiment: Geophys ics, **67**, 1396 1405, doi: 10.1190/1.1512785.

Arns, C. H., M. A. Knackstedt, M. V. Pinczewski, and W. B. Lindquist, 2001, Accurate estimation of transport properties from microtomographic images: Geophysical Research Letters, **28**, 3361 3364, doi: 10.1029/2001GL012987.

Beucher, S., and F. Meyer, 1993, The morphological approach to segmen tation: The watershed transformation: Mathematical Morphology in Im age Processing, **34**, 433 481, doi: 10.1201/9781482277234 12.

Borgomano, J. V. M., L. X. Pimienta, J. Fortin, and Y. Guéguen, 2019, Seis mic dispersion and attenuation in fluid saturated carbonate rocks: Effect of microstructure and pressure: Journal of Geophysical Research, Solid Earth, **124**, 12498 12522, doi: 10.1029/2019JB018434.

Brotons, V., R. Tomás, S. Ivorra, and A. Grediaga, 2014, Relationship be tween static and dynamic elastic modulus of calcarenite heated at different temperatures: The San Julián's stone: Bulletin of Engineering Geology and the Environment, **73**, 791 799, doi: 10.1007/s10064 014 0583 y.

Buades, A., B. Coll, and J. M. Morel, 2005, A non local algorithm for image denoising: IEEE Computer Society Conference on Computer Vision and Pattern Recognition, 60 65.

Chapman, S., J. V. M. Borgomano, H. Yin, J. Fortin, and B. Quintal, 2019, Forced oscillation measurements of seismic wave attenuation and stiffness moduli dispersion in glycerin saturated Berea sandstone: Geophysical Prospecting, **67**, 956 968, doi: 10.1111/1365 2478.12710.

Clarke, D., 1980, Microfracture in brittle solids resulting from anisotropic shape changes: Acta Metallurgica, **28**, 913 924, doi: 10.1016/0001 6160(80)90107 8.

Das, V., T. Mukerji, and G. Mavko, 2019, Numerical simulation of coupled fluid solid interaction at the pore scale: A digital rock physics technology: Geophysics, **84**, no. 4, WA71 WA81, doi: 10.1190/geo2018 0488.1.

Delle Piane, C., A. Arena, J. Sarout, L. Esteban, and E. Cazes, 2015, Micro crack enhanced permeability in tight rocks: An experimental and micro structural study: Tectonophysics, **665**, 149 156, doi: 10.1016/j.tecto.2015 .10.001.

Dvorkin, J., N. Derzhi, E. Diaz, and Q. Fang, 2011, Relevance of computa tional rock physics: Geophysics, **76**, no. 5, E141 E153, doi: 10.1190/geo2010 0352.1.

Dvorkin, J., G. Mavko, and A. Nur, 1995, Squirt flow in fully saturated rocks: Geophysics, **60**, 97 107, doi: 10.1190/1.1443767.

Evans, A. G., and D. R. Clarke, 1980, Residual stresses and microcracking induced by thermal contraction inhomogeneity, *in* D. P. H. Hasselman and R. A. Heller, eds., Thermal stresses in severe environments: Springer US, 629 648, doi: 10.1007/978 1 4613 3156 8 39.

Fredrich, J., K. Greaves, and J. Martin, 1993, Pore geometry and transport properties of fontainebleau sandstone: International Journal of Rock Me chanics and Mining Sciences Geomechanics Abstracts, **30**, 691 697, doi: 10.1016/0148 9062(93)90007 Z.

Fredrich, J. T., and T. Fong Wong, 1986, Micromechanics of thermally in duced cracking in three crustal rocks: Journal of Geophysical Research, Solid Earth, **91**, 12743 12764, doi: 10.1029/JB091iB12p12743.

Gastal, E., and M. Oliveira, 2012, Adaptive manifolds for real time high dimensional filtering: ACM Transactions on Graphics, **31**, 1 13, doi: 10.1145/2185520.2185529.

Golab, A., M. Knackstedt, H. Averdunk, T. Senden, A. Butcher, and P. Jaime, 2010, 3D porosity and mineralogy characterization in tight gas sandstones: The Leading Edge, **29**, 1476 1483, doi: 10.1190/1.3525363.

Gurevich, B., D. Makarynska, O. B. de Paula, and M. Pervukhina, 2010, A simple model for squirt flow dispersion and attenuation in fluid saturated granular rocks: Geophysics, **75**, no. 6, N109 N120, doi: 10.1190/1.3509782.

Hunziker, J., M. Favino, E. Caspari, B. Quintal, J. G. Rubino, R. Krause, and K. Holliger, 2018, Seismic attenuation and stiffness modulus dispersion in porous rocks containing stochastic fracture networks: Journal of Geophysical Research, Solid Earth, **123**, 125 143, doi: 10.1002/2017JB014566.

Jänicke, R., B. Quintal, and H. Steeb, 2015, Numerical homogenization of mesoscopic loss in poroelastic media: European Journal of Mechanics, A, Solids, **49**, 382 395, doi: 10.1016/j.euromechsol.2014.08.011.

Klimentos, T., 1995, Attenuation of P and S waves as a method of distin guishing gas and condensate from oil and water: Geophysics, **60**, 447 458, doi: 10.1190/1.1443782.

Lakes, R., 2009, Viscoelastic materials: Cambridge University Press.

Lissa, S., N. D. Barbosa, E. Caspari, Y. Alkhimenkov, and B. Quintal, 2020, Squirt flow in cracks with rough walls: Journal of Geophysical Research, Solid Earth, **125**, e2019JB019235, doi: 10.1029/2019JB019235.

Madonna, C., B. S. Almqvist, and E. H. Saenger, 2012, Digital rock physics: Numerical prediction of pressure dependent ultrasonic velocities using micro CT imaging: Geophysical Journal International, **189**, 1475 1482, doi: 10.1111/j.1365 246X.2012.05437.x.

Mavko, G., and D. Jizba, 1991, Estimating grain scale fluid effects on velocity dispersion in rocks: Geophysics, **56**, 1940 1949, doi: 10.1190/1.1443005.

Mavko, G., T. Mukerji, and J. Dvorkin, 2009, The rock physics handbook: Tools for seismic analysis of porous media: Cambridge University Press.

Metz, B., O. Davidson, H. de Coninck, M. Loos, and L. Meyer, 2005, IPCC special report on carbon dioxide capture and storage: Cambridge University Press, 431.

Murphy, W. F., K. W. Winkler, and R. L. Kleinberg, 1986, Acoustic relaxation in sedimentary rocks: Dependence on grain contacts and fluid saturation: Geophysics, **51**, 757 766, doi: 10.1190/1.1442128.

O'Connell, R. J., and B. Budiansky, 1977, Viscoelastic properties of fluid saturated cracked solids: Journal of Geophysical Research, **82**, 5719 5735, doi: 10.1029/JB082i036p05719.

Ohser, J., and K. Schladitz, 2009, 3D images of materials structures: John Wiley & Sons Ltd.

Peacock, S., C. McCann, J. Sothcott, and T. Astin, 1994, Seismic velocities in fractured rocks: An experimental verification of Hudson's theory: Geophysical Prospecting, **42**, 27 80, doi: 10.1111/j.1365 2478.1994.tb00193.x.

Pimienta, L., J. Borgomano, J. Fortin, and Y. Guéguen, 2016, Modelling the drained/undrained transition: Effect of the measuring method and the boundary conditions: Geophysical Prospecting, **64**, 1098 1111, doi: 10.1111/1365 2478.12390.

Pimienta, L., J. Fortin, and Y. Guéguen, 2015a, Bulk modulus dispersion and attenuation in sandstones: Geophysics, **80**, no. 2, D111 D127, doi: 10.1190/geo2014 0335.1.

Pimienta, L., J. Fortin, and Y. Guéguen, 2015b, Experimental study of Young's modulus dispersion and attenuation in fully saturated sandstones: Geophysics, **80**, no. 5, L57 L72, doi: 10.1190/geo2014 0532.1.

Pimienta, L., L. F. Orellana, and M. Violay, 2019, Variations in elastic and electrical properties of crustal rocks with varying degree of microfracturation: Journal of Geophysical Research, Solid Earth, **124**, 6376 6396, doi: 10.1029/2019JB017339.

Quintal, B., E. Caspari, K. Holliger, and H. Steeb, 2019, Numerically quantifying energy loss caused by squirt flow: Geophysical Prospecting, **67**, 2196 2212, doi: 10.1111/1365 2478.12832.

Quintal, B., J. G. Rubino, E. Caspari, and K. Holliger, 2016, A simple hydro mechanical approach for simulating squirt type flow: Geophysics, **81**, no. 4, D335 D344, doi: 10.1190/geo2015 0383.1.

Rodriguez Navarro, C., E. Ruiz Agudo, A. Luque, A. B. Rodriguez Navarro, and M. Ortega Huertas, 2009, Thermal decomposition of calcite: Mechanisms of formation and textural evolution of CaO nanocrystals: American Mineralogist, **94**, 578 593, doi: 10.2138/am.2009.3021.

Rubino, J., E. Caspari, T. Müller, and K. Holliger, 2017, Fracture connectivity can reduce the velocity anisotropy of seismic waves: Geophysical Journal International, **210**, 223 227, doi: 10.1093/gji/ggx159.

Ruf, M., and H. Steeb, 2020a, Micro XRCT data set of Carrara marble with artificially created crack network: Slow cooling down from 600°C, doi: 10.18419/darus 754, DaRUS, V1.

Ruf, M., and H. Steeb, 2020b, An open, modular, and flexible micro X ray computed tomography system for research: Review of Scientific Instruments, **91**, 113102, doi: 10.1063/5.0019541.

Saenger, E. H., F. Enzmann, Y. Keehm, and H. Steeb, 2011, Digital rock physics: Effect of fluid viscosity on effective elastic properties: Journal of Applied Geophysics, **74**, 236 241, doi: 10.1016/j.jappgeo.2011.06.001.

Sain, R., T. Mukerji, and G. Mavko, 2014, How computational rock physics tools can be used to simulate geologic processes, understand pore scale heterogeneity, and refine theoretical models: The Leading Edge, **33**, 324 334, doi: 10.1190/tle33030324.1.

Sarout, J., E. Cazes, C. Delle Piane, A. Arena, and L. Esteban, 2017, Stress dependent permeability and wave dispersion in tight cracked rocks: Experimental validation of simple effective medium models: Journal of Geophysical Research, Solid Earth, **122**, 6180 6201, doi: 10.1002/2017JB014147.

Saxena, N., and G. Mavko, 2016, Estimating elastic moduli of rocks from thin sections: Digital rock study of 3D properties from 2D images: Computers & Geosciences, **88**, 9 21, doi: 10.1016/j.cageo.2015.12.008.

Schenk, O., and K. Gärtner, 2004, Solving unsymmetric sparse systems of linear equations with pardiso: Future Generation Computer Systems, **20**, 475 487, doi: 10.1016/j.future.2003.07.011.

Siegesmund, S., K. Ullemeyer, T. Weiss, and E. K. Tschegg, 2000, Physical weathering of marbles caused by anisotropic thermal expansion: International Journal of Earth Sciences, **89**, 170 182, doi: 10.1007/s005310050324.

Sommacal, S., A. Fogden, B. Young, W. Noel, A. Arena, L. Salazar, T. Gerwig, Q. Cheng, A. Kingston, D. Marchal, A. M. P. Mazas, C. H. Naides, G. Kohler, and M. Cagnolatti, 2016, 3D multiscale imaging of the distribution of pores, organic matter and oil in place in Vaca Muerta shale samples: SPE/AAPG/SEG Unconventional Resources Technology Conference, 2564 2579.

Subramaniyan, S., B. Quintal, C. Madonna, and E. H. Saenger, 2015, Laboratory based seismic attenuation in fontainebleau sandstone: Evidence of squirt flow: Journal of Geophysical Research, Solid Earth, **120**, 7526 7535, doi: 10.1002/2015JB012290.

Tester, J. W., B. J. Anderson, A. S. Batchelor, D. D. Blackwell, R. DiPippo, E. M. Drake, J. Garnish, B. Livesay, M. C. Moore, K. Nichols, S. Petty, M. Nafi Toksoz, R. W. Veatch, R. Baria, C. Augustine, E. Murphy, P. Negraru, and M. Richards, 2007, Impact of enhanced geothermal systems on us energy supply in the twenty first century: Philosophical Transactions of the Royal Society A: Mathematical, Physical and Engineering Sciences, **365**, 1057 1094, doi: 10.1098/rsta.2006.1964.

Winter, H. H., 1987, Viscous dissipation term in energy equations, in J. R. Gordon, ed., Calculation and measurement techniques for momentum, energy and mass transfer: American Institute of Chemical Engineers, **7**, 27 34.

Biographies and photographs of the authors are not available.

Appendix B:
X-Ray 3D Imaging–Based Microunderstanding of Granular Mixtures: Stiffness Enhancement by Adding Small Fractions of Soft Particles

X-ray 3D imaging–based microunderstanding of granular mixtures: Stiffness enhancement by adding small fractions of soft particles

K. Taghizadeh[a,b,1] (iD), M. Ruf[a] (iD), S. Luding[b] (iD), and H. Steeb[a,c] (iD)

This research focuses on performing ultrasound propagation measurements and micro-X-ray computed tomography (μXRCT) imaging on prestressed granular packings prepared with biphasic mixtures of monodisperse glass and rubber particles at different compositions/fractions. Ultrasound experiments employing piezoelectric transducers, mounted in an oedometric cell (complementing earlier triaxial cell experiments), are used to excite and detect longitudinal ultrasound waves through randomly prepared mixtures of monodisperse stiff/soft particles. While the fraction of the soft particles is increasing linearly from zero, the effective macroscopic stiffness of the granular packings transits nonlinearly and nonmonotonically toward the soft limit, remarkably via an interesting stiffer regime for small rubber fractions between $0.1 \lesssim \nu \lesssim 0.2$. The contact network of dense packings, as accessed from μXRCT, plays a key role in understanding this phenomenon, considering the structure of the network, the chain length, the grain contacts, and the particle coordination. While the maximum stiffness is due to surprisingly shortened chains, the sudden drop in elastic stiffness of the mixture packings, at $\nu \approx 0.4$, is associated with chains of particles that include both glass and rubber particles (soft chains); for $\nu \lesssim 0.3$, the dominant chains include only glass particles (hard chains). At the drop, $\nu \approx 0.4$, the coordination number of glass and rubber networks is approximately four and three, respectively, i.e., neither of the networks are jammed, and the chains need to include particles from another species to propagate information.

X-ray computed tomography | granular materials | small-strain stiffness | ultrasound waves | particles' contact network

Granular matter has an intrinsic heterogeneous nature; this is expressed, for instance, in discrete force chains developed between the grains within the granular medium. Force chains spread the forces inhomogeneously through the contacts with neighboring particles (1–3). Interactions of particles cause strongly different force magnitudes on close particles and dependent on the boundary condition, nonisotropic stress throughout the medium. Force chains are due to disorder but also depend on small-scale properties like the local stress state, surface roughness of the individual grains, size distribution, particle shape, packing fraction, and interparticle friction. The heterogeneity is manifest in the fact that granular matter exhibits a strong configuration and history dependence, well known for decades in industrial applications and fields like soil mechanics (4).

Noise and vibration constitute a drawback in many technical and geoengineering applications. Acoustic waves produced on roads, railways, or by earthquakes propagate through granular materials (like soil, gravel, or asphalt), with the characteristics of the aggregate affecting the overall response. Mechanical waves are perturbations moving through space and time in a medium where small-enough deformations lead to elastic restoring forces. This produces a transfer of momentum and/or energy from one point to another, usually involving little or no associated mass transport (5–7). Probing a material with (ultra) sound waves can give useful information on its state, structure, and mechanical properties.

The P-wave, or primary wave (also named longitudinal or compressional), exists in solids and fluids—unlike the secondary or S-waves (shear or transversal) that propagate in solid media only (8). The P-wave is the fastest and the first signal detected by seismographs when traveling through the earth's crust. In a P-wave, particle displacements are longitudinal, parallel to the direction of wave propagation, whereas in an S-wave, displacements are perpendicular (9).

The propagation of elastic waves, such as P-waves, is a nondestructive testing method. It involves small perturbations that do not alter the microstructure or cause permanent

Significance

The focus is on structure–property relations of biphasic granular mixtures composed of soft and stiff particles subjected to a range of uniaxial stress conditions. Ultrasonic experiments have shown that for an optimal number of soft inclusions, one can observe material properties different from the mere superposition of ingredients. The impact of particle arrangements, subnetworks, and force chains on the mechanical response of soft-stiff granular compositions is deduced from in situ micro-X-ray computed tomography measurements. Identifying shorter chains of stiff particles at the microscale explains one possible cause behind the stiffening of samples. This interesting nonlinear and nonmonotonic transition from stiff- to soft-controlled media is described by the jamming of subnetworks, which might be useful for the design of materials.

[1]To whom correspondence may be addressed. Email: k.taghizadehbajgirani@utwente.nl or kianoosh. taghizadeh-bajgirani@mib.uni-stuttgart.de.

effects. When the wavelength is significantly longer than the internal scales of granular packings, such as particle or cluster size, the propagation velocity can be defined for the equivalent continuum, where the elastic moduli and mass density refer to the bulk medium (10). Small-strain stiffness, i.e., elastic stiffness, is a fundamental macroscale mechanical parameter for a wide range of engineering problems, and it is used for the prediction of granular response under both static and dynamic loading conditions (11–18). If both conditions, small amplitude and long wavelength, are fulfilled, wave measurements can be used to infer elastic stiffness (19–22).

The composition of granular materials can vary widely, and while some granular systems may consist of differently sized and shaped particles with similar properties, others are mixtures composed of particles with different properties (hundreds in some industrial processes or in natural soil). Nevertheless, their multispecies mechanisms and mixture bulk properties are far from being understood—even for the simplest case of two components. The properties of aggregates made of stiff and soft beads have been extensively studied experimentally (23–29) and numerically (30–38), varying the rubber content and the confining stress. Recent studies have shown that granular mixtures can have a surprisingly large elastic stiffness but are lighter and more dissipative thanks to the soft particles (39, 40). Mixtures with a small number of soft particles propagate sound faster than material made by stiff particles only (24, 39, 40). However, the nature of this phenomenon has yet remained open, for which we extract and investigate deeper the available microinformation of samples.

Earlier investigations have shown the importance of particles' networks, in controlling the effective mechanical properties of particulate systems on larger scales, e.g., elastic moduli (41–47). The particle–particle contacts support large forces are usually correlated in a linelike fashion (though they are not completely linear) over distances of several particle diameters, leading to so-called *force chains* (48–51), i.e., a contact transmitting a force is balanced with a single contact on the opposite side of the grain, and this is repeated on several subsequent grains (22).

In static equilibrium, force chains play a crucial role in transmitting acoustic waves, eventually, the stiffness of the granular packings. Although wave propagation is a promising technique to acquire the small strain stiffness of granular packing, it is unable to reveal crucial microstructural details. The use of micro-X-ray computed tomography (μXRCT) has allowed for unprecedented observations, such as fabric evolution, strain localization, deformation and failure, fracture and fragmentation, segregation, and jamming (52–56) and a renewed understanding of particulate systems by offering a possibility to visualize the internal discrete structure of the media (45, 57–62). Its advantage to provide a representation of particulate systems has led to gaining extensive information down to the scale of single particles (63).

In this study, we apply μXRCT-based characterization to provide access to the discrete microstructure for biphasic packings of glass and rubber particles. The stress state of the sample is controlled by an applied uniaxial compression state. By combining high-resolution μXRCT characterization containing microscale logical information with macroscale ultrasound propagation measurements, we explain the role of particles' contact networks on the effective macroscopic mechanical response of granular mixtures. In a nutshell, this research provides insight into features of wave propagation in randomly packed stiff–soft mixtures to enlighten the fundamental mechanisms controlling small-strain bulk stiffness in such systems.

Results and Discussion

Small-Strain Stiffness. To obtain the P-wave modulus of the biphasic sample, M, the ultrasound velocity ($V_p = L_z/t_p$) is measured knowing the travel time of the wave into the sample (t_p) and the sample height after deformation (L_z). The bulk density of the sample is determined for different rubber fractions as $\rho^0 = \nu \rho_g^0 + (1 - \nu) \rho_r^0$, where ρ_g^0 and ρ_r^0 are the glass and rubber densities ($\rho_g^0 = 1{,}540 \text{ kg m}^{-3}$ and $\rho_r^0 = 860 \text{ kg m}^{-3}$ (40)) at preparation ($p = 0$), and ν is the rubber fraction of samples $\nu = V_r^0/V^0$, where V_r^0 and V^0 are the volume occupied by the rubber beads and the volume occupied by all particles ($V^0 = V_r^0 + V_g^0$), respectively. Thanks to the calculated mass density, ρ^0, of the sample, and the experimentally obtained wave velocity, the longitudinal P-wave modulus is being determined by $M = \rho V_p^2 = \rho^0 (L_z^0/L_z) V_p^2$.

Fig. 1 illustrates the relationship between the small-strain stiffness, denoted as M, and the five vertical stresses, p, which are the resultant of the applied axial stress for samples with varying fractions of soft/stiff particles. Each experiment was repeated five times for every rubber content to obtain new configurations (i.e., new particle arrangements). The SD of the modulus is included in Fig. 1 for $p = 80$ kPa and 160 kPa with vertical bars.

As the applied vertical stress on the sample increases, its porosity decreases, making it denser and resulting in an increase in stiffness. Fig. 1 shows three different regimes highlighted in different colors as we move along the x-axis: i) Up to $\nu \approx 0.3$, the response is mainly controlled by stiff particles (red color in the background of Fig. 1). The tests conducted under uniaxial compression using an oedometer cell show a slight increase in the P-wave modulus, upon adding a small fraction of rubber particles; ii) adding more rubber beads leads to a drop of modulus for $0.4 \lesssim \nu \lesssim 0.6$. This indicates that the samples are weakened, as shown by the cyan color background in Fig. 1; iii) rubber occupies most of the total volume for $\nu \gtrsim 0.6$ where the
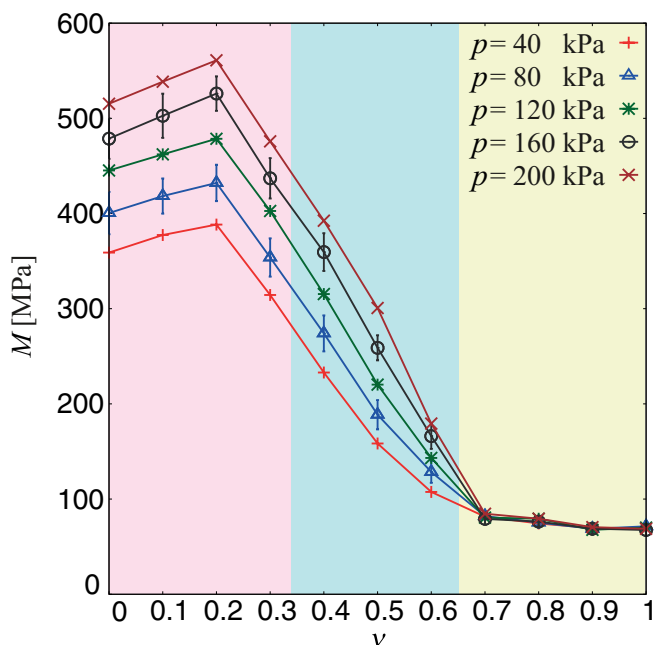

Fig. 1. P-wave modulus plotted against the fraction of rubber particles for samples compressed uniaxially from $p = 40$ kPa to 200 kPa. Each rubber fraction was tested five times with the SDs shown as error bars for $p = 80$ kPa and 160 kPa (others are not shown for the sake of visibility).

sample is fully controlled by soft particles. Thus, the stiffness remains constant even with the addition of more rubber particles (highlighted by the yellow color background in Fig. 1). This is due to the softness of rubber particles, which can deform significantly, leading to surface contacts instead of point-to-point contacts between particles. These samples are more like a porous rubber media with glass inclusions, and the packing seemingly resembles that of an inhomogeneous rubber block (64, 65). It must be noted that the maximum deformation applied to the samples (especially soft samples) is 10% of the initial sample height ($L_z^0 = 80$ mm), which is within the elastic limit of the rubber particles, so they do not deform permanently (30).

The oedometric cell experiment under uniaxial compression with zero lateral strains supports earlier research conducted by the authors using triaxial cells with isotropic stress control (40). However, it is still unclear how rubber strengthens samples for $v = 0.1$ and 0.2. The microstructural mechanisms responsible for the transition from stiff- to soft-dominated networks have yet to be resolved. Therefore, we employ in situ μXRCT to provide a microinvestigation at the particle scale. Another representation of the modulus plotted against the applied stress is shown in *SI Appendix*, Fig. S1. In addition to the wave propagation tests performed under the stress-control condition, we performed complementary tests following a strain-control protocol for samples $v = 0$, 0.1, 0.2, and 0.3, which is given in *SI Appendix*, Fig. S2.

Particles' Contact Network. Mechanical response investigations of samples using (ultrasound) wave propagation have allowed identifying the most interesting regime ($0.1 \lesssim v \lesssim 0.6$) for in situ μXRCT experiments. The particles' contact networks of some samples are studied next using the extracted information such as particles' centroid and their contact locations with one another. To begin with, we classify particles according to the number of particles they are connected to. In Fig. 2*A*, we can see the distribution of particles based on the number of contacts they have. The y-axis (N_p) represents the number of particles, while the x-axis (c) shows the number of contacts within the respective subnetworks. These results are based on images obtained at $p = 160$ kPa and different rubber fractions ranging from 0.1 to 0.6. *SI Appendix*, Fig. S3 displays the analysis carried out on images collected at $p = 80$ kPa.

At first glance, all-network data appear to follow a Gaussian distribution function, as shown in Eq. **1**. The function provides

histograms that represent the number of particles based on the number of contacts they have:

$$N_p(c) = \frac{a}{\sigma \sqrt{2\pi}} \exp^{\frac{-(c-\bar{C})^2}{2\sigma^2}}. \qquad [1]$$

In Eq. **1**, c is the number of contacts carried per particle, a is a fitting parameter, σ is the SD with respect to the mean, and $\bar{C}$ is the coordination number of a sample, which is defined by

$$\bar{C}_i = \frac{\sum_{c_i=1}^{c_i^{max}} c_i.N_p(c_i)}{\sum_{c_i=1}^{c_i^{max}} N_p(c_i)} \qquad i : \{\text{G–G, or R–R, or All contacts}\}.$$

$$[2]$$

Dashed and solid black lines are the fitted plots using Eq. **1** for samples with $v = 0.1$ and 0.6 scanned at $p = 160$ kPa, respectively. The distribution of particles and their contacts indicates that the samples almost coincide on the same function, regardless of particle characteristics. However, when more rubber particles are added ($v \gtrsim 0.4$), the plots shift slightly to the right, due to the nature of rubber particles, which can deform and create more contacts with neighboring particles.

Next, the networks are split into glass (G–G, Fig. 2*B*) and rubber (R–R, Fig. 2*C*) subnetworks for each sample, where only particles belonging to a single species are taken into account. For completeness, we plot in *SI Appendix*, Fig. S4, the connectivity of glass and rubber where only the contacts between rubber and glass particles are considered and not the ones from the glass–glass and rubber–rubber subnetworks. Both N_p and c decrease as v increases. On the contrary, the opposite trend is observed in the rubber subnetwork plots. Comparing the data of $v = 0.1$ (red) and $v = 0.2$ (blue), the number of particles with a high number of contacts is quite similar in the glass networks, i.e., the right tail of the glass network is very similar for both cases. In contrast, this is not observed for rubber networks where almost all rubber particles carry just less than three contacts for $v = 0.1$.

Earlier studies have shown that particles carrying less than three contacts, so-called *rattlers*, are not mechanically stable and do not contribute to force networks since their few contacts are momentary (66–69). The networks that are considered in this study exist in a dense regime under gravity, and as a result, there
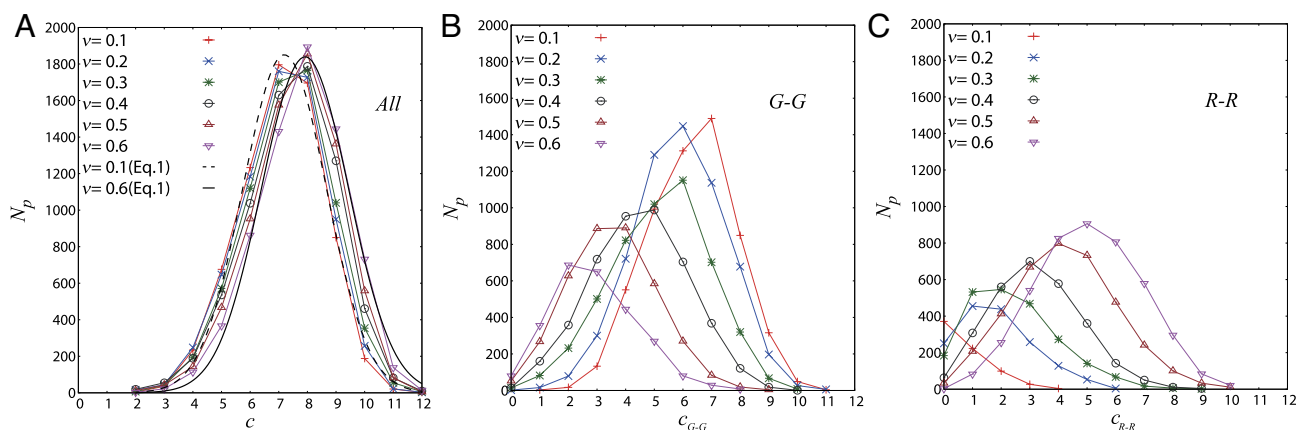

Fig. 2. Number of particles N_p carrying a particular number of contacts c for (*A*) the entire sample, (*B*) the glass subnetwork, and (*C*) the rubber subnetwork, extracted from μXRCT scans for samples with different rubber fractions under uniaxial compression at $p = 160$ kPa.

are very few rattlers. This can be observed in Fig. 2*A*, where the plot shows that only a small number of particles (N_p) have less than four contacts (c). However, when considering only a rubber network with $\nu \approx 0.1$, the isolated clusters of rubber particles exhibit similar characteristics to rattlers in a loose packing. This is due to the fact that rubber has a stiffness that is three orders of magnitude smaller than that of glass, and as a result, rubber particles surrounded by glass, similar to an isolated "void," do not contribute significantly to the force network in comparison to glass–glass contacts. Therefore, the overall response of the entire network is controlled by the glass particles. The main difference between a sample with $\nu = 0.1$ and a pure glass sample is the deformability of the bulk due to the rubber islands, which reduces the length of the sample.

In contrast, samples with $\nu \gtrsim 0.2$ contain more rubber particles with coordination above three. Some of these particles participate in the overall force networks by forming chains, loops, or clusters between themselves and glass particles, but the amount of rubber particles is yet not sufficient to influence the overall network. The sample with $\nu = 0.3$ shows a qualitatively similar response as $\nu = 0.2$. Nevertheless, the overall response of the network is weaker since stiff particles are replaced by soft ones, which leads to a decrease in M-modulus when $\nu \gtrsim 0.3$.

Finally, to illustrate the evolution of networks, glass and rubber subnetworks are shown in Fig. 3 for two samples, $\nu = 0.1$ (*A* and *B*) and $\nu = 0.5$ (*C* and *D*), compressed under $p = 160$ kPa. Comparing (*B*) and (*D*) subfigures (rubber network), we observe many isolated rubber particles with almost zero or one contact which cannot form a chain/path for wave propagation. In contrast, a highly dense network has formed for the rubber
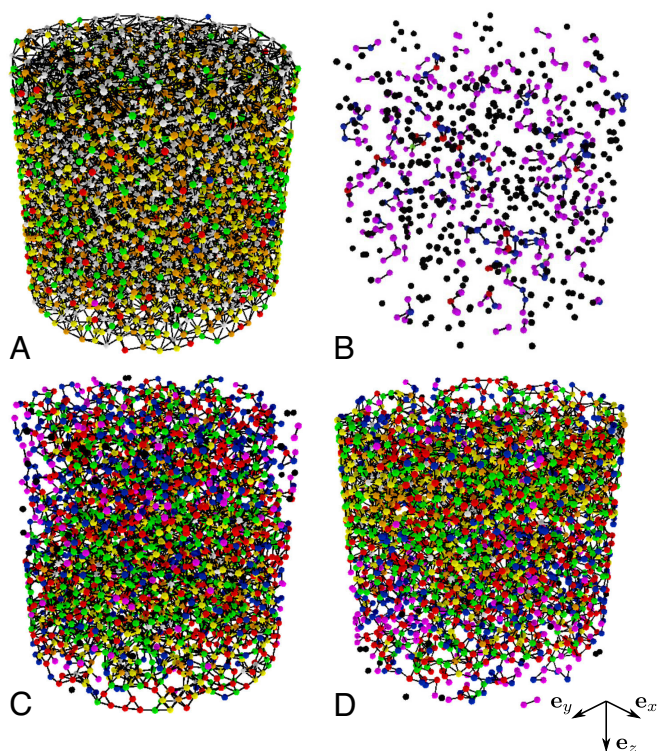

Fig. 4. The coordination number of different networks shown in Fig. 2. The dashed line is $\bar{C}_J = 5.5$ represents a jamming regime of a packing with friction equal to one.

Fig. 3. Glass and rubber networks of samples prepared with $\nu = 0.1$, (*A*) glass network, (*B*) rubber network, and $\nu = 0.5$, (*C*) glass network, (*D*) rubber network, both under $p = 160$ kPa compression. Different colors represent the numbers of contact each particle carries. Particles carrying zero, one, two, three, four, five, or above are colored black, magenta, blue, red, green, yellow, and orange, respectively.
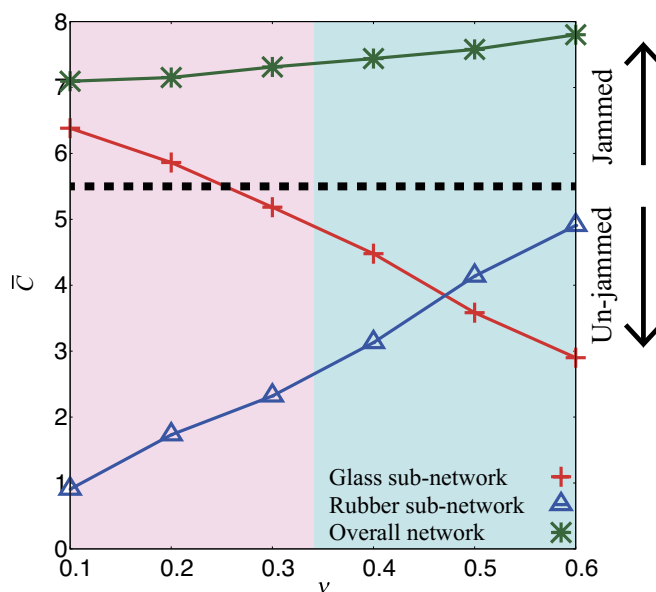
network of $\nu = 0.5$ in subfigure (*D*), indicating an increase in the coordination number and demonstrating the transition from a stiff- to soft-regime.

The next microparameter investigated here is the coordination number, Eq. **2**, which reveals more quantitative information about the microstructure. In Fig. 4, we demonstrate the evolution of the coordination number, $\bar{C}$, of glass subnetwork, rubber subnetwork, and overall networks for samples with different rubber fractions at $p = 160$ kPa. If we take into account all the particles in the networks, we can observe that the coordination number (indicated by the green line) increases slightly as the rubber content increases. This is because the rubber particles are more deformable, which leads to the formation of more contacts between all particles due to the lower bulk volume. As rubber content increases, the glass subnetwork deteriorates further while the rubber–rubber network develops.

Earlier studies have shown that if the coordination number of a system under compression exceeds a certain value, it enters a regime known as a "jammed" state, where contacts are permanently established (3, 68–71). At jamming, where the system transits from liquid-like to solid-like state, the system becomes mechanically stable with finite bulk and shear moduli. Different parameters influence the coordination number. Higher friction lowers the coordination number ($\bar{C}_J \approx 5.5$ for friction equal to one; dashed line in Fig. 4), while lowering friction increases both the coordination number ($\bar{C}_J \approx 6$ for frictionless particles) and the volume fraction of jamming (72, 73).

One key observation one can make from comparing the coordination numbers of subnetworks of samples with rubber fractions $\nu = 0.1, 0.2,$ and 0.3 is whether each of the subnetworks is in a jammed state or not. The coordination numbers of the glass–glass subnetworks of samples with rubber fractions $\nu = 0.1$ and 0.2 are above 5.5, confirming that these networks are surely jammed. This indicates that the glass subnetworks of $\nu = 0.1$ and 0.2 are in a stable state with a finite stiffness not requiring rubber particles. However, the coordination number of the glass–glass subnetwork of the sample with a rubber fraction of $\nu = 0.3$ is close to five, slightly below the jammed state coordination. Therefore, to reach

a mechanical equilibrium with a finite stiffness, the glass–glass subnetwork relies on the rubber particles for $v \gtrsim 0.3$.

Incorporating rubber particles—although it increases the coordination number and eventually offers a jammed packing—the overall stiffness of the packing starts to decay due to the softness of rubber. This explains the nonlinear, nonmonotonic behavior of the M-modulus observed in Fig. 1 for low rubber content samples. The presence of more and more rubber particles for $v = 0.1$ and 0.2 makes the samples more deformable than an only glass sample, $v = 0$, and the sample with $v = 0.2$ is also more deformed in height than the sample with $v = 0.1$, as we can see from *SI Appendix,* Fig. S2A.

Moving along the x-axis of Fig. 1, a further decline in the stiffness occurs at rubber fractions greater than 0.3. This decrease is associated with the change of contact networks from a stiff- to soft-dominated network (40). The regime $0.3 \lesssim v \lesssim 0.5$ in Fig. 4 is where the phase change starts since both glass and rubber networks carry almost the same coordination number. For rubber fractions greater than or equal to 0.5, the overall network behavior, such as stiffness, is fully controlled by soft particles, as their networks have gained a higher coordination number than that of stiff networks.

Contact Network Morphology.

Previous observations (74) indicated that acoustical waves traveling through the granular medium are transmitted by strong force chains. Thanks to µXRCT imaging (61, 75–77), we are able to extract detailed information about the force chains of mixtures to explain the percolation chains of granular mixtures by postulating that the wave travels along the stiffest (fastest) path.

As earlier studies have shown, see refs. 39 and 40 and Fig. 1, increasing pressure leads to an increase in wave velocity and modulus. When a soft particle comes in between hard particles, due to its softness and viscoelastic features, it dissipates more energy, which leads to slower wave travel. If two identified chains have a similar length, the one which is only made of stiff particles is preferred by the wave to travel faster.

From top to bottom of the samples, a number of chains can be identified. Among possible paths for every sample, depending on selection criteria, the shortest length (the most linear-like) is selected as the fastest propagating path. Fig. 5 demonstrates the packings including one of the identified short chains, where red and blue particles represent glass and rubber particles. To identify the shortest possible chains, the following steps are taken: i) The first layer of particles on top of the samples is identified; ii) for
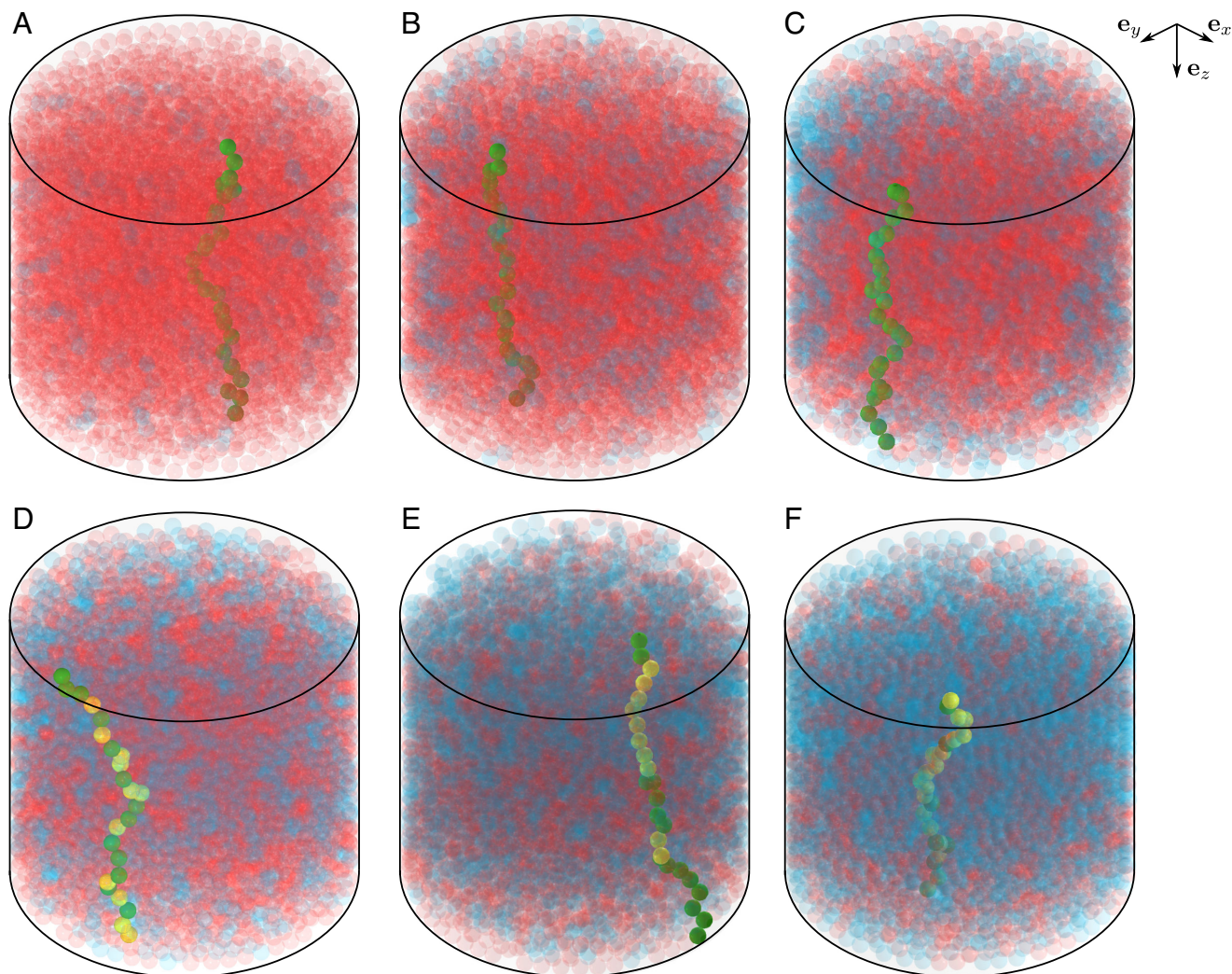

Fig. 5. One of the identified shortest percolating paths of samples with different rubber fractions, $v =$ (A) 0.1, (B) 0.2, (C) 0.3, (D) 0.4, (E) 0.5, and (F) 0.6, under $p = 160$ kPa compression. To indicate the shortest identified percolating path, green and yellow are used to distinguish further between glass and rubber particles. Red and blue indicate glass and rubber particles in the remaining sample area apart from the percolating path.

Table 1. Measured parameters from percolation wave analysis for samples scanned at 160 kPa. $\bar{\mathcal{L}}$ is the mean scaled length of the first ten identified chains with SD, and $\bar{\mathcal{N}}$ is the mean number of particles of chains found, and the shortest path among them is given by $min(\mathcal{L})$

ν	Sample	$\bar{\mathcal{L}}$	SD	$\bar{\mathcal{N}}$	$min(\mathcal{L})$
0.1	1	1.3221	0.0215	24	1.2917
	2	1.3114	0.0323	24	1.2405
	3	1.3126	0.0497	25	1.1839
0.1	Mean ± SD	1.3154 ± 0.0048	0.0345 ± 0.0116	24.3333 ± 0.4714	1.2387 ± 0.0440
0.2	1	1.2536	0.0438	23	1.1916
	2	1.2536	0.0411	23	1.1816
	3	1.3259	0.0296	24	1.2055
0.2	Mean ± SD	1.2777 ± 0.0341	0.0382 ± 0.0062	23.3333 ± 0.4714	1.1929 ± 0.0098
0.3	1	1.3367	0.0340	24	1.2886
	2	1.3231	0.0371	24	1.2370
	3	1.3350	0.0357	24	1.2914
0.3	Mean ± SD	1.3316 ± 0.0061	0.0356 ± 0.0013	24.0000 ± 0.0000	1.2723 ± 0.0250
0.4	1	1.3563	0.0405	25	1.29902
0.5	1	1.3443	0.0284	26	1.30419
0.6	1	1.3501	0.0317	25	1.30524

each individual particle in this layer, the neighboring particles are determined. Two particles are considered neighbors if the distance between their centers is equal or less than the diameter of the particles (4 mm); iii) among the neighboring particles, the one with the smallest vertical coordinate (z-direction) is selected; iv) steps (ii) and (iii) are repeated until the last particle of the chain is found at the bottom of the sample. To have a comparison among the identified chains, their lengths are divided/scaled by the sample heights (almost identical in all cases, $L_z^0 = 80$ mm). Table 1 reports the normalized average length of the first ten identified short chains ($\bar{\mathcal{L}} = \mathcal{L}/L_z$), their SD, number of particles involved in the chains ($\bar{\mathcal{N}}$), and the shortest path among all the ten identified chains ($\mathcal{L}$). As mentioned earlier, we have repeated μXRCT two more times for samples prepared with $\nu = 0.1$, 0.2, 0.3 with new configurations by removing and adding the particles for every test. The statistical characteristics of these tests are also included in Table 1 for completeness.

From Fig. 4, we learned that the sudden drop of modulus for samples with $\nu \gtrsim 0.4$ is due to a change of networks. The chains contain both glass and rubber particles, whereas in the case of lower rubber content, $\nu \lesssim 0.3$, many chains with only stiff particles are being identified. Although the chain length $\bar{\mathcal{L}}$ remains approximately the same among the identified chains, the chains of $\nu \gtrsim 0.4$ are much softer, which leads to a dramatic change in the wave speed (modulus).

Comparing the length of the chains (glass only) at lower rubber content ($\nu \lesssim 0.3$) for three different realizations confirmed that the particles' arrangements for samples with $\nu \approx 0.1$ and 0.2 provide shorter (i.e., straight/stiff) chains. This can be correlated with the fact that the glass subnetworks of these two samples are in a jammed state, therefore stable. The subnetwork of the sample with $\nu = 0.3$ is (possibly) under jamming, which makes the system less stable with weaker force chains (78). Most of the glass networks for $\nu \approx 0.1$ and 0.2 offer relatively short chains in comparison to $\nu \approx 0.3$; therefore, it is not surprising to obtain a higher modulus.

Conclusions

Recent technological developments have enabled the image-based characterization of granular materials at controlled stress states with grain-scale resolution using μXRCT. The current study aimed to understand the effect of granular mixture morphology on the macromechanical response of the assemblies by combining ultrasound propagation and image-based μXRCT characterization. In particular, the nonclassical mixture rule was discussed by combining effective properties with morphological characterization.

First, the wave propagation technique was used to analyze the mechanical response (small-strain stiffness) of mixtures of stiff–soft particulate systems. The effect of the stiff–soft composition on the compressive elastic modulus (P-wave modulus) was shown by means of wave propagation at different uniaxial preload levels. The results showed that low proportions of soft particles can enhance the modulus of the mixtures relative to the stiff-only packings. Adding more soft particles into the assemblies led to a transition from a stiff- to a soft-dominated regime where the bulk behavior of samples is mainly controlled by the soft phase. However, the macrobehavior of such granular samples can hardly be understood without microstructural information.

Next, to correlate the macrobehavior of samples with their microstructures, in situ μXRCT was conducted. Analyzing images clarified the underlying reason behind the transition mechanism from a stiff to a soft-controlled medium by separating glass and rubber subnetworks. The coordination number, i.e., the average number of contacts, provided a qualitative indication of the transition from a stiff-dominated to soft-dominated medium. The coordination number of packings, considering both glass and rubber, remained almost the same throughout different rubber fractions. The topology study of samples after image analysis showed that rubber plays a vital role in low rubber content samples, where the M-modulus stiffens $0.1 \lesssim \nu \lesssim 0.2$, by straightening/shortening the glass-only chains.

The μXRCT images provided insights into the chains' structure. We explained the stiffness improvement adding a small amount of soft particles and the sudden drop occurring in the M-modulus at $\nu \approx 0.4$. Samples with $\nu \lesssim 0.3$ offer chains made of only glass particles, whereas $0.4 \lesssim \nu$ cannot offer stiff chains, i.e., made only from glass particles. The existence of rubber particles in chains of $\nu = 0.4$, 0.5, and 0.6 softens the overall response of the samples; thus, the M-modulus has been weakened. This pioneering output has significant implications for designing materials with high stiffness and low weight, e.g., roads, where a lighter damper material with high stiffness is desired.

Understanding the microstructure of the networks of mixtures and its impact on the effective mechanical behavior of the assemblies will aid more accurate computer modeling [e.g., Discrete Element Modeling (79–81) of stiff–soft interactions] and theories (e.g., mixture theories of porous media) by providing insights into the fundamental mechanisms that govern the behavior of such materials under different conditions. This information can be used to optimize the composition and processing of the material to achieve properties. Although both ultrasound experiments and µXRCT-imaging have provided vital details on the mixtures, some aspects, like the evolution of the microstructure under different loading conditions, remain an open question. In the future, we plan to employ material point method (34, 35, 82) simulations of wave propagation through mixtures based on µXRCT data to expand our micro–macro horizons.

Materials and Methods

Ultrasound Propagation Setup. Low-frequency ultrasound propagation using broadband piezoelectric transducers is a nondestructive way to investigate the small-strain (compression) stiffness of granular materials (14, 83). In the present contribution, cylindrical samples consisting of monodisperse soft (rubber) and stiff (glass) particles with diameters of 4 mm are poured into a custom-made X-ray transparent oedometer cell made of polymethyl methacrylate (PMMA). Glass and rubber beads used in this study are similar to those employed in an earlier study (30, 40), with Young's moduli of 65 GPa and 0.185 GPa, and Poisson's ratios of 0.2 and 0.5 for glass and rubber, respectively. The cell holds cylindrical samples with a length $L_z^0 = 80$ mm and a diameter $D = 80$ mm with initial volume $V^0 = \frac{\pi}{4} L_z^0 D^2$ that are then placed under uniaxial static compression. A pair of P-wave broadband piezoelectric transducers with a frequency of 100 kHz (Olympus-Panametrics Videoscan V1011) are mounted on top and bottom of the cell and connected to an ultrasonic square wave pulser/receiver unit (Olympus-Panametrics 5077PR). The amplified signals were recorded with a resolution of 15 bit and a sampling rate of 125 Ms/s using a digital oscilloscope (PicoScope 5444B). To improve the signal-to-noise ratio, 32 signals were averaged. Samples composed of various rubber fractions ranging from $\nu = 0$ to 1 in 0.1 increments were prepared, where the total volume of the cylinder is occupied by glass particles when $\nu = 0$ and by rubber particles when $\nu = 1$. The samples were prestressed in a gradual manner using static mechanical force. At different quasistatic axial stresses, $p = 40, 80, 120, 160, 200$ kPa, acoustic P-waves are propagated from the top transducer (source) into the prepared samples, and the bottom transducer (receiver) collects the signals. To ensure reproducibility, each mixture was repeated five times, with particles being removed and added to the cell each time to obtain a new particle arrangement and eliminate configuration dependency.

Micro-X-Ray Computed Tomography. µXRCT imaging (84, 85) is arguably the most promising approach to attain the 3D microstructure of particle packings in high resolution by reconstructing the internal structure from a high number of 2D projection images (radiograms) acquired from different directions. The main advantage of µXRCT imaging in comparison to other nondestructive imaging methods (e.g., magnetic resonance imaging) is its ability to resolve the internal microstructure with high accuracy (86, 87). It is generally possible to visualize features down to the single-digit micrometer range (84, 85). Thus, it has been widely used to attain microscopic features of particulate systems. To further enhance a micromechanical insight into the mixture packings, the phase transition from stiff- to soft-dominated ($0.1 \leq \nu \leq 0.6$), and the stiffening behavior of the packings with a low number of soft inclusions ($0.1 \leq \nu \leq 0.2$), at stresses of 80 kPa and 160 kPa, approximately, were visualized by in situ µXRCT. For this, a lab-based modular buildup µXRCT system further described in ref. 88 was used. The underlying used experimental setup is illustrated in Fig. 6A showing the combination of conventional imaging setup and wave propagation measurements into an oedometer cell under uniaxial preload. It is worth mentioning that due to the existence of rubber particles, it is not possible to apply diffraction measurements of contact fabric, i.e., interparticle force, on the samples.

Unlike wave propagation tests, µXRCT scans are expensive both in energy consumption and time. Thus, we performed µXRCT scans on two vertical stresses $p = 80$ kPa and 160 kPa. Nevertheless, three different configurations (networks) were prepared for samples with rubber fractions $\nu = 0.1, 0.2$, and 0.3, whereas for samples with rubber fractions $\nu = 0.4, 0.5$, and 0.6, only one test was performed. All 24 (two vertical stresses × six rubber contents, $3 \times \nu : \{0.1, 0.2, 03\} + 1 \times \nu : \{0.4, 0.5, 06\}$) scans were performed with identical image acquisition settings. To capture the whole cell content ($D = 80$ mm; $L_z^0 = 80$ mm), a geometric magnification of 1.36 was used, given by the ratio of source–detector distance and source–object distance. Using 2×2 detector binning, the final resulting voxel edge length is 149.6 µm and sufficiently high to resolve the beads having a 4 mm diameter. The X-ray tube voltage and flux were set to 110 kV and 110 µA, and the detector exposure time to 1,000 ms. For the scan, the loaded sample was rotated 180° clockwise
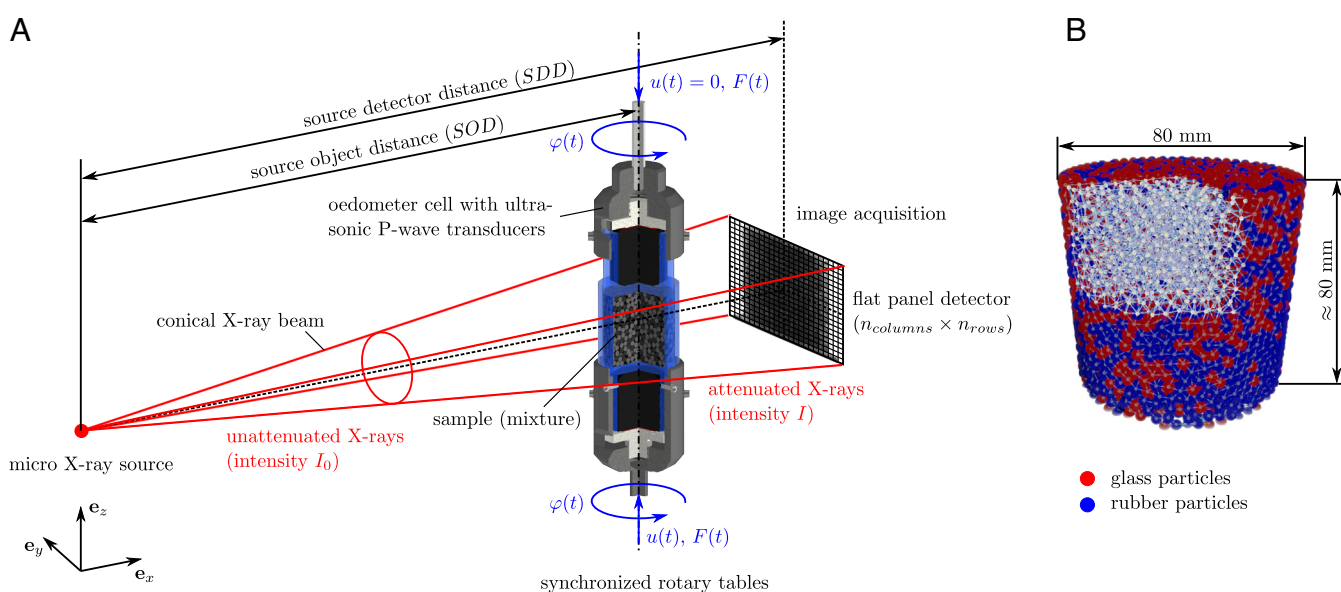

Fig. 6. (*A*) Schematic view of the in situ µXRCT setup with a three-quarter section view of the oedometer cell. (*B*) Segmented 3D reconstructed sample consisting of 50% glass and rubber particles with identified particles centroids and branch vectors, i.e., a vector connects centers of two neighboring particles.

and counterclockwise in 0.25° increments to cover the necessary complete turn. To enhance the final image quality with regard to ring artifacts, two slightly shifted projections for each angle were acquired and combined. Further information on the experimental setup and the used parameters can be found in ref. 89. For each scan, stress relaxation in the order of 10 kPa occurred quickly after switching from force- to a displacement-controlled mode for the imaging. However, we observed a quick recovery of the load upon reloading. Each scan took about 120 min and was performed displacement-controlled to avoid potential movement errors. The 3D volume reconstruction based on the radiograms of each scan was done with the FDK algorithm (90) using the commercial software Octopus Reconstruction (v.8.9.4-64 bit) (91). Image processing of the reconstructed gray value image stacks was performed with Dragonfly software (v.2020.2) (92); see Fig. 6B. First, a mathematical smoothing function (median filter) was applied to reduce unwanted noise in the tomograms. Accurate segmentation of images was achieved due to the high difference in attenuation coefficients between glass, rubber, and air. Finally, glass and rubber particles were identified using a mathematical morphology technique, watershed transform, on defined markers of individual particles to determine grain volumes, grain centroids, and all contact locations and orientations (93–95). To identify contacts between particles, immediate neighbor voxels containing two distinct grain IDs were considered (96, 97). To select a so-called true contact, a minimum of 10 voxels between two particles was set as a threshold for a contact candidate (87, 95).

For further analysis, we demonstrate the samples only at $p = 160$ kPa since the topological response of $p = 80$ kPa is almost unchanged. Results of the analysis of $p = 80$ kPa are reported in supplementary information file. The in situ acquired data of all scanned samples, including metadata, are open-access published (98–101); see *SI Appendix* for more details.

Author affiliations: [a]Institute of Applied Mechanics, University of Stuttgart, Stuttgart 70569, Germany; [b]Multi-Scale Mechanics, University of Twente, AE Enschede 7500, The Netherlands; and [c]Stuttgart Center for Simulation Science, University of Stuttgart, Stuttgart 70569, Germany

1. K. E. Daniels, N. W. Hayman, Force chains in seismogenic faults visualized with photoelastic granular shear experiments. *J. Geophys. Res.: Solid Earth* **113**, B11411 (2008).
2. L. Papadopoulos, M. A. Porter, K. E. Daniels, D. S. Bassett, Network analysis of particles and grains. *J. Complex Networks* **6**, 485–565 (2018).
3. R. Behringer *et al.*, Statistical properties of granular materials near jamming. *J. Stat. Mech.: Theory Exp.* **2014**, P06004 (2014).
4. S. Luding, K. Taghizadeh, C. Cheng, L. Kondic, Understanding slow compression and decompression of frictionless soft granular matter by network analysis. *Soft Matter* **18**, 1868–1884 (2022).
5. K. Aki, P. G. Richards, *Quantitative Seismology* (University Science Books, California, 2002).
6. B. O. Hardin, F. Richart Jr, Elastic wave velocities in granular soils. *J. Soil Mech. Found. Div.* **89**, 33–65 (1963).
7. J. Hall Jr, F. Richart Jr, Dissipation of elastic wave energy in granular soils. *J. Soil Mech. Found. Div.* **89**, 27–56 (1963).
8. J. S. Lee, J. C. Santamarina, Bender elements: Performance and signal interpretation. *J. Geotech. Geoenviron. Eng.* **131**, 1063–1070 (2005).
9. V. Magnanimo *et al.*, Characterizing the shear and bulk moduli of an idealized granular material. *Europhys. Lett. (EPL)* **81**, 34006 (2008).
10. V. Magnanimo, "Wave propagation and elasticity in granular soils: A numerical approach for a micromechanical perspective" in *Views on Microstructures in Granular Materials* (Springer, 2020), pp. 107–135.
11. H. A. Makse, N. Gland, D. L. Johnson, L. M. Schwartz, Why effective medium theory fails in granular materials. *Phys. Rev. Lett.* **83**, 5070 (1999).
12. C. Goldenberg, I. Goldhirsch, Force chains, microelasticity, and macroelasticity. *Phys. Rev. Lett.* **89**, 084302 (2002).
13. J. D. Goddard, Nonlinear elasticity and pressure-dependent wave speeds in granular media. *Proc. R. Soc. A* **430**, 105–131 (1990).
14. K. Walton, The effective elastic moduli of a random packing of spheres. *J. Mech. Phys. Solids* **35**, 213–226 (1987).
15. A. Misra, C. S. Chang, Effective elastic moduli of heterogeneous granular solids. *Int. J. Solids Struct.* **30**, 2547–2566 (1993).
16. J. Jenkins, D. Johnson, L. La Ragione, H. Makse, Fluctuations and the effective moduli of an isotropic, random aggregate of identical, frictionless spheres. *J. Mech. Phys. Solids* **53**, 197–225 (2005).
17. L. La Ragione, J. T. Jenkins, The initial response of an idealized granular material. *Proc. R. Soc. A* **463**, 735–758 (2007).
18. N. P. Kruyt, I. Agnolin, S. Luding, L. Rothenburg, Micromechanical study of elastic moduli of loose granular materials. *J. Mech. Phys. Solids* **58**, 1286–1301 (2010).
19. X. Tang, J. Yang, Wave propagation in granular material: What is the role of particle shape? *J. Mech. Phys. Solids* **157**, 104605 (2021).
20. D. Liu, C. O'Sullivan, J. A. H. Carraro, Use of combined static and dynamic testing to quantify the participation of particles in stress transmission. *J. Geotech. Geoenviron. Eng.* **148**, 04022100 (2022).
21. M. Otsubo, T. T. Dutta, M. Durgalian, R. Kuwano, C. O'Sullivan, "Particle-scale insight into transitional behaviour of gap-graded materials–Small-strain stiffness and frequency response" in *E3S Web of Conferences* (EDP Sciences, 2019), vol. 92, p. 14006.
22. E. T. Owens, K. E. Daniels, Acoustic measurement of a granular density of modes. *Soft Matter* **9**, 1214–1219 (2013).
23. J. R. Valdes, T. M. Evans, Sand–rubber mixtures: Experiments and numerical simulations. *Can. Geotech. J.* **45**, 588–595 (2008).
24. K. Taghizadeh, H. Steeb, V. Magnanimo, S. Luding, "Elastic waves in particulate glass–rubber mixture: Experimental and numerical investigations/studies" in *EPJ Web of Conferences* (EDP Sciences, 2017), vol. 140, p. 12019.
25. Z. Cheng, J. Wang, W. Li, The micro-mechanical behaviour of sand-rubber mixtures under shear: An experimental study based on X-ray micro-tomography. *Soils Found.* **60**, 1251–1268 (2020).
26. A. Platzer, S. Rouhanifar, P. Richard, B. Cazacliu, E. Ibraim, Sand–rubber mixtures undergoing isotropic loading: Derivation and experimental probing of a physical model. *Granular Matter* **20**, 1–10 (2018).
27. I. Benessalah, A. Arab, M. Sadek, R. Bouferra, Laboratory study on the compressibility of sand–rubber mixtures under one dimensional consolidation loading conditions. *Granular Matter* **21**, 1–9 (2019).
28. A. Ari, S. Akbulut, Effect of particle size and shape on shear strength of sand–rubber granule mixtures. *Granular Matter* **24**, 1–20 (2022).
29. M. Cárdenas-Barrantes, J. Barés, M. Renouf, É. Azéma, Experimental validation of a microme-chanically based compaction law for mixtures of soft and hard grains. *Phys. Rev. E* **106**, L022901 (2022).
30. K. Giannis *et al.*, Stress based multi-contact model for discrete-element simulations. *Granular Matter* **23**, 1–14 (2021).
31. M. Cárdenas-Barrantes, D. Cantor, J. Barés, M. Renouf, E. Azéma, Three-dimensional compaction of soft granular packings. *Soft Matter* **18**, 312–321 (2022).
32. J. L. Perez, C. Kwok, K. Senetakis, Effect of rubber size on the behaviour of sand–rubber mixtures: A numerical investigation. *Comput. Geotech.* **80**, 199–214 (2016).
33. T. L. Vu, S. Nezamabadi, S. Mora, Effects of particle compressibility on structural and mechanical properties of compressed soft granular materials. *J. Mech. Phys. Solids* **146**, 104201 (2021).
34. S. Nezamabadi, T. H. Nguyen, J. Y. Delenne, F. Radjai, Modeling soft granular materials. *Granular Matter* **19**, 1–12 (2017).
35. S. Nezamabadi, F. Radjai, J. Averseng, J. Y. Delenne, Implicit frictional–contact model for soft particle systems. *J. Mech. Phys. Solids* **83**, 72–87 (2015).
36. J. Zhang, X. Chen, J. Zhang, P. Jitsangiam, X. Wang, Dem investigation of macro- and micro-mechanical properties of rigid-grain and soft-chip mixtures. *Particuology* **55**, 128–139 (2021).
37. O. Bouillanne *et al.*, How vorticity and agglomeration control shear strength in soft cohesive granular flows. *Granular Matter* **24**, 1–17 (2022).
38. Z. Hu, Y. Shi, N. Guo, Z. Yang, Micromechanical investigation of the shear behaviors of sand–rubber mixtures using a multibody meshfree method. *Granular Matter* **24**, 1–15 (2022).
39. H. K. Kim, J. C. Santamarina, Sand–rubber mixtures (large rubber chips). *Can. Geotech. J.* **45**, 1457–1466 (2008).
40. K. Taghizadeh, H. Steeb, S. Luding, V. Magnanimo, Elastic waves in particulate glass–rubber mixtures. *Proc. R. Soc. A* **477**, 20200834 (2021).
41. R. C. Hidalgo, C. U. Grosse, F. Kun, H. W. Reinhardt, H. J. Herrmann, Evolution of percolating force chains in compressed granular media. *Phys. Rev. Lett.* **89**, 205501 (2002).
42. K. Krishnaraj, P. R. Nott, Coherent force chains in disordered granular materials emerge from a percolation of quasilinear clusters. *Phys. Rev. Lett.* **124**, 198002 (2020).
43. S. C. Cowin, The relationship between the elasticity tensor and the fabric tensor. *Mech. Mater.* **4**, 137–147 (1985).
44. D. S. Bassett, E. T. Owens, K. E. Daniels, M. A. Porter, Influence of network topology on sound propagation in granular materials. *Phys. Rev. E* **86**, 041306 (2012).

45. A. M. Booth, R. Hurley, M. P. Lamb, J. E. Andrade, Force chains as the link between particle and bulk friction angles in granular material. *Geophys. Res. Lett.* **41**, 8862–8869 (2014).

46. L. Kondic *et al.*, Topology of force networks in compressed granular media. *Europhys. Lett.* **97**, 54001 (2012).

47. D. M. Walker *et al.*, Structural templates of disordered granular media. *Int. J. Solids. Struct.* **54**, 20–30 (2015).

48. V. Richefeu, M. S. El Youssoufi, E. Azéma, F. Radjai, Force transmission in dry and wet granular media. *Powder Technol.* **190**, 258–263 (2009).

49. C. Voivret, F. Radjai, J. Y. Delenne, M. S. El Youssoufi, Multiscale force networks in highly polydisperse granular media. *Phys. Rev. Lett.* **102**, 178001 (2009).

50. L. Zhang, Y. Wang, J. Zhang, Force-chain distributions in granular systems. *Phys. Rev. E* **89**, 012203 (2014).

51. J. Peters, M. Muthuswamy, J. Wibowo, A. Tordesillas, Characterization of force chains in granular material. *Phys. Rev. E* **72**, 041307 (2005).

52. S. Schmidt, M. Wiebicke, I. Herle, On the determination and evolution of fabric in representative elementary volumes for a sand specimen in triaxial compression. *Granular Matter* **24**, 1–9 (2022).

53. M. Wiebicke, I. Herle, E. Andò, G. Viggiani, Measuring the fabric evolution of sand-application and challenges. *Geotechnik* **44**, 114–122 (2021).

54. B. Zhao, J. Wang, E. Andò, G. Viggiani, M. R. Coop, Investigation of particle breakage under one-dimensional compression of sand using X-ray microtomography. *Can. Geotech. J.* **57**, 754–762 (2020).

55. Z. Karatza, E. Andò, S. A. Papanicolopulos, G. Viggiani, J. Y. Ooi, Effect of particle morphology and contacts on particle breakage in a granular assembly studied using X-ray tomography. *Granular Matter* **21**, 1–13 (2019).

56. D. Lee, N. Karadimitriou, M. Ruf, H. Steeb, Detecting micro fractures: A comprehensive comparison of conventional and machine-learning-based segmentation methods. *Solid Earth* **13**, 1475–1494 (2022).

57. Y. Xing *et al.*, X-ray tomography investigation of cyclically sheared granular materials. *Phys. Rev. Lett.* **126**, 048002 (2021).

58. S. Hasan *et al.*, Direct characterization of solute transport in unsaturated porous media using fast X-ray synchrotron microtomography. *Proc. Natl. Acad. Sci. U.S.A.* **117**, 23443–23449 (2020).

59. J. Baker, F. Guillard, B. Marks, I. Einav, X-ray rheography uncovers planar granular flows despite non-planar walls. *Nat. Commun.* **9**, 1–9 (2018).

60. S. A. Hall *et al.*, Can intergranular force transmission be identified in sand? *Granular Matter* **13**, 251–254 (2011).

61. R. Hurley, S. Hall, J. Andrade, J. Wright, Quantifying interparticle forces and heterogeneity in 3D granular materials. *Phys. Rev. Lett.* **117**, 098005 (2016).

62. C. Zhai *et al.*, Quantifying local rearrangements in three-dimensional granular materials: Rearrangement measures, correlations, and relationship to stresses. *Phys. Rev. E* **105**, 014904 (2022).

63. P. Wochner *et al.*, X-ray cross correlation analysis uncovers hidden local symmetries in disordered matter. *Proc. Natl. Acad. Sci. U.S.A.* **106**, 11511–11514 (2009).

64. M. Asadi, A. Mahboubi, K. Thoeni, Discrete modeling of sand–tire mixture considering grain-scale deformability. *Granular Matter* **20**, 1–13 (2018).

65. M. Asadi, K. Thoeni, A. Mahboubi, An experimental and numerical study on the compressive behavior of sand–rubber particle mixtures. *Comput. Geotech.* **104**, 185–195 (2018).

66. A. Ikeda, T. Kawasaki, L. Berthier, K. Saitoh, T. Hatano, Universal relaxation dynamics of sphere packings below jamming. *Phys. Rev. Lett.* **124**, 058001 (2020).

67. P. Rissone, E. I. Corwin, G. Parisi, Long-range anomalous decay of the correlation in jammed packings. *Phys. Rev. Lett.* **127**, 038001 (2021).

68. N. Kumar, S. Luding, Memory of jamming-multiscale models for soft and granular matter. *Granular Matter* **18**, 1–21 (2016).

69. D. Bi, J. Zhang, B. Chakraborty, R. P. Behringer, Jamming by shear. *Nature* **480**, 355–358 (2011).

70. S. Luding, So much for the jamming point. *Nat. Phys.* **12**, 531–532 (2016).

71. R. P. Behringer, B. Chakraborty, The physics of jamming for granular materials: A review. *Rep. Prog. Phys.* **82**, 012601 (2018).

72. F. Göncü, S. Luding, Effect of particle friction and polydispersity on the macroscopic stress–strain relations of granular materials. *Acta Geotech.* **8**, 629–643 (2013).

73. K. Taghizadeh Bajgirani, "Elasticity and wave propagation in granular materials," PhD thesis, University of Twente (2019).

74. E. T. Owens, K. E. Daniels, Sound propagation and force chains in granular materials. *Europhys. Lett.* **94**, 54005 (2011).

75. C. Zhai, E. B. Herbold, R. C. Hurley, The influence of packing structure and interparticle forces on ultrasound transmission in granular media. *Proc. Natl. Acad. Sci. U.S.A.* **117**, 16234–16242 (2020).

76. A. H. Clark, A. J. Petersen, L. Kondic, R. P. Behringer, Nonlinear force propagation during granular impact. *Phys. Rev. Lett.* **114**, 144502 (2015).

77. J. Liu, A. Wautier, S. Bonelli, F. Nicot, F. Darve, Macroscopic softening in granular materials from a mesoscale perspective. *Int. J. Solids Struct.* **193**, 222–238 (2020).

78. D. M. Walker *et al.*, Percolating contact subnetworks on the edge of isostaticity. *Granular Matter* **13**, 233–240 (2011).

79. S. Luding, Introduction to discrete element methods: Basic of contact force models and how to perform the micro–macro transition to continuum theory. *Eur. J. Environ. Civil Eng.* **12**, 785–826 (2008).

80. K. Taghizadeh, S. Luding, V. Magnanimo, DEM applied to soil mechanics. ALERT Doctoral School 2017 Discrete Element Modeling (2017), p. 129.

81. F. Radjai, F. Dubois, *Discrete-Element Modeling of Granular Materials* (Wiley-ISTE, 2011).

82. A. Larese, I. Iaconeta, B. Chandra, V. Singer, Implicit MPM and coupled MPM–FEM in geomechanics. *Comput. Mech.* **175**, 226–232 (2019).

83. X. Jia, Codalike multiple scattering of elastic waves in dense granular media. *Phys. Rev. Lett.* **93**, 154303 (2004).

84. S. R. Stock, *Micro-Computed Tomography: Methodology and Applications* (CRC Press, Boca Raton, FL, ed. 2, 2019).

85. P. J. Withers *et al.*, X-ray computed tomography. *Nat. Rev. Methods Primers* **1**, 18 (2021).

86. I. Zanette *et al.*, X-ray microtomography using correlation of near-field speckles for material characterization. *Proc. Natl. Acad. Sci. U.S.A.* **112**, 12569–12573 (2015).

87. E. Andò, S. A. Hall, G. Viggiani, J. Desrues, P. Bésuelle, Grain-scale experimental investigation of localised deformation in sand: A discrete particle tracking approach. *Acta Geotech.* **7**, 1–13 (2012).

88. M. Ruf, H. Steeb, An open, modular, and flexible micro X-ray computed tomography system for research. *Rev. Sci. Instrum.* **91**, 113102 (2020).

89. M. Ruf, K. Taghizadeh, H. Steeb, Multi-scale characterization of granular media by in situ laboratory X-ray computed tomography. *GAMM-Mitteilungen* **45**, e202200011

90. L. A. Feldkamp, L. C. Davis, J. W. Kress, Practical cone-beam algorithm. *J. Opt. Soc. Am. A* **1**, 612 (1984).

91. J. Vlassenbroeck *et al.*, Software tools for quantification of X-ray microtomography at the UGCT. *Nucl. Instrum. Methods Phys. Res. Sec. A* **580**, 442–445 (2007).

92. Dragonfly 2021.1. Object Research Systems (ORS) Inc., Montreal, QC, Canada, Dragonfly 3.1 (computer software) (2022).

93. A. G. Athanassiadis *et al.*, X-ray tomography system to investigate granular materials during mechanical loading. *Rev. Sci. Instrum.* **85**, 083708 (2014).

94. I. Vlahinić, E. Andò, G. Viggiani, J. E. Andrade, Towards a more accurate characterization of granular media: Extracting quantitative descriptors from tomographic images. *Granular Matter* **16**, 9–21 (2014).

95. M. Wiebicke, E. Andò, I. Herle, G. Viggiani, On the metrology of interparticle contacts in sand from X-ray tomography images. *Meas. Sci. Technol.* **28**, 124007 (2017).

96. M. Wiebicke, E. Andò, V. Šmilauer, I. Herle, G. Viggiani, A benchmark strategy for the experimental measurement of contact fabric. *Granular Matter* **21**, 1–13 (2019).

97. M. Wiebicke, E. Andò, G. Viggiani, I. Herle, Measuring the evolution of contact fabric in shear bands with X-ray tomography. *Acta Geotech.* **15**, 79–93 (2020).

98. M. Ruf, K. Taghizadeh, H. Steeb, micro-XRCT data sets and in situ measured ultrasonic wave propagation of a pre-stressed monodisperse rubber and glass particle mixture with 50% volume rubber content (2021). 10.18419/DARUS-2208. Accessed 26 September 2022.

99. M. Ruf, K. Taghizadeh, H. Steeb, micro-XRCT data sets and in situ measured ultrasonic wave propagation of a pre-stressed monodisperse rubber and glass particle mixture with 30% volume rubber content (2022). 10.18419/DARUS-2833. Accessed 30 November 2021.

100. M. Ruf, K. Taghizadeh, H. Steeb, micro-XRCT data sets and in situ measured ultrasonic wave propagation of pre-stressed monodisperse rubber and glass particle mixtures with 10%, 20%, 40%, and 60% volume rubber content: Sample 1 (2023). 10.18419/DARUS-3436. Accessed 4 May 2023.

101. M. Ruf, K. Taghizadeh, H. Steeb, micro-XRCT data sets and in situ measured ultrasonic wave propagation of pre-stressed monodisperse rubber and glass particle mixtures with 10%, 20%, and 30% volume rubber content: Samples 2 and 3 (2023). 10.18419/DARUS-3437. Accessed 4 May 2023.

Appendix C:
Nonuniqueness of Hydrodynamic Dispersion Revealed Using Fast 4D Synchrotron X-Ray Imaging

APPLIED PHYSICS

Nonuniqueness of hydrodynamic dispersion revealed using fast 4D synchrotron x-ray imaging

Yongqiang Chen[1], Holger Steeb[2], Hamidreza Erfani[1], Nikolaos K. Karadimitriou[2], Monika S. Walczak[1], Matthias Ruf[2], Dongwon Lee[2], Senyou An[1], Sharul Hasan[3], Thomas Connolley[4], Nghia T. Vo[4], Vahid Niasar[1]*

Experimental and field studies reported a significant discrepancy between the cleanup and contamination time scales, while its cause is not yet addressed. Using high-resolution fast synchrotron x-ray computed tomography, we characterized the solute transport in a fully saturated sand packing for both contamination and cleanup processes at similar hydrodynamic conditions. The discrepancy in the time scales has been demonstrated by the nonuniqueness of hydrodynamic dispersion coefficient versus injection rate (Péclet number). Observations show that in the mixed advection-diffusion regime, the hydrodynamic dispersion coefficient of cleanup is significantly larger than that of the contamination process. This nonuniqueness has been attributed to the concentration-dependent diffusion coefficient during the cocurrent and countercurrent advection and diffusion, present in contamination and cleanup processes. The new findings enhance our fundamental understanding of transport processes and improve our capability to estimate the transport time scales of chemicals or pollution in geological and engineering systems.

INTRODUCTION

The characterization of solute transport is important to many subsurface processes, such as contaminant hydrogeology (*1*) and soil remediation (*2*, *3*), seawater intrusion into coastal aquifers (*4*), leachate of fertilizer nutrients in agricultural systems (*5*), as well as in engineering applications (*6*, *7*), such as enhanced oil recovery (*8*). There are two key processes in the named applications: increase in the resident chemical concentration as a result of injection of chemicals at higher concentrations compared to the initial resident concentration referred to as loading (e.g., saltwater intrusion) and decrease in the resident chemical concentration as a result of injection of chemicals at lower concentrations compared to the initial resident concentration referred to as unloading (e.g., soil cleanup or low-salinity waterflooding). There are studies in the literature showing longer unloading process compared to the loading process at the same injection rate. For example, De Smedt and Wierenga (*9*) showed that at the same injection rates, the unloading process required 1.4 times longer time compared to the loading process in an unsaturated glass bead packing [see figure 5 in (*9*)]. Similarly, Huang *et al.* (*10*) reported 2.5 times longer time for the unloading versus loading process in a 12.5-m-long, horizontal heterogeneous soil column. In a recent two-dimensional (2D) micromodel study, similar observations were reported (*11*) demonstrating larger hydrodynamic dispersion coefficient during the unloading compared to the loading. All former experimental studies show that even for nonreactive solutes under the same hydrodynamic conditions, the unloading process is much slower than the loading one. However, no clear and physically based explanation for the effect of transport direction (loading versus unloading) on the transport time scale has been provided. Different transport time scales mean different hydrodynamic dispersion coefficients during loading and unloading for the same hydrodynamic conditions, while in numerous analytical and numerical studies, an identical hydrodynamic dispersion coefficient has been applied to both processes, and nonunique hydrodynamic dispersion coefficient as a function of flow dynamics has not been accounted for (*12*, *13*).

Almost all reported 3D experimental measurements are point measurements, either with a probe inside or at the boundary of porous media with very little information (almost none) about the resident concentration field in the porous media. However, there are very few exceptions. Recently, 4D, high-resolution, synchrotron-based x-ray computed tomography (sXRCT) has been used to delineate the transport process under unsaturated (commonly referred to as two-phase flow) conditions in a glass bead packing (*14*). In addition, with the use of optical imaging (*15*) and the magnetic resonance imaging method (*16*–*18*), hydrodynamic dispersion and velocity field were studied in 3D glass bead packing. Here, we used fast, 4D, synchrotron x-ray imaging of single-phase flow experiments to provide two critical contributions that can lead to revisiting the theory of transport in geosystems. (i) The relation between the hydrodynamic dispersion coefficient and the pore velocity for loading and unloading is established and the nonunique behavior is explained, and (ii) a valuable dataset comprising 4D resident concentration fields at different injection rates for loading and unloading is provided.

RESULTS

Dynamic solute distribution during loading and unloading

The fast 4D x-ray imaging of solute transport generated a valuable dataset and the possibility to visualize the evolution of full concentration field at the pore scale. In Fig. 1, the 2D cross sections of the sand packing and the corresponding concentration field at different times, for loading and unloading, at the rate of 1.6 μl/s, respectively,

[1]Department of Chemical Engineering and Analytical Science, The University of Manchester, Manchester M13 9PL, UK. [2]Institute of Applied Mechanics (CE), University of Stuttgart, Stuttgart, Germany. [3]School of Chemical and Energy Engineering, Universiti Teknologi Malaysia, 81310 Johor Bahru, Johor, Malaysia. [4]Diamond Light Source Ltd., Diamond House, Harwell Science and Innovation Campus, Didcot, Oxfordshire, OX11 0DE, UK.
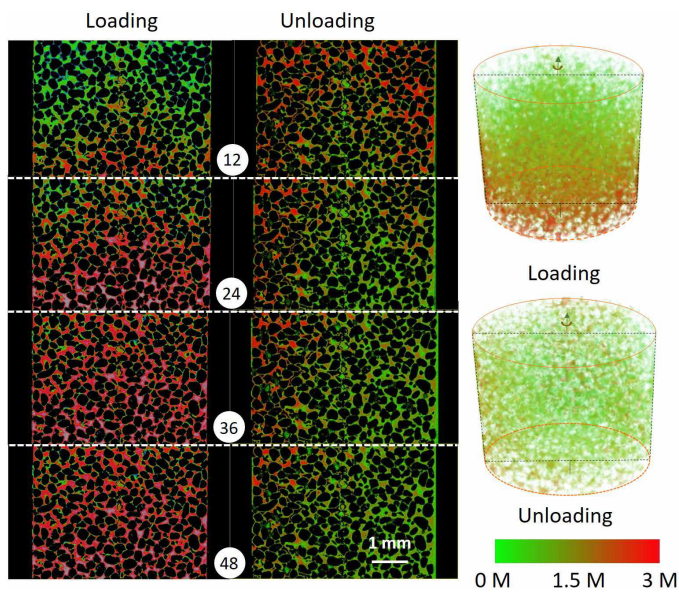*Corresponding author. Email: vahid.niasar@manchester.ac.uk

Fig. 1. 2D cross-sectional presentation of concentration field along the flow direction at an injection rate of 1.6 μl/s. The flow direction is from bottom to top, and the numbers in circles indicate time in seconds. The red to green color indicates the KI concentration in water from high (3 M) to low (0 M) concentrations. The right panel shows the 3D presentation of the concentration field for the same experiments.

are presented. To demonstrate the ratio of advection to diffusion, we used the pore-scale Péclet number. The pore-scale Péclet number is defined as $Pe = \frac{vL}{D}$, where v denotes the pore velocity, L is the characteristic length (pore size), and D is the diffusion coefficient. The peak pore body diameter (refer to fig. S2) is 90 μm, and the diffusion coefficient for KI in water is equal to 2.44×10^{-9} m^2/s (19). Using the pore velocity (estimated from the injection rate divided by the effective cross-sectional area), the Péclet number for the injection rate of 1.6 μl/s is 21.75, which does not correspond to a highly advective transport (20) but representative for many natural subsurface systems such as aquifers. In Fig. 1, the flow direction is upward, meaning from bottom to top. Red and green colors indicate high and low KI concentrations, respectively. During the loading process, we observed a relatively homogeneous global and local KI distribution. As shown in Fig. 1 (loading column), a parabolic shape of the KI concentration front is visible. This indicates a faster flow at the center of the sample compared to the sides of the sample. This was possible due to side wall (no flow) boundary conditions. In addition, note that the entrance effect (17) may lead to these concentration profiles too, which was also observed in the micromodel experiments (21). However, given that the inlet covered the whole cross section of the flow cell, the entrance effect was not expected to be considerable in these experiments.

Figure 1 (unloading column) shows four snapshots of the 2D concentration field during unloading for 12, 24, 36, and 48 s. Unlike the loading process, the KI concentration front during unloading is
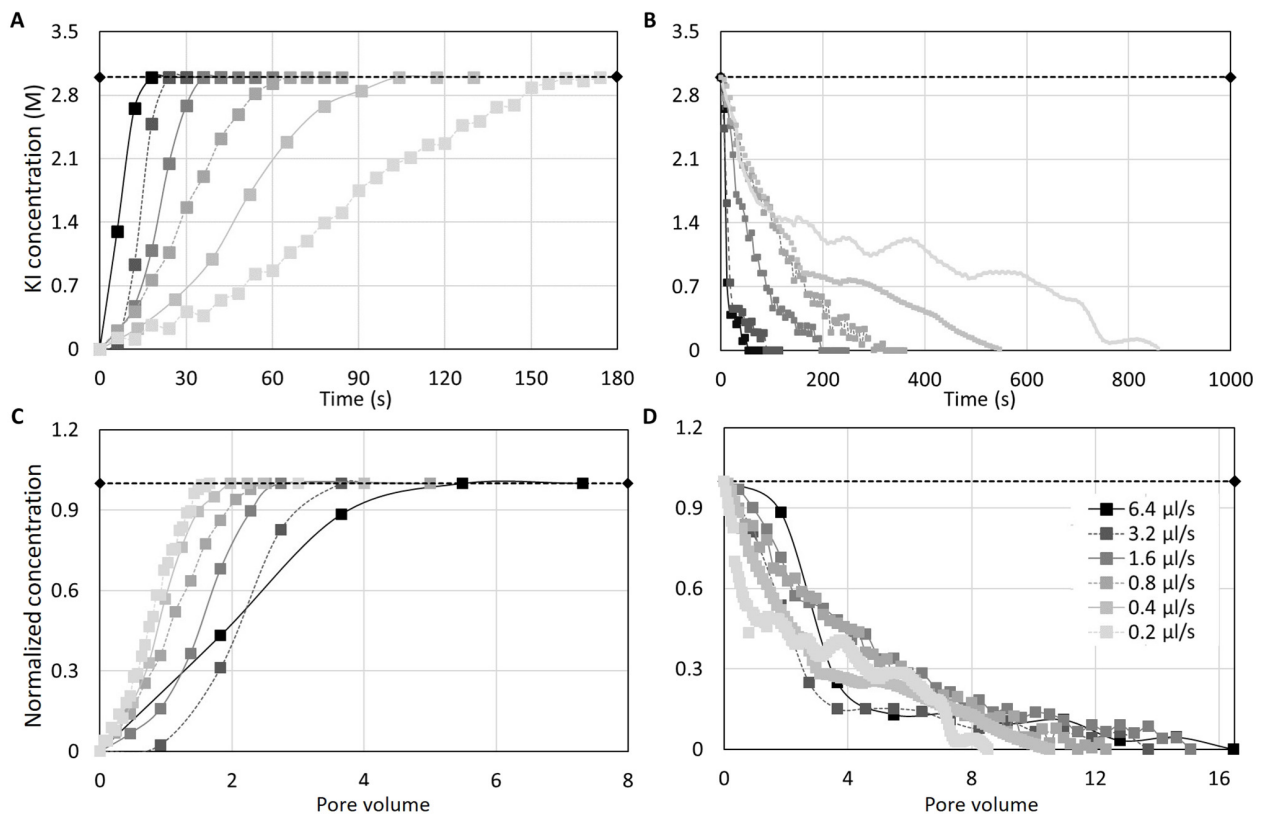

Fig. 2. Variation of the resident concentration within the field of view with time and pore volume, quantified on the basis of the sXRCT images. (**A**) The loading experiments at six injection rates. (**B**) The unloading experiments at six injection rates. The normalized average resident concentration (with respect to 3 M concentration) versus the injected pore volumes are shown for the loading (**C**) and unloading (**D**), respectively. The horizontal dash lines denote a reference resident concentration of 3.0 M.

rather irregular. For example, in the left section of the frame at 24 s, a high KI concentration remains in the sample, while the deionized water front reached the outlet of the field of view. The irregularity in the concentration distribution during the unloading was not related to the velocity field, as the sample packing and injection rates and boundary conditions were exactly identical to those during the loading process. Thus, comparing the concentration fields for loading versus unloading, we can hypothesize that the difference in the concentration fields is exclusively related to the interaction between advection and diffusion. This will be further investigated in the follow-up section.

Temporal evolution of average resident concentration

To address this hypothesis, we performed experiments at different injection rates corresponding to different Péclet numbers. The injection rates varied between 0.2 and 6.4 μl/s, corresponding to Péclet numbers varying between 2.7 and 87, respectively. The average resident concentrations versus time were estimated (Fig. 2). The experimental data show that even without macroscopic heterogeneity, the unloading process was around four to five times slower than the loading one for the same injection rate. Note that these results have been established on the basis of the averaging of the resident pore-scale concentration. For example, for the injection rate of 6.4 μl/s, the average resident KI concentration decreased from 3 to 0 M within 54 s, whereas the average resident KI concentration changed from 0 to 3 M during the loading process in 18 s. Just to establish a comparison basis, we estimated the times required to reach 50% of the final concentration for the loading cases (t_{50}^l) and the time to reach 50% of the initial concentration for the unloading cases (t_{50}^{ul}). The corresponding values for t_{50}^l were 9, 12, 42, 84, 102, and 150 s for injection rates of 6.4, 3.2, 1.6, 0.8, 0.4, and 0.2 μl/s, respectively. Similarly, values of t_{50}^{ul} were 45, 78, 156, 240, 450, and 762 s for the same injection rates as in the loading case, respectively. This leads to a delay ratio (t_{50}^{ul}/t_{50}^l) of 5, 6.5, 3.7, 2.85, 4.4, and 5.08 for the rates of 6.4, 3.2, 1.6, 0.8, 0.4, and 0.2 μl/s, respectively.

The average residual concentration during the loading process shows a smooth behavior. However, for lower fluxes such as 0.2 μl/s ($Pe = 2.7$), in which diffusion is the dominant transport mechanism, there were some fluctuations in the concentration curves. This might be due to the redistribution of concentration inside the field of view. However, it is not possible to assess the cause of the fluctuations for this specific case. To confirm that there was no instability effect due to large density contrast or centrifugal effect due to the rotation of the sample for imaging, we performed further analysis as reported in the Supplementary Materials. We can conclude that that the effect of density-dependent instability, viscosity contrast effect, and centrifugal force are negligible in the reported experiments.

The unloading process, especially for slow injection fluxes, showed long tailing. As an example, the average resident concentration decreased quickly from 3 to 1 M in 150 s for the injection rate of 0.4 μl/s. However, the dilution of the remaining 1 M required additional 396 s. This tailing is characteristic of a non-Fickian behavior, which is mostly pronounced at high rates where two distinct transport time scale (e.g., advective versus diffusive) of transport were observed (22–24). The presence of stagnant regions was even reported in fully saturated porous materials (25). However, the pore-scale x-ray images of this study did not show detectable stagnant regions. Thus, we do not expect considerable stagnant regions in this fully saturated homogeneous sand packing. Thus, the long tailing cannot be related

to the presence of a fully stagnant (diffusion-controlled) region. To compare the experiments based on a dimensionless time, we converted time to injected pore volumes using the following equation $Q \times t/V_p$, in which Q and V_p denote the volumetric flux and the pore volume, respectively. Normalized concentration curves versus the injected pore volumes are shown in Fig. 2 (C and D). Figure 2D shows that for higher fluxes during unloading, a tailing of the concentration is visible, which reflects the non-Fickian behavior. However, such a non-Fickian behavior is not visible during the loading process. This observation again implies the nonunique behavior of transport during the corresponding processes for the same injection rate and the same porous medium.

To explicitly illustrate this nonuniqueness, we estimated the corresponding hydrodynamic dispersion coefficients for each process and injection rate by fitting an analytical advection-dispersion equation. Note that the fitting results report the hydrodynamic dispersion as the summation of diffusion and mechanical dispersion. Details of the fitting procedure can be found in the Supplementary Materials. The results for the hydrodynamic dispersion coefficient versus the pore velocity (and equivalent Péclet number) are shown in Fig. 3. The hydrodynamic dispersion coefficient for loading (D^l) is smaller than the hydrodynamic dispersion for the unloading process (D^{ul}). The difference between D^l and D^{ul} can be larger than one order of magnitude for some cases. However, the difference slightly decreases with the decrease in the injection flux (i.e., Péclet number). This again emphasized the fact that difference in values of hydrodynamic dispersion is induced by the competition between the advection and diffusion transport.

DISCUSSION

New knowledge about the hydrodynamic dispersion

These results highlight the critical gaps and potential misconceptions in the application of hydrodynamic dispersion for practical problems: (i) A nonunique relation between the hydrodynamic dispersion coefficient and pore velocity has been identified for
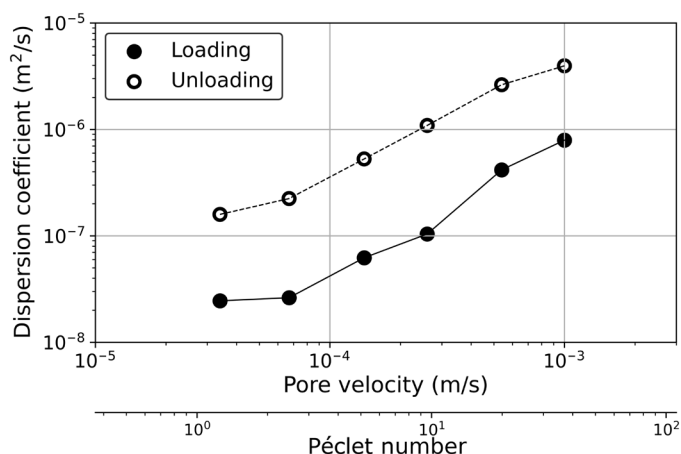

Fig. 3. Nonuniqueness of hydrodynamic dispersion coefficient for loading and unloading experiments at the same injection rates. The figure shows the hydrodynamic dispersion coefficient versus the pore velocity and the corresponding Péclet number for loading and unloading processes. Hydrodynamic dispersion coefficient and pore velocity were estimated by fitting the advection-dispersion equation as explained in the Supplementary Materials.
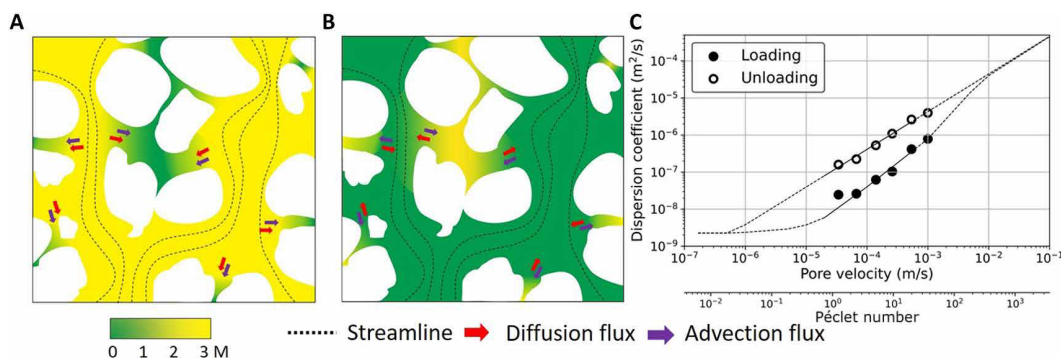
Fig. 4. Proposed transport diagram delineating the nonuniqueness of hydrodynamic dispersion coefficient as a function of Péclet number. Schematic pore-scale presentation of cocurrent and countercurrent advective and diffusive transport mechanisms during loading (**A**) and unloading (**B**), respectively. Proposed transport diagram (**C**), which suggests for large and very small Péclet numbers, the discrepancies between the loading and unloading hydrodynamic dispersion coefficient reduce.

loading versus unloading, even for such a small sand packing, which has not been addressed in the literature before. (ii) With a decrease in the Péclet number, the difference between D^l and D^{ul} becomes smaller.

Hydrodynamic dispersion is, by definition, the summation of molecular diffusion and mechanical dispersion, and this is what is being shown in Fig. 4C. For large Péclet numbers, mechanical dispersion is the dominant part, so the two processes, loading and unloading, should exhibit similar behaviors. Assuming that there is no spatial concentration heterogeneity, the same should stand for the case of very low Péclet number, where molecular diffusion is the dominant process. For intermediate Péclet numbers though, it is expected that the advective forces will create a heterogeneous concentration field, strongly affecting the corresponding molecular diffusion, depending on the process followed.

On the basis of this trend, it can be conjectured that for a mixed advection-diffusion regime, the countercurrent and cocurrent advection and diffusion transport leads to the observed difference, and with an increase in the Péclet number, the nonlinear interaction between diffusion and advection decreases. To be specific, the advection and diffusion act in the same direction during the loading process (as shown in Fig. 4). However, given that diffusion is governed by the chemical potential gradient, it acts in the opposite direction of advection during unloading (Fig. 4). We conjecture that because of a nonlinear interaction between these two transport processes, a significant difference between the time scales of loading and unloading processes was resulted. A potential reason for the nonlinearity can be the concentration-dependent diffusion coefficient, which has been formerly addressed in the literature (*26*) but was considered negligible in the hydrodynamic dispersion for porous media applications. Dunlop and Stokes (*19*), Carey *et al.* (*27*), and other literature (*19*, *27–29*) showed that concentration-dependent diffusion coefficients indicate a decreasing diffusion coefficient with the increase in KI concentration. We performed a molecular dynamics simulation, and a similar trend was verified (refer to the Supplementary Materials). Given the spatial distribution of concentration field during loading and unloading, the diffusion transport during loading and unloading will not be spatially similar. However, the heterogeneous concentration field is highly controlled by the advective flux. This leads us to the hypothesis that for a range of Péclet numbers, a nonunique hydrodynamic dispersion versus

Péclet number for loading versus unloading is expected. These results and explanations led us to propose a new transport diagram (Fig. 4C). Because, with increasing Péclet number, the difference between D^{ul} and D^l decreases, it is justifiable to assume that a unique hydrodynamic dispersion coefficient would be obtained for high Péclet numbers ($\gg 100$), as in this case, diffusion is negligible. In addition, for no-flow conditions, transport will be purely controlled by a unique diffusion coefficient. On the basis of the results and physical-based justifications, we propose a transport diagram that has not been addressed in the literature. Note that the range of pore velocity and pore-scale Péclet number in many transport phenomena in geological systems such as aquifers are within the loop presented in Fig. 4C (*30*). The result is of significant importance for better estimation of the time scale of transport processes especially the unloading processes related to contaminant hydrogeology, soil remediation, and groundwater quality modeling.

MATERIALS AND METHODS
Materials and fluids
Deionized water and a 3 M KI water solution were used for the loading and unloading experiments. The porous medium was a sand packing made of acid-washed sand grains sieved using a 150-µm sieve size. The sample diameter was 4.5 mm, and the imaged height was 3.47 mm with a porosity of 37.8% and pore volume of 21 µl. To derive the pore size distribution, we extracted the pore network from the XRCT images using the maximal ball algorithm (refer to the Supplementary Materials) (*31*). The extracted pore network had 6452 pore bodies and 24,205 throats. The histogram (with 100 bins) and the cumulative probability distribution of pore radii are shown in fig. S2. There are two peaks in the pore size distribution histogram, representing the pore throat and pore body radii with 10 and 45 µm, respectively. An intrinsic permeability of 4.8×10^{-12} m² was estimated from flow field simulations.

Experimental setup and imaging
The key feature of the experiments and this study is the reconstruction of the in situ concentration field based on sXRCT that provided the microscale, spatiotemporal information of transport for different injection fluxes. To quantify the transient variation of solute

concentration, we performed 4D fast sXRCT during transport processes. We used monochromatic sXRCT at the Diamond Light Source, beamline I12 (*32*) to establish the correlation between the concentration and CT number (referred to as the calibration curves) and achieve high-resolution images in time (3 s of scanning and 3 s of data acquisition time) and space (3.25 μm) with minimum artifacts. Following the methodology established by Hasan *et al.* (*24*), the reference time (*t* = 0) was established on the basis of the change in the x-ray intensity value for the field of view. The calibration curve established for the sXRCT values versus the actual KI solution concentration for the range of 0.1 to 3 M did not show any sensitivity of the errors to the concentration. Given the similar sensitivity of XRCT values at high and low concentrations for the loading and unloading, within the selected range of KI, start and end times were determined.

For each scanning frame, the sample was projected 600 times with the photon energy of 53 keV, with each projection lasting for 0.005 s. The raw data were reconstructed using I12 in-house Python codes (*33*). A data-processing pipeline includes a flat-field correction; zinger removal (*33*), which is a process for removing the image artifact in the form of a bright straight or zinger; ring artifact removal (*34*); denoising by a low-pass filter (*33*); automated determination of the center of rotation (*35*); and reconstruction using a direct Fourier inversion method (*36, 37*). The reconstructed data were then prepared for segmentation and statistical analysis. Note that during the imaging of one full scan (3 s), the concentration field would evolve too. Thus, the reconstructed image is the integration of all the projections (0.005 s per projection) of the scanning period (3 s). After 600 projections, the collected data would be averaged to get the responding x-ray intensity at each location of the sample. The fluid distribution was assumed not to change markedly in this short projection time for the slow flow rates. However, because of this technical limitation, it was not possible to image the transport of solutes at injection rates higher than 6.4 μl/s. Nevertheless, yet at high flow rate (such as 6.4 μl/s), x-ray imaging can still capture the dynamic evolution of KI concentration field.

The experimental setup is schematically shown in fig. S1. The flow cell was made of polyether ether ketone with dimensions of 4.8 mm in diameter and 50 mm in height, filled with fine sand grains. The flow cell was connected to two syringe pumps for the injection of deionized water and the KI solution. There was a back pressure of 0.5 bar to avoid the gas bubble generation during the exposure to high-energy x-ray radiation. The sample was positioned in the vertical direction and injection was from the bottom of the sample. To prepare the clean water-saturated sample, the sample was saturated with deionized water at a high injection rate of 10 μl/s. Samples saturated with the KI solution were initiated at the same rate.

Each experiment was continued at excessive time to accommodate hundreds of pore volume. After the initialization of the samples, either loading or unloading was performed: injection of 3 M KI solution at a controlled rate into the sample filled with deionized water (referred to as loading) or injection of deionized water at a controlled rate into the sand packing filled with 3 M KI solution (referred to as unloading). The loading and unloading experiments were performed at rates of 0.2, 0.4, 0.8, 1.6, 3.2, and 6.4 μl/s. During the whole injection, x-ray images were taken with 600 projections for each tomography, and, in total, more than 23 terabytes of data were produced and analyzed for imaging a field of view with a diameter of 4.5 mm and a height of 3.47 mm.

REFERENCES AND NOTES
1. M. J. Ascott, D. C. Gooddy, L. Wang, M. E. Stuart, M. A. Lewis, R. S. Ward, A. M. Binley, Global patterns of nitrate storage in the vadose zone. *Nat. Commun.* **8**, 1416 (2017).
2. R. Kumar, F. Heße, P. Rao, A. Musolff, J. Jawitz, F. Sarrazin, L. Samaniego, J. Fleckenstein, O. Rakovec, S. Thober, S. Attinger, Strong hydroclimatic controls on vulnerability to subsurface nitrate contamination across europe. *Nat. Commun.* **11**, 6302 (2020).
3. V. Joekar-Niasar, B. Ataie-Ashtiani, Assessment of nitrate contamination in unsaturated zone of urban areas: The case study of tehran, iran. *Environ. Geol.* **57**, 1785–1798 (2009).
4. A. D. Werner, C. T. Simmons, Impact of sea-level rise on sea water intrusion in coastal aquifers. *Groundwater* **47**, 197–204 (2009).
5. L. Harper, R. Sharpe, G. Langdale, J. Giddens, Nitrogen cycling in a wheat crop: Soil, plant, and aerial nitrogen transport. *Agron. J.* **79**, 965–973 (1987).
6. G. F. Froment, K. B. Bischoff, J. De Wilde, *Chemical Reactor Analysis and Design* (Wiley New York, 1990), vol. 2.
7. O. Levenspiel, Chemical reaction engineering. *Ind. Eng. Chem. Res.* **38**, 4140–4143 (1999).
8. R. Aziz, V. Niasar, H. Erfani, P. J. Martínez-Ferrer, Impact of pore morphology on two-phase flow dynamics under wettability alteration. *Fuel* **268**, 117315 (2020).
9. F. De Smedt, P. Wierenga, Solute transfer through columns of glass beads. *Water Resour. Res.* **20**, 225–232 (1984).
10. K. Huang, N. Toride, M. T. Van Genuchten, Experimental investigation of solute transport in large, homogeneous and heterogeneous, saturated soil columns. *Transp. Porous Media* **18**, 283–302 (1995).
11. H. Erfani Gahrooei, N. Karadimitriou, A. Nissan, M. Walczak, S. An, B. Berkowitz, V. Niasar, Process-dependent solute transport in porous media. *Transp. Porous Media* **140**, 421–435 (2021).
12. A. Polak, A. S. Grader, R. Wallach, R. Nativ, Chemical diffusion between a fracture and the surrounding matrix: Measurement by computed tomography and modeling. *Water Resour. Res.* **39**, 1106 (2003).
13. R. M. Greenwald, S. M. Gorelick, Particle travel times of contaminants incorporated into a planning model for groundwater plume capture. *J. Hydrol.* **107**, 73–98 (1989).
14. S. Hasan, V. Niasar, N. K. Karadimitriou, J. R. A. Godinho, N. T. Vo, S. An, A. Rabbani, H. Steeb, Direct characterization of solute transport in unsaturated porous media using fast x-ray synchrotron microtomography. *Proc. Natl. Acad. Sci. U.S.A.* **117**, 23443–23449 (2020).
15. M. Souzy, H. Lhuissier, Y. Méheust, T. Le Borgne, B. Metzger, Velocity distributions, dispersion and stretching in three-dimensional porous media. *J. Fluid Mech.* **891**, A16 (2020).
16. M. Deurer, I. Vogeler, B. E. Clothier, D. R. Scotter, Magnetic resonance imaging of hydrodynamic dispersion in a saturated porous medium. *Transp. Porous Media* **54**, 145–166 (2004).
17. A. Lehoux, S. Rodts, P. Faure, E. Michel, D. Courtier-Murias, P. Coussot, Magnetic resonance imaging measurements evidence weak dispersion in homogeneous porous media. *Phys. Rev. E* **94**, 053107 (2016).
18. J. Raimbault, P.-E. Peyneau, D. Courtier-Murias, T. Bigot, J. Gil Roca, B. Béchet, L. Lassabatère, Investigating the impact of exit effects on solute transport in macroporous media. *Hydrol. Earth Syst. Sci.* **25**, 671–683 (2021).
19. P. Dunlop, R. Stokes, The diffusion coefficients of sodium and potassium iodides in aqueous solution at 25°[1]. *J. Am. Chem. Soc.* **73**, 5456–5457 (1951).
20. M. Babaei, V. Joekar-Niasar, A transport phase diagram for pore-level correlated porous media. *Adv. Water Resour.* **92**, 23–29 (2016).
21. N. K. Karadimitriou, V. Joekar-Niasar, M. Babaei, C. A. Shore, Critical role of the immobile zone in non-fickian two-phase transport: A new paradigm. *Environ. Sci. Technol.* **50**, 4384–4392 (2016).
22. N. K. Karadimitriou, V. Joekar-Niasar, O. G. Brizuela, Hydro-dynamic solute transport under two-phase flow conditions. *Sci. Rep.* **7**, 6624 (2017).
23. S. An, S. Hasan, H. Erfani, M. Babaei, V. Niasar, Unravelling effects of the pore-size correlation length on the two-phase flow and solute transport properties: Gpu-based pore-network modeling. *Water Resour. Res.* **56**, e2020WR027403 (2020).
24. S. Hasan, V. Joekar-Niasar, N. K. Karadimitriou, M. Sahimi, Saturation dependence of non-fickian transport in porous media. *Water Resour. Res.* **55**, 1153–1166 (2019).
25. K. Coats, B. Smith, Dead-end pore volume and dispersion in porous media. *Soc. Pet. Eng. J.* **4**, 73–84 (1964).
26. D. W. McCall, D. C. Douglass, The effect of ions on the self-diffusion of water. I. Concentration dependence. *J. Phys. Chem.* **69**, 2001–2011 (1965).

27. A. E. Carey, S. W. Wheatcraft, R. J. Glass, J. P. O'Rourke, Non-fickian ionic diffusion across high-concentration gradients. *Water Resour. Res.* **31**, 2213–2218 (1995).

28. R. Matuura, Y. Koga, Self-diffusion of iodide ion and strontium ion in strontium iodide solutions. *Bull. Chem. Soc. Jpn.* **32**, 1143–1148 (1959).

29. H. S. Harned, R. L. Nuttall, The differential diffusion coefficient of potassium chloride in aqueous solutions. *J. Am. Chem. Soc.* **71**, 1460–1463 (1949).

30. V. Rønde, U. McKnight, A. Sonne, N. Balbarini, J. Devlin, P. Bjerg, Contaminant mass discharge to streams: Comparing direct groundwater velocity measurements and multi-level groundwater sampling with an in-stream approach. *J. Contam. Hydrol.* **206**, 43–54 (2017).

31. A. Q. Raeini, B. Bijeljic, M. J. Blunt, Generalized network modeling: Network extraction as a coarse-scale discretization of the void space of porous media. *Phys. Rev. E* **96**, 013312 (2017).

32. M. Drakopoulos, T. Connolley, C. Reinhard, R. Atwood, O. Magdysyuk, N. Vo, M. Hart, L. Connor, B. Humphreys, G. Howell, S. Davies, T. Hill, G. Wilkin, U. Pedersen, A. Foster, N. D. Maio, M. Basham, F. Yuan, K. Wanelik, I12: The joint engineering, environment and processing (JEEP) beamline at diamond light source. *J. Synchrotron Radiat.* **22**, 828–838 (2015).

33. N. Vo, R. Atwood, M. Drakopoulos, T. Connolley, Data processing methods and data acquisition for samples larger than the field of view in parallel-beam tomography. *Opt. Express* **29**, 17849–17874 (2021).

34. N. T. Vo, R. C. Atwood, M. Drakopoulos, Superior techniques for eliminating ring artifacts in x-ray micro-tomography. *Opt. Express* **26**, 28396–28412 (2018).

35. N. T. Vo, M. Drakopoulos, R. C. Atwood, C. Reinhard, Reliable method for calculating the center of rotation in parallel-beam tomography. *Opt. Express* **22**, 19078–19086 (2014).

36. J. D. O'Sullivan, A fast sinc function gridding algorithm for fourier inversion in computer tomography. *IEEE Trans. Med. Imaging* **4**, 200–207 (1985).

37. D. Gürsoy, F. De Carlo, X. Xiao, C. Jacobsen, Tomopy: A framework for the analysis of synchrotron tomographic data. *J. Synchrotron Radiat.* **21**, 1188–1193 (2014).

38. J. Schindelin, I. Arganda-Carreras, E. Frise, V. Kaynig, M. Longair, T. Pietzsch, S. Preibisch, C. Rueden, S. Saalfeld, B. Schmid, J.-Y. Tinevez, D. J. White, V. Hartenstein, K. Eliceiri, P. Tomancak, A. Cardona, Fiji: An open-source platform for biological-image analysis. *Nat. Methods* **9**, 676–682 (2012).

39. G. Bradski, A. Kaehler, *Learning OpenCV: Computer Vision with the OpenCV library* (O'Reilly Media Inc., 2008).

40. H. M. D. Agbogun, T. A. Al, E. M. A. Hussein, Three dimensional imaging of porosity and tracer concentration distributions in a dolostone sample during diffusion experiments using X-ray micro-ct. *J. Contam. Hydrol.* **145**, 44–53 (2013).

41. Y. Zhang, P. Mostaghimi, A. Fogden, A. Sheppard, A. Arena, J. Middleton, R. T. Armstrong, Time-lapsed visualization and characterization of shale diffusion properties using 4d x-ray microcomputed tomography. *Energy Fuel* **32**, 2889–2900 (2018).

42. M. T. Van Genuchten, *Analytical Solutions of the One-Dimensional Convective-Dispersive Solute Transport Equation* (no. 1661, U.S. Department of Agriculture, Agricultural Research Service, 1982).

43. E. Lindeberg, D. Wessel-Berg, Vertical convection in an aquifer column under a gas cap of CO_2. *Energy Convers. Manag.* **38**, S229–S234 (1997).

44. M. C. K. Kim, Onset of buoyancy-driven convection in a variable viscosity liquid saturated in a porous medium. *Chem. Eng. Sci.* **113**, 77–87 (2014).

45. S. Plimpton, Fast parallel algorithms for short-range molecular dynamics. *J. Comput. Phys.* **117**, 1–19 (1995).

46. A. I. Jewett, D. Stelter, J. Lambert, S. M. Saladi, O. M. Roscioni, M. Ricci, L. Autin, M. Maritan, S. M. Bashusqeh, T. Keyes, R. T. Dame, J.-E. Shea, G. J. Jensen, D. S. Goodsell, Moltemplate: A tool for coarse-grained modeling of complex biological matter and soft condensed matter physics. *J. Mol. Biol.* **433**, 166841 (2021).

47. H. J. C. Berendsen, J. R. Grigera, T. P. Straatsma, The missing term in effective pair potentials. *J. Phys. Chem.* **91**, 6269–6271 (1987).

48. S. Koneshan, J. C. Rasaiah, R. M. Lynden-Bell, S. H. Lee, Solvent structure, dynamics, and ion mobility in aqueous solutions at 25 °C. *J. Phys. Chem. B.* **102**, 4193–4204 (1998).

Curriculum Vitae

Personal data:

Name:	Matthias Ruf
Date of birth:	October 24, 1988
Place of birth:	Singen (Hohentwiel), Germany
Nationality:	German
Parents:	Hans Jürgen Ruf and Renate Ruf
Siblings:	Isabelle Ruf

Education:

08/1995 – 02/1997	elementary school "Grundschule Überlingen am Ried", Singen (Hohentwiel), Germany
03/1997 – 07/1999	elementary school "Grundschule Orsingen-Nenzingen", Orsingen-Nenzingen, Germany
08/1999 – 06/2008	secondary school "Nellenburg Gymnasium", Stockach, Germany
06/2008	degree: "Allgemeine Hochschulreife" (high school diploma)
07/2008 – 07/2009	paramedic professional training at the DRK LV Badisches Rotes Kreuz e. V. Landesrettungsschule Bühl, and DRK KV Konstanz e. V., Germany
07/2009	degree: "Rettungssanitäter" (paramedic certificate)
10/2011 – 10/2014	bachelor studies in aeronautical engineering at Hamburg University of Applied Sciences, Germany
10/2014	degree: "Bachelor of Engineering (B.Eng.) Flugzeugbau"
04/2013 – 09/2020	bachelor studies in business administration and economics at the FernUnversität in Hagen, Germany
09/2020	degree: "Bachelor of Science (B.Sc.) Wirtschaftswissenschaft"
10/2014 – 02/2017	master studies in mechanical engineering at Clausthal University of Technology, Germany
02/2017	degree: "Master of Science (M.Sc.) Maschinenbau"

Voluntary social year:

08/2008 – 07/2009   voluntary social year and practical paramedic training at the
DRK KV Konstanz e. V., Germany

Professional occupation:

08/2009 – 03/2011   paramedic (ambulance and emergency rescue service) at the
DRK KV Konstanz e. V., Germany

03/2014 – 08/2014   internship and bachelor's thesis at the
Composite Technology Center (CTC) GmbH
(an Airbus Company), Stade, Germany

05/2017 – 12/2017   research assistant at the Institute of Aircraft Design,
University of Stuttgart, Germany

01/2018 – today   research and teaching assistant at the
Institute of Applied Mechanics (Civil Engineering),
University of Stuttgart, Germany

Presently published contributions in this report series

IAM 1   Matthias Leuschner: *Numerically Efficient Computational Homogenization: Fourier-Accelerated Nodal Solvers and Reduced Basis Model Order Reduction*, 2018.

IAM 2   Daniel Vallicotti: *Magneto-Electro-Mechanical Coupling Phenomena Across Multiple Length Scales: Variational Framework and Stability Analysis*, 2019.

IAM 3   Lukas Böger: *Saddle-Point and Minimization Principles for Diffusion in Solids: Phase Separation, Swelling and Fracture*, 2020.

IAM 4   Matthias Rambausek: *Magneto-Electro-Elasticity of Soft Bodies Across Scales*, 2020.

IAM 5   Ashish Sridhar: *Phase-Field Modeling of Microstructure and Fracture Evolution in Magneto-Electro-Mechanics*, 2020.

IAM 6   Osorno Tejada, Maria Camila: *Multiscale Modelling of Hydro-Mechanical Coupling in Porous Media*, 2021.

IAM 7   Malte Sauerwein: *Simulation of Coupled Transfer and Transport Phenomena in Multi-Phase Materials with Application to Polymer Gels*, 2021.

IAM 8   Stephan Teichtmeister: *Variational Methods for Dissipative Multifield Problems in Solid Mechanics*, 2021.

IAM 9   Oliver Kunc: *Finite Strain Hyperelastic Multiscale Homogenization via Projection, Efficient Sampling and Concentric Interpolation*, 2021.

IAM 10   Patrick Schmidt: *Hydro-Mechanical Coupling of Flow in Deformable High-Aspect Ratio Fractures*, 2022.

IAM 11   Daniel Kienle: *Phase-Field Modeling of Multi-Field Problems with Applications to Hydraulic-Elastic-Plastic Fracturing*, 2022.

IAM 12   Felix Selim Göküzüm: *Fast Solvers for Homogenization Problems: Fast Fourier Transform- and Neural Network-Based Approaches*, 2022.

IAM 13   Aref Nateghi: *A View of the Interplay Between Chemistry and Mechanics: Strain-Induced Crystallization in Rubbers and Thermo-Chemo-Mechanical Modeling of Electrode Particles in Lithium-Ion Batteries*, 2023.

IAM 14   Matthias Ruf: *Experimental Multi-Scale Characterization Using Micro X-Ray Computed Tomography*, 2023.

The effective mechanical and hydro-mechanical behavior of porous media, granular solids, and related materials with complex morphologies is intimately linked to their internal microstructure on the pore/grain scale. For microstructural characterization, transmission micro X-Ray Computed Tomography (µXRCT) has emerged as a crucial three-dimensional imaging technique that can provide structural information from the micrometer to centimeter scale. Due to its non-destructive nature, it can be excellently combined with time-dependent investigations, either ex situ or in situ. This allows to study many physical phenomena in more detail and consequently to understand them more comprehensively. In order to be able to perform such multi-scale studies, a modular, open, and versatile lab-based µXRCT system with an integrated universal testing machine was developed. With this, in situ compressive, tensile, and torsional studies as well as their combinations can be performed. Employing the established system, various multi-scale phenomena from different material classes (rocks, foams, granular media) are motivated and partly investigated in more detail.